UNIVERSITY OF CALIFORNIA, SAN DIEGO

Experimental and Computational Methods for the Analysis of the Mechanical Function of Marine Mammal Auditory Structures

A dissertation submitted in partial satisfaction of the
requirements for the degree
Doctor of Philosophy

in

Structural Engineering

by

Stephen Patrick Oberrecht

Committee in charge:

Professor Petr Krysl, Chair
Professor John Hildebrand
Professor Hyonny Kim
Professor Francesco Lanza di Scalea
Professor Michael D. Todd

2014

The dissertation of Stephen Patrick Oberrecht is approved, and it is acceptable in quality and form for publication on microfilm and electronically:

_____

_____

_____

_____

_____
Chair

University of California, San Diego

2014

DEDICATION

To my loving wife Kimberly, and to my delightful boys Jackson and Truman.

EPIGRAPH

Convictions are more dangerous foes of truth than lies.

—Friedrich Nietzsche

TABLE OF CONTENTS

LIST OF FIGURES

LIST OF TABLES

LIST OF SYMBOLS

α_i Stabilization factor: the fraction of the rigid part of the material compliance that is shifted to flexible part for stabilization.

$\bar{B}$ "B-bar," the effective strain-displacement operator used in B-bar finite element methods.

β Newmark-Beta parameter for displacement predictor.

δ Phase shift between stress and strain.

δ_i Cantilever beam deflection at $x = x_i$.

δ_{ij} Kronecker delta.

$\dot{u}_n^i$ The velocity of i^{th} DOF at the n^{th} times-step.

ε Infinitesimal or Cauchy strain.

ε_0 Initial or reference strain.

η Viscosity, as used in Maxwell and Kelvin-Voigt models.

η' The dynamic viscosity.

Γ The boundary of the computational domain, typically a two dimensional surface.

γ Infitesimal shear strain.

γ Newmark-Beta parameter for velocity predictor.

γ_0 Initial or reference shear strain.

γ_i Principal value (eigenvalue) of the compliance matrix.

κ The elastic bulk modulus.

$[\mathbf{C}]$ Damping matrix.

$[\mathbf{K}]$ Stiffness matrix.

$[\mathbf{M}]$ Mass matrix.

$[\mathbf{S}]$ $[\mathbf{M}]+\gamma h[\mathbf{C}]+\beta h^2[\mathbf{K}]$, A Newmark-Beta solution matrix.

$\ddot{\mathbf{u}}$ Acceleration, (second time derivative of displacement).

$\dot{\mathbf{u}}$ Velocity, (time derivative of displacement).

$\mathbf{F_0}$ Amplitude vector of the MDOF sinusoidal excitation force.

$\mathbf{f_k}$ Kinetic frictional force vector.

$\mathbf{f_s}$ Static frictional force vector.

$\mathbf{f_{sin}}(t)$ Sinusoidal excitation force vector MDOF.

$\mathbf{u}$ Displacement.

$\mathscr{U}$ Total potential energy of an infinitesimal deformable elastic body.

$\mathscr{U}_\xi$ Strain energy limit value arising from Richardson's extrapolation.

$\mathbf{D}$ Elasticity matrix, in Voigt-Mandel notation.

$\mathbf{D}_d$ The flexible, deviatoric, component of the nearly incompressible isotropic elasticity matrix (Voigt-Mandel).

$\mathbf{D}_f$ The flexible component of the elasticity matrix (Voigt-Mandel).

$\mathbf{D}_r$ The stiff component of the elasticity matrix (Voigt-Mandel).

$\mathbf{D}_v$ The stiff, dilational, component of the nearly incompressible isotropic elasticity matrix (Voigt-Mandel).

$\mathbf{I}_d$ “Deviatoric,” or flexible component projection matrix in 3-field formulation.

$\mathbf{N}_p$ The finite element basis functions for the effective stress variable in the 3-field formulation.

$\mathbf{N}_v$ The finite element basis functions for the effective strain variable in the 3-field formulation.

ν_{ij} The i-j component of Poisson’s ratio in orthotropic elasticity.

Ω The computational domain, typically a three dimensional volume.

ω Angular frequency in radians per second.

ω_d Damped natural angular frequency.

ω_n Undamped natural angular frequency.

$\Phi(th, \nu)$ Discrete stiffness to shear modulus conversion factor as a function of thickness and Poisson’s ratio.

$\Phi(th, E)$ Discrete stiffness to shear modulus conversion factor as a function of thickness and Young’s modulus.

Ψ Strain energy error.

ρ Density (mass per unit volume).

σ_0 Initial or reference stress.

ε_v Effective constrained strain.

σ Stress.

τ Period of harmonic motion.

τ_{shear} Shear stress.

ε	Vector representation of the second order strain tensor (Voigt-Mandel).
σ	Vector representation of the second order stress tensor (Voigt-Mandel).
σ_d	The deviatoric stress vector (Voigt-Mandel).
m_i	Principal direction (eigenvector) of the nearly incompressible isotropic compliance matrix.
v_i	Principal direction (eigenvector) of the compliance matrix.
ζ	Damping ratio.
C	Viscous damping coefficient.
c_{mat}	Speed of sound in a material.
E	Young's modulus.
E'	Young's storage modulus.
E''	Young's loss modulus.
E^*	Complex Young's modulus.
E_i	The ith component of Young's modulus in orthotropic elasticity.
$Error$	A defined error quantity.
f	Frequency in Hertz.
f_k	Kinetic frictional force 1DOF.
f_k^i	The kinetic frictional force of i^{th} DOF.
f_s	Static frictional force 1DOF.
f_s^i	The static frictional force of i^{th} DOF.

$f^i_{sin}(t_{n+1})$ The excitation force of the i^{th} DOF at the n^{th} times-step.

G Shear modulus.

G' Shear storage modulus.

G'' Shear loss modulus.

G^* Complex Shear modulus.

G_{ij} The i-j component of the shear modulus in orthotropic elasticity.

K Stiffness.

K_i Effective bulk modulus.

M Mass.

p Effective constrained stress.

P_i The i^{th} polynomial coefficient where $f(x) = P_1x^n + P_2x^{n-1} + ... + P_n$.

$R_i(\theta)$ Three dimensional rotation matrix about the ith axis by angle θ.

t Time, in seconds.

$tan\delta$ "Tan delta" a measure of frequency dependent viscosity.

u_x The x-component of Lagrangian displacements.

u_y The y-component of Lagrangian displacements.

u_z The z-component of Lagrangian displacements.

u_ξ Maximum displacement limit value arising from Richardson's extrapolation.

u_{max} Maximum displacement.

v^i_{stick} The sticking velocity of i^{th} DOF.

F_0 Amplitude of the 1DOF sinusoidal excitation force.

$f_{sin}(t)$ 1DOF Sinusoidal excitation force.

f_{n+1}^{i} The total force of the i^{th} DOF at the $n+1^{st}$ times-step.

C3D20 ABAQUS's Quadratic serendipity hexahedral elements.

C3D20R ABAQUS's Quadratic serendipity hexahedral elements with reduced integration.

C3D8 ABAQUS's Linear hexahedral elements.

C3D8H ABAQUS's Linear hexahedral hybrid elements.

C3D8I ABAQUS's Quadratic hexahedral element) with reduced integration.

C3D8I ABAQUS's Quadratic hexahedral elements with incompatible modes.

C3D8IH ABAQUS's Linear hexahedral hybrid elements with incompatible modes.

H20 Quadratic serendipity hexahedral elements.

H20R Quadratic serendipity hexahedral elements with reduced integration.

H27 Quadratic hexahedral elements.

H64 Cubic hexahedral (elements).

H8 Linear hexahedral elements.

H8-3F6KS Presented linear 3-field spectral λ (eigenvalue) scaled hexahedral elements.

H8-3F6KU Presented linear 3-field uniform λ (eigenvalue) scaled hexahedral elements.

H8-3F6MS Presented linear 3-field spectral **M** (eigenvector) scaled hexahedral elements.

H8-3F6MU Presented linear 3-field uniform **M** (eigenvector) scaled hexahedral elements.

T10 Quadratic tetrahedral elements.

ACKNOWLEDGEMENTS

I would like to thank my adviser Professor Petr Krysl for his unfailing ability to provide cunning insight, relevant suggestions, benevolent patience, and project support. On innumerable occasions he both took the time to teach me, and allowed the time for me to learn. If he didn't have an answer to one of my questions he invariably had a book that did. He has a rare combination of intelligence and kindness that makes his leadership natural.

My doctoral committee deserves my sincere gratitude. Professor Hyonny Kim was exceedingly gracious in allowing me to occupy prime real estate in his laboratory while I worked on the design of the my experimental device. Dr. John Hildebrand was of great help from the inception of the experimental component of this work and his research laid much of the groundwork for the tissue characterization efforts. Professors Michael Todd and Francesco Lanza Di Scalea have helped me on numerous occasions and I have benefited from their efforts and talents as top engineering instructors.

I would also like to thank Dr. Christofer Latham for his guidance. He would often drop by and offer casual insights about instrumentation design, programming, or calibration that would help immensely–if not that day, another. I would like to thank Professor Yuri Bazilevs for his help with methods for fully coupled thermo-elasticity.

Mike Weise at the Office of Naval Research deserves special acknowledgement for funding this research. Thanks are also extended to Lindsay Walton and Jenniffer Bourgeois, both of whom worked hard to help me to order and catalog the expenses of the hundreds of components that were needed to fabricate my experimental equipment.

Dr. Jan Novák has been a great source of advice and a critical ear for ideas, both good and bad.

Dr. Maya Yamato deserves my gratitude both for sharing her enormous enthusiasm for Cetacean acoustics, and for providing me with a skinny baker's dozen beautiful original references on the history of whale research. Her research in the area of baleen whale acoustics has been of great interest to me.

The real fruits of this endeavor have often hidden in casual discussions with other graduate students. In particular, I would like to thank (now Dr.) Bob Phillips, Poorya Mirkhosravi, Joel Lanning, Daniel Whistler, Sara White, Matt Bockman, Everett Criss, and the late Jiddu Bezarez-Chávez.

I owe the greatest debt of gratitude to my wife Kimberly, who has not only shown unwavering moral support but was on innumerable occasions forced to listen to me ramble on about some very dry research topics. I would like to thank my mom and dad for encouraging my education. I would like to thank my uncle Kenn; he taught me how to correctly use a semicolon. He should not, however, be held responsible for the lazy grammar and myopic engineer-shrift scattered throughout this dissertation. I also extend my sincere appreciation to my brother John, my sister Julie, and my Aunt Patricia.

Chapter 2 is in part a reprint of the material submitted for publication in, "Sound transmission validation and sensitivity studies in numerical models," *2013 Effects of Noise on Aquatic Life*. 20130276-000115. Steve Oberrecht, Petr Krysl, and Ted Cranford. 2013. The author of this dissertation was the primary author of this paper.

Chapter 6 is in part a reprint of the material published in, "B-bar Finite Element Methods for Anisotropic Elasticity," *International Journal for Numerical Methods in Engineering*. 2013; 00:1-15. Steve Oberrecht, Jan Novák, and Petr Krysl. 2013. The author of this dissertation was the primary author of this paper.

VITA

2007	B. S. in Structural Engineering, University of California San Deigo, Cum Laude
2007-2012	Graduate Teaching Assistant, University of California, San Diego
2009	M. S. in Structural Engineering, University of California San Deigo
2014	Ph. D. in Structural Engineering, University of California, San Diego

PUBLICATIONS

S. P. Oberrecht, J. Novák, P. Krysl. “B-bar Finite Element Methods for Anisotropic Elasticity,” *IJNME*, 314, 2013.

S. P. Oberrecht, P. Krysl, T. Cranford. “Sound transmission validation and sensitivity studies in numerical models” *2013 Effects of Noise on Aquatic Life*,0276-000115, 2013.

ABSTRACT OF THE DISSERTATION

Experimental and Computational Methods for the Analysis of the Mechanical Function of Marine Mammal Auditory Structures

by

Stephen Patrick Oberrecht

Doctor of Philosophy in Structural Engineering

University of California, San Diego, 2014

Professor Petr Krysl, Chair

Methods exploring the role of viscoelastic material characterization in vibroacoustic simulations of marine mammal structural responses are presented. This work is guided by a sensitivity analysis performed using the Vibroacoustic Toolkit VATK. In this sensitivity study, computational results are compared with published experimental results arising from the 1974 efforts of Kenneth S. Norris and George W. Harvey.

Experimental efforts include the development, calibration, and testing of a portable dynamical mechanical rheometer. For each sample tested the Young's modulus, shear modulus, and viscosity are sought. Mechanical forces, less than a pound, are applied to the tissue through an adhesive interfacial layer. A post-processing routine is developed and results are evaluated.

Certain anisotropic elastic materials, such as the homogenized model of a fiber-reinforced matrix, are nearly rigid under stresses applied in a direction of material rigidity–the resulting strains are comparatively small when viewed against the strains that would occur in response to otherwise directed stresses. Isotropic materials may have dilational rigidity, which we show to be a special case of this generalized treatment.

Some common finite element techniques are effective in dealing with volumetric locking, but are not suited to handle anisotropic materials that lock under non-hydrostatic stress states. The failure of the traditional B-bar method is attributable to the fundamental assumption that the mode of deformation to be relieved is one of near incompressibility. The proposed remedy exploits the spectral decomposition of the compliance matrix of the anisotropic material. The spectrum separates nearly-rigid and flexible modes of stress and strain leading naturally to a generalized selective reduced integration. What's more, this decomposition also enables a three-field formulation, of elastic strain energy conservation, which results in a B-bar method applicable to general anisotropic materials with nearly-rigid fibers.

When materials with multiple rigid fiber directions are treated with more than one spectrally defined deformation mode, element stabilization may be necessary. A working stabilization method is provided. This stabilization leads to a variable treatment model that also offers improved performance for isotropic materials that do not have rigid strain modes.

Chapter 1

Introduction and Background

Proceeded by a review of pertinent background fundamentals, this work is comprised of three distinct but related efforts to better understand and develop methods for the vibroacoustic analysis of aural structures in marine mammals: Part I, a sensitivity analysis comparing vibroacoustic simulations to published experimental results; Part II, the design, fabrication, and testing of an experimental rheometer; and Part III, improved methods to treat anisotropic materials simulated using the finite element method. Although the thrusts are in their essence analytical, a good portion of this dissertation is devoted to the development of a portable experimental device used to determine the viscoelastic properties of biological tissues.

1.1 Marine Mammals

The study of marine mammal acoustic pathways and is a rich and advancing science. While a great interest in the topic has been seen in recent years, the study of whale acoustics has a long history. There are several important topics within the study of underwater acoustics including the means of communication and the methods of ecolocation employed by marine mammals.

Whales (cetaceans) have advanced ears, which are considered to be the most derived of all the mammals. Toothed whales in particular are known to hear extraordinarily high frequen-

cies, up to 180 kHz in some species [2]. Baleen whales on the other hand are thought to have the ability to hear frequencies lower than any other animal [3].

In 1787, John Hunter observed that whale ears have the same structures as quadruped ears; they have an external opening, a tympanic membrane, the eustachian tube, ossicles, cochlea, and semicircular canals [4]. By the 1920s other scientists were comparing the skulls of current species to fossil cetaceans in search of an improved understanding of different evolutionary modifications that accompanied the move to an aquatic environment [5]. A hearty debate with numerous competing theories of the auditory mechanism of cetaceans ensued.

In 1962 Dudok Van Heel concluded that the ear canal is vestigal [6]. In 1984 Norris suggested that odontocetes receive sound by way “acoustic fats” surrounding their lower jaws [7]. In 1966 Purves insisted that the ear canal is indeed not vestigal [2]. In 1968 auditory evoked potentials were used to support Norris’ conclusion [8]. In 1970 McCormick and his colleagues stipulated that the ear canal is not functional after all and supported the bone conduction theory [9]. In 1974 Norris and Harvey used hydrophones implanted in dead porpoise heads to strengthen the lower jaw acoustic fat pathway; in 1988 Brill used a hood on the lower jaws of live odontocetes to perform tests that mark widening acceptance of Norris’ theory [10]. In 2001 Navy sonar is linked the beaching of whales in the Bahamas [2], and in 2009 it was determined that hearing loss can be attributed to intense and prolonged exposure to sonar [11]. In this dissertation, some attention will be given to the 1974 publication of Norris and Harvey. Emerging computational techniques are used to generate simulations which will be compared to the experimental results of their seminal work.

The continued study of marine mammal underwater acoustics is driven in part by concerns about how modern shipping and the use of sonar adversely affects the well being of marine mammals. Background noise may be making it difficult for whales to communicate over long distances and hindering the effectiveness of their echolocation. Furthermore, an essential step is understanding how residual aquatic noise affects which frequencies they can hear. It is hoped that these and similar efforts could lead to improved conservation measures [12]. The present work is concerned with engineering methods that will assist marine mammologists in

understanding the structural response of cetaceans to underwater acoustic signals such as sonar and shipping noise.

1.2 Auditory Systems

Marine mammal auditory systems are complex. Understanding acoustic pathways requires more than inspecting the details of the biological systems themselves. It also requires exploring structural dynamics, material science, and acoustic wave propagation. There are several important components that make up the aural and echolocation structures of marine mammals, and a brief review of the relevant biological terminology is warranted.

There are two suborders of Cetacians (whales): Odontoceti (toothed whales) and Mysticeti (baleen whales). Cetacians are descendants of land dwelling mammals. Odontecetes include the dolphins, porpoises, and orcas; they possess sharp teeth suited to hunting. The mystecetes, sometimes called the “great whales,” include some often endangered large species such as the blue whale, and humpback whale. Although sperm whales are indeed large, they are in fact toothed whales. Unlike odontocetes, mysticetes have sieve-like structures in the upper jaw that are adapted to filter nutrient rich plankton from the water. It is believed that Baleen whales are likely to be sensitive to lower acoustic frequencies than any other mammal alive today [3].

The auditory anatomy of cetaceans is highly adapted for underwater hearing. They don’t have outer ears, external pinnae, as do most terrestrial mammals. Their ear canals are no more than a very narrow channels, considered to be vestigial in odontocetes [13, 6, 9, 14]. As the animals evolved, the middle and inner ears found locations laterally outward from the skull and became encapsulated in the protective structure of the typanoperiotic complex [4, 15, 16]. Beyond these general anatomical structures the anatomies of auditory systems are suborder specific.

In 1964 scientist Ken Norris offered an important breakthrough suggesting that specialized fat bodies surrounding the lower jaws of dolphins provide a potential low impedance

pathway for sound to get to the ears. Eventually, after a series of validation studies, this hypothesis became widely accepted and is now the prevailing model of how sound enters the inner ears of odontocetes [12, 2].

Terrestrial mammals receive sound by way of an air filled outer ear and an impedance matching liquid filled middle ear. Odontocete aural structures have foregone the outer ear in lieu of multiple lobes of fatty tissue leading to the tympanoperiotic complex (TPC) [14]. The lobes of acoustic fats are separated by a very thin portion of the jaw bone called the “pan bone” whose precise role remains an issue of continued research [14, 17, 3].

Sound conduction through bone is not considered to be a significant acoustic pathway since there is, in most odontocetes, no connective tissue adherent among the skull and tympanoperiotic complex [18, 19, 20, 21]. When sound waves arrive at the inner ear of whales, a fluid filled spiral shaped channel (cochlea) sends the signals to the basilar membrane which stimulates hair cells. These in turn transmit electrical pulses to the brain to be perceived as distinctive sounds.

Odontoceti rely on acoustic fats to transmit sound from the surrounding water to the middle and inner ears. The most likely pathway for sound reception in odontocetes is through acoustic fats in the lower jaw, which connect the tympanic and periotic bones that make up the tympanoperiotic complex of the ears [14, 17, 22, 23].

These acoustic fats are comprised of inner and outer lobes covering different portions of the lower jaw (Norris 1968, Ketten 1994, 1997, Ridgway 1999). Some research suggests the existence of a third fat channel lateral to the TPC and near the external auditory meatus opening, which is sensitive to sonic excitation below 3 kHz (Bullock et al. 1968). Later research suggests that this opening is more sensitive to sound below 20 kHz [24]. The existence of this third acoustic fat channel was eventually verified using magnetic resonance imaging [17].

Two acoustic windows in the bottlenose dolphin were confirmed and characterized using auditory brainstem response latencies. The acoustic window was estimated to be near the meatus opening and to be sensitive to frequencies below 22 kHz. Sounds above 32 kHz were determined to be transmitted by the lower jaw [25].

The auditory pathways of Odontoceti have been well described, but are less known in Mysticeti whose tempanomandibular anatomies are known to be quite different. However, recent research suggests the existence of a fat body which is hypothesized to act as an important sound reception pathway. It lies lateral to the typanoperiotic complex of the minke whale (Yamato et al. 2012). In a noteworthy experiment, an area of the minke whale tympanic bone was stimulated with a 20 nm amplitude at frequencies ranging from 20 Hz to 50 kHz using a piezoelectric stack. This resulted in movement of the stapes bone, which provides an acoustic input to the cochlea [26, 3].

The mysticete ear fats and odontocete acoustic fats are likely homologous anatomical structures which underwent continued adaptation for high-frequency hearing and echolocation in the odontocetes. It is thought that exploration of both bone and soft-tissue anatomy around ear is instrumental in advancing our understanding of sound reception mechanisms in mysticetes [3].

There exists a significant and growing body of experimental work that focuses on the use of audiograms, or frequency threshold graphs measured by an audiometer, to identify the audible frequency ranges as well as frequencies of greatest auditory sensitivity in odontocetes. These results vary widely, and suggest a broad range of hearing from 0.25 to 200 kHz. The estimated frequencies of greatest sensitivity range anywhere from 1.6 to 160 kHz across many species [2]. The meaning of these results is complicated by many factors including: limited sample sizes within a species; age related hearing loss; and poorly understood background noise effects.

Since the passing of the Marine Mammal Protection act of 1972, invasive electrophysiological studies of whales in the United States has slowed markedly. In all, the search for understanding of hearing in cetaceans is well served by structural analysis efforts.

When a rare, possibly endangered, whale is beached teams of marine mammologists flood the scene. Whales are usually large and unwieldy and dissection must be done quickly, before tissue decay renders the efforts futile. If it is possible an entire head is removed, frozen, and transported to a special laboratory to be scanned in industrial sized Computed Tomog-

raphy (CT) scanners. These scans allow a three-dimensional visualization of the anatomical structures before the cutting begins. Because soft tissue loses its native shapes when cut, the scanned models are an essential tool in understanding the original shapes and orientations of key anatomical features.

Marine mammologists dissect beached whales in hopes of finding out how sound is transmitted from the ocean to the animal's inner ears and how the ears themselves function. Ascertaining which frequencies they can hear and whether active sonar is likely to damage whale hearing is of primary concern.

While much can be learned from traditional methods of dissection in exploring the functional morphololgy of whale aural systems, there are many gaps in this approach which lead to much speculation and debate. Computational modeling of marine mammal bioacoustics provides a means to begin to fill these gaps.

1.3 Computational Modeling of Bioacoustics

In collaborative efforts, marine mammologists and engineers have developed computational models of the anatomical structures involved in whale bioacoustictics. These are used to intelligently guide investigations of functionality in mandibular strucrues, manibular fats, cranial air sacs,and typmanic structures [27, 28].

Aroyan et al. [27] developed two dimensional finite difference techniques to investigate the roles that skull shape and tissue-air boundary interfaces play in providing an acoustic mirror for the propagation of generated echolocation pulses. This study also supported the notion that melon fats provide a means to narrowly focus these beams.

Vibro-acoustic simulation is a valuable tool used to gain insight into the multifaceted phenomena at play in marine mammal acoustic responses. Key to these simulation, as well as to any structural simulation, is a well defined set of material property inputs. For our biological structures of interest a viscoelastic model is usually the best choice. However, this can be problematic. There is no easy way to quantify the viscoelastic properties of tissues. An important

task of the present work explores ways to bridge this gap.

Studying cetacean soft-tissues is not easy. Adequate specimens are rare and dissections are difficult, often being performed on a beach. The size of the animals alone makes the task of whale anatomy exploration a logistical challenge. Many researchers are combining methods of dissection with noninvasive imaging techniques the likes of computerized tomography and magnetic resonance imaging to map complex anatomical structures [23, 3].

Whale heads are placed in industrial CT scanners and images are taken in planar slices of 0.1to 3 mm thicknesses. These scans provide information rich three dimensional images that can be used to construct finite element meshes used in vibroacoustic simulations [28].

Vibroacoustic finite element simulations of scanned whale heads provide a practical means of assembling a unified theory of underwater sound reception. Since a good portion of this dissertation is dedicated to the experimental determination of viscoelastic material properties, a review of fundamental concepts is warranted.

1.4 Viscoelasticity

Viscoelasticity is the property of matter that describes how it resists and recovers from applied loads. Even for small strains, such as those undergone under acoustic excitation, prior research has found that viscoelastic properties must be acounted for when modeling tissue behavior [29]. The elastic contribution involves the reversible effects–its ability to recover to its unloaded state. The viscous part describes the energy loss and how the response depends on the time-rate of loading. A special class of viscoelastic materials, called anelastic materials, recover fully to their unloaded kinematic state, provided enough time is allowed for this recovery. Anelastic solids recover fully from viscoelastic creep, and are a focus of this work. Here the time-dependent response is recoverable, unlike familiar visco-plastic flow. The remainder of this section is dedicated to a review of some notions key to the study of viscoelasticity.

Rheology is concerned with the study of viscous flow, elasticity, and any combination of the two. A material is said to be viscoelastic if its deformation response produces stresses

that depend on both strain and strain rate. Some examples of viscoelastic materials include: rubbers, polymers, glasses, and tissues. Viscoelastic materials behave in a way that is in some ways like a viscous fluid and in some ways like an elastic solid.

These materials exhibit creep, which is an increasing deformation response to a sustained load or state of stress in the way that very old glass flows downward under its own weight. Viscoelastic materials also exhibit relaxation, which is a decreasing stress response to a sustained state of deformation or strain in the way that rubber band loses its pull over time. The hysteresis response is elliptical and the area circumscribed is directly related to the heat energy lost in the cycle.

Viscoelastic materials dissipate energy and the viscosity is often described in terms of a loss modulus. In this sense, a solid with high viscosity is sometimes said to be a lossy material. When deformed adequately, polymers undergo a molecular rearrangement. In particular, long polymer chains are disturbed and reconfigured. In so-called "linear viscoelasticity" the stress and strain responses are separable.

Some phenomena that are observed in viscoelastic materials include [30]: (1) "creep" which occurs if the stress is held constant, and the strain increases with time; (2) "relaxation" which occurs if the strain is held constant, and the stress decreases with time; (3) the effective stiffness depends on the rate of application of the load; (4) if cyclic loading is applied, a phase lag occurs, leading to a dissipation of mechanical energy; (5) acoustic waves experience attenuation; (6) rebound of an object following an impact is less than 100 percent; and (7) during rolling, frictional resistance occurs.

Viscoelastic parameters are often represented as a complex modulus such as: the complex Young's modulus $E^* = E' + iE''$; or the complex shear modulus $G^* = G' + iG''$. The real component of a complex modulus (E' or G') is referred to as the storage modulus, and the imaginary component (E'' or G'') is the loss modulus. Complex elastic moduli are extensions of their real counterparts, where the imaginary components account for phase shift effects.

In his book *Theory of viscoelasticity* (p.71) R.M. Christensen describes the utility of this complex expression of moduli:

Steady state harmonic problems, either with or without inertia terms in the equations of motion, can be solved in a manner formally the same as that for comparable elasticity type problems. In fact, steady state harmonic elastic solutions can be converted to corresponding viscoelastic solutions through the replacement of the elastic moduli by the corresponding complex viscoelastic moduli. The actual computation of solution variables involves complex number arithmetic which accounts for phase angle shift effects [31].

The steady-state harmonic response provides the following useful relations:

$$\sigma(t) = \sigma_0 sin(2\pi\omega t)\,, \tag{1.1}$$

and

$$\varepsilon(t) = \varepsilon_0 sin(2\pi\omega t - \delta)\,. \tag{1.2}$$

The areas circumscribed by the stress-strain hysteresis ellipse is indicative of energy dissipated per cycle. The viscosity is neatly related to the phase shift angle δ which is suitably quantified by its tangent having

$$tan\delta = \frac{G''}{G'}\,, \tag{1.3}$$

and

$$\delta = tan^{-1}\frac{G''}{G'}\,. \tag{1.4}$$

The magnitudes of the complex viscoelastic moduli are

$$|G^*| = \sqrt[2]{G'^2 + G''^2}\,, \tag{1.5}$$

and

$$|E^*| = \sqrt[2]{E'^2 + E''^2}\,. \tag{1.6}$$

The dynamic viscosity can be expressed as

$$\eta' = \frac{G''}{\omega}\,, \tag{1.7}$$

where highly dissipative materials exhibit greater dynamic viscosities. The damping ratio ζ is a measure of damping, or energy dissipation qualities, with

$$\zeta = \frac{G''}{G'} \tag{1.8}$$

($\zeta < 1$ is under-damped, $\zeta = 1$ is critically damped, and $\zeta > 1$ is overdamped [30]).

The isotropic, elastic constitutive relation reads

$$\sigma_{ij} = 2\mu\varepsilon_{ij} + \lambda\varepsilon_{kk}\delta_{ij}\,, \tag{1.9}$$

and the viscolastic version reads

$$\sigma_{ij} = \int_0^t 2\mu(t-\tau)\frac{d\varepsilon_{ij}}{d\tau}d\tau + \int_0^t \lambda(t-\tau)\delta_{ij}\frac{d\varepsilon_{kk}}{d\tau}d\tau\,. \tag{1.10}$$

The complex viscoelastic constitutive relation reads

$$\tau_{shear}(t) = (G' + iG'')\gamma_0 e^{i\omega t} = |G^*|e^{i\omega t-\delta}\,; \tag{1.11}$$

in one dimension we have $\frac{\sigma}{\varepsilon_0} = E' + iE''$, and $\frac{\tau_{shear}}{\gamma_0} = G' + iG''$.

Creep and relaxation are key notions of viscoelasticity. Creep is the progressive deformation of a material under constant stress $\sigma(t) = \sigma_0 H(t)$. Whereas relaxation is the gradual decrease of stress at constant strain $\varepsilon(t) = \varepsilon_0 H(t)$. The material response is most affected by its recent history, a notion referred to as "fading memory [31]."

The phase shift or “phase lag" δ, that temporally separates the stress and strain steady state responses under controlled harmonic excitation, is a measure of viscous damping or dissipated energy. The loss tangent is a measure of viscosity in viscoelastic material. Sometimes called $tan\delta$, pronounced “tan-delta," it relates the phase shift δ to the storage and loss moduli by: $tan\delta = \frac{G''}{G'} = \zeta$. The dynamic viscosity $\eta' = \frac{G''}{\omega}$, where ω is the excitation frequency in radians per second, is a strain-rate dependent expression of a material’s dissipative qualities.

Tissues are viscoelastic materials; they behave like elastic solids and like viscous fluids. The speed of acoustic waves traveling through a tissue depends on the tissue’s elastic properties, and the severity of signal attenuation depends on viscosity. Viscoelastic properties, such as elastic moduli and loss tangent, are important inputs to our vibroacoustic computational simulations.

Numerical modeling often assumes a Maxwell or Kelvin-Voigt element. A Maxwell element consists of spring and a dashpot in series. The Kelvin-Voigt model provides a similar

element wherein the spring and dashpot are parallel to one another. The Maxwellian model reads

$$\frac{1}{E}\frac{d\sigma(t)}{dt}+\frac{\sigma(t)}{\eta}=\frac{d\varepsilon(t)}{dt}=\dot{\varepsilon}(t)\,, \tag{1.12}$$

while the Kelvin-Voigt model reads

$$\sigma(t)=E\varepsilon(t)+\eta\frac{d\varepsilon(t)}{dt}=E\varepsilon(t)+\eta\dot{\varepsilon}(t)\,. \tag{1.13}$$

Tissues are rarely homogeneous or isotropic, and they also change appreciably when removed from their biological environments. To further complicate endeavors, biological processes often directly effect key properties such as: elastic stiffness; viscosity; history of pathological processes; and chemical reactivity to name a few [32]. Experimental data on tissue elasticity is not only scarce, it is a primary limiting factor in using elasticity imagining as a way to distinguish diseased from normal tissues [33]. Palpation is a time-honored method of qualitatively determining the elastic response of tissues for disease diagnosis [34]. In the present work, equipment and devices used to quantify tissue properties by way of automated "palpation," or Dynamic Mechanical Analysis (DMA) are presented.

1.5 Tissue Characterization Methods

Dynamic Mechanical Analysis involves applying harmonic mechanical excitation and measuring the material response. In a purely elastic material, the stress and strain responses are in phase with one another. If the material is viscous, the strain will lag behind the stress. In principle, a sample is excited with the application of a well controlled boundary force as instrumentation records the material response.

Commercially available material testing devices are not specifically intended for the range of elastic moduli seen in soft biological tissues. Some researchers have adapted available instruments towards this end. Others develop their own mechanical devices to perform such

tests. The majority of these methods use compressive methods that are highly dependent on both the size and shape of the indenter tip and the geometry of the sample[34].

A scientist named Eric Goodyer introduced a Linear Skin Rheometer (LSR) for use in viscoelastic characterization of human vocal fold in-situ [35]. The device is, at heart, a dynamic mechanical analyzer operating in a displacement-control configuration. Some important limitations of the LSR involve the significant, and difficult to account for, inertial effects of its moving axis as well as the poor boundary contact that develops as a shearing contact-pin deforms the sample during excitation.

Magnetic resonance elastography (MRE) is a promising technology that uses medical imagining techniques on a tissue body as is subjected to varying states of mechanical stress. The image provides a view of the kinematic state which, when considered in combination with the known stress state, provides a rheological–typically elastic–characterization of that body. Unfortunately, MRE requires very expensive equipment that is not portable.

There is a significant body of research dedicated to the use of ultrasonic time-of-flight methods in characterizing the properties of soft solids. Measuring the bulk modulus with ultrasonic methods involves sending a pulse through a sample and measuring the time is takes the traverse the distance. The speed of transit is simply related to the bulk modulus of the material. This relation depends on the density of the material and is given by $c_{mat} = \sqrt{\frac{\kappa}{\rho}}$. Some success has been realized, but ultrasonic methods are generally better suited for materials that are much stiffer than typical tissues. Nonetheless, this is a promising direction worthy further consideration.

While many of these methods are well suited to a controlled laboratory testing environment, few are readily adaptable for field work. There is a pressing need for viscoelastic material estimation that is conducive to in situ dissection where sample preparation is minimal and time is of the essence. In hopes of fulfilling this need a new device has been fabricated and tested.

1.6 Experimental Rheometer

This work presents a prototype linear shear rheometer that takes advantage of a unique boundary configuration and novel instrumentation for dynamical mechanical analysis. The device is not far removed from the linear skin rheometer [35]. The design is, however, notably different and improvements include the use of a voice coil for force generation, automated sample positioning control capability, improved instrumentation, a controlled boundary configuration, and the use of an advanced data acquisition board capable of megahertz sampling. The design accommodates several testing modes in either force or displacement control, and the advanced instrumentation allows point-of-contact analysis that gives results that are independent of the moving mass of the control axis.

The thick sample assumption in the fixture design allows for material characterization assertions that are not bound to discrete descriptions. Continuum properties are estimated for both semi-infinite and cylindrical sample geometries. Furthermore, these estimations are not highly sensitive to input estimation such as sample thickness, centering of the loaded boundary, and the assumed value of Poisson's ratio. The development of this experimental device has been undertaken with particular goals in sight. It must be portable, robust, and relatively easy to use.

1.7 Dissertation Outline

Part I is a sensitivity analysis comparing vibroacoustic simulations to published experimental results. This work is entirely contained within Chapter 2.

Part II chronicles the design, fabrication, and testing of an experimental rheometer. Chapter 3 provides an overview of the mission objective, design considerations, prototyping, and fabrication of the experimental device. Chapter 4 provides the theoretical and computational framework key to interpreting the experimental results and converting instrumentation signals to viscoelastic properties such the shear storage and loss modulus. To conclude Part II,

Chapter 5 details instrument calibration, provides results that are compared to independently obtained data, and puts the device to the test with real biological tissues.

Part III presents improved methods to treat anisotropic materials simulated using the finite element methods that are not prone to rigid locking and underestimated deformation states. Chapter 6 introduces the Generalized Selective Reduced Integration and modified B-bar methods with the treatment of the most rigid mode of the compliance matrix, and Chapter 7 extends the methods to treat multiples modes. Chapter 8 introduces stabilization methods and part III concludes with Chapter 9 which offers some naturally arising variable treatments with surprising performance characteristics.

Finally, Chapter 10 discusses the findings and suggests future research directions related to the work presented here.

Part I

Vibroacoustic Analysis

Chapter 2

Sensitivity Analysis and Another Look at the Norris and Harvey Study of 1974

In 1974, Norris and Harvey performed an experiment involving sound transmission into the head of the bottlenose dolphin. They measured generated broadband acoustic pressure signals at various receiver locations in the dolphin's head. The sources were positioned at different locations in the surrounding water [1], as shown in figure 2.1.

We qualitatively compare the experimental data from the previous study to the results of simulations made using the vibro-acoustic toolkit VATk [28]. The computational model is used to predict the pressure profiles using input data such as material properties, transducer and hydrophone locations, and the geometry of the animal's head. The material input parameters are estimated using values that have been published for similar tissues. No reliable material properties are available for the actual specimen used to create the 3-D geometry used in the simulations. Furthermore, the simulations use the geometry of a different specimen than did the experimental efforts. As such, significant modeling error is expected to be propagated throughout the simulations. Nonetheless, comparing the simulations to the rare experimental data provides valuable insight. It should be clearly emphasized here, that no quantitative assertions are made in this study. Only the quality, or shapes, of the experimental and simulated data are compared.

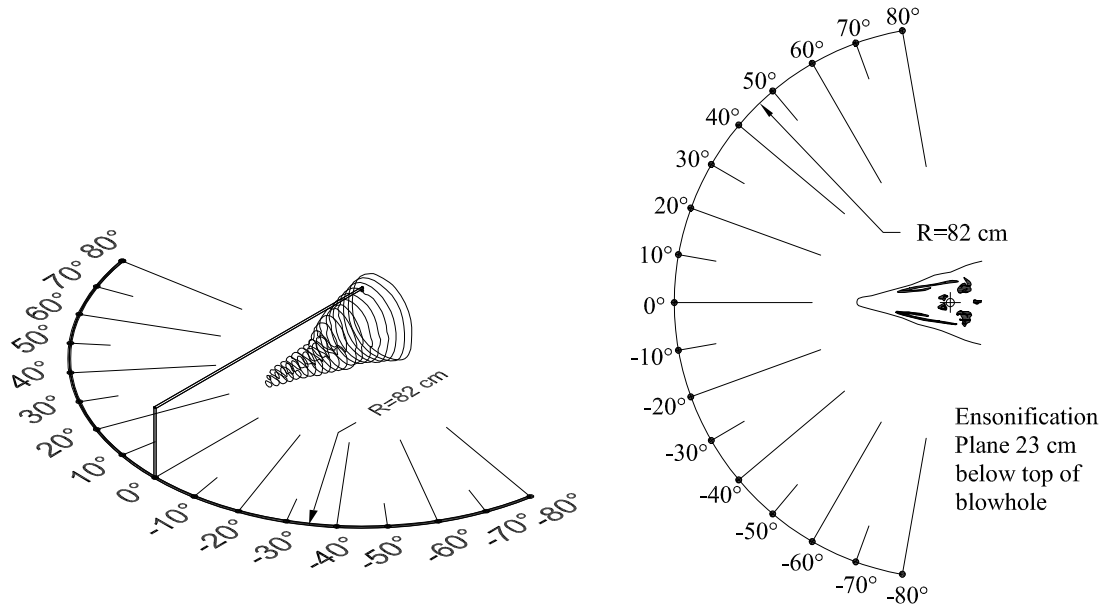

Figure 2.1: Norris and Harvey experimental setup.

2.1 A Second Look at the Original Study

In their 1974 study, Norris and Harvey suspended the head of a recently deceased mature Tursiops truncatus in saltwater. They installed an 82 cm arm that was rotated horizontally around the head. At the end of the arm, transducers were installed to generate sounds which would be received by implanted hydrophones. These hydrophones were placed in various key locations of the carcass. The sound pressure curves were published in Figure 1 of Reference [1]. These values represent the sensor voltages which were never converted to pressures. Even uncalibrated, these data offer a rare source for use in validation of our vibroacoustic model, which is described in detail in Reference [28]. This rare source of data is used to validate the Vibroacoustic Toolkit VATK.

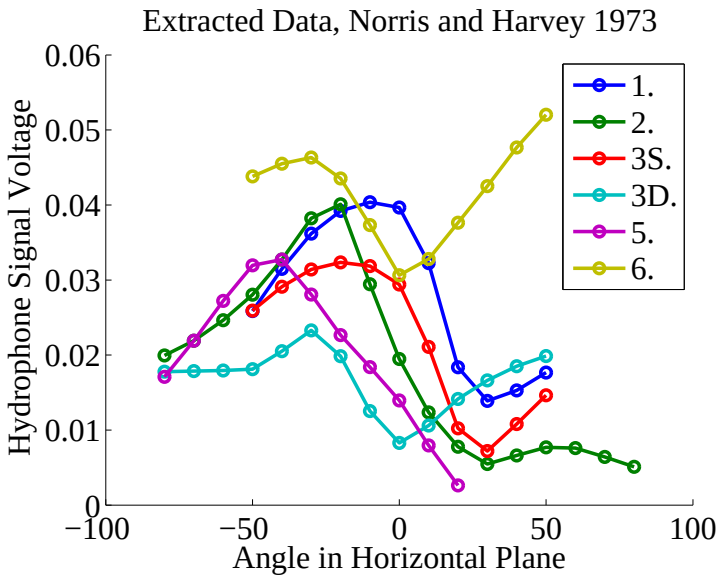

Figure 2.2: Norris and Harvey [1] curves (Reproduced).

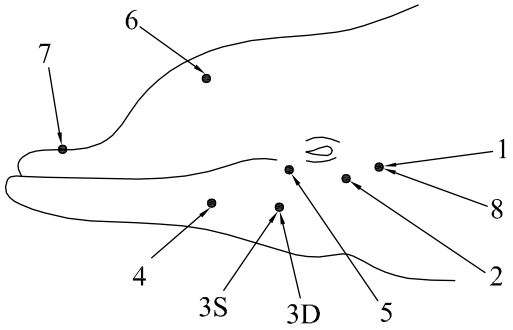

1	External auditory meatus (1.8 cm deep)
2	Mandibular fat anterior to bulla (6.8 cm deep)
3S	Blubber over pan bone (1.8 cm deep)
3D	Mandibular fat body (6.8 cm deep)
4	Anterior mandibular canal (4.1 cm deep)
5	Antorbital notch (4.2 cm deep)
6	Melon, midlateral (5.3 cm deep)
7	Upper rostrum (3 cm deep)
8	Peribullary sinus and inside bulla

Figure 2.3: Norris and Harvey [1] hydrophone locations (Reproduced).

2.2 Vibroacoutic Model

The effectiveness of the VATk model rests on the superposition of the known incident pressure field and the unknown perturbation field. This software is used to predict the pressure curves using input data that is based on informed guesses guided by published properties of similar tissues. The estimated inputs include viscoelastic material properties, hydrophone and transducer locations, and the geometry of the animal's head.

Since an acceptable computed tomography (CT) scan of a Tursiops truncatus is not available, our computational predictions were made using the CT scan of a similar species, Delphinus delphis (specimen KDX198). The 3-D image voxel dimensions were $0.625\,x\,0.625\,x\,0.625\ mm$. The input volume was made up of $840\,x\,461\,x\,524$ voxels.

The voxel block is divided into elements of identical size and shape. The finite element method discretizes the domain into elements that coincide with these voxels. The central difference method is used to integrate the dynamic response of the scattered wave. Forcing is provided by the incident wave. The scattered pressure wave, however, is subject to absorbing boundary conditions at the computational boundary. This boundary treatment only allows waves to leave, and not to enter, the volume of the computational domain. The plane-wave approximation is used for the absorbing boundary conditions.

In order to limit computational costs, resampling of the original CT scan is required. This works to reduce the total number of voxels. The voxel dimensions of the model were 2.5 x 2.5 x 2.48 mm. Empty space in the resampled mesh is filled with voxels having an intensity that corresponds to that of seawater. This is done to fill the space between the hydrophones and the transponder locations at the end of the 82 cm long arm. The computational domain ends up being a 3-D image of 485 x 266 x 731 voxels. These voxels are in turn converted to, nearly cubical, finite elements.

Norris and Harvey [1] reported good data for the hydrophones, six of which were located in the following locations: (1) external auditory meatus, (2) mandibular fat body anterior to bulla, (3S) blubber over pan bone, (3D) mandibular fat body (6.8 cm deep), (6) Mellon, made

lateral (5.3 cm deep). The focus of the present study is limited to these five locations. The remaining locations were excluded because they gave zero-voltage signals throughout testing. In the original experimental setup the authors do provide only vague indication of the locations of the specific data points used.

In the simulations, the receiver and transducer locations are reversed, as justified by the principle of acoustic reciprocity. The sound "sources" are located in one of the five "receiver" locations (1), (2), (3S), (3D), (6), and the receiver stations are located at the end of the "arm" at 10° increments between -80° and +80° . Throughout, 0° represents the location directly in front of the animal. A pure tone over a single cycle at 20 kHz is used as the source of acoustic excitation. The propagated wave is tracked for enough time so that the signal burst traverses beyond all of the receiver stations.

The material properties used in the simulations are not considered to be function of exctitation frequency. The excitation frequencies are takes to be $20000|:Hz$ throughout.

2.3 Published Material Properties

Published literature provides the estimated mechanical properties for the tissues involved. The assumed mechanical properties of bone are: Young's modulus E=20000 MPa, Poisson ratio $\nu = 0.2$ and density $\rho = 2600\,kg \cdot m^{-3}$ [36]. The estimated material properties of the soft tissues, as published in [37] except for the acoustic fats for which Norris and Harvey provide values [1], are as follows: (1) connective tissue having a sound speed of $c = 1620\,m \cdot s^{-1}$, a density of $\rho = 1087\,kg \cdot m^{-3}$, and a Young's modulus of $E = 0.124\,MPa$; (2) muscle tissue having a sound speed of $c = 1520\,m \cdot s^{-1}$, a density of $\rho = 993\,kg \cdot m^{-3}$, and a Young's modulus of $E = 0.1\,MPa$; (3) blubber having a sound speed of $c = 1465\,m \cdot s^{-1}$, a density of $\rho = 935\,kg \cdot m^{-3}$, and a Young's modulus of $E = 0.065\,MPa$; and (4) four categories of acoustic fats having graduated sound speeds of $c = 1450$, 1430, 1370, and $1340\,m \cdot s^{-1}$, a mass density $\rho = 937\,kg \cdot m^{-3}$, and a Young's modulus of $E = 0.065\,MPa$. The seawater is assumed to have a density and sound speed of $\rho_w = 1000\,kg \cdot m^{-3}$ and $c_w = 1500\,m \cdot s^{-1}$ respectively.

Estimations of material properties are fundamentally important to most any structural simulation, and it has been established that mechanical properties of materials undergoing large shear deformations at high frequencies are of vital importance to numerical simulations of soft tissues [38]. The tissues of interest here have widely varying material properties. Bone is typically several orders of magnitude stiffer than its surrounding tissue and characterizing the properties of muscle tissue introduces a number of challenges. Most obviously, muscles become more stiff when they are contracted making estimation of in vivo properties difficult at best. The connective tissue that holds bones in position includes a few types which should be modeled. While much more elastically compliant than bone, fat is nonetheless very important to the vibroacoustic response. All of these property inputs are important to accuracy of the computational predictions. Unfortunately, accurate estimations of these properties are not usually available.

2.4 Sensitivity Analysis

A series of sensitivity analyses were performed to help in determining which of these estimated parameters have the greatest influence on the final solution, and to get a better idea about whether the model is more dependent on estimates of material properties or geometry. Small changes in material properties lead to appreciable changes in the overall structural responses, which are often very difficult to intuitively predict. Sensitivity analysis helps with this.

Sensitivity analysis (SA) reveals the manner in which changes to the model's inputs influence the model's outputs. This can help to build understanding of a complicated model by revealing and helping to interpret unexpected model behavior, determining which inputs have the greatest effect on certain outputs, investigating the way the inputs combine to affect outputs, and providing insight into which additional information might improve the model's ability to predict experimentally verifiable physical responses.

Although a computational model may not reproduce the exact behavior the physical sys-

tem, its sensitivities are often useful in providing information about key features. The results of this study supply a valuable source of information for simulating the interactions among sound and anatomy. One of the conclusions drawn from this sensitivity analysis is that estimates of material properties need not be highly accurate to help in understanding these complex structural responses. Even crude estimations are often valuable.

2.5 Comparisons in the Sensitivity Analysis

Comparisons are based on the correlation of the simulated curves with the normalized published experimental data of the Norris and Harvey study. The pressure amplitudes are compared across the given ranges of the incident ensonificiation angle. Because the information provided in the aforementioned study is based on instrumentation voltage values, with undetermined pressure field calibrations, the curves are normalized, with respect the Euclidean norms of the data vectors for the experimental and simulated curves individually. Qualitative comparisons are drawn by considering the standard correlation coefficients and coefficients of determination. In some cases, mere visual observation of the plotted curves provides the best understanding of input variation. It should be emphasized that only qualitative comparisons are made.

2.6 Results

In general, the simulations faithfully reproduce the qualitative behavior of the experimental data presented in the Norris and Harvey study. There is particularly close agreement in the “Anterior bulla Left” region, where the predicted angle of maximum acoustic response is a very close match. In certain data sets both the fit and general shapes of the curves are improved if the Young’s modulus of the bone is reduced to 50% of its assumed value from the literature. It is plausible that the porosity of the bone causes its macroscopic structural behavior to appear less rigid than material properties that were characterized at a local scale would suggest. This

would account for the improved fit with the reduced value of Young's modulus.

While changes in the Young's modulus of the bone outweigh changes in the elastic properties of the soft tissues, altering the bulk modulus of the soft tissues still has an appreciable effect. Among the soft tissues considered, estimations of the bulk modulus of the acoustic fats have the most influence on the simulated pressure fields. Including the additional consideration of viscosity in the soft tissues, however, does not affect the solutions to the extent that the viscosity of the bone does.

Changing the bulk modulus of the fats fosters a significant change in the resulting pressure magnitudes for 8 of 10 configurations, and shows the greatest sensitivity for 4 out 5 data sets tested. Including viscosity gives appreciable changes in the outputs only when the viscosity is applied to the bone. Inclusion of bone viscosity produces changes in the resulting pressure fields for 5 out 5 data sets. Of the hydrophone configurations tested, simulations of data set 2 (Anterior Bulla Left) provided the best fit when using the reference material properties.

The qualitative match among the simulation and experimental results are improved slightly by increasing the viscosity of bone and by increasing the bulk modulus of the acoustic fats. Agreement of the shapes of the curves, taken by comparing the locations of local maxima and minima, is substantially improved when reducing the Young's modulus of the bone by 50% for data sets: 1, 3S, 3D and 6. The angle of maximum pressure, determined from the simulations, fit the experimental data with a rather large margin of plus or minus 30°. The predicted angle of maximum signal matches the experimental results in the second data set (Anterior Bulla Left). The overall shapes of all the curves are a reasonable match to those of the experimental results.

2.6.1 Errors at the External Auditory Meatus Hydrophone Location

We first consider the difference of the simulated and experimental curves for qualitative comparison. Again, no quantitative assertions are made. The errors are defined as the simple difference of the simulated and experimental pressure response vectors, each divided by it's

respective Euclidean norm.

Take the errors to be defined as

$$Error = \|simulated\,data\| - \|experimental\,data\|, \tag{2.1}$$

where $\|simulated\,data\|$ is the vector of simulated pressure responses divided by it's Euclidean norm, and $\|experimental\,data\|$ is the vector of experimental pressure responses divided by it's Euclidean norm.

Figure 2.4 shows the error surfaces of the response amplitudes sensed at the "Data 1" position (external auditory meatus,see 2.3) as the bulk modulus the acoustic fats was varied from a minimum of 20% below to a maximum of 20% above the reference value. The results show that the error does not exceed 30% when the normalized simulated curves are compared to the normalized experimental curves all for the ensonification angles of the original Norris and Harvey study. At this hydrophone location, the maximum error occurs with the lowest estimation of the bulk modulus at an ensonification angle of 45°, which is on the right-hand side of the animal.

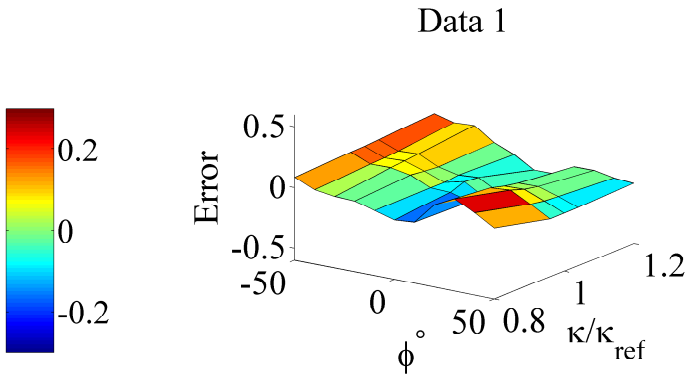

Figure 2.4: Fats error surface for varying κ, data set 1, vary κ of fats.

Figure 2.5 shows the error surfaces of the response amplitudes sensed at the "Data 1" as the bulk modulus the connective tissue was varied from a minimum of 20% below to a maximum of 20% above the reference value. The results show that the error does not exceed 20% when the normalized simulated curves are compared to the normalized experimental curves all

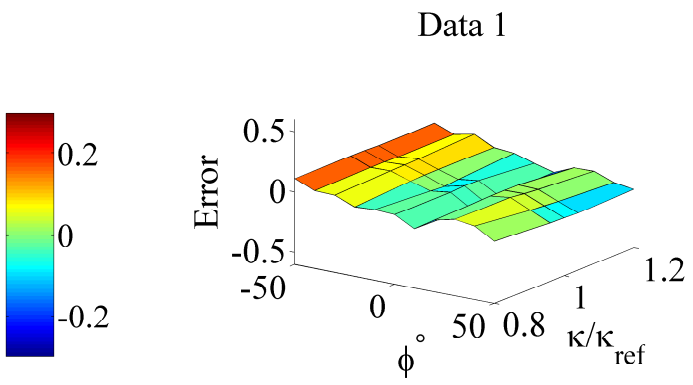

Figure 2.5: Error surface for varying κ, data set 1, vary κ of connective tissue.

for the ensonification angles of the original Norris and Harvey study. At this hydrophone location, the maximum error occurs with all estimations of the bulk modulus at an ensonification angle of $-50°$, which is on the left-hand side of the animal.

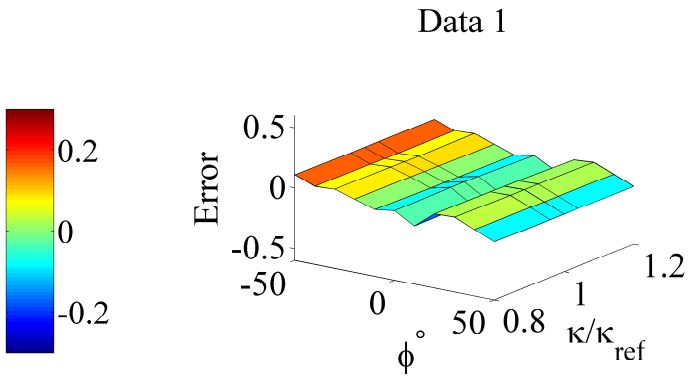

Figure 2.6: Muscle error surface for varying κ, data set 1, vary κ of muscle.

Figure 2.6 shows the error surfaces of the response amplitudes sensed at the "Data 1" as the bulk modulus the muscle was varied from a minimum of 20% below to a maximum of 20% above the reference value. The results show that the error does not exceed 20%. At this hydrophone location, the maximum error occurs with all estimations of the bulk modulus at an ensonification angle of $-50°$, which is on the far left-hand side of the animal.

Figure 2.7 shows the error surfaces of the response amplitudes sensed at the "Data 1" as the Young's modulus the muscle was varied from a minimum of 75% below to a maximum

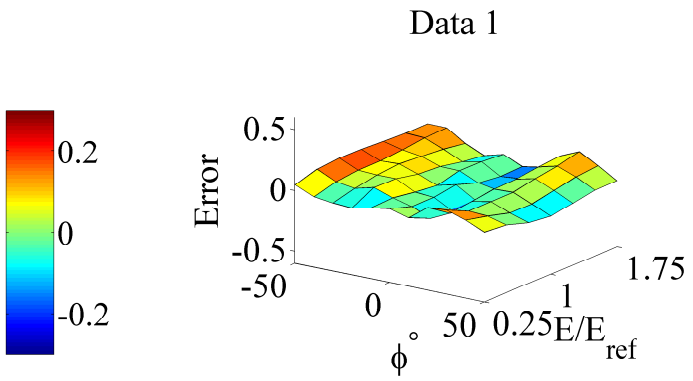

Figure 2.7: Bone Error surface for varying κ, data set 1, vary Young's modulus, E, of bone.

of 75% above the reference value. The results show that the error does not exceed 10%. At this hydrophone location, the maximum error occurs with all estimations of the Young's modulus at an ensonification angle of $-50°$, which is on the far left-hand side of the animal.

2.6.2 Errors at the Mandibular Fat Anterior to Bulla Hydrophone Location

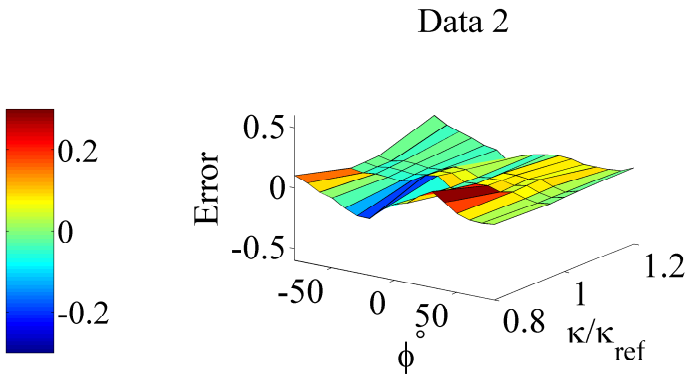

Figure 2.8: Fats error surface for varying κ, data set 2, vary κ of fats.

Figure 2.8 shows the error surfaces of the response amplitudes sensed at the "Data 2" position (mandibular fat anterior to the bulla, see 2.3). At this hydrophone location, the maximum error occurs with the lowest estimation of the bulk modulus at an ensonification angle of $50°$.

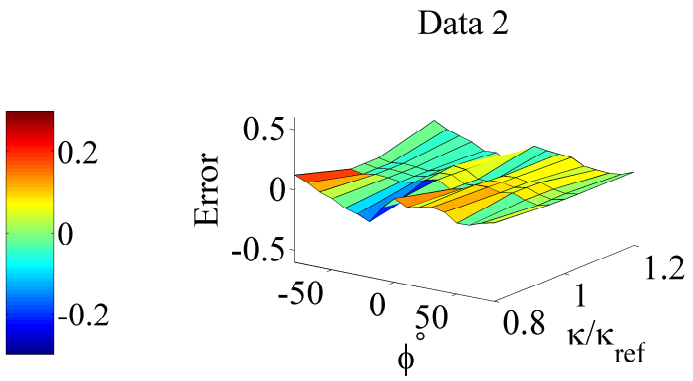

Figure 2.9: Error surface for varying κ, data set 2, vary κ of connective tissue.

Figure 2.9 shows the error surfaces of the response amplitudes sensed at the "Data 2" as the bulk modulus the connective tissue was varied from a minimum of 20% below to a maximum of 20% above the reference value. The results show that the error does not exceed 20% when the normalized simulated curves are compared to the normalized experimental curves all for the ensonification angles of the original Norris and Harvey study. At this hydrophone location, the maximum error occurs with the lowest estimation of the bulk modulus at an ensonification angle of $-50°$, which is on the left-hand side of the animal.

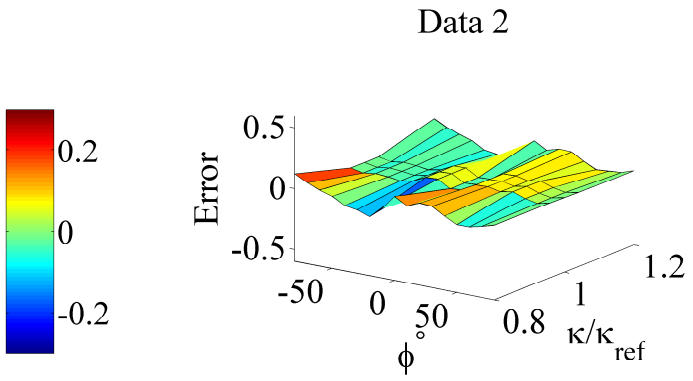

Figure 2.10: Muscle error surface for varying κ, data set 2, vary κ of muscle.

Figure 2.10 shows the error surfaces of the response amplitudes sensed at the "Data 2" as the bulk modulus the muscle was varied from a minimum of 20% below to a maximum of 20% above the reference value. The results show that the error does not exceed 15%. At

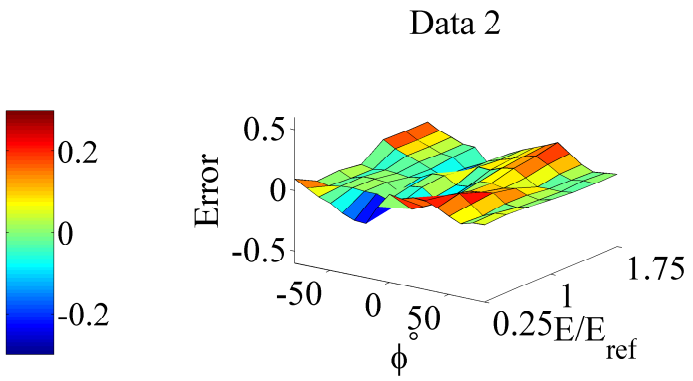

Figure 2.11: Bone Error surface for varying κ, data set 2, vary Young's modulus E of bone.

this hydrophone location, the maximum error occurs with the lowest estimations of the bulk modulus at an ensonification angle of -50°.

Figure 2.11 shows the error surfaces of the response amplitudes sensed at the "Data 2" as the Young's modulus the muscle was varied from a minimum of 75% below to a maximum of 75% above the reference value. The results show that the error does not exceed 30%. At this hydrophone location, the maximum error magnitudes occur over a wide range of Young's modulus estimation and ensonification angles.

2.6.3 Errors at the Blubber of Pan Bone Hydrophone Location

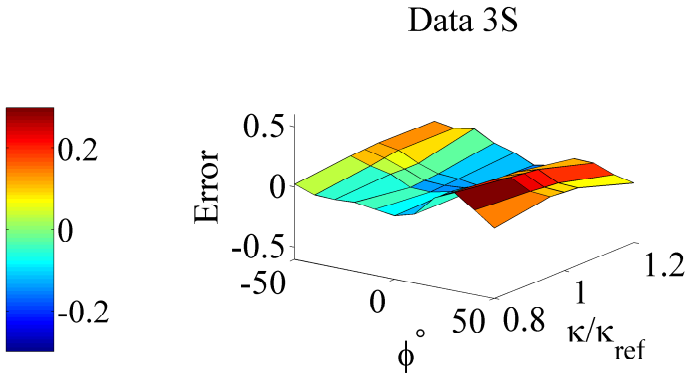

Figure 2.12: Fats error surface for varying κ, data set 3S, vary κ of fats.

Figure 2.12 shows the error surfaces of the response amplitudes sensed at the "Data

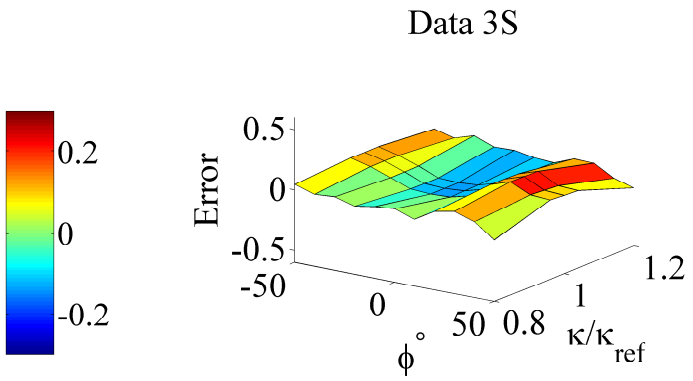

Figure 2.13: Error surface for varying κ, data set 3S, vary κ of connective tissue.

3S" position (blubber over pan bone,see 2.3). At this hydrophone location, the maximum error occurs with the lowest estimation of the bulk modulus at an ensonification angle of 45°.

Figure 2.13 shows the error surfaces of the response amplitudes sensed at the "Data 3S" as the bulk modulus the connective tissue was varied from a minimum of 20% below to a maximum of 20% above the reference value. The results show that the error does not exceed 20% when the normalized simulated curves are compared to the normalized experimental curves all for the ensonification angles of the original Norris and Harvey study. At this hydrophone location, the maximum error occurs near the reference value of the bulk modulus at an ensonification angle of 45°, which is on the right-hand side of the animal.

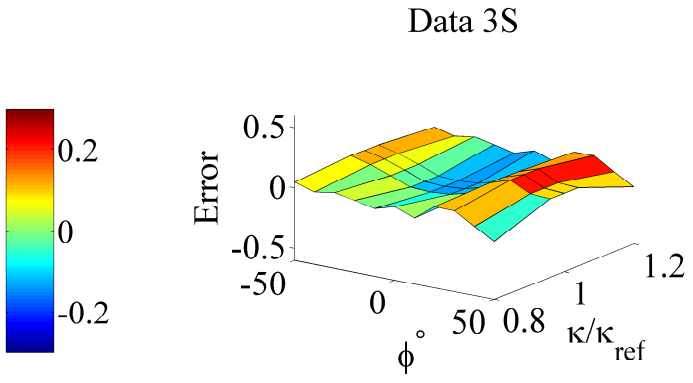

Figure 2.14: Muscle error surface for varying κ, data set 3S, vary κ of muscle.

Figure 2.14 shows the error surfaces of the response amplitudes sensed at the "Data 3S"

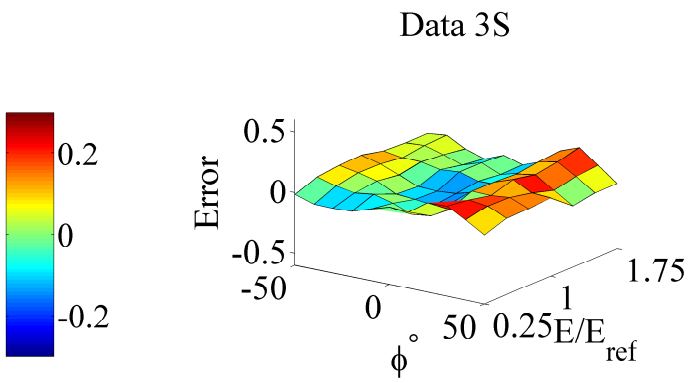

Figure 2.15: Bone Error surface for varying κ, data set 3S, vary Young's modulus E of bone.

as the bulk modulus the muscle was varied from a minimum of 20% below to a maximum of 20% above the reference value. The results show that the error does not exceed 15%. At this hydrophone location, the maximum error occurs with the middle to highest estimations of the bulk modulus at an ensonification angle of 40°.

Figure 2.15 shows the error surfaces of the response amplitudes sensed at the "Data 3S" as the Young's modulus the muscle was varied from a minimum of 75% below to a maximum of 75% above the reference value. The results show that the error does not exceed 30%. At this hydrophone location, the maximum error magnitudes occur over a wide range of Young's modulus estimation at ensonification angles near 40°.

2.6.4 Errors at the Mandibular Fat Body Hydrophone Location

Figure 2.16 shows the error surfaces of the response amplitudes sensed at the "Data 3D" position (mandibular fat body,see 2.3). At this hydrophone location, the maximum error occurs near the reference value the bulk modulus at an ensonification angle of 0°. Although the reference values give larger errors there is no clear indication that lower or higher estimations of the bulk modulus offer an improvement as changes in both direction offer quantitatively similar improvements.

Figure 2.17 shows the error surfaces of the response amplitudes sensed at the "Data 3D" as the bulk modulus the connective tissue was varied from a minimum of 20% below to

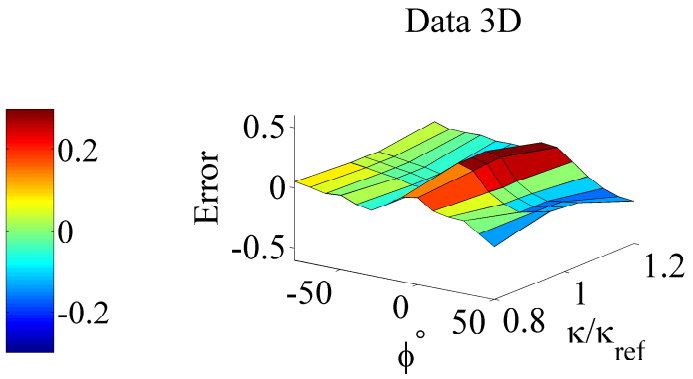

Figure 2.16: Fats error surface for varying κ, data set 3D, vary κ of fats.

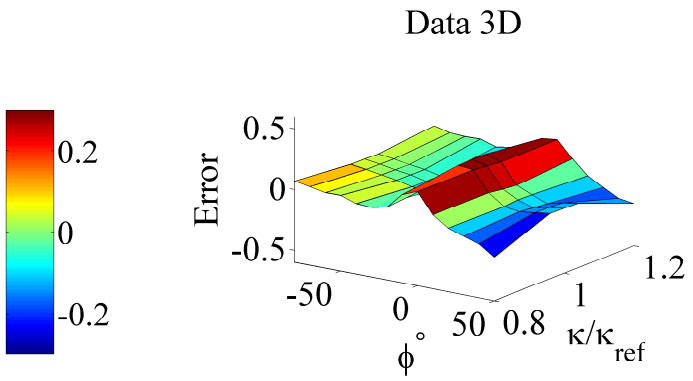

Figure 2.17: Error surface for varying κ, data set 3D, vary κ of connective tissue.

a maximum of 20% above the reference value. The results show that the error does not exceed 30% when the normalized simulated curves are compared to the normalized experimental curves all for the ensonification angles of the original Norris and Harvey study. At this hydrophone location, the maximum error occurs near the reference value of the bulk modulus at an ensonification angle of 0°, which is in front of the animal.

Figure 2.18 shows the error surfaces of the response amplitudes sensed at the “Data 3D” as the bulk modulus the muscle was varied from a minimum of 20% below to a maximum of 20% above the reference value. The results show that the error does not exceed 30%. At this hydrophone location, the maximum error occurs with the middle to highest estimations of the bulk modulus at an ensonification angle of 0°.

Figure 2.19 shows the error surfaces of the response amplitudes sensed at the “Data 3D”

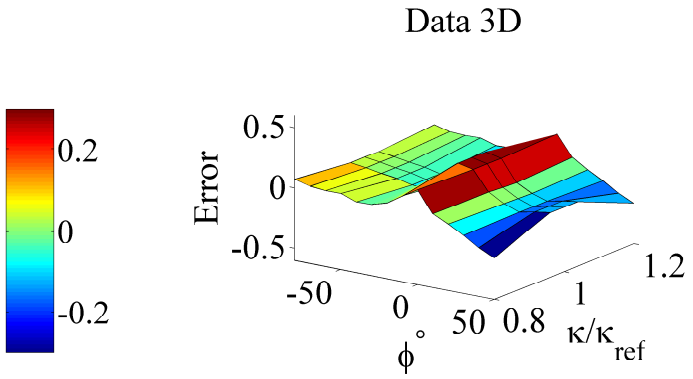

Figure 2.18: Muscle error surface for varying κ, data set 3D, vary κ of muscle.

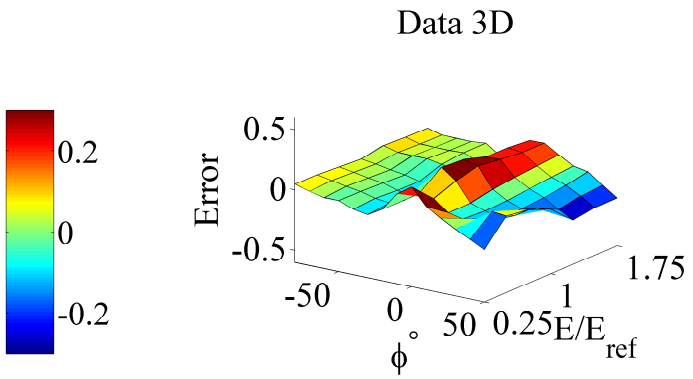

Figure 2.19: Bone Error surface for varying κ, data set 3D, vary Young's modulus E of bone.

as the Young's modulus the muscle was varied from a minimum of 75% below to a maximum of 75% above the reference value. The results show that the error does not exceed 30%. At this hydrophone location, the maximum error magnitudes occur over a wide range of Young's modulus estimation at ensonification angles near 0°. Here the low errors can be clearly seen at a 50% reduced Young's modulus. A closer look 2.27 will show that this reduced estimation makes for overall better fit.

2.6.5 Errors at the Melon Hydrophone Location

Figure 2.20 shows the error surfaces of the response amplitudes sensed at the "Data 6" position (melon,see 2.3). At this hydrophone location, the maximum error is less than 10% and occurs along all values of the bulk modulus at an ensonification angle of 0°. Here again, there

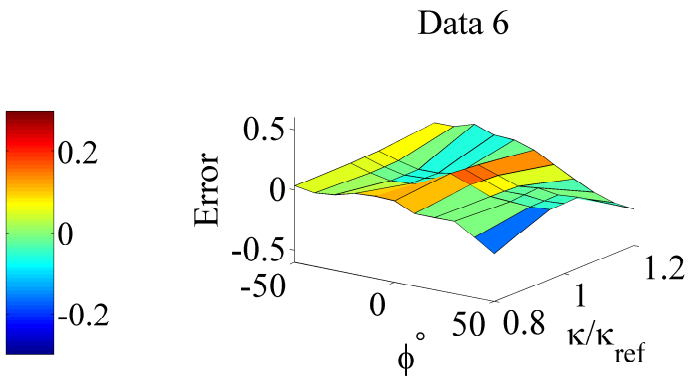

Figure 2.20: Fats error surface for varying κ, data set 6, vary κ of fats.

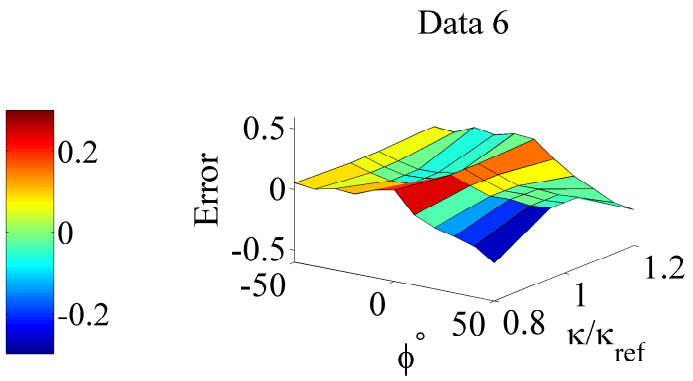

Figure 2.21: Error surface for varying κ, data set 6, vary κ of connective tissue.

is no clear indication that increasing or decreasing the estimated bulk modulus is in order since changes in both direction offer no decisive improvement.

Figure 2.21 shows the error surfaces of the response amplitudes sensed at the “Data 6” as the bulk modulus the connective tissue was varied from a minimum of 20% below to a maximum of 20% above the reference value. The results show that the error does not exceed 30% when the normalized simulated curves are compared to the normalized experimental curves all for the ensonification angles of the original Norris and Harvey study. At this hydrophone location, the maximum error occurs at the lower end of the bulk modulus estimations at an ensonification angle of 0°, which is in front of the animal.

Figure 2.22 shows the error surfaces of the response amplitudes sensed at the “Data 6” as the bulk modulus the muscle was varied from a minimum of 20% below to a maximum

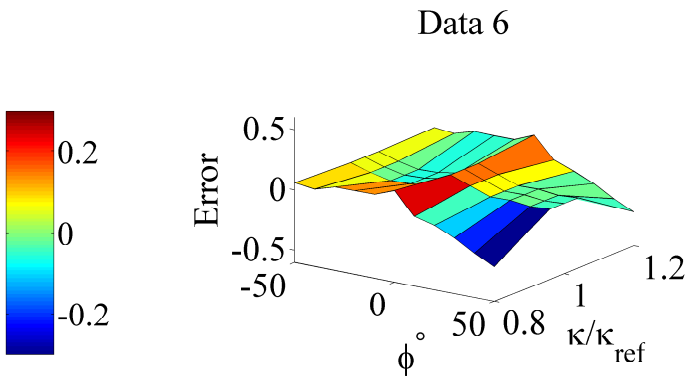

Figure 2.22: Muscle error surface for varying κ, data set 6, vary κ of muscle.

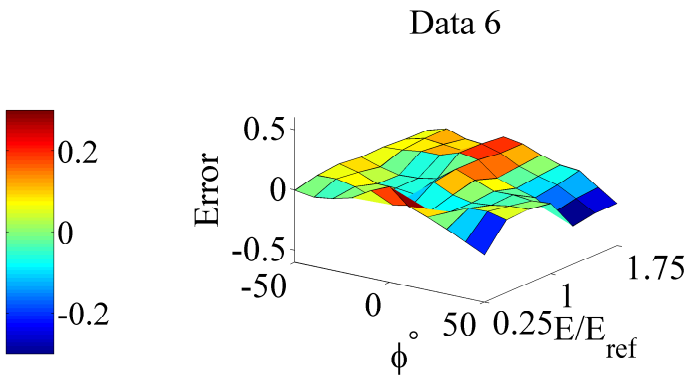

Figure 2.23: Bone Error surface for varying κ, data set 6, vary Young's modulus E of bone.

of 20% above the reference value. The results show that the error does not exceed 20%. At this hydrophone location, the maximum error occurs with the lower estimations of the bulk modulus at an ensonification angle of 0°.

Figure 2.23 shows the error surfaces of the response amplitudes sensed at the "Data 6" as the Young's modulus the muscle was varied from a minimum of 75% below to a maximum of 75% above the reference value. The results show that the error does not exceed 30%. At this hydrophone location, the maximum error magnitudes occur over a wide range of Young's modulus estimation and ensonification. Although no clear trend is apparent, the low errors at a 50% Young's modulus are observable.

2.7 Overall Trends

Varying the bulk modulus of the acoustic fats has a strong affect on the outcome of the model. The range of resulting pressure amplitudes seen in figure 2.24 suggests that by carefully choosing local properties, the behavior of the experiment could be reproduced. This does not mean that material property estimation are more influential than structural geometry, but it does suggest that the two animals were close enough in structural geometry to grant informative comparisons. These curves often best understood with some though of the pulse location in relation to the hydrophone location. If the pulse is generated at a location in the water that is on the opposite side of the animal from the sensor location, very low amplitudes may be explained by the intervening structures of bone and tissue. This is well observed in the shape of the "Data 2" curves throughout.

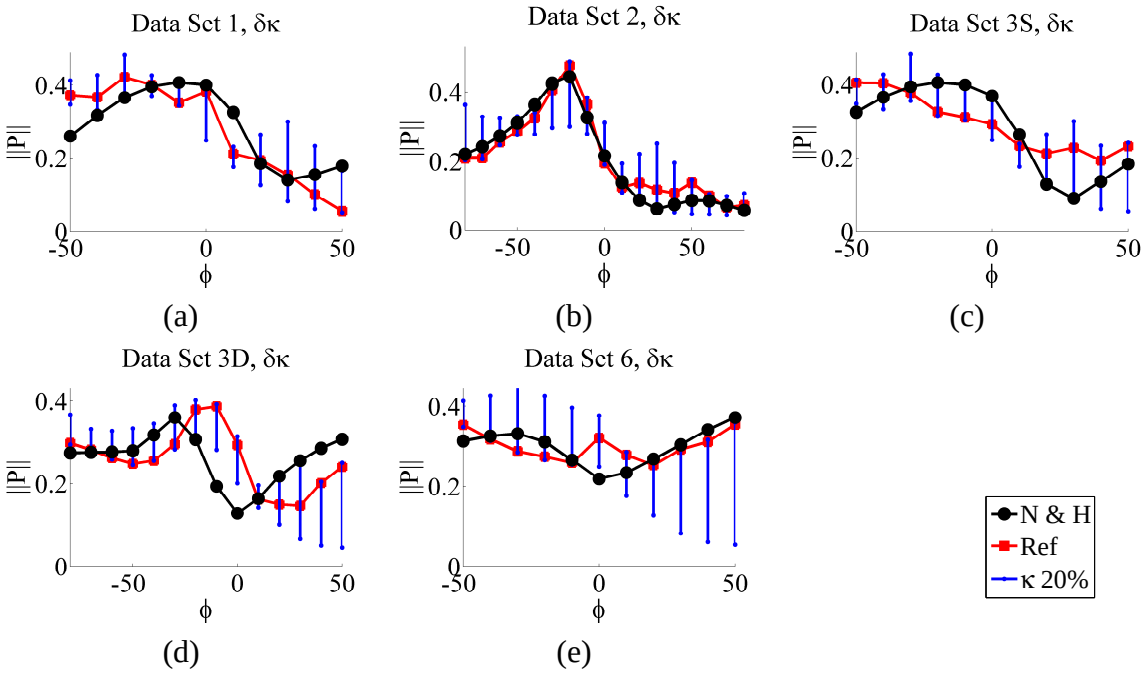

Figure 2.24: Varying κ of acoustic fats up/down 20%: (a) Data set 1 (b) Data set 2 (c) Data set 3S (d) Data set 3D (e) Data set 6.

Varying the Young's modulus of the bone from half to twice the reference value in simulations gives results that comfortably enclose the experimental results as can be seen in

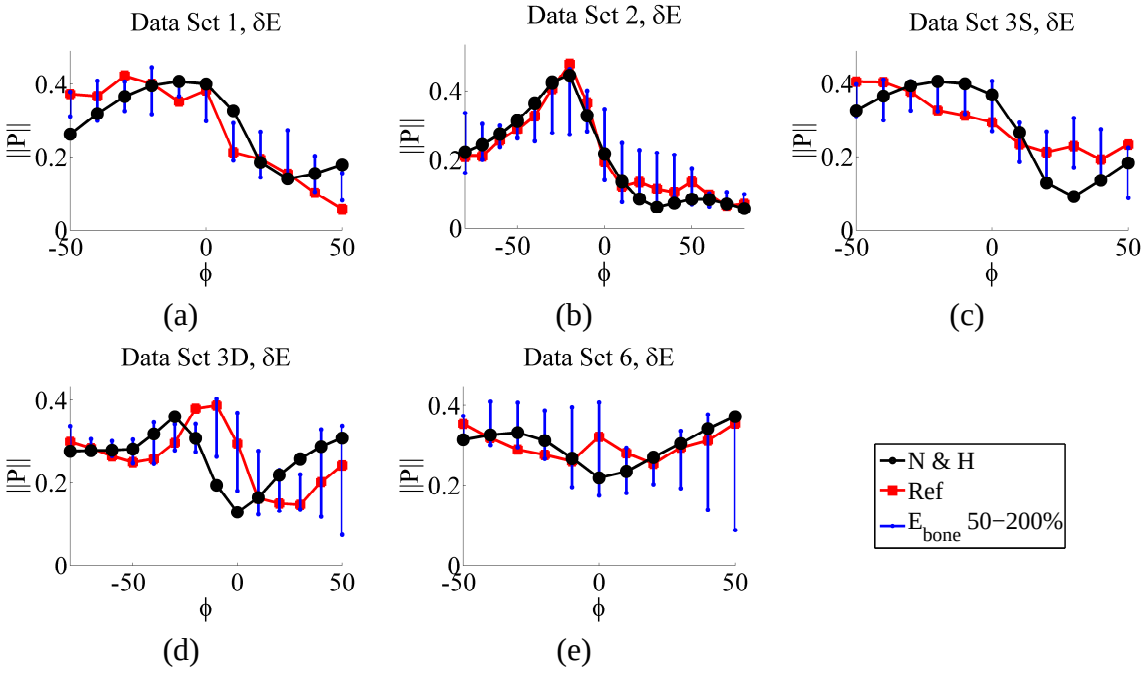

Figure 2.25: Varying *E* of bone 50-200%: (a) Data set 1 (b) Data set 2 (c) Data set 3S (d) Data set 3D (e) Data set 6.

figure 2.25.

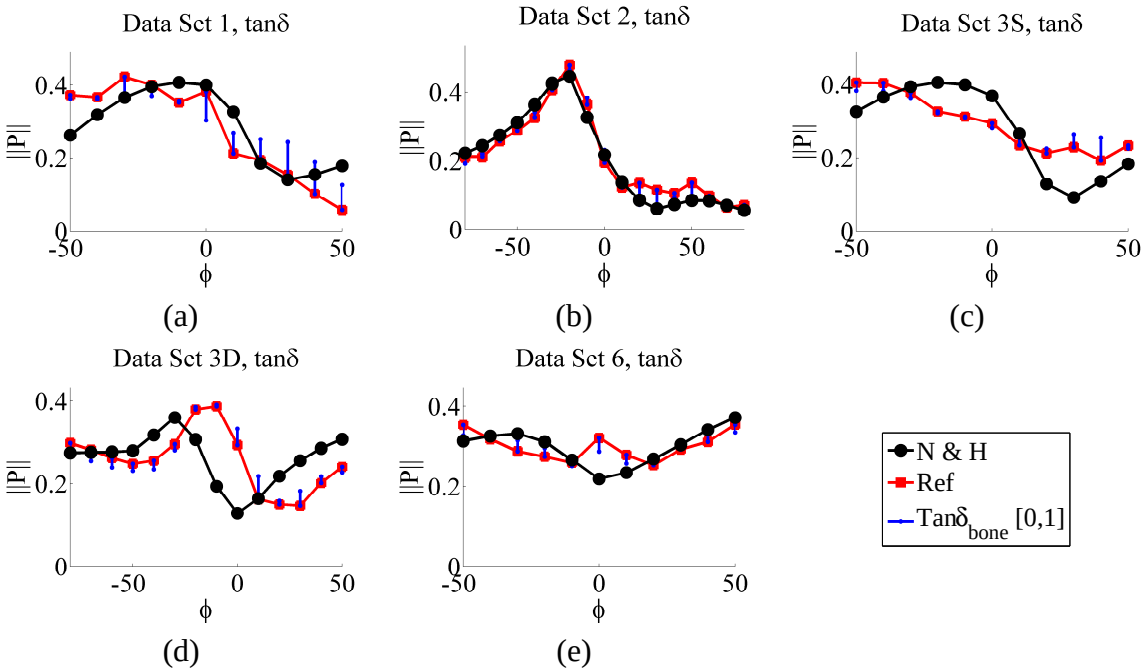

Figure 2.26: Increasing tanδ to a maximum of 1: (a) Data set 1 (b) Data set 2 (c) Data set 3S (d) Data set 3D (e) Data set 6.

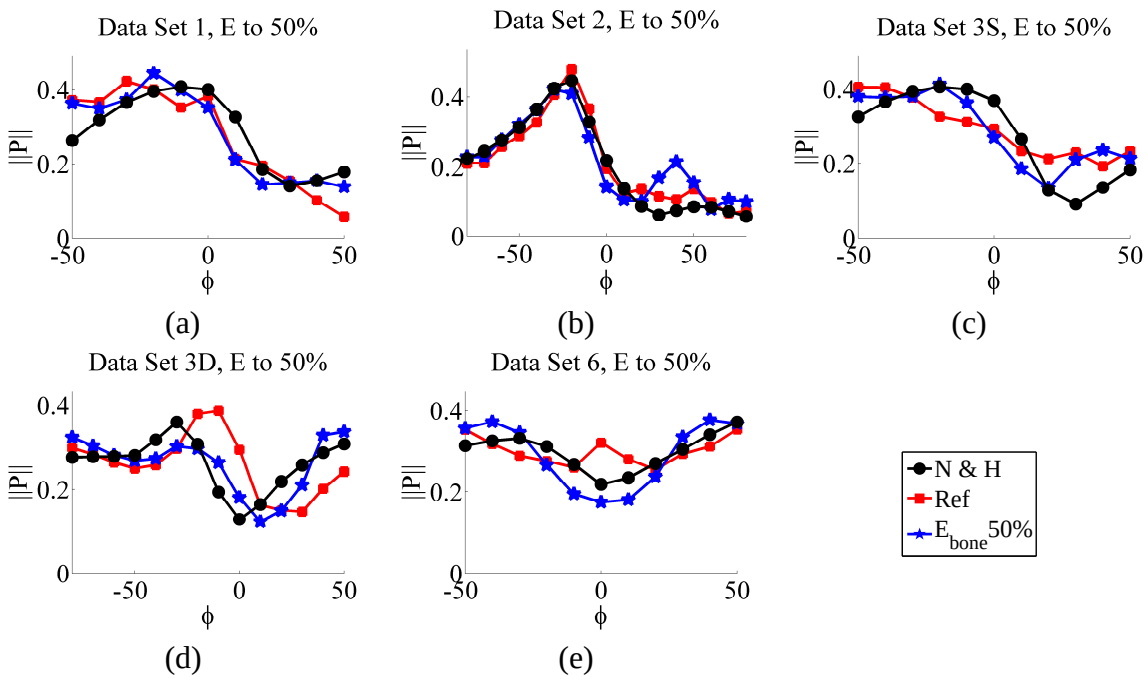

Figure 2.27: Decreasing Young's Modulus of bone to 50% of the reference value: (a) Data set 1 (b) Data set 2 (c) Data set 3S (d) Data set 3D (e) Data set 6.

Varying the viscosity of the acoustic fats has little affect on the outcome of the model. This can be seen in figure 2.26, where even very high values of $\tan\delta$ engender only very small changes in the resulting curves. Again, this conclusion must be treated with care as only the shapes (not the amplitudes) of the curves are compared. If the experimental data had been calibrated to give pressure units, a quantitative analysis of the results would be possible. Absent this calibration, the curves must be normalized for comparisons to be made and overall amplitudes are lost. Increased viscosity would be reasonably expected to significantly decrease the resulting pressure amplitudes by way of acoustic signal attenuation. Unfortunately, these comparisons cannot verify this effect.

Lowering the estimated Young's modulus to 50% of the reference value for all of the curves improves the match among the shapes of the experimental and simulated curves for many of the hydrophone locations (figure 2.27). This suggests that the estimated bone stiffness from the literature may have been adopted with haste. This could be accounted for by considering the bone's porosity. The estimated Young's modulus of the bone from the literature was

likely measured over sample regions that were local enough to not include large voids. Assuming that the bones are a continuous solid for the purposes of simulation requires lowering the estimated modulus to account for porous void space, or modeling the individual voids. This was not done in the current simulations.

While varying the bulk modulus of the fats did invoke a discernible variation in the resulting pressure fields, there is no clear indication that changing the estimations, high or low, would improve things. These conclusions would be better informed by experimental results with calibrated instruments that would allow non-normalized amplitude comparisons. The low errors suggest that the model provides a reasonable qualitative simulation of the experiment, despite the fact that the modeled animal was not the same one involved in the experiments.

While the simulations show a high sensitivity to estimations of the bulk modulus of the acoustic fats, the models were much less sensitive to changes in the estimated bulk modulus of the connective tissue.

In general, the model was not highly sensitive to estimation of the bulk modulus of the muscle tissue. However, in the mandibular fat body (data 3S) the sensitivity was greater than at the other locations. This may suggest that the properties of muscles have a significant influence on received pressures along the proposed acoustic pathway.

Estimates of the Young's modulus of the bone have a less pronounced general affect on the pressure amplitudes than seen in the study of the bulk modulus of the acoustic fats. However, especially in the mandibular region, the sensitivity is appreciable.

2.8 Acknowledgements

Chapter 2 is in part a reprint of the material submitted for publication in, "Sound transmission validation and sensitivity studies in numerical models," *2013 Effects of Noise on Aquatic Life*. 20130276-000115. Steve Oberrecht, Petr Krysl, and Ted Cranford. 2013. The author of this dissertation was the primary author of this paper.

Part II

Prototype Rheometer

Chapter 3

Prototype Rheometer Design and Fabrication

A working experimental rheometer for use in soft tissue characterization has been designed, built, calibrated, and tested. The device is used to characterize the viscoelastic properties of tissue. With it, one can estimate the complex Young's and shear moduli of a soft sample. It is portable and DC powered, which makes it well suited to field work. The first intended use is to characterize acoustic fats in whales.

This is an improvement over existing bench-top rheometers, especially for use on soft solids. It facilitates any combination of normal and shear testing modes in either displacement or force control. A novel instrumentation configuration uses a very light-weight, cantilevered, load cell as well as a fiber optic displacement sensor installed at a location near the sample interface. In being so located, they circumvent the effects of friction and the moving mass of the instrument. Both force and displacement instrumentation data are collected in a way that does not adversely affect the signal's ability to faithfully represent the physical response of the sample.

The current prototype has been modified to include improved strain gauge force sensing and fiber optic displacement sensing at the sample interface, as diagrammed in Figure 3.1. Most rheometers available today require significant corrections for inertial and frictional

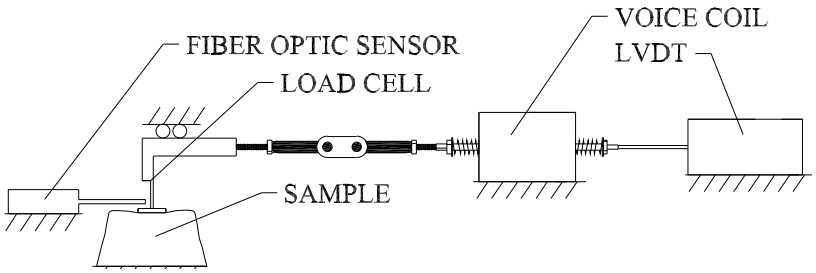

Figure 3.1: Rheometer instrumentation block diagram.

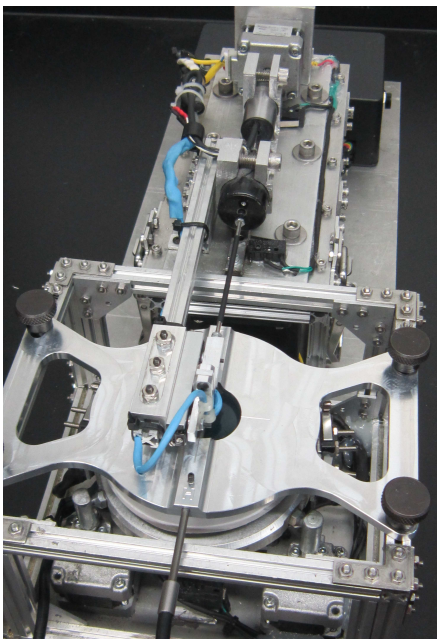

Figure 3.2: Third Prototype, voice coil driven.

effects, which reduces accuracy and complicates analysis. This design addition, however, sidesteps these effects with unique fixturing geometry and clever instrumentation which makes use of new advances in strain gauge as well as fiber optic displacement sensor technologies.

3.1 Development Platform Scope

This project was approached with a broad range of research and development capabilities in mind. The device was conceived as platform upon which device designs as well as samples themselves could be tested. Several considerations were carefully weighted at the out-

set to ensure that initial designs would allow for the changes necessary for ultimate success. The electro-mechanical device was designed and constructed specifically to be used in marine mammal tissue characterization. Portability and ease of use in an outdoor environment were primary concerns. A wide range of sample shapes and compositions needed to be accomodated. The design was split in three prototyping stages followed by data processing and assessment.

3.1.1 Multiple Instrumentation

The instrumentation was chosen to give both force and displacement information at the sample interface as well as along the control axis. The instrumentation at the sample interface includes a high sensitivity load cell and a fiber-optic displacement probe. The load cell is very fragile and should not be used if the sample is thought to have a shear modulus above 100 kPa. If the sample is "squishy" and easily squeezed with the fingers it should not damage the load cell. If the sample is harder than rubber, the tip load cell should be replaced with a rigid extension and force readings of the coil current are sufficient. The load cell configuration is preferred because it gives reliable force indication in a way that separates the response from the moving mass of the control axis.

The fiber-optic probe has great value for its ability to take local displacement readings at the sample interface without adding moving mass or friction to the system. Unfortunately, the probe has a very small linear range and non-linear calibration compensation is required.

The force and displacement data are also gathered on the moving control axis. The drive coil force, with includes forces needed to overcome system friction and the substantial moving mass of the drive axis, is taken to be proportional to the current in the coil itself. The moving mass introduced by the device resides in the moving axis seen in figure 3.8 and is estimated to be $46.5 \pm 5.0g$. The servo amplifier provides a current-proportional readout that is sent directly the DAQ. Instrument calibration with static weights verifies that the coil current (voltage readout) is indeed linear in the entire useful range of the device.

The displacement of the moving axis is recorded using a very sensitive LVDT with local

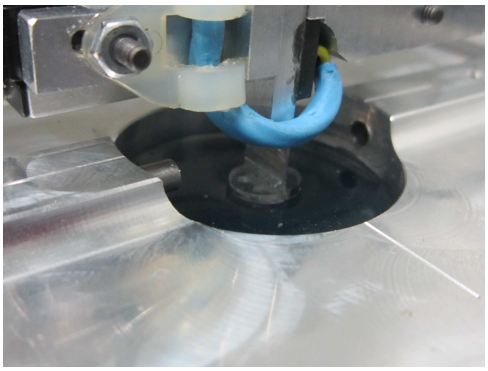

Figure 3.3: Strain gauge and fiber-optic sensor at sample interface.

signal modulation. This instrument also gives a very strong, clean, and linear signal.

Along the moving axis the instrumentation is very good, but the effects observed are fraught with inertial and frictional effects. At the sample interface, the frictional and inertial effects are negligible, but the instrumentation is fragile with limited linearity. Careful analysis of all of the data allows useful conclusions to be drawn about both the sample and the apparatus itself. In this way, the dynamic characteristic of the apparatus are revealed as well as the viscoelastic characteristic of the sample. While characterizing the sample has obvious value, characterizing the apparatus provides the more subtle service. It allows monitoring of real-time performance attributes such as the total inertia of the system, the elastic restoration of the voice coil's centering springs, and–most importantly–variable frictional effects from the instruments and slide rail.

3.1.2 Both Normal and Shear Testing Modes Accommodated

To date only shear modes have been estimated with the device, but instrumentation is in place which will allow simple estimations of Young's modulus. This will be done by moving the sample stage vertically using the stepper motors while a fixed spherical tip mounted above indents the sample. The resulting the force will be measured by a calibrated precision scale-type load cell that was installed beneath the articulating sample stage.

The use of an electronic balance with a linearly actuated indenter has been found ef-

fective in measuring the Young's modulus of soft tissues [34]. The device used by Egorov et al. also used a half-space geometry to frame the mechanics of the problem, and was found to be effective in both laboratory and clinical environments. The experimental design presented our device uses similar methods to estimate Young's modulus. Moreover, the presented device will also be capable of indentation tests used to approximated Young's modulus. This has not yet been implemented in the current stage of development, and to date values of Poisson's ratio must be estimated for use in processing the complex shear modulus of the sample. For most polymers, rubbers, and tissues tested the assumption of near incompressibility is a reasonable one.

3.1.3 Precise, Automated, Positioning Capabilities

From the outset of the design, precise knowledge of the thickness (compression state) of the sample, the angle of the sample stage with respect to the coil axis, and the exact location of the sample adhesion boundary have been important considerations. The goal has been to make knowledge of these qualities inherent to the setup in hopes of foregoing the tedium of intensive caliper and micrometer measurements during time-sensitive field use. Toward this goal, stepper motors with a fixed resolution of 0.01 mm per step of translation were installed for all positioning requirements. These stepper motors can either be controlled manually or by the digital output channels of the same MCC-USB 2537 DAQ used for data acquisition. Efforts were made to enable controlling and processing data for the entire device within a single programming environment.

The sample stage positioning system can be seen as it was being constructed in figure 3.6. Because part of structural purpose of the sample stage includes providing a rigid constraint against shear forces generated within the sample, care was taken to design the stage in a way that allows vertical articulation without compromising its ability to remain laterally rigid under operational loading conditions. Toward this end, a vertically aligned slide rail bearing was installed in the center.

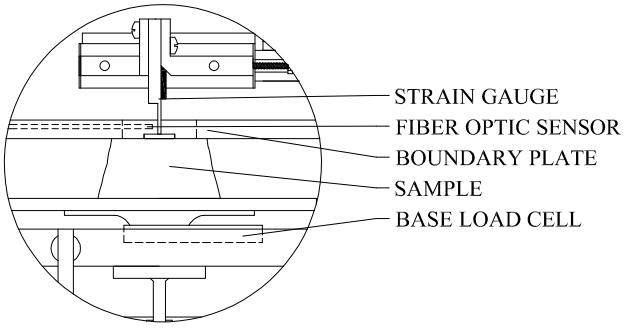

Figure 3.4: Close up of sample interface and instrumentation.

For additional support, and to ensure proper stepper axis alignment, turnbuckle-tensioned threaded rods are installed between any two adjacent stepper motor axes. Ball joints attach the stepper axes to the sample stage, allowing for independent positioning of the three axes. This was intended to allow accounting for angled sample geometries. Some thought was given to testing for coupled responses as the sample stage angle was changed maintaining horizontal shear loading. To date this has not been tested, as a clear advantage of the method has yet to be analytically identified. Even so, the stage is well-equipped to perform such an operation up to 20° of stage incline.

3.1.4 Ability to Quickly Change Samples

Time sensitive field work makes it essential to have the ability to quickly change samples without having the dissemble key components of the device. This required designing a coil axis that can be tilted up while samples are loaded and easily locked back in place for testing. This locking mechanism should be secure enough to support the assumption that the fixturing around the sample is effectively rigid relative to the sample itself. The rigidity requirement of the axis locking was achieved by using a single vertical latch on each side of the articulating coil-instrument axis as seen in figure 3.5. Once the drive axis is tilted up and out of the way, the top-boundary plate can be easily cleared by removing four threaded knurled knobs. At this point a new sample and boundary plate can be set back in place. The sample stage is

positioned using the stepper-motor control system which gives the precise thickness of the new sample without the necessity of manual measurement. The drive axis is latched back into the run position and testing may resume.

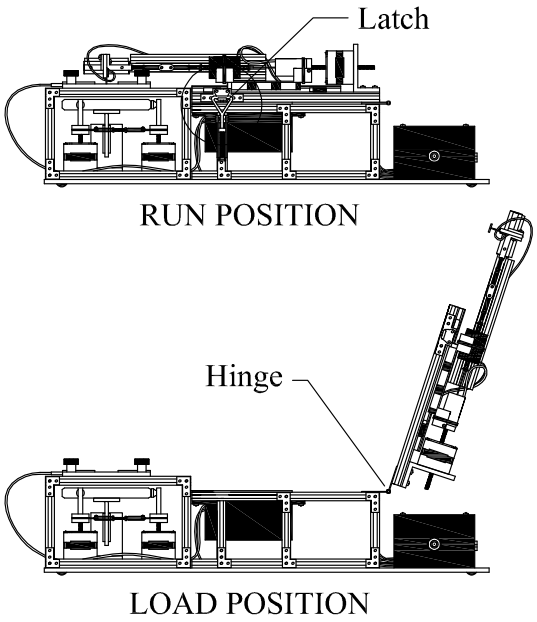

Figure 3.5: Running and loading positions.

3.1.5 Wide Range of Sample Geometries Accommodated

This method of sample fixturing, justified by the "thick sample assumption" makes accurate characterization possible without precisely controlled sample shape and thickness. This is an important improvement over existing designs which require often painstaking sample preparation before each test. With the high frequency shear device of Arbogast et al. a micrometer is used to determine the sample gap [38]. The complex modulus apparatus of Adkins et al. not only requires careful measurement of sample geometry, but the samples themselves were made using a specially designed mold [39]–a procedure not available to for naturally occurring tissue samples. The device of Madsen and Frank limits its scope to "tissue-like" materials which are specially modeled [40]. Once molded, their sample geometries are carefully

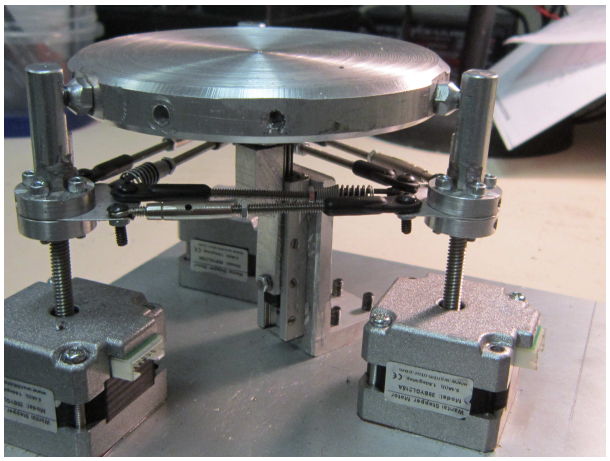

Figure 3.6: Third Prototype, sample stage positioning system.

recorded using a microscope equipped with a manual translator and vernier scale. In order to test muscles in compression, Van Loocke et al. fabricated a special cutting bench with a rotary table was designed to ensure a uniform sample geometry. Although labor intensive, the tissue cutting method seems attractive unless the tissues are soft enough to immediately lose their shape once cut. This kind of sample preparation is not practical during the in situ dissection of a marine mammal.

All of the these consideration were at play during the initial design of the experimental device; our sample geometry is made precise by the fixturing boundary not the sample. Furthermore, stepper motors position and automatically record all necessary dimensions. The small forces the arise from kinematically containing the sample were deemed negligible through the analysis detailed in the chapter 4. Here again, robust instrumentation is used to experimentally verify these analytical conclusions. Because a load cell was installed in the sample stage to detect normal forces in the sample, the compressive state was slightly varied and the material response results were confirmed to remain consistent.

3.1.6 Instrumentation Details

Displacements are measures using two independent instruments: (1) a precision Linear Variable Differential Transformer (LVDT), and (2) a fiber optic displacement sensor. Forces are

measured using a high precision low force cantilever load cell. Data acquisition uses a MCC USB-2537 multipurpose DAQ.

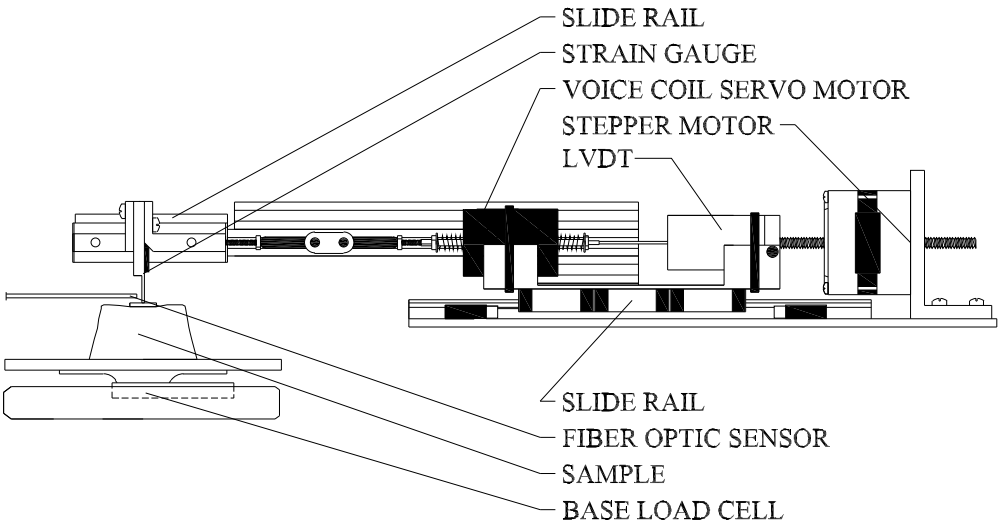

Figure 3.7: Third prototype instrumentation.

The device is made up of three primary components: the battery power supply; the control box; and the mechanical assembly.

3.1.7 Assumptions

It is assumed that all fixturing components, including sample plates and bearing mounts, are rigid relative to the sample being tested. Some materials lend themselves to the assumptions of incompressibility which leads to the a loss tangent in shear that equals that of tension-compression [39]. In this case, the magnitude of the complex shear modulus should also be one third of the magnitude of the complex Young's modulus. Here,it is not assumed that all materials are incompressible.

As the sample thickness increases without bound the relationships among the applied force, the resulting displacement at the location of force application, and the elastic moduli of

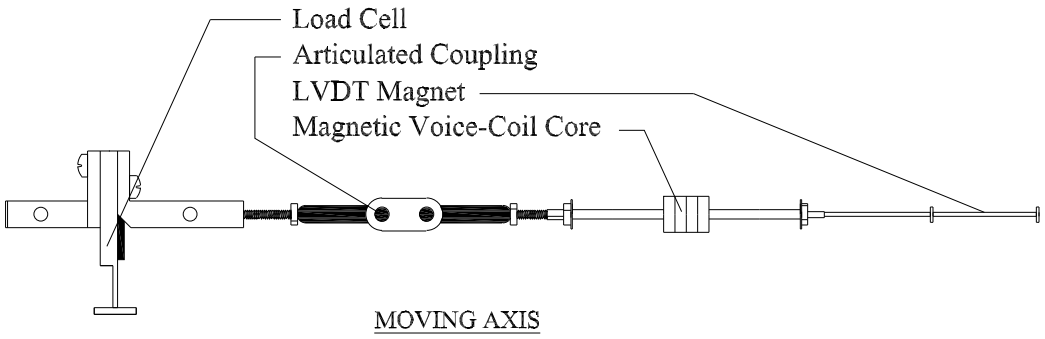

Figure 3.8: The parts that comprise the moving axis, etimated $46.5 \pm 5.0g$.

the sample approach the half-space solution. Furthermore, finite element analysis reveals that when the radius of the boundary opening of the top plate and the thickness of the sample exceed 15 mm the results are comparatively insensitive to small errors in the estimated geometry. More details of this analysis are provided in 4. This study was also used verify that the results are not sensitive to slight sample compression at the adhesion boundary.

3.2 Prototype Evolution

The first prototype was used to test basic operation principles and verify the practicality of the setup with a sample interface and Linear Variable Differential Transformer (LVDT) to record time dependent displacement data. This also provided a test-bed for Data Acquisition (DAQ) functionality. It was obvious from initial testing the force producing properties of the solenoid were poorly suited to well controlled sinusoidal excitation. A better choice would be a voice coil, which provides a force that is linear in current over a wide range of excitation parameters. The use of a voice coil as an excitation source for DMA is nothing new. A shear plate DMA device using voice coil excitation was found to be effective in testing soft tissues [38]. The device described by Arbogast et al. used a vertical double shear sandwich configuration and required ignoring the boundary effect at the open ends.

The second prototype implemented a voice coil–servo motor and a simple acrylic base.

This design allowed useful experiments but no way to control boundary force application or sample fixturing. The sample was essentially stuck to the table and the application plate was stuck to the sample, relying on the negative pressure produced while compressing the sample. A more controllable method of sample fixturing would be needed. This led to the third, and final prototype (figure 3.2).

The experimental rheometer described here uses a new boundary fixture methodology that exploits the aforementioned benefits of an effective half-space sample geometry. Other key improvements include the use of a highly accurate LVDT as well an innovative tip design that gives point-of-contact force and displacement data with the use of a fiber optic displacement sensor and a highly sensitive strain gauge.

The use of inertial corrections factors in commercial rheometers has been widespread [38]. It has been found that as sample density and excitation frequency are increased, the relative effect of inertia becomes more significant [41]. In cases where intertial effects are significant analytical corrections must be made [42]. Because the current design uses local instrumentation to determine the stress and strain relations at the sample interface, only the very small contribution of the moving volume of the sample is considered. Because this mass is very small, it can be neglected an no intertial corrections are necessary.

This design features precise stepper motor control to hold the samples between a movable stage and a top boundary plate. The movable stage can tilted and raised or lowered to provide a desired state of material compression, and the boundary plate provides a lateral restraints in a manner that lends itself to analysis.

Experiments require a carefully controlled environment. Of particular importance is the establishment of well defined boundary conditions. For the current work, this requires careful examination of sample fixtures and force application methods. The latter requires consideration of boundary adhesion at the dynamic loading surface. The viscoelastic properties of polymers, including many tissues, have been found to be temperature dependent. While it is important to maintain temperature control within 5 $\circ$ C, prior research demonstrates that silicone rubbers are relatively insensitive to changes in temperature in the vacinity of room temperature [39]. The

elastic properties of many polymers are also comparatively insensitive to temperature changes at room temperatures which we have verified for the plastisol calibration samples. There was no observable difference in estimated viscoelastic properties tested from 18 C° to 24 C°. At a very minimum, the temperature at the time of testing should be recorded.

3.2.1 Frequency Sweeps

Prior research reveals that complex viscoelastic material characterization over a wide range of excitation frequencies and strain levels can be determined from simple measurements of amplitude ratio and phase angle. However, this theory is best applied to cases of infinitesimal strains [39]. For this reason, methods presented here are directed toward small deformation processes. A feasible experimental setup is constrained by the bounds of practical specimen geomtery, realizable boundary conditions, and the framework of linear viscoelastic theory.

Frequency sweeps are the main data collection method used in obtaining dynamic mechanical properties. Frequency sweeps are typically conducted starting at a low frequency between one and ten Hertz. The excitatation is held until transient responses have subsided and all important instrument data are collected. The frequency is then increased sequentially and the excitation cycles are repeated. The frequency sweeps give a valuable indication of the dynamic properties by indicating time-scale dependent effects, such as phase-lag proportional loss moduli.

3.3 Comparison of Force Configurations

A limited number of force instrumentation configurations were tested. Redundant instrumentation by way of an in-line compressive load cell was installed along the excitation axis between the voice coil and strain gauge carriage. This is considered a redundant force measurement because it gives indication of the force applied by the strain gauge which is quite accurately determined by monitoring the current of the voice coil itself. As the in-line force

instrument did not prove to be as accurate as the voice coil current signal, from the servo amplifier, the redundant instrumentation was removed. This has the additional benefit of reducing the mass of the moving axis which reduces resonant effects of the device which do not reflect the physical response of the sample being tested.

3.4 Prototype Linear Rheometer, Raw Results

Some real-time results are indicated prior to post-processing. These are typical in the form of time-domain signal curves or hysteresis ellipses whose areas represent the loss energy density. A few kinds of data filtering are used during real-time signal processing. At the end of each excitation run, consisting of 20 to 200 complete oscillatory cycles, data is filtered by both running averages and band-pass methods.

3.5 Characterizing Elasticity and Viscosity

Elasticity and viscosity are characterized by first looking at the amplitudes and phases of the force and displacement signals. Then, these data must be considered along with geometric configurations to extract the continuum stress and strain information. The later is then used to derive the complex moduli of interest, typically the complex shear modulus. The real component of the complex modulus gives indication of material elasticity while the imaginary component indicates the material viscosity.

3.5.1 Two Independent Elastic Parameters

Because the isotropic material response is coupled, and the sample is not loaded in pure shear, other moduli such as the Young's modulus must be estimated. Since many tissues are nearly incompressible, assuming that Poisson's ratio is nearly one half is a good starting point. More accurate estimation requires determining coupled moduli either by use of the sample

stage stage and stepper motors–in normal mode–or alternate methods such as ultrasonic time-of-flight.

Chapter 4

Rheometer Analysis

The sample geometry for analysis is based on a radially cut cylinder symmetric about the vertical mid-plane. It is loaded in shear on a circular patch in a direction parallel to the cut plane; more details are provided in sub-section 4.0.3. The relationship among the discrete stiffness magnitude and continuous elastic modulus of concern is determined in the form a linear conversion factor that is based on static analysis. Closed-form half-space solutions as well as finite element solutions are investigated. It is determined that for a reasonable range of sample thicknesses, $10\,mm$ to $20\,mm$, the half-space solution provides a good approximation of the stiffness-to-modulus relation. The simulations provide improvements in the manner of conversion factors accounting for the finite sample geometries of the samples. These conversion factors are found to be insensitive to small errors in sample thickness and boundary radius inputs.

4.0.2 Half-Space Solutions and Semi-Infinite Sample Geometry

Closed form solutions are consulted as bounds for the analysis of results. The half-space solutions of Dydo and Busby [43] provide an important upper bound to any quasi-static deformation responses seen in finite geomtries. Half space solutions of the Boussinesq type have been applied to both normal and tangential loading of a semi-infinite half-space [44].

Conditions not far removed from a semi-infinite half-space are chosen both to facilitate

analysis and to render the results less sensitive to small changes in geometry at all boundaries except the one defining the excitation contact. This configuration has been used in compressive devices [34], and for similar reasons, we apply the same principle here.

When the sample geometry is chosen with a sufficiently large tickness and boundary radius along with a sufficiently small loaded patch radius, the solution is not sensitive to small errors in the boundary plate radius, slighlty non-centered force application, and small changes in boundary plate normal forces.

4.0.3 Bounded Finite Element Solutions and Stiffness to Modulus Relations

The relationships relating the discrete stiffness obtained from experimental data and the continuous material properties sought are estimated using static finite element models. Prior research support our finding that stiffness corrections can be expressed as a function Poisson's ratio and sample thickness [45].

The simulations of the statically loaded experimental sample conditions are described. The sample is cylindrical having a radius of $16\,mm$ and a thickness that is varied from $10\,mm$ to $20\,mm$.

The sample is loaded in shear with a force of $0.05\,N$ directed along positive x-axis (see Figure 4.1). The shear traction is applied uniformly over the circular patch on the top of the sample at $z = th$ and the thickness th is varied as needed. The loaded patch has a radius of $4\,mm$ and Dirichlet boundary conditions depress it into the sample by $0.5\,mm$ to produce the effects of tip indentation. The amount was varied the solutions were found to be insensitive to changes in tip indentation when the amount was less than about a tenth of the thickness of the sample.

The essential boundary conditions on the bottom of the sample, at $z = 0$, are

$$u_x = u_y = u_z = 0\,. \tag{4.1}$$

The essential boundary conditions at the circumference of the sample, at $r = 16\,mm$, are

$$u_x = u_y = u_z = 0\,. \tag{4.2}$$

The natural boundary conditions on the circular patch are

$$\tau_{zx} = 0.05\,N\,, \tag{4.3}$$

on $r \leq 4\,mm$, $z = th$. On the remaining boundaries zero tractions are applied.

As seen in Figure 4.2 a symmetry boundary condition is applied to reduce the number of equations. Along $y = 0$ the out of plane deformation is precluded by enforcing $u_y = 0$.

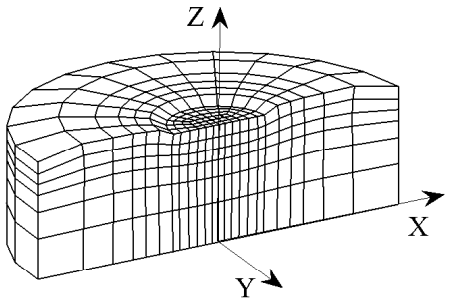

Figure 4.1: Typical disc analysis Cartesian axes.

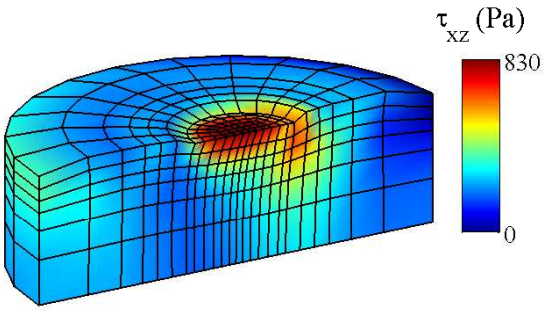

Figure 4.2: Typical disc analysis, shear load of $0.05\,N$ with $u_x = 1.2\,mm$.

Figures 4.3 and 4.4 show how the conversion factor Φ varies with estimations of Poisson's ratio or Young's modulus respectively for sample thicknesses in the range of interest. The

half-space solution provides an upper bound for the computed displacements. As expected, the sample solutions approach the half-space solutions as the sample thickness is increased. A sample with fixed boundaries is more constrained than semi-infinite solution suggests. Otherwise put, the finite sample behaves as would a semi-infinite sample with rigid material properties applied anywhere outside of the Dirichlet boundary surfaces. This increased rigidity of the structure renders the solutions less compliant than the semi-infinite idealization. The results shown are based on the experimental configuration that uses a boundary radius of $16\,mm$ but analysis was also done to verify that the solutions very quickly approach the half-space solution if both thickness and radius are increased.

The curves shown in Figures 4.3 and 4.4 reveal that the stiffness-to-modulus relation depends on estimations of the remaining elastic parameter ν or E, but the low slopes of the curves suggest that the conversions are not highly sensitive to these estimations. In fact if the estimated Poisson's ratio was taken to be zero for an incompressible material–a very wrong assumption–the accuracy of the shear modulus estimation would only suffer by about 12%. Since most tissues can be reasonably assumed to be nearly incompressible the likely errors introduced would be much smaller with an estimated Poisson's ratio of 0.49. This shows that the experimental setup is dominated by the shear response with minimal, but not negligible, coupling to the other elastic moduli.

These results also show that as the sample thickness is increased the conversion curves get closer and closer together. This means that when thicker samples are tested, the input thickness need not be of high accuracy to yield useful results. This is another advantage for an in situ testing environment. The curves of the finite samples are well approximated by cubic functions of ν or E, a fact that will be exploited in obtaining the stiffness-to-modulus conversion factors.

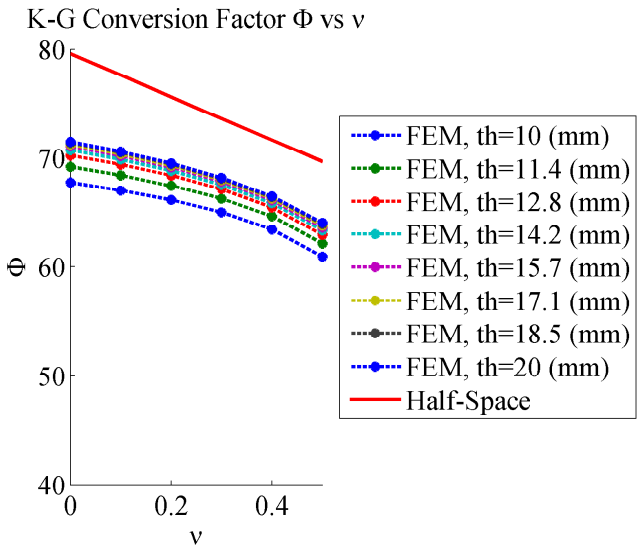

Figure 4.3: Comparing $\Phi(th, \nu)$ to the half-space solution.

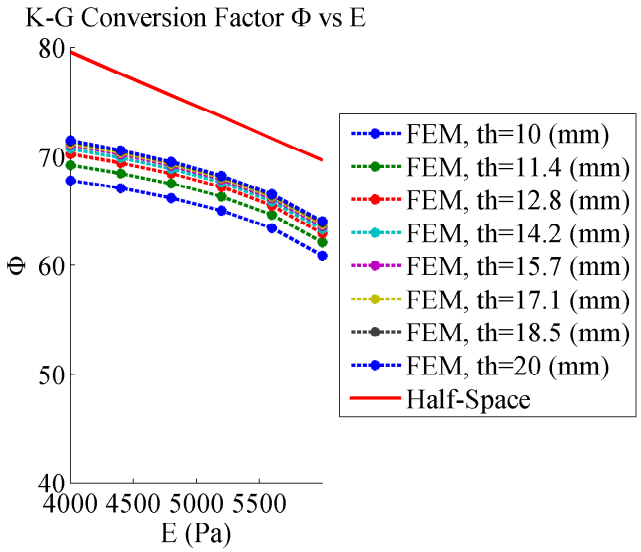

Figure 4.4: Comparing $\Phi(th, E)$ to the half-space solution.

4.1 Φ cubic function in ν and th.

The conversion function $\Phi(th, nu)$ provides a practical means of translation the the magnitude of the sample stiffness K to the magnitude of the complex shear modulus $|G^*|$. The conversion function is well approximated by a cubic function of ν, whose coefficients are well approximated by a cubic function of the sample thickness th.

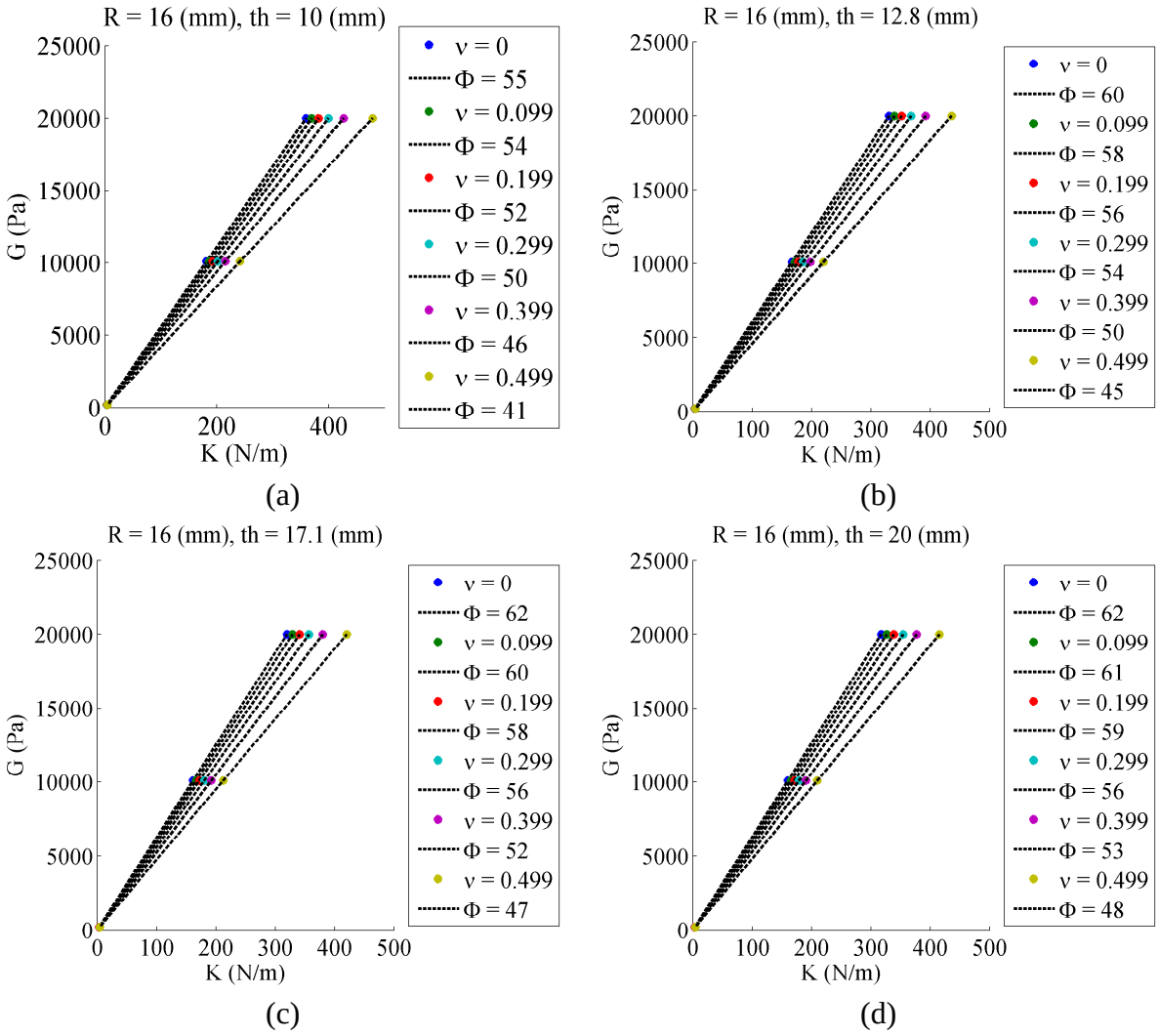

Figure 4.5: Computationally resolved relations $G = \Phi(th, \nu)K$ for $th = 10\,mm$, $13\,mm$, $17\,mm$, and $20\,mm$.

The linear relationship among stiffness and shear modulus can be seen in figures 4.5 (a) -(d) as the sample thickness is varied from $10\,mm$ in Figure 4.8 (a) to $20\,mm$ in Figure 4.8 (d). The conversion factor, or slope, decreases with an increasing estimation of Poisson's ratio.

The coefficients for the conversion factor Φ are determined using finite element solutions and a cubic fit. For the range of thickness values appropriate for testing ($10mm - 20mm$). The boundary radius was taken to match the hole in the boundary plate which has a radius of $16mm$. The loaded region was applied over a central region with a $4mm$ radius, to match the adhesion disc at the tip of the load cell. This is detailed in Figure 4.6.

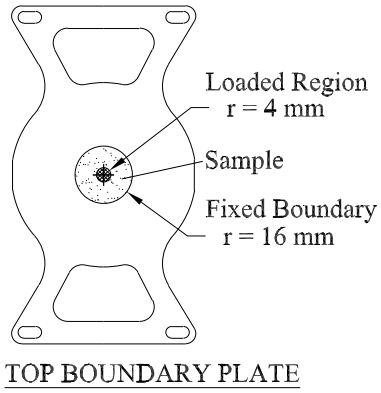

Figure 4.6: The top boundary plate with the fixed radius and loaded region shown.

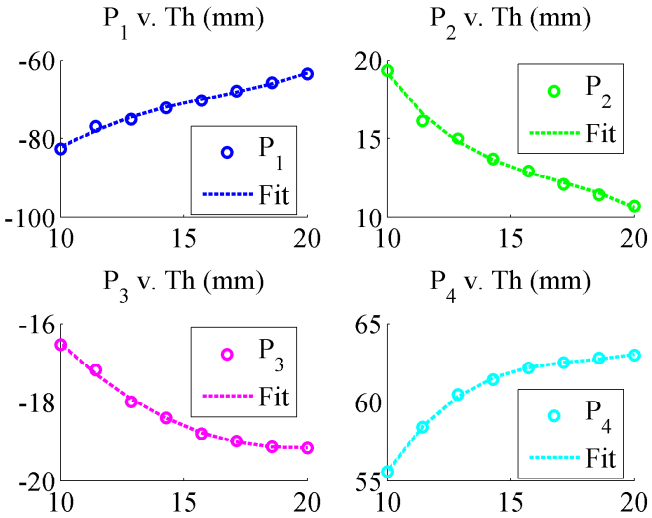

Figure 4.7: Cubic fit of cubic coefficients $P_i(th) = f(th^3)$ for $\Phi(th, v) = P_1 v^3 + P_2 v^2 + P_3 v + P_4$.

Taking thickness th in *mm* the fucntion is

$$P_1(th) = 0.020305\,th^3 - 0.990230\,th^2 + 17.384655\,th - 177.387718,$$

$$P_2(th) = -0.012153\,th^3 + 0.615038\,th^2 - 10.795137\,th + 77.767416,$$

$$P_3(th) = -0.000438\,th^3 + 0.050747\,th^2 - 1.481435\,th - 6.327286,$$

$$P_4(th) = 0.011650\,th^3 - 0.628897\,th^2 + 11.454462\,th - 7.708364, \text{ and}$$

$\Phi = P_1 v^3 + P_2 v^2 + P_3 v + P_4$ such that $G = \Phi K$ provides a way to convert the discrete structural response of the sample to a continuous material properties. Here, the polynomial coefficients P_i are obtained by computing a cubic fit to the data represented in Figure 4.7.

4.2 Φ function in E and th.

The linear relationship among stiffness and shear modulus can be seen in figures 4.8 (a) -(d) as the sample thickness is varied from 10 *mm* in Figure 4.8 (a) to 20 *mm* in Figure 4.8 (d). The conversion factor, or slope, increases as the estimated value of Young's modulus is increased. Clearly, as the estimated value of Young's modulus decreases the curves get closer and closer. This increasing estimation of Young's modulus, with the shear modulus held constant, corresponds to a decreasing estimation Poisson's ratio.

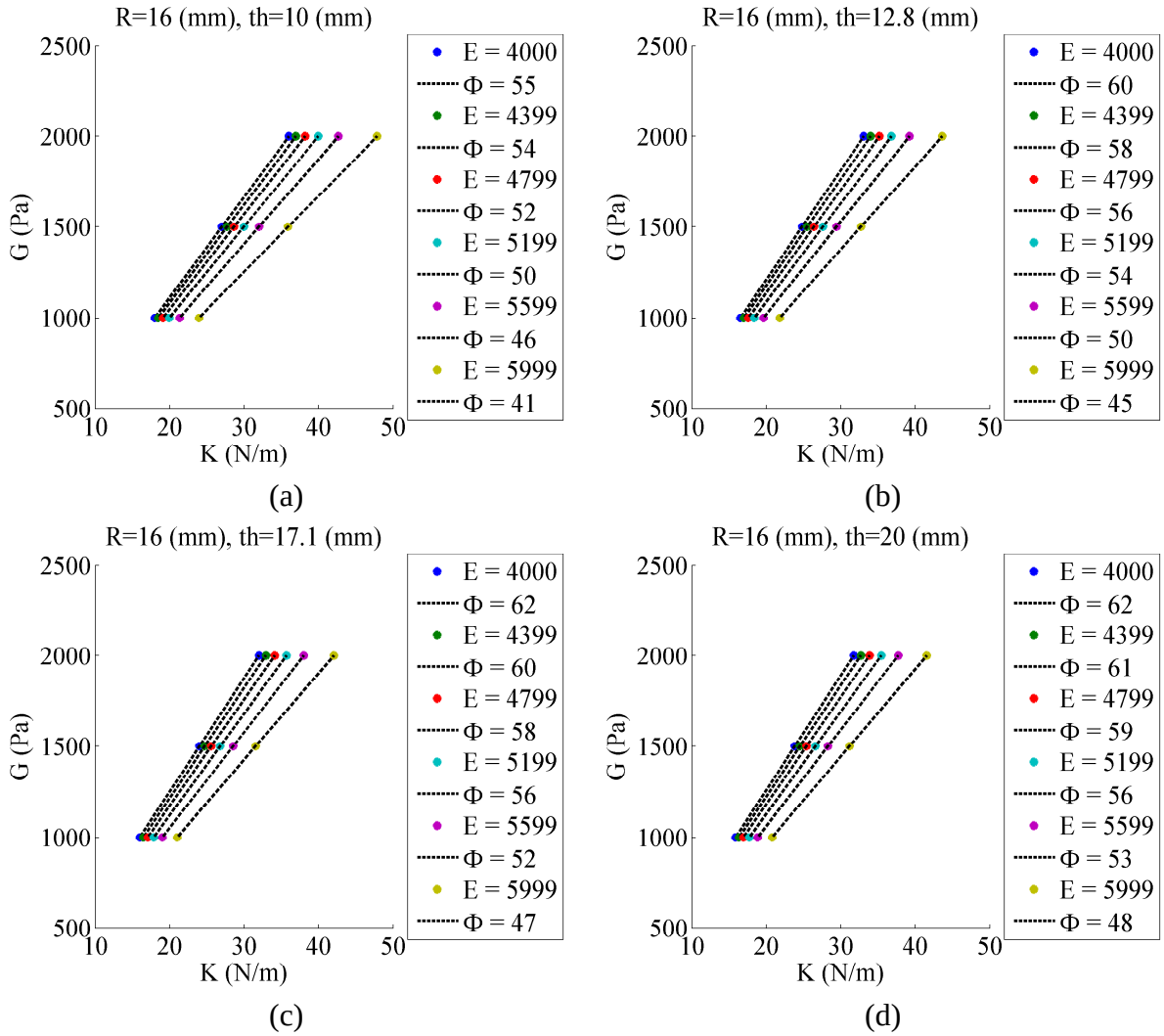

Figure 4.8: Computationally resolved relations $G = \Phi(th, E)K$ for $th = 10\,mm$, $13\,mm$, $17\,mm$, and $20\,mm$.

The conversion $\Phi(th,E)$ is well approximated by a cubic function of Young's modulus (E), whose coefficients are well approximated by linear functions of the sample thickness th. Taking thickness th in mm the fucntion is

$P_1(th) = 2.76127e-11\,th - 1.53463e-09,$

$P_2(th) = -3.79902e-07\,th + 2.00149e-05,$

$P_3(th) = 1.64808e-03\,th - 9.00401e-02,$

$P_4(th) = -1.60954e+00\,th + 1.88871e+02,$ and

$\Phi = P_1 E^3 + P_2 E^2 + P_3 E + P_4.$

This time, polynomial coefficients P_i are obtained by computing a linear fit to the data represented in Figure 4.9.

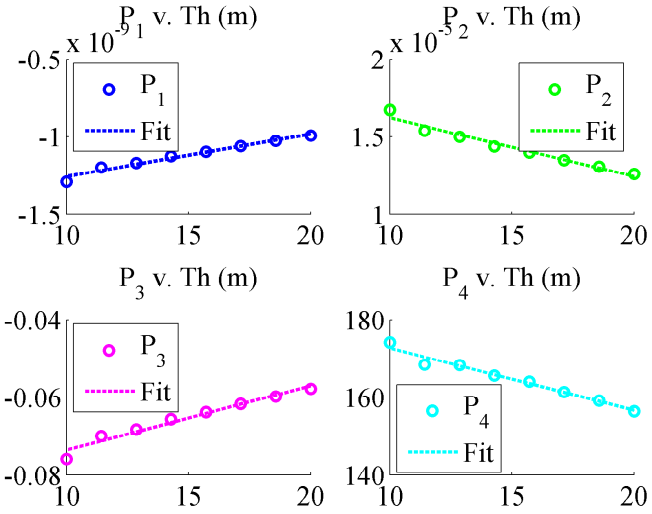

Figure 4.9: Linear fit of cubic coefficients $P_i(th) = f(th^3)$ for $\Phi(th,E) = P_1E^3 + P_2E^2 + P_3E + P_4$.

4.2.1 Insensitivity to Estimations of Thickness and Boundary Radius

As the boundary radius of the plate opening and the sample thickness are increased the solutions show greater agreement with the half-space solutions. This can be seen in Figure 4.10 where the error surface flattens out as the radius and thickness both approach $20\,mm$. This is per-

haps better understood looking at the contour plots of Figure 4.11 were the error fall below 20% for all radii greater than 14 *mm*. For a 16 *mm* boundary (as in the experimental setup)sample thicknesses exceeding 12 *mm* give solutions that are within 16% of the half-space solution. This confirms that thicker samples are less susceptible to errors introduced with estimations of sample geometries, but also suggests that, even without the conversion factor introduced in this section the experimental, results can be converted to continuous material properties using the half-space approximation. The quality of such an approximation would, admittedly, suffer increasingly for samples with a thickness less than 10 *mm* and a boundary plate radius less than 15 *mm*. Similarly, these approximation rely on a comparatively small loaded patch, 4 *mm* radius for our experimental setup.

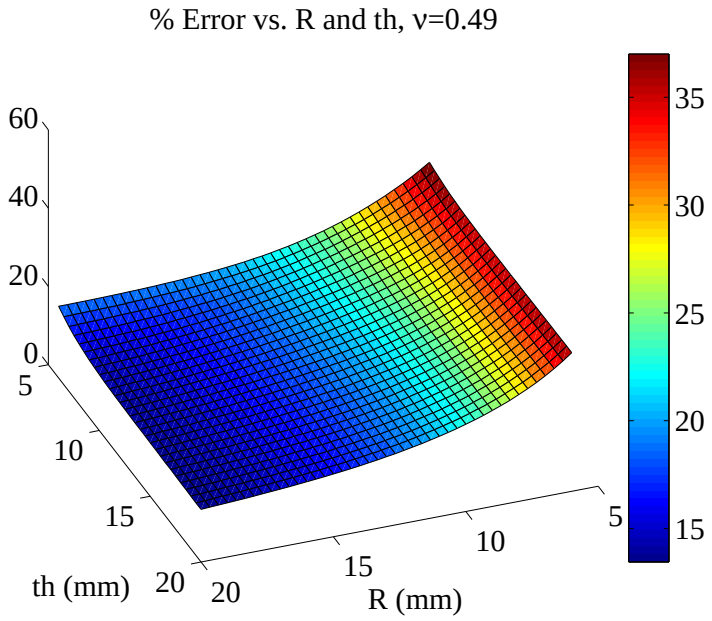

Figure 4.10: FEM vs half-space solution errors.

Figure 4.12 shows the sensitivity of the results as the sample radius and thickness are varied by looking at the total derivative with respect to the two extensional quantities. The derivatives are very small and the surface is nearly flat above 15 *mm* on both axes. In the practical regime of the experimental device, the total derivatives are 10^{-5}.

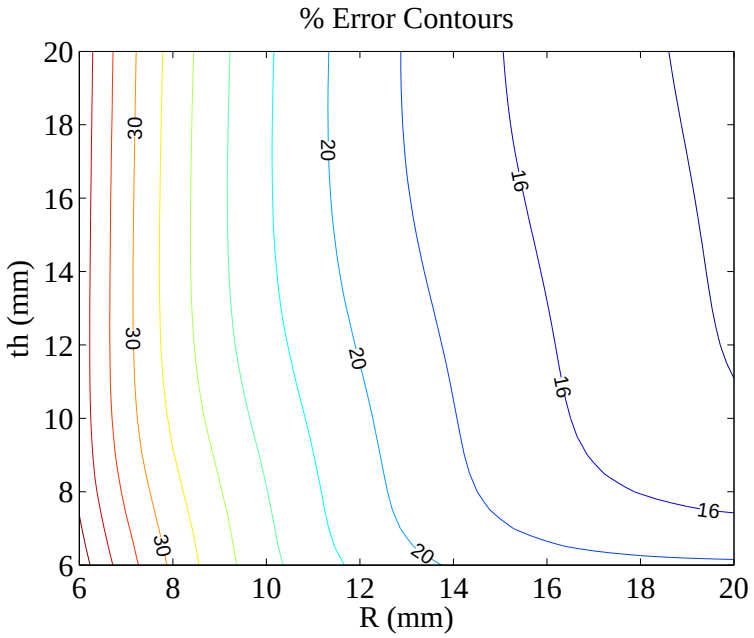

Figure 4.11: FEM vs half-space solution error contours.

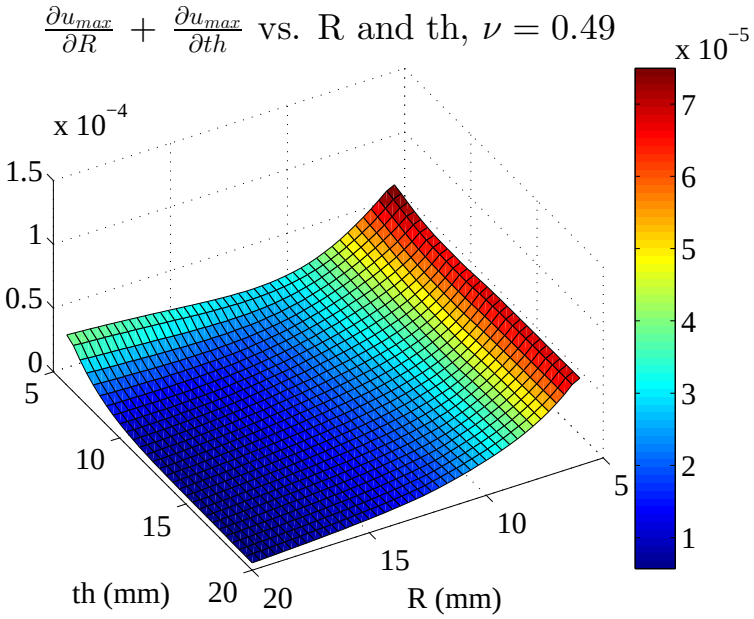

Figure 4.12: Geometric sensitivity for typical geometries with $\nu = 0.49$.

4.3 Newmark-Beta Numerical Integration Algorithm

Much about the ideal frequency response behavior can be observed in discrete solutions to the linear dynamic equilibrium equations. The last several decades have marked a dedicated

effort to improve methods of numerical integration techniques applied to the basic equation of motion of structural dynamics [46]. The discrete equations of motion for structural dynamics read:

$$[\mathbf{M}]\ddot{\mathbf{u}}(t) + [\mathbf{C}]\dot{\mathbf{u}}(t) + [\mathbf{K}]\mathbf{u}(t) = \mathbf{f}(t) \tag{4.4}$$

Where [**M**], [**C**], and [**K**] are the mass, damping, and stiffness matrices respectively. And, $\ddot{\mathbf{u}}(t)$, $\dot{\mathbf{u}}(t)$, and $\mathbf{u}(t)$ are the acceleration, velocity, and displacement vectors respectively. Typical methods use discrete time-stepping schemes that update the vectors $\ddot{\mathbf{u}}$, $\ddot{\mathbf{u}}$, and $\ddot{\mathbf{u}}$ at the current time t_n to the time at the next step $t_{n+1} = t_n + h$, where h is the interval of the time step. Where at least second order accuracy and unconditional stability are sought, the Newmark-Beta method is a good choice. The Newmark-Beta method's approach involves considering an integrated form of the equation of motion wherein velocity and displacement appear as state variables with acceleration algebraically isolated [47]. A limitation of this method occurs when high frequency components of the solutions are mere artifacts of the spatial discetization, and are related to the Nyquist frequency [46]. This can be controlled using numerical damping but such approaches reduce the accuracy of the integration scheme to first order. However, in systems where some physical damping is present, these artificial modes can be controlled. For this reason, these analyses are best suited to materials that have viscosity. They will be used here only for analysis where physical viscous damping is present. Furthermore, the need for accurate extraction of higher modes in absent from simple efforts to extract frequency response functions aimed at the resolution of a single steady-state mode under forced excitation.

4.3.1 Newmark-Beta Integration Scheme

First the displacement and velocity are expressed in terms of their values at time t_n and the acceleration at time t_{n+1}:

$$\dot{\mathbf{u}}_{\mathbf{n+1}} = \dot{\mathbf{u}}_{\mathbf{n}} + (1-\gamma)h\ddot{\mathbf{u}}_{\mathbf{n}} + \gamma h\ddot{\mathbf{u}}_{\mathbf{n+1}} \tag{4.5}$$

$$\mathbf{u_{n+1}} = \mathbf{u_n} + (\frac{1}{2} - \beta)h^2\ddot{\mathbf{u}}_\mathbf{n} + \beta h^2 \ddot{\mathbf{u}}_\mathbf{n+1} \tag{4.6}$$

Where γ is a parameter that is varied from zero to one to control how implicit or explicit the velocity predictor behaves. When $\gamma = 1$ the velocity predictor is fully explicit and as γ is decresed to zero, the velocity predictor becomes increasingly implicit.

The above expressions are substituted into the equation of motion to provide the following update equation in terms of $\dot{\mathbf{u}}_\mathbf{n}$ and $\mathbf{u_n}$:

$$([\mathbf{M}] + \gamma h[\mathbf{C}] + \beta h^2[\mathbf{K}])\ddot{\mathbf{u}}_\mathbf{n+1} = \mathbf{f}_{n+1} - [\mathbf{C}](\dot{\mathbf{u}}_\mathbf{n} + h(1-\gamma)\ddot{\mathbf{u}}_\mathbf{n}) - [\mathbf{K}](\mathbf{u_n} + h\dot{\mathbf{u}}_\mathbf{n} + h^2(\frac{1}{2} - \beta)\ddot{\mathbf{u}}_\mathbf{n}) \tag{4.7}$$

Letting:

$$[\mathbf{S}] = [\mathbf{M}] + \gamma h[\mathbf{C}] + \beta h^2[\mathbf{K}] \tag{4.8}$$

Gives a solution for subsequent acceleration in the form:

$$\ddot{\mathbf{u}}_\mathbf{n+1} = [\mathbf{S}]^{-1}(\mathbf{f}_{n+1} - [\mathbf{C}](\dot{\mathbf{u}}_\mathbf{n} + h(1-\gamma)\ddot{\mathbf{u}}_\mathbf{n}) - [\mathbf{K}](\mathbf{u_n} + h\dot{\mathbf{u}}_\mathbf{n} + h^2(\frac{1}{2} - \beta)\ddot{\mathbf{u}}_\mathbf{n})) \tag{4.9}$$

Now, the velocity and displacement solution for t_{n+1} can be updated according the rules defined in the previous two equations.

The ideal solutions can be easily modified to include the effects of apparatus friction though the use of numerical models with as few as one or two degrees-of-freedom (DOF).

4.3.2 Newmark-Beta Time-stepping Algorithm with Implemented Nodal Friction

Classic one degree of freedom vibrations solutions are important in characterizing frequency response trends. The one DOF model with included frictional effects is key in defining the effects associated with device friction. Kinetic and static friction are implemented in a way that modifies the forcing function by criteria defined by the velocity predictor. When the

predicted velocity is below a predefined limit, the frictional force added to the excitation force is adjusted by an certain amount. This is the prescibed static friction, known as the Coulomb condition.

When the predicted velocity surpasses the "sticking" velocity, the appended frictional force assumes a different, typically lower, value. This is the prescribed kinetic friction. Since the force is still continuous in the open interval of the time-step the Newmark-Beta methods is perfectly suited to these discontinuous forcing functions. Similar uses of the Newmark-Beta method in modeling stick-slip instabilities have been successfully implemented [48]. The instabilities predicted by the numerical solutions that account for Coulomb friction are also seen in our experimental results. Furthermore, the numerical results successfully reproduce the time-domain displacement response typically realized as a deviation from a smooth sine wave toward a step wave.

Static and kinetic friction is implemented in the integration scheme with a simple conditional choice of offsetting force terms. Let

$$\mathbf{f_{sin}}(t) = \mathbf{F_0} sin(\omega t) \tag{4.10}$$

be the excitation control force exerted by the voice coil, and let $\mathbf{f_k}$ and $\mathbf{f_s}$ be the kinetic and static friction respectively. And, $\mathbf{v_{stick}}$ be the sticking velocity defined for each DOF independently.

Now we can define conditional update rules for the Coulomb friction implementation for i^{th} degree-of-freedom at the n^{th} time-step:

$if\ |\dot{u}_n^i| > v_{stick}^i$

$$f_{n+1}^i = f_{sin}^i(t_{n+1}) + f_k^i \tag{4.11}$$

else

$$f_{n+1}^i = f_{sin}^i(t_{n+1}) + f_s^i \tag{4.12}$$

end

The $sign(f_k^i)$ is opposite of the predicted velocity, and the $sign(f_s^i)$ opposite of $(f_{n+1}^i - [\mathbf{M}]\ddot{u}_n^i - [\mathbf{C}]\dot{u}_n^i - [\mathbf{K}]u_n^i)$.

The magnitudes are limited so that friction does not create motion by $min(|f_k^i|, |f_{n+1}^i - [\mathbf{M}]\ddot{u}_n^i - [\mathbf{K}]u_n^i|)$, and $min(|f_s^i|, |f_{n+1}^i - [\mathbf{M}]\ddot{u}_n^i - [\mathbf{K}]u_n^i|)$.

Where $\dot{u}_n^i$ is the velocity of i^{th} DOF at the n^{th} times-step, $f_{sin}^i(t_n)$ is the excitation force of the i^{th} DOF at the n^{th} times-step, f_k^i is the kinetic frictional force of i^{th} DOF, f_s^i is the static frictional force of i^{th} DOF, and f_{n+1}^i is the total force of the i^{th} DOF at the $n+1^{st}$ times-step.

This loop will be used to assemble the $\mathbf{f_{n+1}}$ forcing vector in the Newmark-Beta time-stepping scheme. Since the condition that chooses whether kinetic or static frictional forces will be used depends explicitly on the current velocity $\dot{\mathbf{u}}_\mathbf{n}$, the scheme can be repeated iteratively using the updated velocity to provide an improved value of $\mathbf{f_{n+1}}$ that is based on the predicted velocity in the updating condition. Simulations show that the use of more than one iteration has virtually no effect on the behavior of concern. Therefore, to save computational cost, only one update iteration is typically used.

4.4 Frequency Response Functions

The frequency response functions generated by the time-stepping algorithm show resonant system behavior, phase shift asymptotes, and jumps in the response curve resulting from system friction. This goes far to explain some of the effects seen in the system response of the experimental rheometer. Although friction has little effect on the data gathered by instruments at the sample adhesion boundary, the LVDT and coil-current signals are very dependent on system friction as well inertial and resonant effects.

4.4.1 Zero Friction Case (C=1)

When system friction is neglected, the response is smooth with a clear phase transition having a value of $\frac{\pi}{2}$ at the resonant frequency seen as a peak in the transfer function (Figure

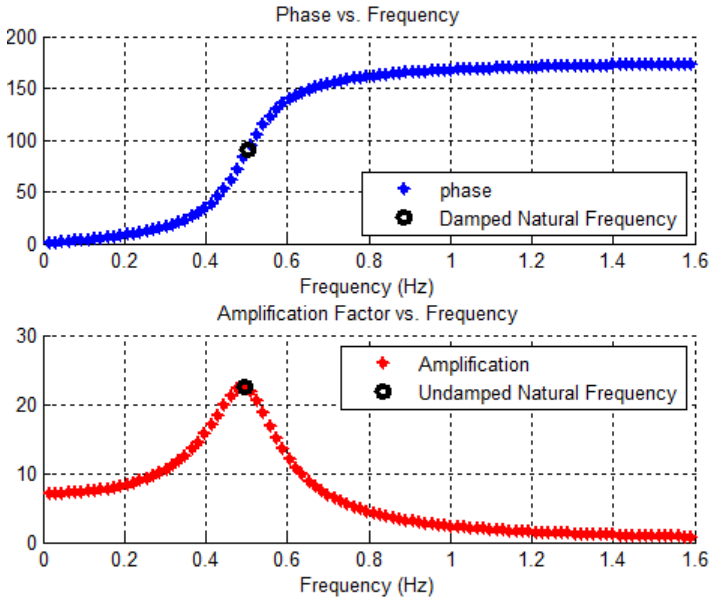

Figure 4.13: Zero friction case, C=1.

4.13). The analytical solution to the zero-friction case, for a single degree of freedom, is readily available and was verified to agree with these solutions. As will be shown, the greatest use of this model is in analyzing a two DOF system where friction inclusive analytical solutions are not at hand.

The model input parameters are: n timesteps per period $= 100$, $M = 1$, $K = 10$, $C = 1$, $\omega_n = 3.1623$, $\omega_d = 3.1225$, $\zeta = 0.15811$, $f_k = 0$, $f_s = 0$. The Newmark coefficients as set as $\beta = 1/4$ and $\gamma = 1/2$, which is typical throughout this work.

4.4.2 Kinetic Friction Only (C=1)

When sliding friction is introduced, but not stick-slip friction, as seen in Figure 4.14 jumps can be seen in the system response curves, especially at low frequencies. This is problem that plagues the experimental results, reveling itself as divergence of the displacement control algorithms due to low frequency sticking.

The model input parameters are: n timesteps per period $= 100$, $M = 1$, $K = 10$, $C = 1$, $\omega_n = 3.1623$, $\omega_d = 3.1225$, $\zeta = 0.15811$, $f_k = 0.3F_0$, $f_s = 0.5F_0$, $v_{stick} = 0$.

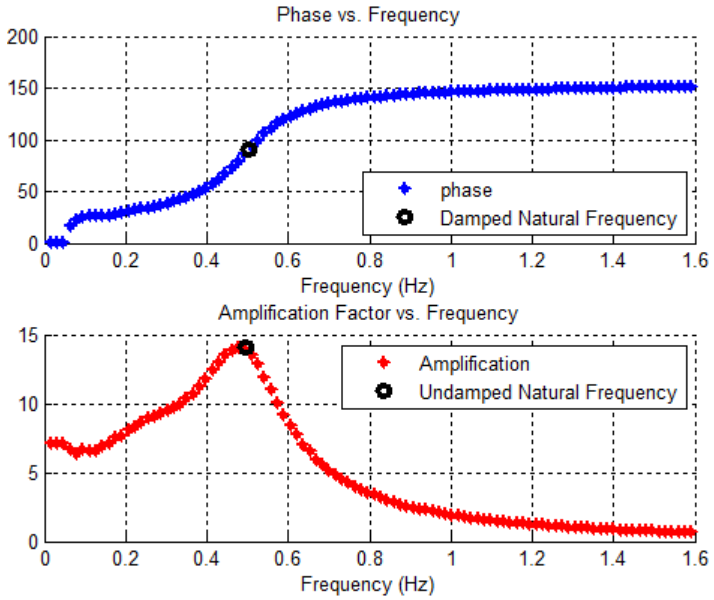

Figure 4.14: Zero sticking friction case, C=1.

4.4.3 Static and Kinetic Friction with High Sticking Velocity (C=1)

When stick-slip friction is included in the analysis , as seen in Figure 4.15 increasingly troublesome jumps can be seen in the system response curves, especially at sub-resonant frequencies. This is also a problem that plagues the experimental results, reveling itself as divergence of the displacement control algorithms due to low frequency sticking.

The model input parameters are: n timesteps per period $= 100$, $M = 1$, $K = 10$, $C = 1$, $\omega_n = 3.1623$, $\omega_d = 3.0$, $\zeta = 0.15811$, $f_k = 0.3F_0$, $f_s = 0.5F_0$, $v_{stick} = 0.2$.

4.4.4 Zero Friction with Increased Viscous Damping (C=2)

When friction is neglected, increasing damping has the expected effect of smoothing the resonant peak and blurring the phase shift transition. Again, these results were verified to match the analytical solution. This is demonstrated in Figure 4.16.

The model input parameters are: n timesteps per period $= 100$, $M = 1$, $K = 10$, $C = 2$, $\omega_n = 3.1623$, $\omega_d = 3.0$, $\zeta = 0.15811$, $f_k = 0$, $f_s = 0$.

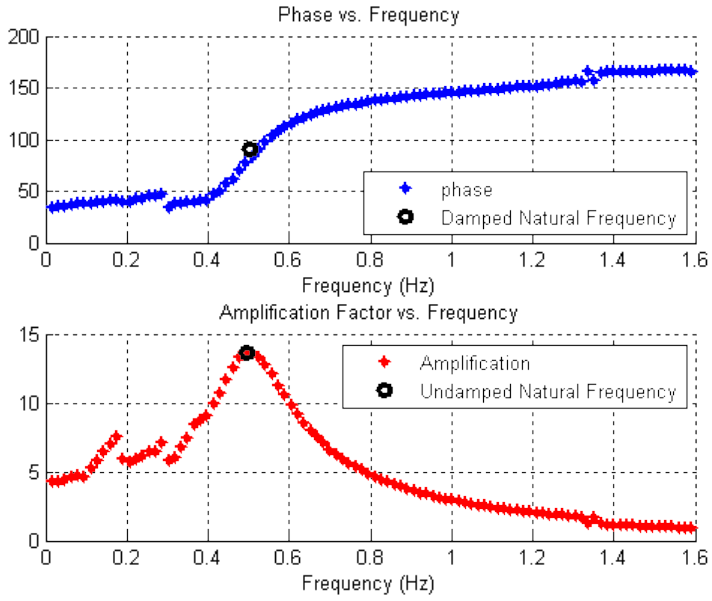

Figure 4.15: High sticking velocity case, C=1.

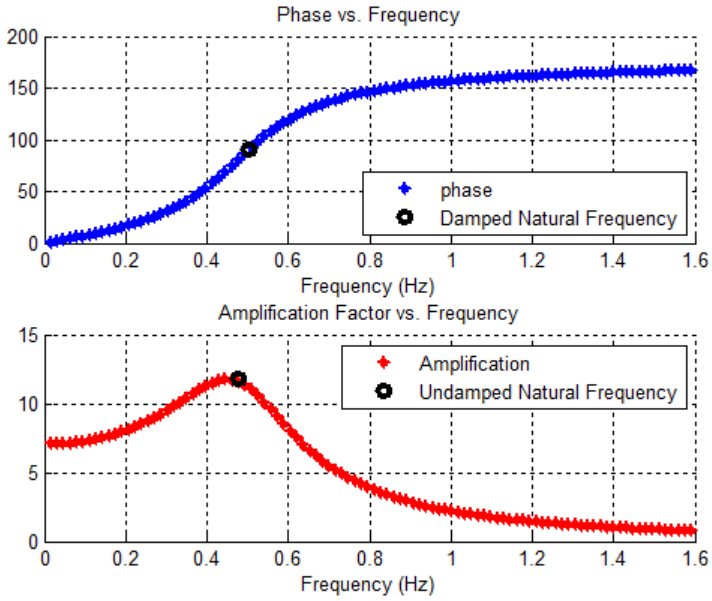

Figure 4.16: Zero friction case, C=2.

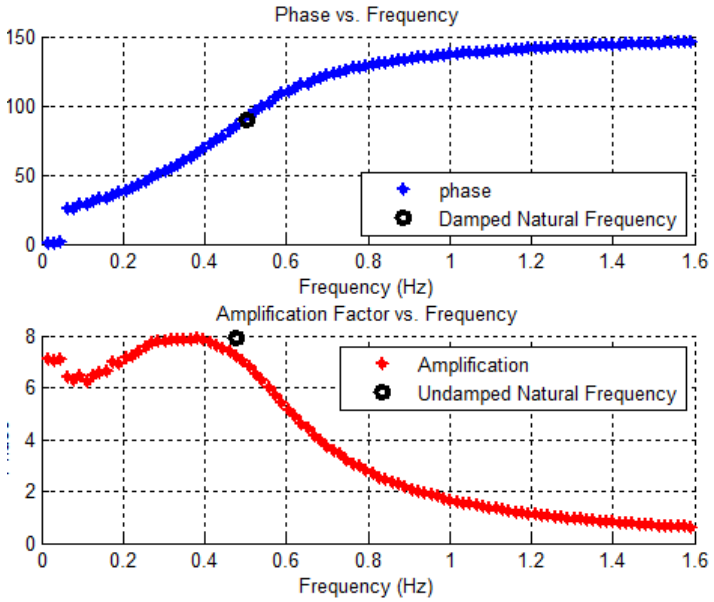

Figure 4.17: Zero sticking velocity case, C=2.

4.4.5 Kinetic Friction Only with Increased Viscous Damping (C=2)

If damping is increased in the model that considers only sliding-friction, the resonant response is mitigated and the low frequency jumps are still observed. This is demonstrated in Figure 4.17.

The model input parameters are: n timesteps per period $= 100$, $M = 1$, $K = 10$, $C = 2$, $\omega_n = 3.1623$, $\omega_d = 3.0$, $\zeta = 0.31623$, $f_k = 0.3F_0$, $f_s = 0.5F_0$, $v_{stick} = 0$.

4.4.6 Static and Kinetic Friction with High Sticking Velocity and Increased Damping (C=2)

Considering increased system damping results in more response jumps in the stick-slip system of Figure 4.18. In this case, the frequency jumps also occur at super-resonant frequencies.

The model input parameters are: n timesteps per period $= 100$, $M = 1$, $K = 10$, $C = 2$, $\omega_n = 3.1623$, $\omega_d = 3.0$, $\zeta = 0.31623$, $f_k = 0.3F_0$, $f_s = 0.5F_0$, $v_{stick} = 0.2$.

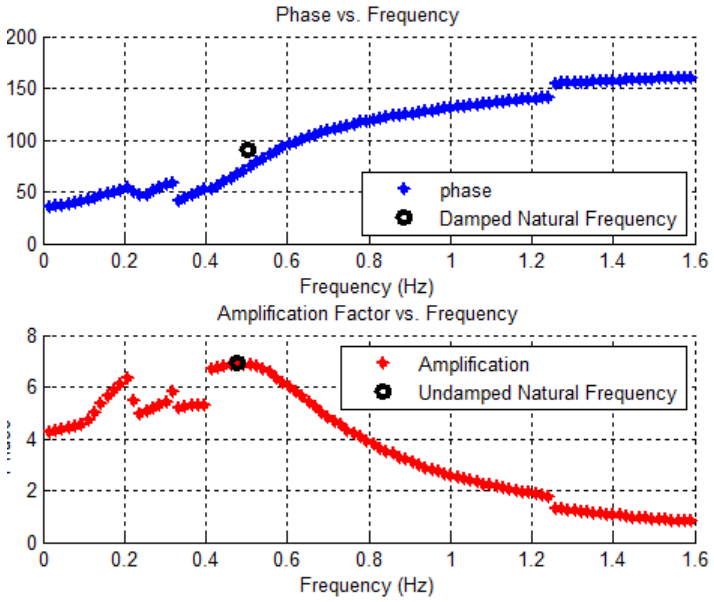

Figure 4.18: High sticking velocity case, C=2.

These single DOF models verify the working of the algorithm and give insight to some frequency response behavior that would be otherwise difficult to interpret from the experimental responses alone. This is invaluable to device development where anamolous results may be attributable to anything from non-linear material responses to poorly callibrated instruments or channel cross-talk. Knowing that jumps in amplitude can be readily explained by considering the effects of stick-slip friction dramatically simplifies troubleshooting.

While the single DOF response is quite informative, the experimental setup is not quite so simple. While the moving axis of the voice-coil represents one degree-of-freedom, the independent data collected at the sample interface represents another. To better characterize the physical system, a two DOF model is called for. This is easily accomplished with the existing Newmark time-stepping algorithm as it was modified to include frictional effects.

4.5 Multiple Degree-of-freedom Newmark Time-stepping Algorithm with Implemented Nodal Friction

The multiple-degree-of-freedom (MDOF) model is used to analyze the strain gauge tip style setup. In this experimental setup, the forces and displacements are observed at two distinct DOF locations: the moving linear axis; and the tip itself.

Stick-slip friction can explain some experimental anomalies. Although much more computationally expensive to run, finite element models of the dynamic response lead to similar observed behavior. The experimental system is well represented by a simple two degree-of-freedom system, and finite element analysis is unnecessary to characterize the basic system response.

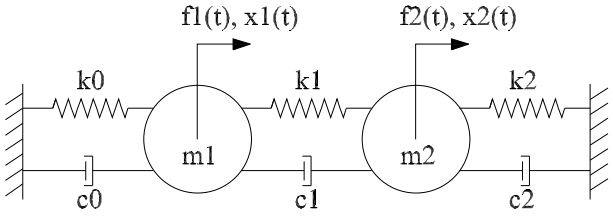

m1- Mass of the moving axis
m2- Moving mass of the sample

k0- Voice-coil return spring stiffness
k1- Cantilever load cell stiffness
k2- Sample stiffness

c0- Viscous damping of coil and slide
c1- Viscous damping of load cell
c2- Sample viscosity

Figure 4.19: The experimental setup is well modeled by a simple two-degree-of-freedom system of masses, springs and dashpots. The friction-inclusive Newmark time-stepping solution can explain much of the experimental response.

Figure 4.19 shows how the experimental setup is effectively modeled using a simple

two-degree-of-freedom system. The DOF at m_1 represents the the excitation axis, while the DOF at m_2 represents the sample at the loaded boundary.

The moving mass of the excitation axis is taken as $46.5\,g$ and the stiffness of the voice-coil centering spring is taken as $k_0 = 766\,N \cdot m^{-1}$. The strain gauge stiffness is estimated to be about $k_1 = 50000\,N \cdot m^{-1}$.

In the physical system, $f1(t)$ is the force provided by the voice-coil motor as measured in the current proportional coil voltage signal. The axis displacement of the physical system is measured by the LVDT and is modeled as $x1(t)$. The sample response in the physical system is measured at the dynamically loaded boundary by the strain gauge and fiber optic probe. The strain gauge measures the force, which is modeled by $f2(t) = (k1)(x1(t) - x2(t)$. The fiber optic probe measures the sample displacement $x2(t)$.

For use in the MDOF, friction inclusive, Newmark model the mass matrix is

$$[\mathbf{M}] = \begin{bmatrix} m_1 & 0 \\ 0 & m_2 \end{bmatrix}, \tag{4.13}$$

the stiffness matrix is

$$[\mathbf{K}] = \begin{bmatrix} k_0 + k_1 & -k_1 \\ -k_1 & k_1 + k_2 \end{bmatrix}, \tag{4.14}$$

and the viscosity matrix is

$$[\mathbf{C}] = \begin{bmatrix} c_0 + c_1 & -c_1 \\ -c_1 & c_1 + c_2 \end{bmatrix}. \tag{4.15}$$

This gives the system

$$\begin{bmatrix} m_1 & 0 \\ 0 & m_2 \end{bmatrix} \begin{Bmatrix} \ddot{x_1} \\ \ddot{x_2} \end{Bmatrix} + \begin{bmatrix} c_0 + c_1 & -c_1 \\ -c_1 & c_1 + c_2 \end{bmatrix} \begin{Bmatrix} \dot{x_1} \\ \dot{x_2} \end{Bmatrix} + \begin{bmatrix} k_0 + k_1 & -k_1 \\ -k_1 & k_1 + k_2 \end{bmatrix} \begin{Bmatrix} x_1 \\ x_2 \end{Bmatrix} = \begin{Bmatrix} f_1(t) \\ f_2(t) \end{Bmatrix}, \tag{4.16}$$

which is sent to the Newmark solver.

The Newmark-Beta method with the described algorithm for modeling friction is used to verify the experimentally observed response. The system variables can be modelled across a frequency spectrum, but the current application highlights how the system parameters of the numerical (two DOF) solution can be tailored to explain the behavior at a given frequency. The moving axis of the voice-coil and LVDT are represented here as DOF1 and the local response at the sample interface is represented as DOF2.

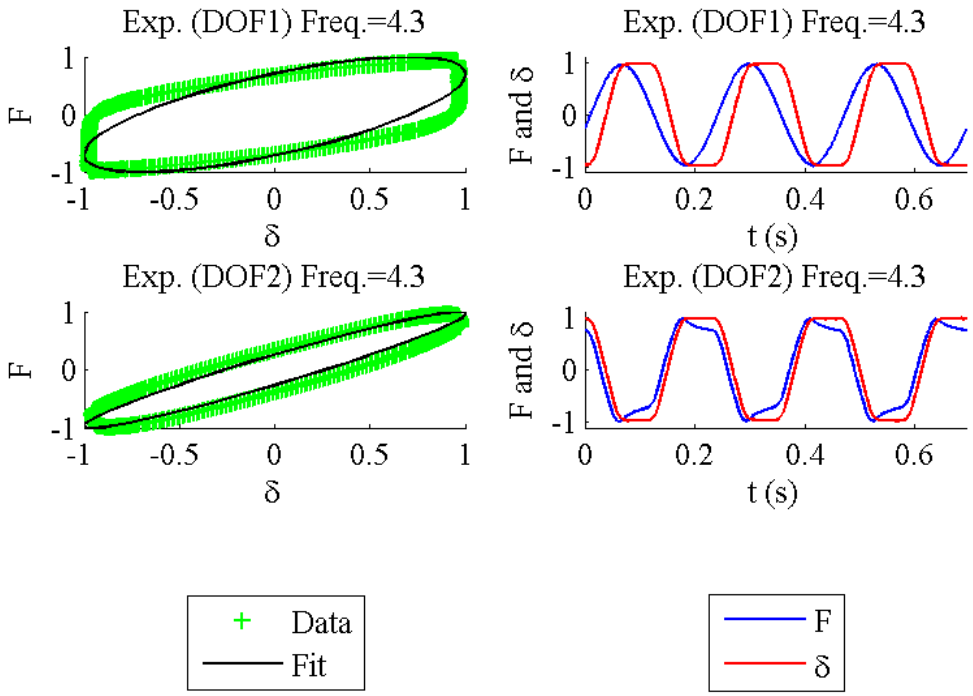

Figure 4.20: Porcine tissue response at 4.3 *Hz*.

As a particular example, to show the models ability to capture phenomena seen in the physical system, the response of the porcine tissue detailed in the results chapter is analyzed here at the relatively low frequency of 4.3 *Hz*. This response is complex in it's subtleties and is indicative of the loop readouts seen throughout a frequency sweep. The hysteresis ellipse of the device response has vertical jumps at the extremes of the displacement response, as seen in Figure 4.20. This is caused by stick-slip friction, and it is well modeled by the algorithm (Figure 4.21). Stick-slip (static) friction is also responsible for the squared wave patterns observed at

low frequencies. The stick slip friction is applied to DOF1 to model the sicking of the control axis. This sticking is caused by slight misalignment of the LVDT and coil axes as well as simple contact friction in the instruments and the linear slide rail.

Kinetic friction is also applied to DOF1. The consideration of kinetic friction causes a widening of the hysteresis ellipse at DOF1 which can also be seen as a corresponding increase in the phases-lag. This has a subsequent effect on the force curve of DOF2 which arises as a local force contribution at the sample interface.

The input parameters used in the soutions of Figure 4.21 are as follows:

the coil return spring stiffness is $k_0 = 76\,N \cdot m^{-1}$; the cantilever load cell stiffness is $k_1 = 50000\,N \cdot m^{-1}$; the sample stiffness is $k_2 = 300\,N \cdot m^{-1}$; the coil axis viscosity is $c_0 = 10\,kg \cdot s^{-1}$; the load viscosity is $c_1 = 0\,kg \cdot s^{-1}$; and the sample viscosity is $c_2 = 3\,kg \cdot s^{-1}$; the moving axis mass is $m_1 = 46.5\,g$; and the moving mass of the sample is $m_2 = 1\,g$.

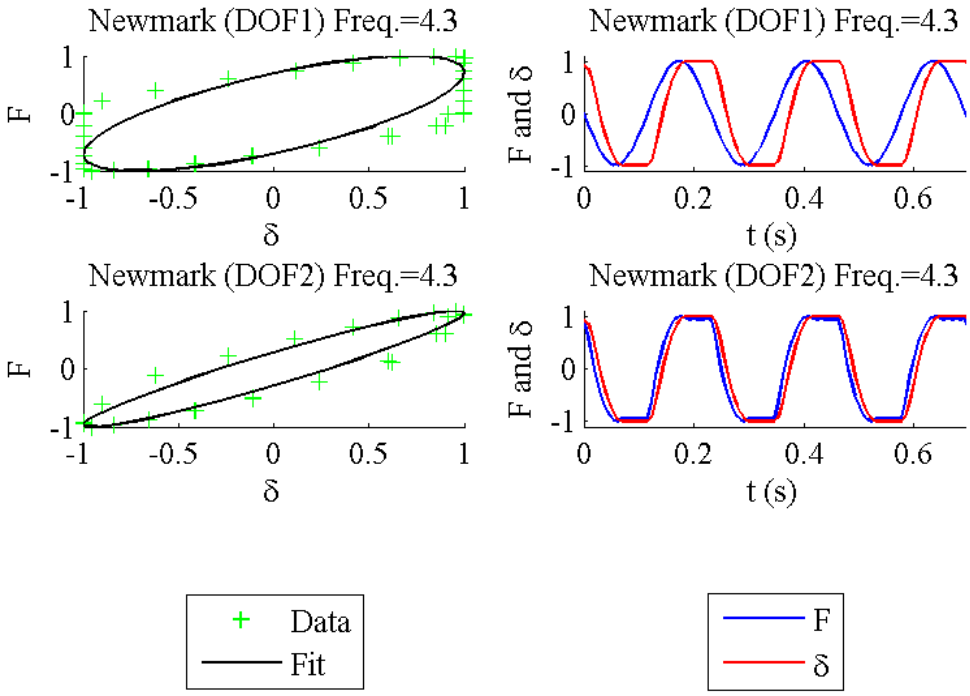

Figure 4.21: Friction-inclusive Newmark-Beta solution at $4.3\,Hz$.

The kinetic friction at the first DOF is taken to be $f_k = 0.2\,N$ and the static friction at

the first DOF is taken to be $f_s = 1.5 \cdot f_k = 0.3\,N$. No friction is applied to the second DOF where losses are assumed to be entirely viscous. The excitation frequency is $4.3\,Hz$ and thirty time steps are taken per cycle for a time-step of $0.0077\,s$. The algorithm is run to an assumed steady-state after 600 cycles have completed and any remaining transients are shifted out with a moving average offset. The phase shifts are determined using a root finding procedure based bisection with a bracket that is informed by the know excitation period of $\tau = 0.2308\,s$. The Newmark coefficients remain set at $\beta = 1/4$ and $\gamma = 1/2$, which is typical throughout this work.

Key features such as the force to displacement phase-lag and the respective amplitudes at the two locations instrumented on the device are captured. In figures 4.20 and 4.21 the results are shown normalized to make a phase comparison between the force and displacement signals convenient.

Chapter 5

Calibration and Performance Assessment

The ability of the experimentally device described in this work (the Elviscolator), to accurately and consistently produce useful estimations of the viscoelastic shear properties of an arbitrary soft solid is tested on both synthetic tissue phantoms and real tissues. A two tiered approach to calibration was adopted: first, the instruments themselves were independently calibrated; then the final results were calibrated with the use characterized tissue samples. Initially each instrument is calibrated in turn, and finally the whole device is linearly calibrated against independently obtained trusted results for a stable synthetic polymer sample.

5.1 Instrument Calibration, and Resolution

The resolutiona of the four primary instruments are conservatively calculated by scaling the maximum signal noises by the individual calibration factors to give physical units. Table 5.1 lists the resolutions of the force and displacement instruments for the moving axis and sample interface. The resolution achieved during testing is much better due the use of moving averages and very high sampling rates. Using these conservative estimates, the resolution of the stiffness calculations are calculated with

$K_{res} = 1 - \frac{1-SG_{res}}{1+FO_{res}} = 0.2086$. When multiplied the upper limit of the conversion factor Φ, which occurs with infinite thickness and $\nu = 0$, the calculated resolution of the computed

shear modulus magnitude is $|G*|_{res} = 17\,Pa$. Here, K_{res} is the resolution of the discrete stiffness of the sample interface, SG_{res} is the resolution of the strain gauge, FO_{res} is the resolution of the fiber-optic sensor, and $|G*|_{res}$ is the maximum resolution of the calculated shear modulus magnitude.

Table 5.1: The resolution of the coil current, LVDT, strain gauge, and fiber optic sensor signals.

Signal	Resolution
Coil Current	83.1 (N)
LVDT	0.0524 (mm)
Strain Gauge	0.0821 (N)
F.O Sensor	0.1598 (mm)

The linear range of each instrument is independently determined by calibration testing and linear curve fitting. The following instruments were independently calibrated: (1) the LVDT; (2) the stepper motors for real-time sample adjustment; (3) the current signal—proportional to applied force; (4) the fiber-optic displacement sensor; and (5) the cantilever tip strain gauge.

Figure 5.1 (a) shows the stepper motor calibration with a result of 100 $steps \cdot mm^{-1}$, and the LVDT 5.1 (b) weighs in at $0.86\,mm \cdot V^{-1}$. The fiber optic displacement sensor has limited linear range that begins at $0.2\,mm$ and extends out to $1.7\,mm$, as can be seen in figures 5.1 (a) and (b). The calibration factor of the fiber optic displacement sensor is $2.0\,mm \cdot V^{-1}$.

Figure 5.2 (a) shows the linear calibration of the voice coil giving a calibration factor of $639\,N \cdot V^{-1}$. In 5.2 (b) the strain gauge factor is $442\,N \cdot V^{-1}$, and in 5.2 (c) the base scale signal calibration is $3501\,N \cdot V^{-1}$. Figure 5.2 (d) shows the spring constant calibration for the two centering springs of the voice coil–giving a spring constant of $766\,N \cdot m^{-1}$.

Once rheological data are collected efforts to understand them may begin. This involves a host of post-processing techniques and associated methods. Each of these is usually implemented through a collection of algorithms.

Processing the signal outputs of the fiber optic probe requires special consideration.

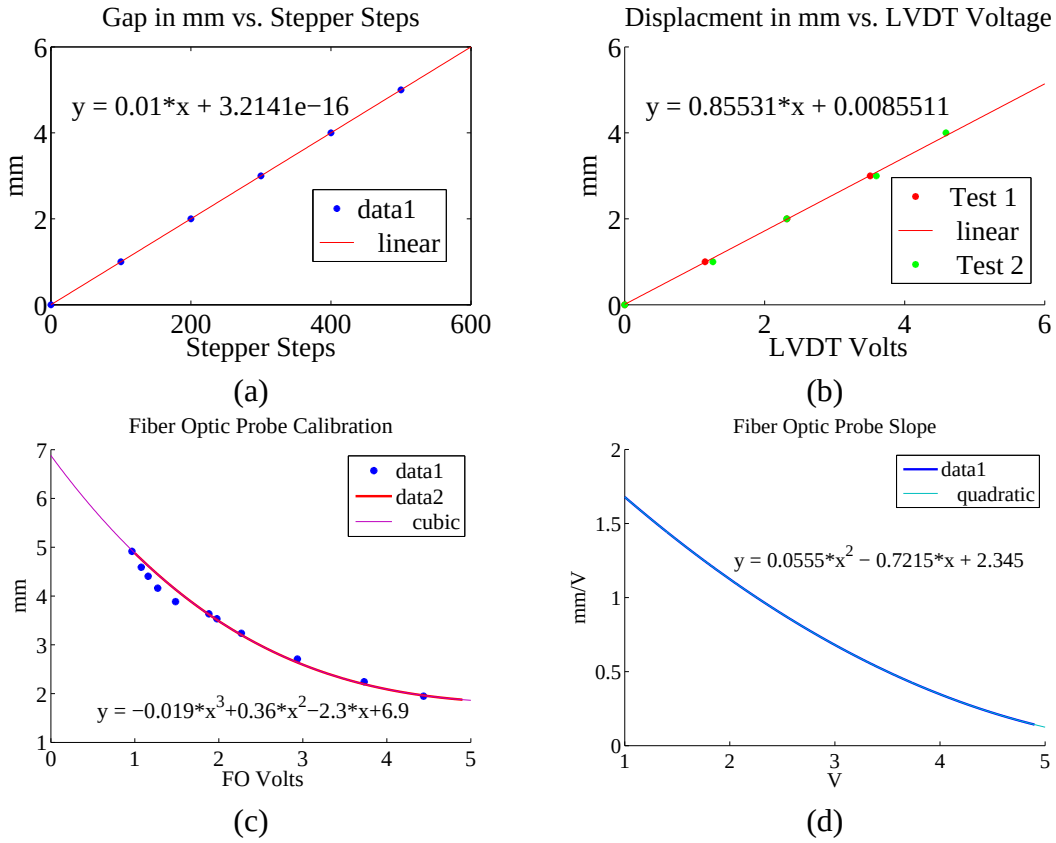

Figure 5.1: Displacement Instrument Calibration: (a) Stepper motors, (b) LVDT, (c) Fiber optic sensor cubic fit, and (c) Fiber optic sensor slope.

Because the desired displacement range is greater than the (rather small) linear range of the instrument, non-linear conversions are required. Fortunately, the sensor has a very repeatable non-linear output that is well approximated by a cubic fit. The fit shown in figure 5.2 (c) is used to get the quadratic conversion factors shows in 5.2 (d). The cubic coefficient can be easily adjusted during setup calibration by ensuring that the void-sample signal agrees with the, very linear response, of the LVDT. The probe should also be centered in its voltage range, somewhere near 2.5 volts. If the differential amplitude of the signal exceeds 0.75 volts, an slight increase in the calibration factor is applied–such that the secant of the calibration profile is used instead of the tangent–to a maximum of 0.133 when the differential amplitude reaches 2.5 volts (the entire range of the instrument).

The calibration factor of the fiber optic probe is taken as

$$FO_{factor} = 0.0555(V - 6.5)^2 . \tag{5.1}$$

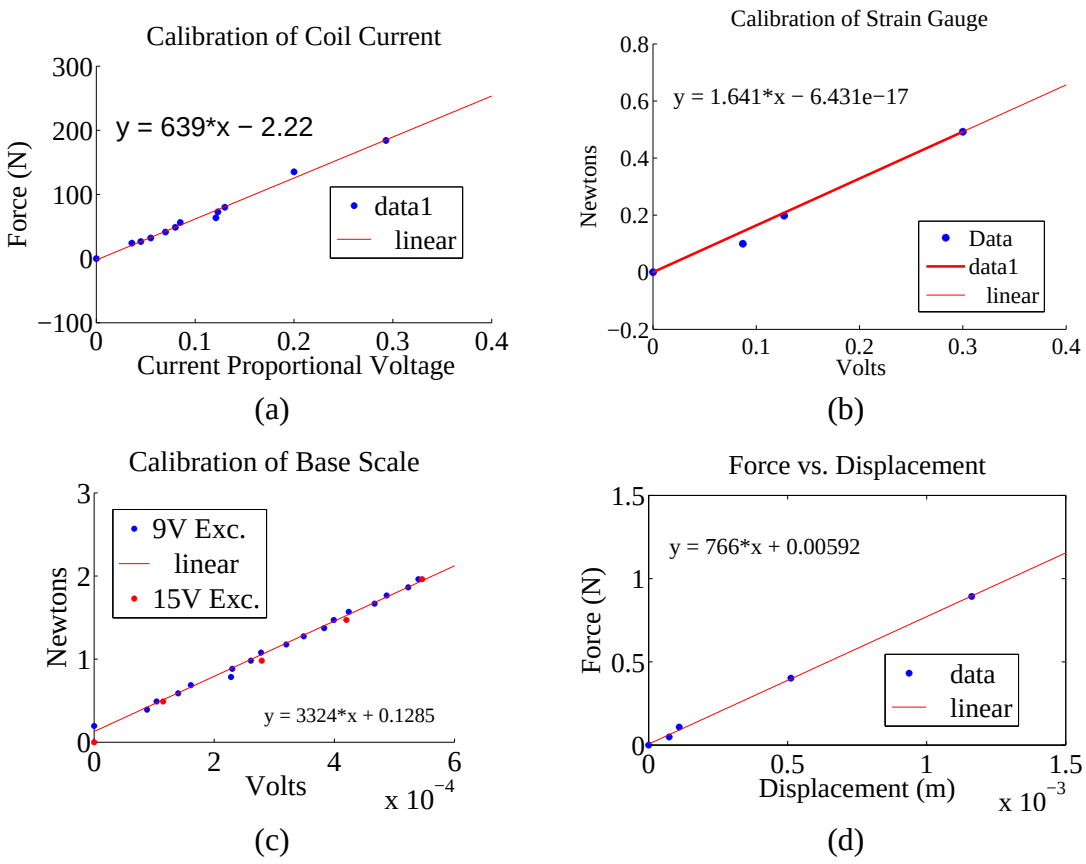

Figure 5.2: Force Instrument Calibration: (a) coil current, (b) strain gauge tip, (c) base scale, and (d) spring constant.

where V is volts and the coefficient 0.0555 can be adjusted during setup calibration.

5.1.1 Cantilever Strain Gauge Bending Compensation

Euler-Bernoulli beam theory is adequate for calculating the estimated sample interface displacement using to instrumentation at two points along the length of the cantilevered, strain gauge based, load cell.

The deflection of a cantilevered beam can be determined by

$$\delta_x = \frac{Fx^2}{6EI}(3L - x) \tag{5.2}$$

where δ_x is the transverse deflection of the beam at the w direction at extensional location x. The LVDT deflection is measured as $w = d_1$ at $x = 0$, the fiber optic sensor (F.O.) deflection is measured as $w = d_2$ at $x = L_2$ and the desired interface displacement is calculated from the previous two as $w = d_3$ at $x = L$.

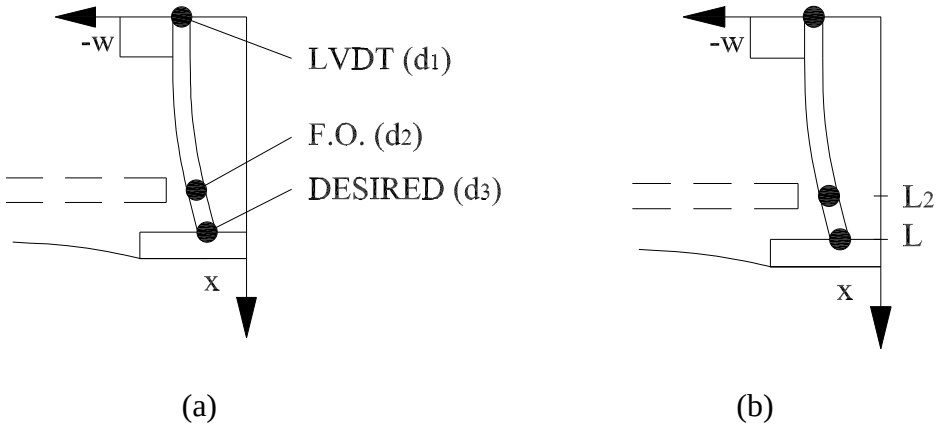

Figure 5.3: Bending of the strain gauge between the fiber optic displacement sensor and sample interface is compensated for analytically using Euler-Bernoulli beam theory: (a) x locations are $x = 0$ and $x = L_2$, and (b) the deflections are considered at $w = d_1$ at $x = 0$, $w = d_2$ at $x = L_2$ and $w = d_3$ at $x = L$.

Staring with the cantilever deflection formula, let

$$\delta_2 = (d1 - d2) = \frac{FL_2^2}{6EI}(3L - L_2)\,, \tag{5.3}$$

and let

$$\delta_3 = (d1 - d3) = \frac{FL^3}{3EI}\,. \tag{5.4}$$

Applying equation 5.3 to equation 5.4 gives the compensated sample displacement

$$d_3 = d_1 - \frac{2(d_1 - d_2)L^3}{L_2^2(3L - L_2)}\,. \tag{5.5}$$

A major challenge has been that of obtaining appropriate standards for comparison of results. While tissues are in reality neither homogeneous nor isotropic tracking of sample orientation and exact location renders such considerations a matter of future work. For our purposes, thermoplastics have proven to be practical for this purpose. Thermoplastics are elastomers that are catylized at high temperatures (around $300\,F^\circ$). The research of Egorov et al. used the "Tissue Elastometer," a compressive device of similar methodology, to test fresh store bought poultry breast, bovine liver, kidneys, hind shank, and porcine samples [34]. We will do similar tests in a subsequent section, but we begin here by taking a look at the device's ability to con-

sistently predict the viscoelastic characteristics of plastisol tissue phantoms that were produced in a well controlled laboratory environment.

The plastisol samples were sent to two independent labs with widely varying results. The characterization of the elastomer tissue phantoms was performed by two independent laboratories and the results vary significantly. Unfortunately, one set of results was clearly off by several orders of magnitude due to their use of a nano-indentation laboratory designed for much stiffer materials. Those results were discarded. This performance assessment is an ongoing process which will become more conclusive as independently characterized tissue phantoms are more readily available.

Viscoelastic calibration standards are not readily available, and the most commonly used calibration material (PDMS) is not well suited to this device due to its propensity to flow.

5.2 Performance Assessment

Due to the expense of independent sample characterization, performance assessments are limited to the evaluation of a few plastisol samples. Three samples were sent to an independent lab (Polymer Diagnostics in Avon Lake, Ohio) where they were tested using a TA Instruments ARES G2 commercial rheometer. The scientist in charge of the testing reported some difficulty with the softest of the three samples sent. He could not achieve adequate adhesion and used super glue to improve the adhesion. In doing so, the sample was made much stiffer and the results reveal this. As the soft plastisol sample was obviously softer than the medium plastisol sample, the results for the soft sample are not used for performance assessment and comparison. The results of the experimental rheometer, called “Elviscolator” in the included plots, are about 15% more elastically stiff than the ARES G2 results when no calibrating adjustments are made.

If the ARES G2 results for the hardest sample are assumed to be correct, and linear calibrations to the Elviscolator are made accordingly, the results for the medium sample are in very close agreement with the ARES G2 results. Furthermore, the results for the soft plastisol

sample are about 75% of the stiffness of the medium sample. This is a very reasonable value, and is more reliable than the ARES G2 data.

The results are given in the remainder of this section. The black sample is the hardest one, the red sample is the medium one, and the white sample is the softest one. Elviscolator results that have not been calibrated with the hard-sample results of the ARES G2 are denoted "Blind" in the figures. Results that include the one-time calibration are denoted "Cal."

5.2.1 Black Samples, Hard Plastisol

As can be seen in Figure 5.4 The blind results for the low frequency tests are quite good. Even so, it is valuable to calibrate with respect to the independent results to ensure that changes track well with the softer red sample. In Figure 5.4 (a) the system stiffnesses are compared. The error bars denote the standard deviations over 10 independent frequency sweeps.

Figure 5.4 (b) shows typical phase shift results. The high values reported for the Elviscolator at low frequencies (below 10 Hz) are attributable to sample slipping and adverse effects of stick-slip friction on the excitation axis. The sample slipping can be prevented by the use of super-glue which will not have the adverse stiffening effect that plagues the ARES G2 soft sample results. This is because of the much greater thickness of our samples; the local effects are ameliorated by bulk effects. However, using super-glue is avoided in hopes of allowing future re-testing of the samples.

Figure 5.4 (c) shows typical shear storage and loss modulus results.

Figure 5.5 shows the high frequency performance. Although comparison data is only available up to $16\,Hz$ the trends up to about $60\,Hz$ are commensurate with theoretical transfer function and trace a reasonable extrapolation of the ARES G2 curves.

Above $60\,Hz$, the Elviscolator results show some anomolous behavior. As seen in Figure 5.5(c), there are jumps in the system response that cannot be easily explained. Although strain gauge resonances seem to be a possible explanation, these results could not be reproduced analytically using the two-degree-of-freedom model.

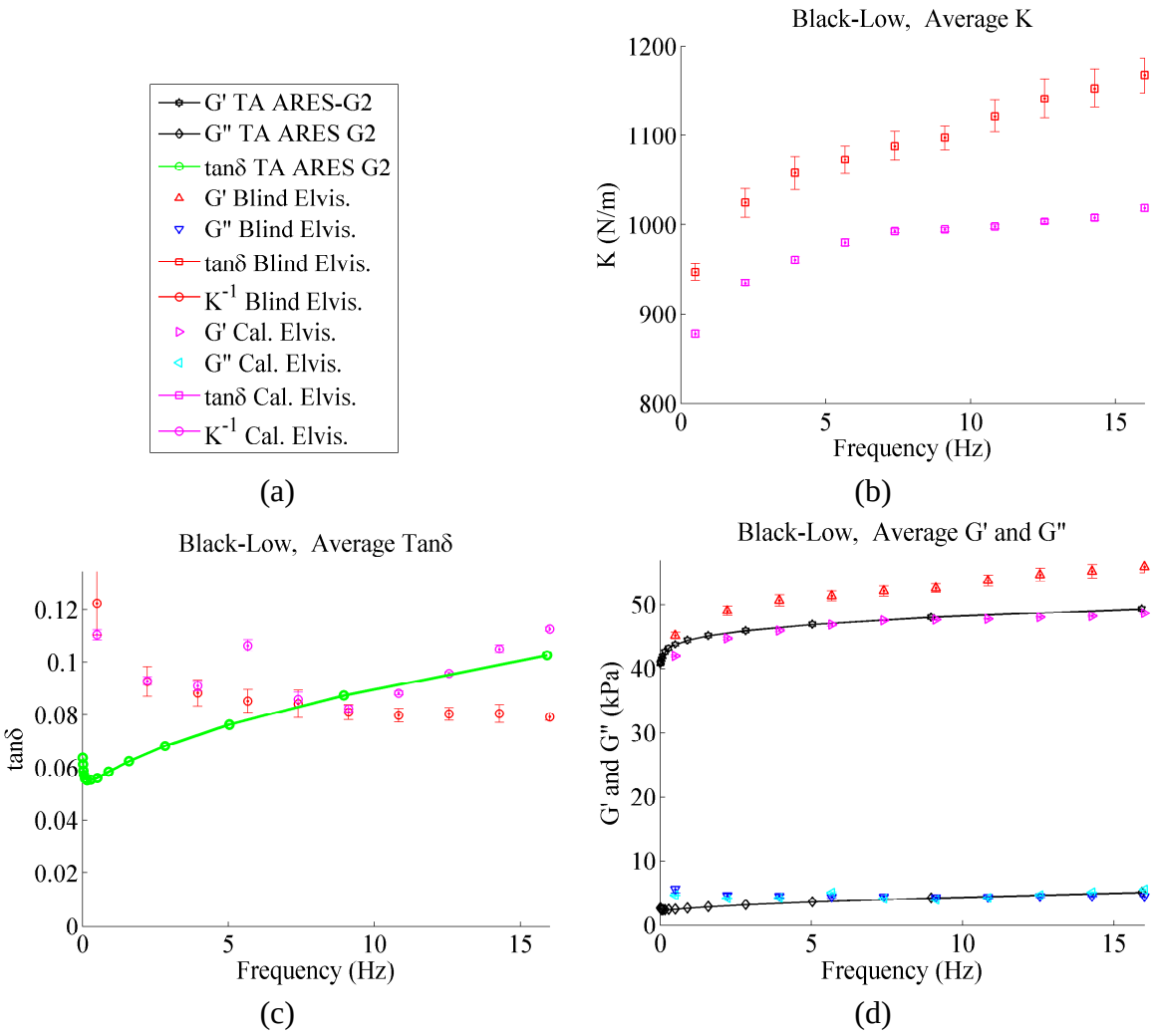

Figure 5.4: Hard plastisol low frequency sweep, comparison of results with standard deviations represented by error bars: (a) Legend; (b) Amplification; (c) tanδ , and (d) Storage and Loss Moduli (shear).

It is considered likely that as the excitation frequency is increased beyond 60 *Hz*, the substantial increase in voice-coil current draw exacerbates capacitive cross-talk over channels in both the instrument wiring and in the internal switching of the mega-Hertz capable DAQ. This is suspected to cause signal degradation that is not indicative of the actual material or system response. This issue requires further investigation and, at this point, results obtained above 60 *Hz* should be verified or discarded.

The standard deviations increase dramatically at the highest frequencies. This is caused by divergence of the displacement control algorithm which cannot achieve the minimum dis-

placements prescribed without exceeding the user-defined coil current limit.

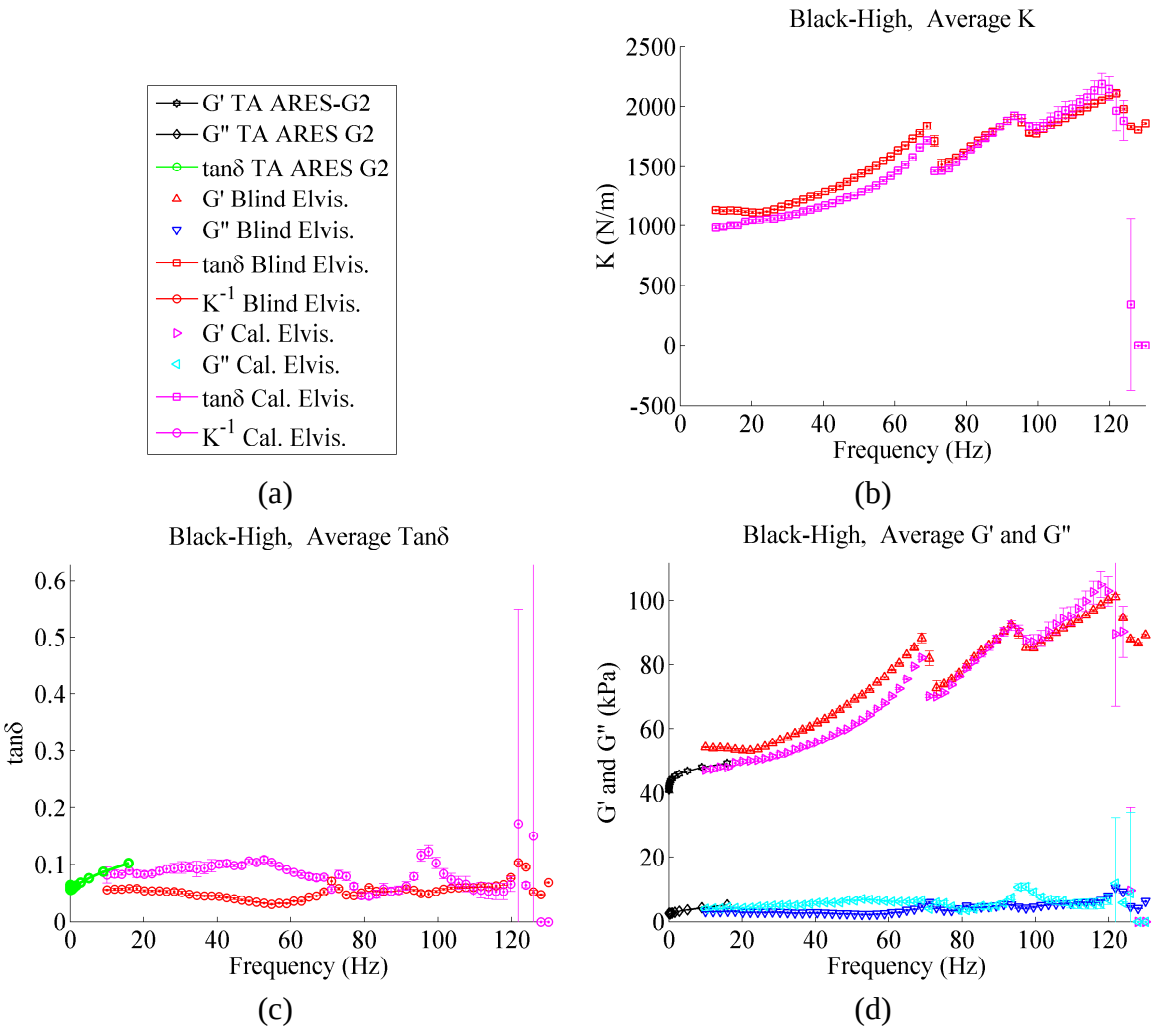

Figure 5.5: Hard plastisol high frequency sweep, comparison of results with standard deviations represented by error bars: (a) Legend; (b) Stiffness; (c) tanδ , and (d) Storage and Loss Moduli (shear).

5.2.2 Red Samples, Medium Plastisol

Figure 5.7 shows the high frequency performance of the red (medium stiffness) sample. Since we used the ARES G2 data of the hard sample for calibration purposes, comparison to the medium sample results show promise for the predictive capabilities. This is well observed in the low frequency data depicted in Figure 5.6. Please note, that the calibrations done with

the ARES G2 data resulted in comparatively small changes in the predicted material properties, fostering changes that don't exceed 20%. As before, above 60 Hz the Elviscolator results show some anomolous behavior. Overestimated tanδ at low frequency can be attributed, at least in part, to sample interface slipping. This could be easily remedied with the use of superglue, which was avoided in hopes of preserving the samples for future reuse.

It should be noted that resonances of the cantilevered load cell, which typically occur above 60 Hz should be considered. Although these resonance don't explain all of the complex high frequency behavior seen, they bolster the justification for discarding high frequency results.

5.2.3 White Samples, Soft Plastisol

Figure 5.9 shows the high frequency performance of the white (lowest stiffness) sample. As can be seen in the low frequency results of Figure 5.8 the ARES G2 data are of suspect reliability due to some difficulties reported by laboratory technicians. Significant sample slipping evidently required their use of super-glue which had the likely effect of rendering the thin samples stiffer than normal. The experimental device, however, did not have this problem and the results are correctly softer than those of the medium sample. It is not the case that the soft sample is in actuality stiffer than the medium sample, which can be verified by tactile examination of the samples.

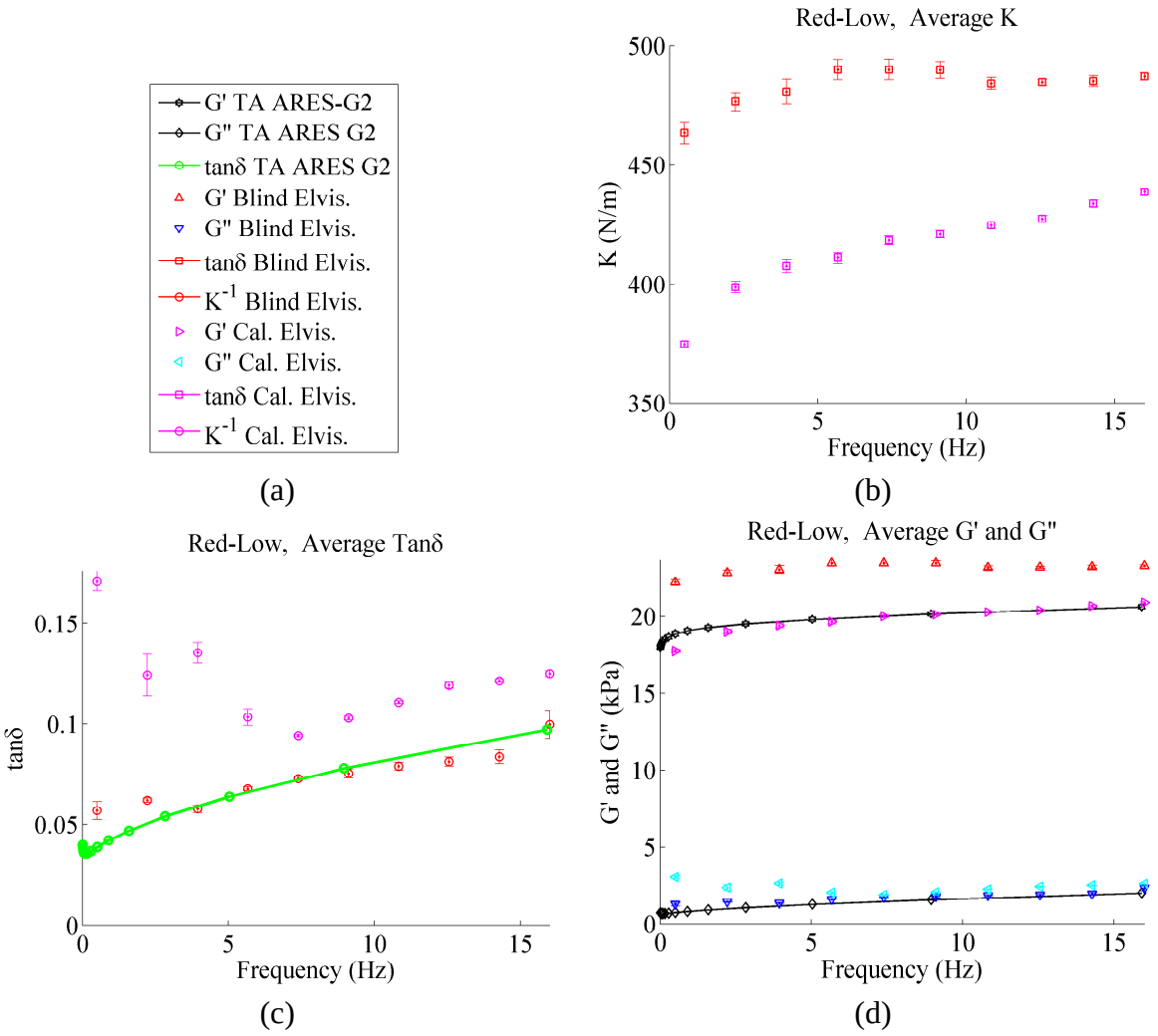

Figure 5.6: Medium plastisol low frequency sweep, comparison of results with standard deviations represented by error bars: (a) Legend; (b) Stiffness; (c) tanδ , and (d) Storage and Loss Moduli (shear).

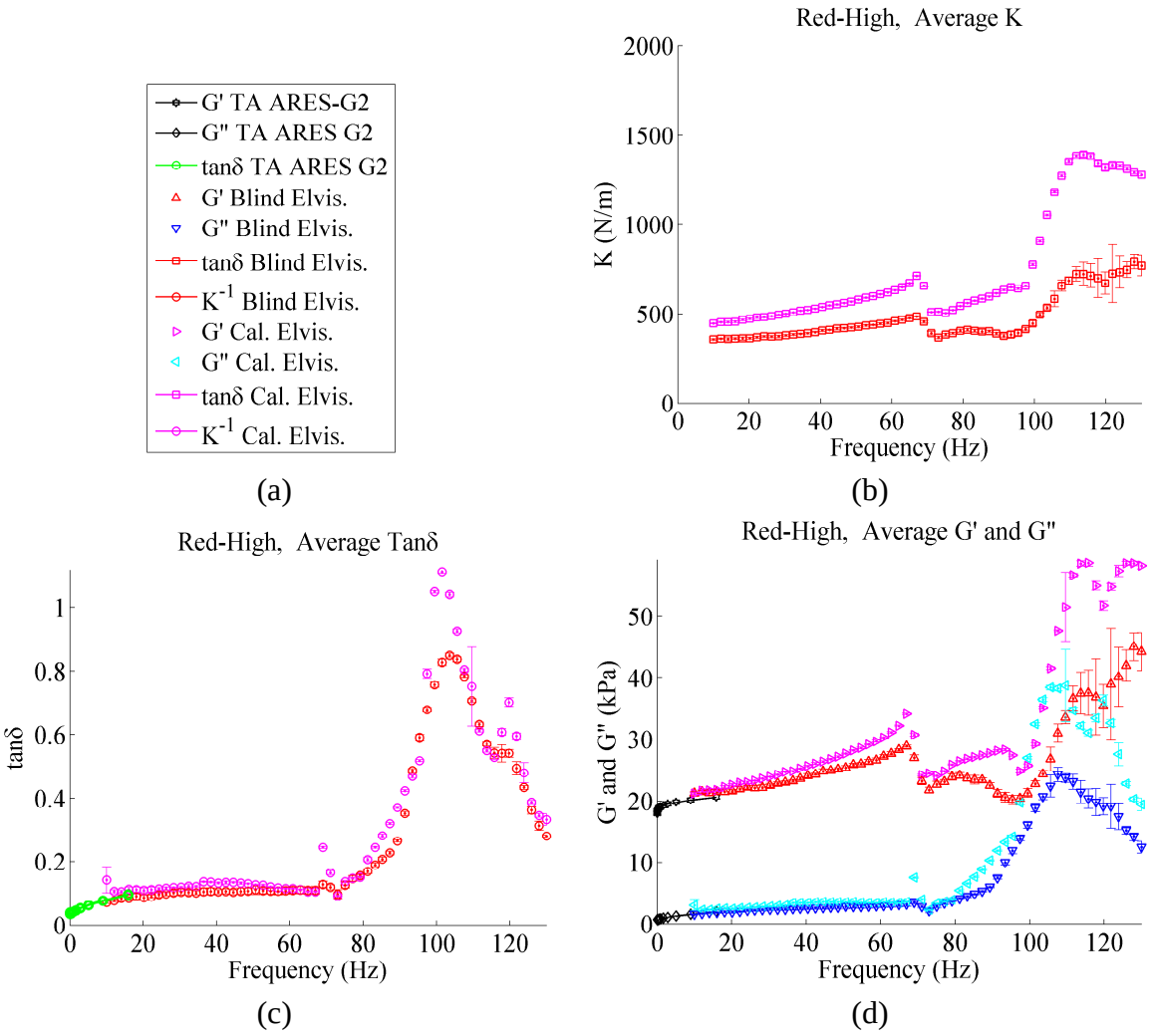

Figure 5.7: Medium plastisol high frequency sweep, comparison of results with standard deviations represented by error bars: (a) Legend; (b) Stiffness; (c) tanδ , and (d) Storage and Loss Moduli (shear).

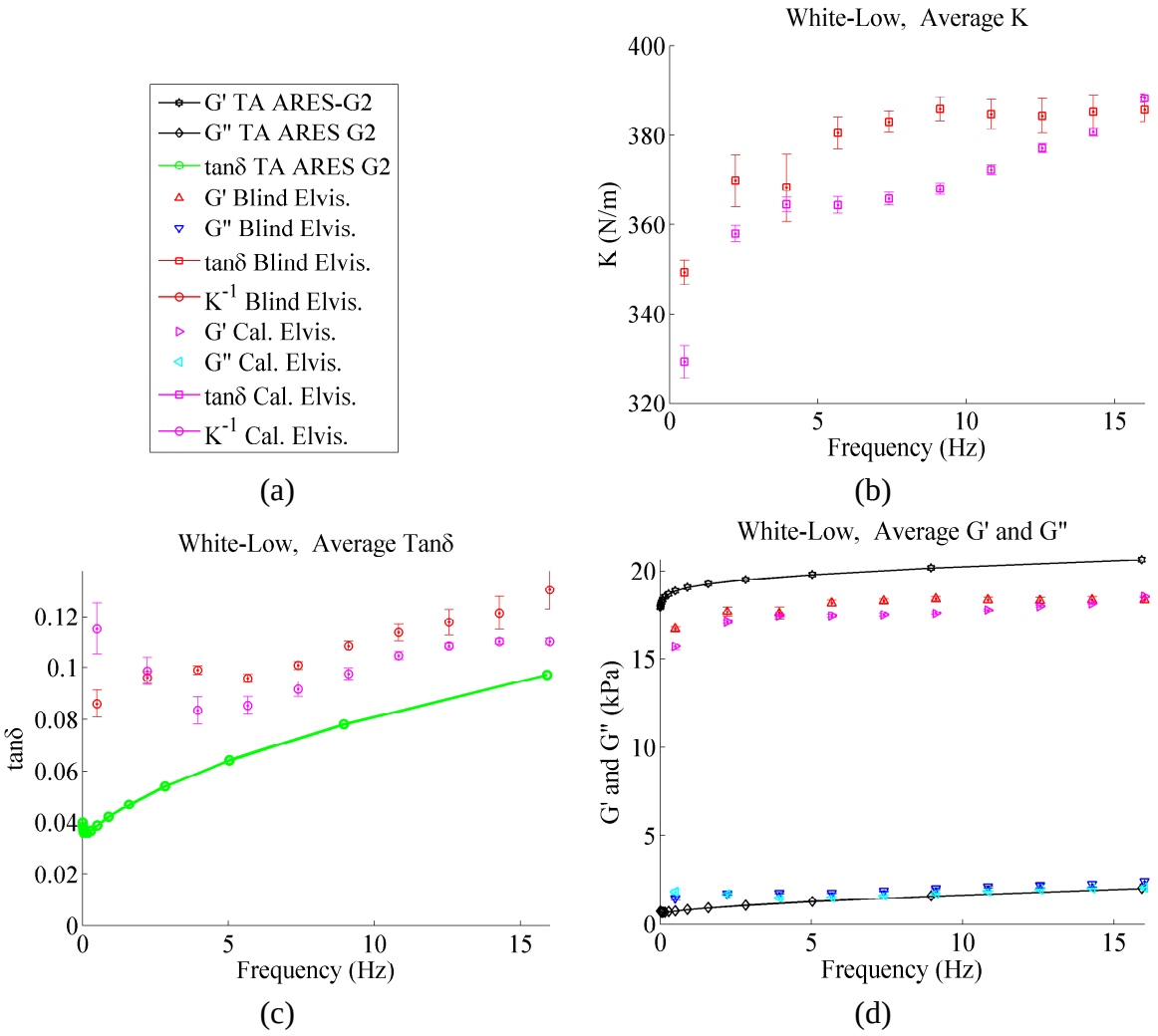

Figure 5.8: Soft plastisol low frequency sweep, comparison of results with standard deviations represented by error bars: (a) Legend; (b) Stiffness; (c) tanδ , and (d) Storage and Loss Moduli (shear).

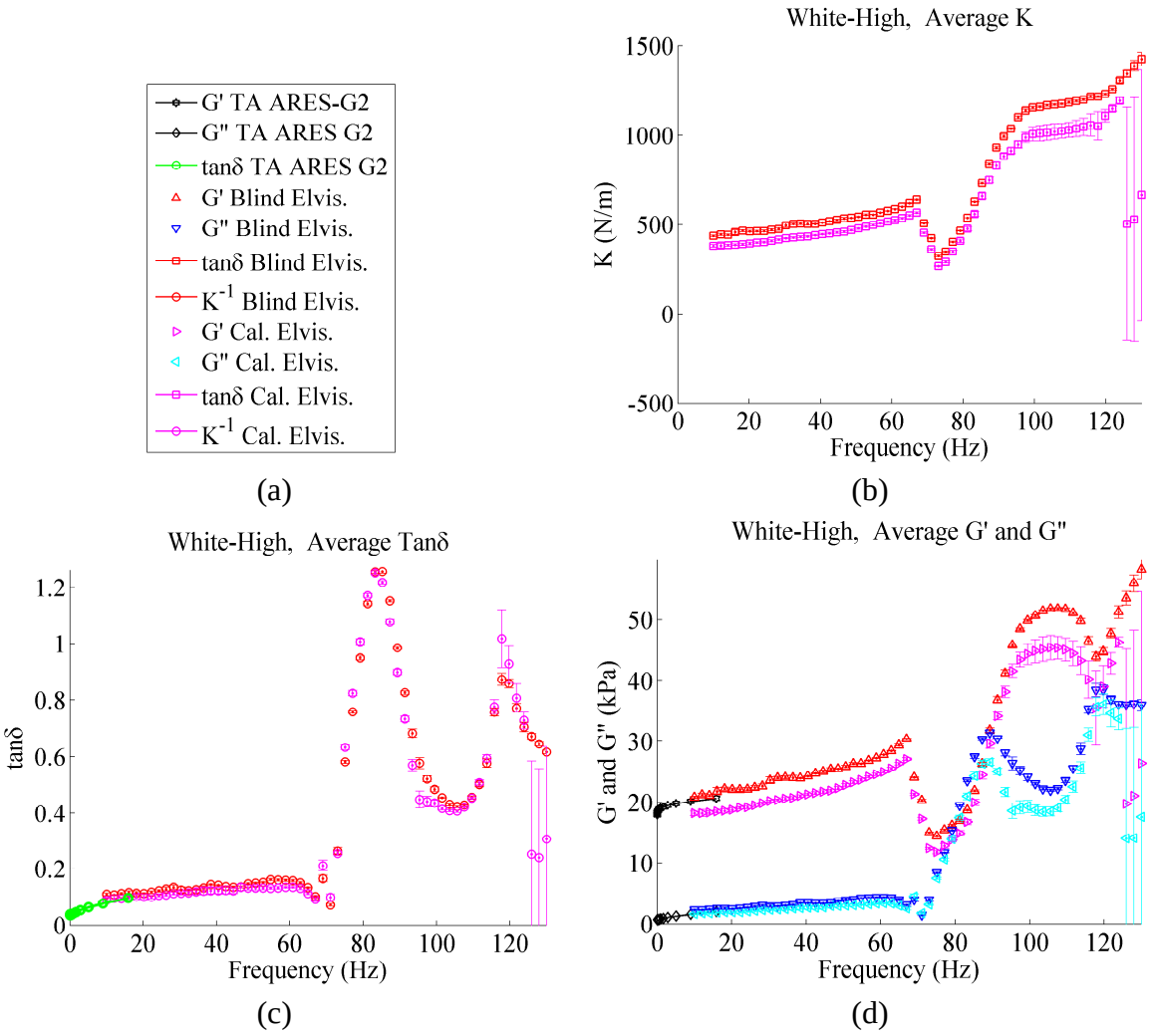

Figure 5.9: Soft plastisol high frequency sweep, comparison of results with standard deviations represented by error bars: (a) Legend; (b) Stiffness; (c) tanδ , and (d) Storage and Loss Moduli (shear).

5.3 Tissue Characterization

Having shown that the Elviscolator performs well when compared against the ARES G2 using laboratory produced plastisol samples, actual tissue testing was undertaken. As the plastisol samples were anelastic in their response, much more viscous flow was found using real tissues. Unfortunately, there is no "gold standard" method for quantitatively determining the elastic properties of tissues [49]. However, some comparisons to published results for a number of experimental setups is instructive. In their work with the soft tissue elastometer, Egorov et. al suggest that "most normal soft tissues have a Young's modulus on the order of $10\,kPa$" [34]. As the samples tested here have been obtained from a butcher, they have been bled and aged. This can be expected to have stiffen the tissues to some degree.

In the year 2000, Kruse et. al used techniques of Magnetic Resonance Elastography (MRE) to estimate the shear modulus porcine semitendinosus skeletal muscle which was estimated be in the range of $12-32\,kPa$ at $300\,Hz$, and porcine liver which was estimated to be about $3\,kPa$ at $100\,Hz$ and $5\,kPa$ at $300\,Hz$ [49]. In 2007, also using MRE, Klatt et. al estimated the shear modulus of human liver to be in the range of $1-3\,kPa$ [50].

Pneumatic indentation methods were used by Palevski et. al in 2006 to estimate the short term shear modulus of porcine gluteus muscle to be about $8.5\,kPa$ [51]. Van Loocke, Lyons, and Simms used quasi-static compression tests to estimate the shear modulus of porcine gluteus muscle to be $523\,Pa$ [29].

In 2008, Egorov et. al used indentation methods to estimate the Young's modulus of pork loin samples to be in the range of $11-16\,kPa$ and the Young's modulus of bovine liver to be in range of $6-11\,kPa$ [34]. If these tissue are assumed to be incompressible, the corresponding shear moduli would be in the ranges of $3-6\,kPa$ for the pork loin and $2-4\,kPa$ for the bovine liver.

We tested porcine hind quarter muscle and bovine liver tissue for these purposes. The porcine tissue was of medium stiffness, comparable to the medium plastisol sample tested in the previous section. The bovine liver tissue was, however, not only much softer than anything

previously tested but was also very liquid having a “soupy” consistency. While the exact tissue samples tested were not tested by an independent method or laboratory, we can determine much from these tests.

5.3.1 Porcine Muscle Tissue Thin Sample

The thin sample results for the porcine loin tissue show a much more viscous response than was observed for the elastomer phantoms used for calibration and performance evaluation. The thin sample were cut be about 11 mm in thickness and 10 frequecy sweeps were averaged (typical for all of the reported prototype results in this section).

Figures 5.10 and 5.11 show the discrete stiffness results in (a), the viscosity or tanδ results in (b), and the shear storage and loss modulus results in (c). The estimated elastic shear modulus for the pork loin tissue is to the order of 20 kPa, which is a bit stiffer than some of the published results $(3-10|:kPa)$ but is still well within the range of what is physically reasonable. The increased stiffness can be explained by the draining and aging of the tissue prior to testing.

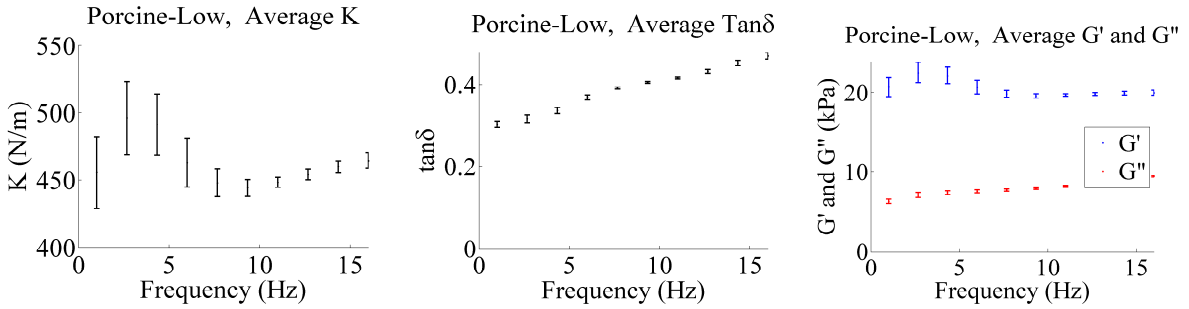

Figure 5.10: Porcine muscle tissue low frequency sweep, thin sample $th = 11.5\,mm$: (a) Amplification; (b) tanδ , and (c) Storage and Loss Moduli (shear). Error bars represent the standard deviations over 10 sweeps.

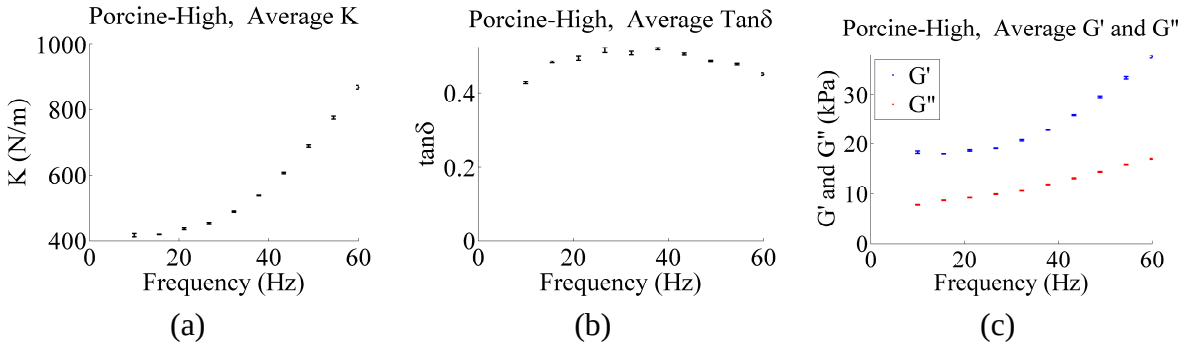

Figure 5.11: Porcine muscle tissue high frequency sweep, thin sample $th = 11.5\,mm$: (a) Amplification; (b) tanδ , and (c) Storage and Loss Moduli (shear). Error bars represent the standard deviations over 10 sweeps.

5.3.2 Porcine Muscle Tissue Thick Sample

The thick sample results are in good agreement with those of the thin sample. This demonstrates that the device and methods presented here are robust for field work where precise, uniform sample preparation is not practical.

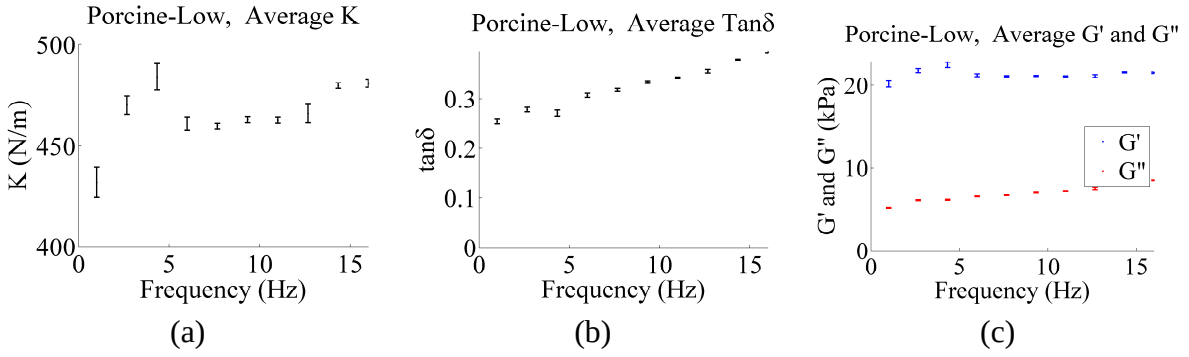

Figure 5.12: Porcine muscle tissue low frequency sweep, thick sample $th = 16.5\,mm$: (a) Amplification; (b) tanδ , and (c) Storage and Loss Moduli (shear). Error bars represent the standard deviations over 10 sweeps.

5.3.3 Bovine Liver Tissue Thin Sample

The bovine liver tissue was found to be very soft and lossy. In fact, the tissue was about as soft as can be reliably tested without having to resort to large deformations to overcome axis friction. Above $40\,Hz$ the phase shift skyrockets as seen in Figure 5.15 (b). This means that the

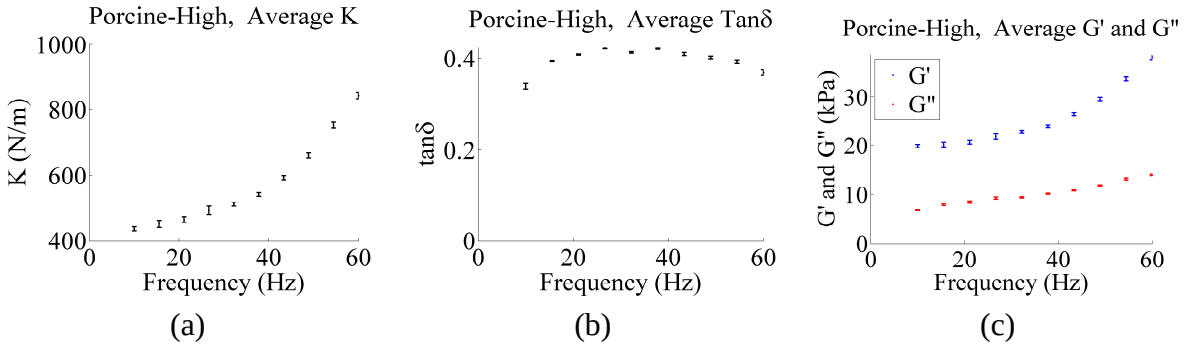

Figure 5.13: Porcine muscle tissue high frequency sweep, thick sample $th = 16.5\,mm$: (a) Amplification; (b) tanδ , and (c) Storage and Loss Moduli (shear). Error bars represent the standard deviations over 10 sweeps.

liver tissue shear response is highly loss dominated at high frequencies which is evident in the high values of G'' above $20\,Hz$ in Figure 5.15 (c).

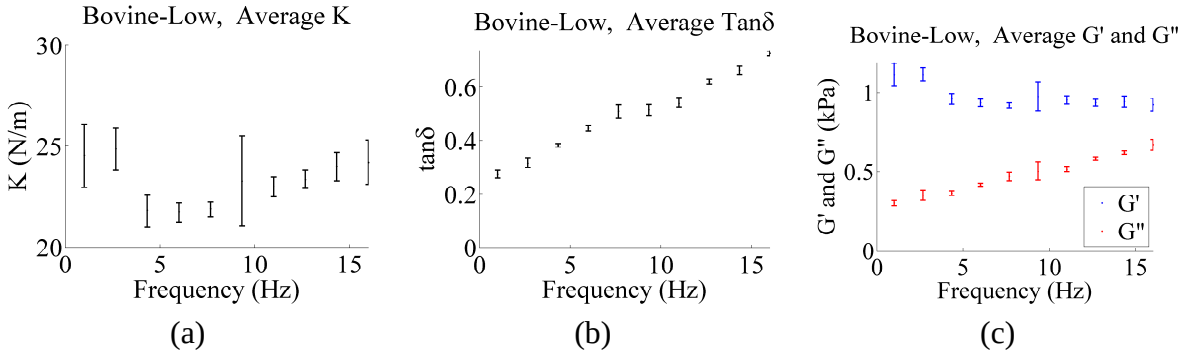

Figure 5.14: Bovine liver tissue low frequency sweep, thin sample $th = 9\,mm$: (a) Amplification; (b) tanδ , and (c) Storage and Loss Moduli (shear). Error bars represent the standard deviations over 10 sweeps.

5.3.4 Bovine Liver Tissue Thick Sample

As was seen with the porcine loin tissue results, the thick sample numbers for the bovine liver tissue are in good agreement with the thin sample data. This shows that the device can give consistent results with very little sample preparation.

The published tissue properties span a wide range of values obtained with very diverse methodologies and samples, but although they are an imprecise comparison standard they do

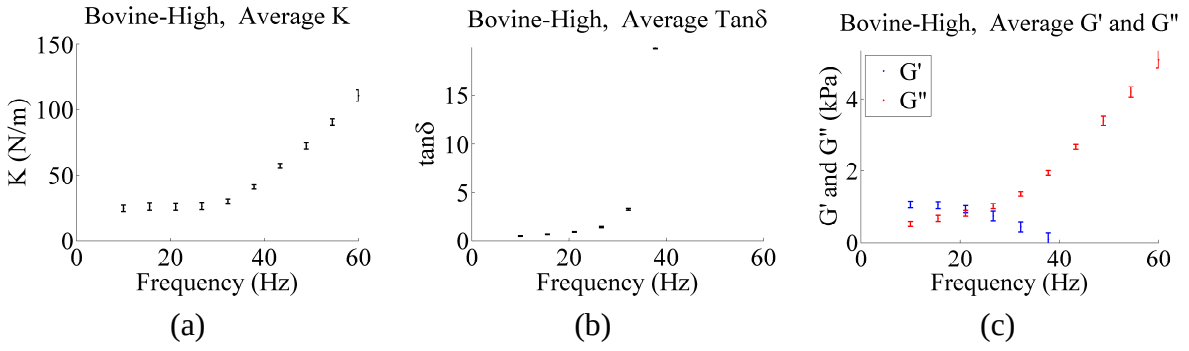

Figure 5.15: Bovine liver tissue high frequency sweep, thin sample $th = 9\,mm$: (a) Amplification; (b) tanδ , and (c) Storage and Loss Moduli (shear). Error bars represent the standard deviations over 10 sweeps.

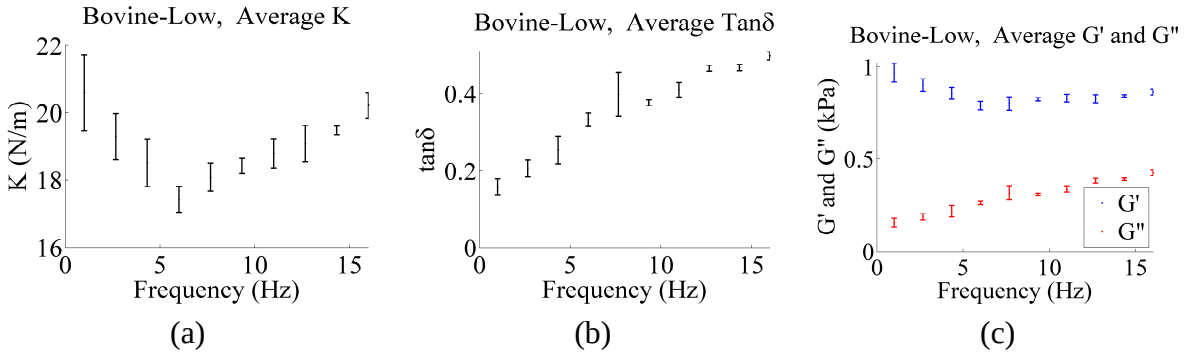

Figure 5.16: Bovine liver tissue low frequency sweep, thick sample $th = 14\,mm$: (a) Amplification; (b) tanδ , and (c) Storage and Loss Moduli (shear). Error bars represent the standard deviations over 10 sweeps.

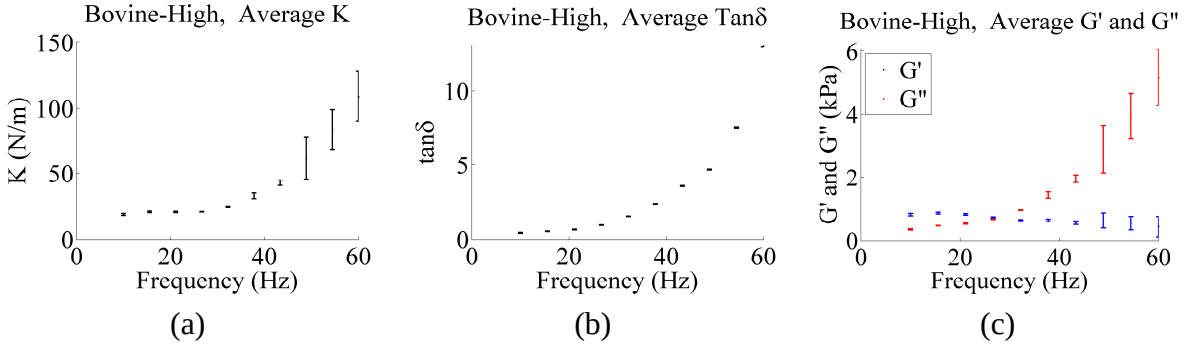

Figure 5.17: Bovine liver tissue high frequency sweep, thick sample $th = 14\,mm$: (a) Amplification; (b) tanδ , and (c) Storage and Loss Moduli (shear). Error bars represent the standard deviations over 10 sweeps.

give some indication of the kind of shear modulus magnitudes to expect. Our experimental results are found to be quantitatively reasonable in this context.

Most importantly, we were able to test how satisfactorily the excitation boundary would adhere to the wet tissue sample surfaces where biological enzymes threaten to present some difficulty. No such difficulties arose. Also, published data for the elastic properties of similar tissues tell us that our results are within the realm of what is physically feasible.

Because the tissues were cut imprecisely, these experiments also put the practicality of the device for field use, where samples must be cut with some haste, to the test. The samples were cut at various thickness and no great efforts were made to ensure that the top and bottom surfaces would be parallel. In this way, the thick sample implications determined analytically were verified experimentally. The thick sample assumptions led to some convenient geometric features such as insensitivity to small errors in the thickness estimation. The same reasoning suggests that the sample geometries need not be prepared with precise cut-planes to allow for useful results. These conclusions were verified experimentally by comparing the results of different tissue samples cut to different thicknesses with little attention paid to cut precision. Tissue testing also reveals the importance of using an adherent agent, such as superglue, at the loaded boundary; which was not as crucial to the plastisol tests.

Part III

Finite Element Methods for Rigidtropic Anisotropy

Chapter 6

Spectral Treatments for Rigidtropic Locking

The finite element method is well suited to exploring the effects of anisotropy of the kind associated with tissues having directionally aligned stiff fibers. In particular, skeletal muscle in known to have a complex fibrous structure [29]. A notable shortcoming in the use of existing finite element methods involves the propensity for solution locking in the direction of stiff fibers. This locking reveals itself in solutions that underestimate deformation and converge very slowly. Here, a few remedies that exploit the spectral decomposition of the elasticity matrix, as commonly written in Voigt-Mandel notation, are explored. One proposed remedy is a generalization of selective reduced integration, another is a special B-bar method arising from the 3-field variational formulation, and some stabilized methods are introduced. The stabilized methods deserve special attention due their potential for improved convergence, even when applied to general problems such as simple isotropic elasticity.

6.1 The Spectral Decomposition of the Compliance Matrix

Certain anisotropic elastic materials, such as the homogenized model of a fiber-reinforced matrix, are nearly rigid under stresses applied in a direction of material rigidity—the

resulting strains are comparatively small when viewed against the strains that would occur in response to otherwise directed stresses. Isotropic materials may have dilational rigidity, which we show to be a special case of this generalized treatment.

Some common finite element techniques are effective in dealing with volumetric locking, but are not well suited to handle anisotropic materials that lock under stress states other than those that are described as mostly hydrostatic. The failure of the traditional B-bar method is attributable to the fundamental assumption that the mode of deformation to be relieved is one of near incompressibility.

The proposed remedy exploits the spectral decomposition of the compliance matrix of the anisotropic material. The spectrum separates nearly-rigid and flexible modes of stress and strain; this leads naturally to a generalized selective reduced integration. What's more, this decomposition also enables a three-field formulation, of elastic strain energy conservation, which results in a B-bar method applicable to general anisotropic materials with nearly-rigid fibers.

When materials with multiple stiff fiber directions are treated with more than one spectrally defined deformation mode, element stabilization may be necessary. A working stabilization method is presented.

Traditional Selective Reduced Integration (SRI), is a method usually attributed to the efforts of Doherty et al. [52]. It is considered an effective repair of finite elements that lock when subjected to certain modes of deformation. The technique is able to handle isotropic nearly incompressible elastic solids, where volumetric locking cuases problems. Hughes [52] offers a derivation based on Lamé parameters, but an analogous approach based on the split of the deformation energy into bulk and shear terms gives an alternative [53].

One key to the successful use of the SRI technique is the separation of volumetric and deviatoric energy. Because this split is not clean for solids with anisotropic material responses, traditional SRI is awkward and inapplicable for materials such as fiber-reinforced composites.

This shortcoming motivated the development of the now widespread B-bar method. In [54], the B-bar method was presented as a treatment for anisotropic materials, but the volumet-

ric and deviatoric energy split originally intended for isotropic materials, remained fundamental to this formulation. It stands to reason that the locking deformation modes could go well beyond the case of waning compressibility. Claims that B-bar methods are an effective treatment for anisotropic materials have to our knowledge never been tested.

In the presented method, we separate the mechanical material responses into constrained and unconstrained deformations which are redrawn in terms of strain, stress, and energy. The proposals rely on the spectral decompositions of the compliance matrices. We appeal to the formulations offered by Felippa and Oñate [55], and proceed to apply them as improvements on existing finite element techniques.

6.2 Motivation for Spectral Treatments GSRI and B-bar Variant

Consider materials that consist of a soft matrix reinforced with aligned stiff fibers. The system of locally parallel fibers is typically represented macroscopically using material models that have transversely isotropic homogenized properties. We can deduce that for very stiff fibers the material is effectively rigid when loaded in the direction of the fibers. This causes underestimated deformations in locking finite element formulations.

Take a fiber-reinforced cantilevered beam as an example. The beam is clamped at the fixed end and loaded by a transverse shear force at the free end as shown in Figure 9.8 (a). The x-axis is parallel to the beam's axis, the $z-$axis is vertically transverse. The dimensions are: width $W = 1$ cm, length $L = 9$ cm, and thickness $t = 2$ cm. The boundary conditions at $x = 0$, Fig. (9.8)(a), are

$$u_x = u_y = u_z = 0\,, \tag{6.1}$$

and the Neumann boundary conditions are prescribed on at $x = L$ as

$$\tau_{xz} = -10 \text{ kPa}. \tag{6.2}$$

We consider both an isotropic material, and an anisotropic material with one of two different orientations of the local coordinate system. The anisotropic material is assumed to be a model suitable for a soft matrix reinforced with stiff uni-directional fibers. The elastic modulus along the stiff fiber is 100000 times higher than in the transverse directions, and the shear terms comparatively very small in magnitude. The anisotropic elastic properties are $E_1 = 100000\,\text{GPa}$, $E_2 = E_3 = 1\,\text{GPa}$, $G_{12} = G_{13} = G_{23} = 0.2\,\text{GPa}$, and $\nu_{12} = \nu_{13} = \nu_{23} = 0.25$. The fibers are oriented at an angle with respect to the beam's longitudinal axis as described by an orientation vector with components in the Cartesian coordinate system.

Throughout, strain energy error is defined as

$$\Psi_{SE} = \left| \frac{\mathscr{U}}{\mathscr{U}_\xi} - 1 \right| , \tag{6.3}$$

where $\mathscr{U}$ is the computed strain energy, and $\mathscr{U}_\xi$ is the limit value arising from Richardson's extrapolation. Similarly, maximum displacement error is defined as

$$\Psi_\delta = \left| \frac{\delta}{\delta_\xi} - 1 \right| , \tag{6.4}$$

where δ is the computed maximum displacement and δ_ξ is the limit value arising from Richardson's extrapolation. The data for the extrapolation are taken from results for progressive refinements obtained with a well-behaved finite element (except where indicated otherwise).

The mechanical response of the beam in terms of the normalized true error of the maximum deflection is shown in Fig. (9.8)(b,c,d). It bears emphasis that the elements used to discretize the beam are elongated (aspect ratio of 4.5), which has significant implications for the accuracy of linear elements without any enhancement of the bending stiffness. The behavior for isotropic compressible material is shown in Fig. (9.8)(b). As expected the quadratic 20-node serendipity hexahedron C3D20R is very accurate. The ABAQUS incompatible-mode C3D8I and one-point reduced integration hybrid elements C3D8RH also perform rather well. The elements whose bending stiffness is not improved in any way (the ABAQUS linear hybrid C3D8H, the linear isoparametric element C3D8, and the original B-bar Q1/Q0 hexahedron [52] H8-Bbar-ISO) perform identically.

Now we look at the case of the anisotropic material with the fiber orientation $[\sqrt{2}/2, -\sqrt{2}/2, 0]$ in Fig. (9.8)(c). All input data remained unchanged, especially the mesh, and therefore we conclude that the relative performance hit of an order of magnitude greater error taken by the quadratic 20-node serendipity hexahedron C3D20R is clearly due to the introduction of material anisotropy. The performance of the linear isoparametric element C3D8, the original B-bar Q1/Q0 hexahedron, and the H8-Bbar-ISO has also deteriorated by an order of magnitude. On the other hand, the ABAQUS linear hybrid C3D8H, the incompatible-mode (C3D8I) and one-point reduced integration hybrid C3D8RH elements are essentially as accurate as for the isotropic material. Moreover note that there is a new element in the graph Fig. (9.8)(c): hexahedron H8-Bbar based on a modification of the B-bar method for anisotropic materials as introduced in the present paper. The relative performance of this element compared to the C3D8I and the C3D8RH is essentially the same as that of the original technique to these elements for the isotropic material. Clearly, if this holds for any orientation of the stiff fibers we have made the B-bar formulation robust for anisotropic materials.

This is indeed supported by the findings in Fig. (9.8)(d) where we look at the case of the anisotropic material with the fiber orientation $[\sqrt{2}/2, 0, -\sqrt{2}/2]$. The quadratic 20-node serendipity hexahedron C3D20R takes another performance hit, having an order of magnitude greater error. The performance of the linear isoparametric element C3D8, and the original B-bar Q1/Q0 hexahedron H8-Bbar-ISO has also deteriorated by an additional order of magnitude. As before, the incompatible-mode C3D8I and one-point reduced integration hybrid C3D8RH elements maintain their reasonable performance. The accuracy of the ABAQUS linear hybrid C3D8H has also significantly deteriorated. In contrast, the new hexahedron H8-Bbar element in the graph Fig. (9.8)(d) compares better with the incompatible-mode C3D8I and one-point reduced integration hybrid C3D8RH elements.

In summary, the incompatible-mode C3D8I, one-point reduced integration hybrid C3D8RH elements, and the new hexahedron H8-Bbar element are the only finite elements insensitive to the character of the elastic material; whether isotropic or anisotropic with an arbitrary orientation, the finite elements deliver essentially the same accuracy with the same

mesh. The main contribution of the present paper is the generalization of the B-bar technique to furnish existing hexahedral elements, both linear and quadratic, with insensitivity to the anisotropy of the material stiffness matrix.

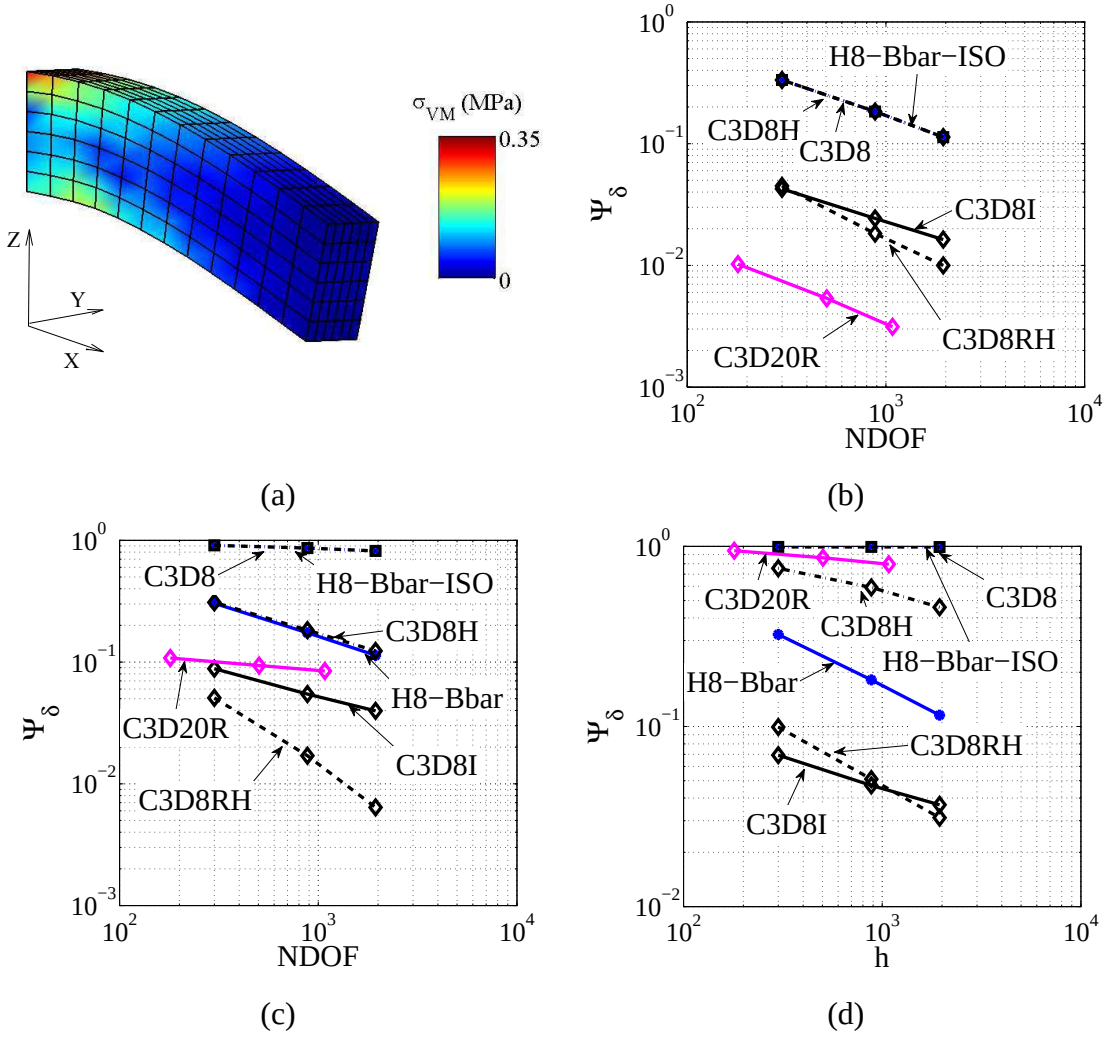

Figure 6.1: Displacement error Ψ_δ of cantilever beam subject to shear load at the free end. (a) Uniform mesh with 125 nodes; element aspect ratio of 1 : 4.5. In (b), (c), and (d) we show the estimated true error of the maximum deflection. (b) Isotropic material. (c) Anisotropic material, stiff fiber aligned with $[\sqrt{2}/2, -\sqrt{2}/2, 0]$. (d) Anisotropic material, stiff fiber aligned with $[\sqrt{2}/2, 0, -\sqrt{2}/2]$. Key: C3D8 – linear hexahedron, C3D8H – linear hybrid hexahedron with uniform pressure, C3D8I – hexahedron with incompatible modes, C3D20R – the uniformly reduced integration quadratic serendipity hexahedron, H8-Bbar-ISO – B-bar Q1/Q0 hexahedron as in Hughes [52], H8-Bbar – linear hexahedron with present B-bar formulation.

6.3 Split the Constitutive Relation

The use of the spectral decomposition to represent the strain, stress, and the constitutive relations in linear elasticity goes way back. As carefully reviewed by Helbig [56], these ideas likely originated with a 1856 publication by Lord Kelvin. Another take on this work reappeared in 1878, however not a single citation of this original work can be found until much later. In 1984 Rychlewski [57] formulated an extensive theory of constitutive relations based on the spectral decomposition. Not long thereafter, theoretical publications by Mehrabadi and Cowin [58] and Theocaris [59] appeared. These powerful ideas were, to the best of our knowledge, never used in modern computations.

In the recent paper of Felippa and Oñate [55], who don't mention the prior publications described above, discussions are given of stress and strain decomposition appropriate to linearly elastic anisotropic materials with volumetric locking using the spectral decomposition of the compliance matrix. In so doing, they introduce the so called "*rigidtropic*" materials, which develop little to no strains under a stress pattern that follows a nearly zero eigenvector. These material models include, as a special case, isotropic incompressible materials, whose null eigenvector corresponds to the hydrostatic stress. The main conclusion contended in [55] is that with anisotropic material models the quantities that correspond to hydrostatic pressure and volumetric strain in incompressible isotropic materials need to be redefined in terms of *effective* quantities. A material is taken as effectively rigid when it undergoes numerically zero strains under a stress pattern proportional to the eigenvector associated with a vanishing principal compliance. In this sense, the term "effective" has no relation to its usual meaning in homogenization theory.

The compliance matrix expressed in terms of the spectral decomposition reads

$$\mathbf{D}^{-1} = \frac{1}{3}\sum_{i=1}^{6} \gamma_i v_i v_i^T \ , \tag{6.5}$$

where γ_i and v_i are the principal value and principal direction of the compliance matrix (eigenvalue and eigenvector), which are assumed to be given in the order $\gamma_1 \leq \ldots \leq \gamma_6$, and

normalized with respect to length $\sqrt{3}$ through the definition

$$v_j^T v_i = 3\delta_{ji} \,, \tag{6.6}$$

to simplify linkages to isotropic incompressible elasticity. In the decomposition in Eq. (6.5), a material is coined "nearly rigidtropic" when $\gamma_1 \to 0$ [55]. This is a way of saying that the strain vanishes in the direction of v_1.

Using this decomposition, the compliance matrix is split into the stiff and the flexible) parts, respectively, as

$$\mathbf{D}^{-1} = \frac{1}{3}\gamma_1 v_1 v_1^T + \frac{1}{3}\sum_{i=2}^{6} \gamma_i v_i v_i^T \,. \tag{6.7}$$

It can be shown, as is done in Reference [55], that for isotropic incompressible materials

$$v_1 = m = [1,1,1,0,0,0]^T,$$

and we obtain as the constrained/unconstrained split the volumetric/deviatoric partitioning of the constitutive equation.

6.4 Generalized Selective Reduced Integration

The SRI method is a well established technique for the treatment of isotropic incompressible materials with conventional finite elements (see [54, 52] for background). Here we introduce a generalization that facilitates the handling of constrained anisotropic materials.

Starting with the total potential energy of an infinitesimal deformable elastic body in the form

$$\mathscr{U} = \frac{1}{2}\int_\Omega \varepsilon^T \mathbf{D}\varepsilon d\Omega \,, \tag{6.8}$$

emerges, where $\varepsilon = [\varepsilon_{11}, \varepsilon_{22}, \varepsilon_{33}, 2\varepsilon_{32}, 2\varepsilon_{31}, 2\varepsilon_{12}]^T$ is the Voigt-Mandel version of the second order strain tensor and the material stiffness matrix $\mathbf{D}$ follows from Eq. (6.5) as

$$\mathbf{D} = \sum_{i=1}^{6} \frac{1}{3\gamma_i} v_i v_i^T \,. \tag{6.9}$$

The quantity

$$K_i = \frac{1}{3\gamma_i}\,, \tag{6.10}$$

is called the effective stiffness (called the "effective bulk modulus" in Reference [55]).

In drawing an analogy to Eq. (6.5), the material stiffness can be recast as

$$\mathbf{D} = \mathbf{D}_r + \mathbf{D}_f\,, \tag{6.11}$$

where for the stiff and flexible parts we have

$$\mathbf{D}_r = K_1 v_1 v_1^T, \quad \mathbf{D}_f = \sum_{i=2}^{6} K_i v_i v_i^T\,. \tag{6.12}$$

Substituting Eq. (6.11) into Eq. (6.8) results in an additive split of the constrained and unconstrained energy contributions. Carefully choosing integration rules for each of these energy contributions–full integration to the flexible part and reduced integration for its nearly rigid counter part–leads to the GSRI technique. A modified version of the B-bar formulation is presented as an alternative to the GSRI method.

6.5 Three-field formulation of anisotropic elasticity

Introducing two basic relations, to be used in a mixed approximation, leads to a novel treatment for nearly rigidtropic materials. Initially define the effective constrained stress as

$$p = \frac{1}{3} m^T \sigma\,, \tag{6.13}$$

and the effective constrained strain as

$$\varepsilon_v = m^T \varepsilon\,. \tag{6.14}$$

Now, the strain field is derived from the displacement vector as $\varepsilon = \mathbf{B}u$. For a clear compatibility with the vernacular of isotropic nearly incompressible elasticity we keep the notation p (i.e. pressure) and ε_v (i.e. volumetric strain). For simple isotropic materials the vector m is given as

$$m = [1,1,1,0,0,0]^T\,. \tag{6.15}$$

Here, we take

$$m = v_1 \,, \tag{6.16}$$

which allows writing the constitutive relation between the effective pressure and the volumetric strain as

$$p = K_1 \varepsilon_v \,. \tag{6.17}$$

Moving forward, the unconstrained stress is linked to the unconstrained strain as

$$\sigma_d = \mathbf{D}_d \varepsilon \,, \tag{6.18}$$

where we now use $\mathbf{D}_d = \mathbf{D}_f$. In the name of backward compatibility we employ the notation $\mathbf{D}_d$, which for isotropic materials is the deviatoric part of the material stiffness matrix. The total stress reads

$$\sigma = \sigma_d + pm \,.$$

Therefore, the principle of virtual work is rendered as

$$\int_\Omega \delta\varepsilon^T \left(\sigma_d + pm\right) \mathrm{d}\Omega - \int_\Omega \delta u^T b \, \mathrm{d}\Omega - \int_{\Gamma_t} \delta u^T t \, \mathrm{d}\Gamma = 0 \,, \tag{6.19}$$

or, introducing Eq. (6.18),

$$\int_\Omega \delta\varepsilon^T \mathbf{D}_d \mathbf{B} u \, \mathrm{d}\Omega + \int_\Omega \delta\varepsilon^T pm \, \mathrm{d}\Omega - \int_\Omega \delta u^T b \, \mathrm{d}\Omega - \int_{\Gamma_t} \delta u^T t \, \mathrm{d}\Gamma = 0 \,. \tag{6.20}$$

Note, that in these equilibrium relations the vector b represents the generalized forces in a body Ω, and t represents the Neumann boundary conditions on the traction boundary Γ_t. Now, Eq. (6.20) is expressed with the weakly enforced kinematics in Eq. (6.14)

$$\int_\Omega \delta p \left(m^T \mathbf{B} u - \varepsilon_v\right) \mathrm{d}\Omega = 0 \,, \tag{6.21}$$

where $\mathbf{B}$ is the standard symmetric gradient operator [53] and with the weak form of the constitutive equation (6.17)

$$\int_\Omega \delta\varepsilon_v \left(K_1 \varepsilon_v - p\right) \mathrm{d}\Omega = 0 \,. \tag{6.22}$$

Equations (6.20), (6.21) and (6.22) constitute together with Eq. (6.16), the three-field $u-p-\varepsilon_v$ formulation of *anisotropic* elasticity. For isotropic elastic materials the above formulation is identical to that described in the literature, see e.g. [53].

A similar variational framework was developed by Key [60]. The author considered incompressible materials and developed a variant of the Reissner-Hellinger principle which accounts for pressure as an independent variable. Replacing pressure with "extensional stress variable" was mentioned in passing.

Taylor et al. [61] have also developed a formulation based on additional pressure and dilatation variables. The projection vector in equation (11) of [61] denotes the direction of hydrostatic stress, which the authors take to be appropriate for both isotropic and anisotropic elastic materials with (nearly) zero dilatation.

Since this choice is the same one made in the original formulation of the B-bar technique [54], it is ineffective in handling fiber-reinforced materials where the rigidity constraints are not volumetric. It is, therefore, not suited to deal with specific anisotropic materials whose rigidity is not volumetric.

6.6 B-bar variant formulation

In treatment of Eqs. (6.20, 6.21) and (6.22) with the finite element method the following approximations are adopted (we use the notation of [53])

$$u \approx \mathbf{N}_u \tilde{u}, \quad p \approx \mathbf{N}_p \tilde{p}, \quad \varepsilon_v \approx \mathbf{N}_v \tilde{\varepsilon}_v \,. \tag{6.23}$$

It is also assumed that $\mathbf{N}_v$ equals $\mathbf{N}_p$, as discussed in [53]. This appeals to the "discontinuous pressure/condensation" formulation so that the p and ε_v can be locally eliminated on an element-by-element basis.

The mixed approximation is thus obtained in the form

$$\begin{bmatrix} \mathbf{A} & \mathbf{C} & \mathbf{0} \\ \mathbf{C}^T & \mathbf{0} & -\mathbf{E} \\ \mathbf{0} & -\mathbf{E}^T & \mathbf{H} \end{bmatrix} \begin{Bmatrix} \tilde{u} \\ \tilde{p} \\ \tilde{\varepsilon}_v \end{Bmatrix} = \begin{Bmatrix} f_1 \\ 0 \\ 0 \end{Bmatrix}. \tag{6.24}$$

The matrices above are defined as [53]

$$\mathbf{I}_d = \mathbf{I} - \frac{1}{3} m m^T, \quad \mathbf{A} = \int_\Omega \mathbf{B}^T \mathbf{D}_d \mathbf{B} \, \mathrm{d}\Omega, \quad \mathbf{E} = \int_\Omega \mathbf{N}_v^T \mathbf{N}_p \, \mathrm{d}\Omega,$$
$$\mathbf{H} = \int_\Omega \mathbf{N}_v^T K_1 \mathbf{N}_v \, \mathrm{d}\Omega, \quad \mathbf{C} = \int_\Omega \mathbf{B}^T m \mathbf{N}_p \, \mathrm{d}\Omega. \tag{6.25}$$

Eliminating the effective strain from the second equation yields

$$\tilde{\varepsilon}_v = \mathbf{E}^{-1} \mathbf{C}^T \tilde{u} = \mathbf{W} \tilde{u}, \tag{6.26}$$

where we introduce $\mathbf{W} = \mathbf{E}^{-1}\mathbf{C}^T$, so that subsequent substitution into the third term in Eq. (6.24) yields

$$\tilde{p} = \mathbf{E}^{-T} \mathbf{H} \tilde{\varepsilon}_v = \mathbf{E}^{-T} \mathbf{H} \mathbf{W} \tilde{u}. \tag{6.27}$$

Now we obtain a linear system in terms of the displacements alone

$$\bar{\mathbf{A}} \tilde{u} = f_1, \tag{6.28}$$

where

$$\bar{\mathbf{A}} = \mathbf{A} + \mathbf{W}^T \mathbf{H} \mathbf{W}, \tag{6.29}$$

by using the first row in Eq. (6.24). It follows from Eq. (6.20), Eq. (6.22) and the given approximations in Eq. (6.23), that we can now write Eq. (6.30) as

$$\bar{\mathbf{A}} = \int_\Omega \mathbf{B}^T \mathbf{D}_d \mathbf{B} \, \mathrm{d}\Omega + \int_\Omega \mathbf{W}^T \mathbf{N}_v^T K_1 \mathbf{N}_v \mathbf{W} \, \mathrm{d}\Omega. \tag{6.30}$$

Noting the aforementioned relations for effective stiffness

$$\mathbf{D}_d = \mathbf{I}_d \mathbf{D} \mathbf{I}_d, \quad K_1 = \frac{1}{3} m^T \mathbf{D} \frac{1}{3} m, \tag{6.31}$$

allows reformulating Eq. (6.30) as

$$\bar{\mathbf{A}} = \int_\Omega \mathbf{B}^T \mathbf{I}_d \mathbf{D} \mathbf{I}_d \mathbf{B} \, \mathrm{d}\Omega + \int_\Omega \mathbf{W}^T \frac{1}{3} \mathbf{N}_v^T m^T \mathbf{D} \frac{1}{3} m \mathbf{N}_v \mathbf{W} \, \mathrm{d}\Omega \,. \tag{6.32}$$

Finally, Eq. (6.32) combines in forming

$$\int_\Omega \left[\left(\mathbf{I}_d \mathbf{B} + \frac{1}{3} m \mathbf{N}_v \mathbf{W} \right)^T \mathbf{D} \left(\mathbf{I}_d \mathbf{B} + \frac{1}{3} m \mathbf{N}_v \mathbf{W} \right) \right] \mathrm{d}\Omega = \int_\Omega \bar{\mathbf{B}}^T \mathbf{D} \bar{\mathbf{B}} \, \mathrm{d}\Omega \,, \tag{6.33}$$

where the assumed-strain B-bar matrix is taken as

$$\bar{\mathbf{B}} = \mathbf{I}_d \mathbf{B} + \frac{1}{3} m \mathbf{N}_v \mathbf{W} \,. \tag{6.34}$$

Note that the **W** matrix is expressed from the three-field coupling terms **E** and **C**, which can be integrated with a lower quadrature rule than that used for the remaining part of the element stiffness matrix (6.33).

For certain distinctly inhomogeneous models, this leads to improved monotonic convergence. For more on this see appendix B. The resolved maximum displacements and strain energies for solutions with the fully integrated and reduced-order integrated **W** matrix agree with one another to several decimal places for the examples investigated.

The GSRI and the B-bar methods use a variety of Gauss quadrature rules each: the selective integration rules are denoted (1,2) for the linear elements and (2,3) for the quadratic elements; and the full integration rules are denoted (2,2) and (3,3). The first number of the rule indicates the number of Gauss points per dimension for the stiffness matrix corresponding to the nearly-rigid modes of deformation (GSRI) or the **W** matrix (B-bar), and the second number indicates the number of Gauss points per dimension stiffness matrix corresponding to the flexible modes of deformation (GSRI) or the stiffness matrix (B-bar).

Note that the discrete formulation in this section exactly matches that of Reference [53]. The only difference is the use of *effective strain, stress, and moduli* arising from the spectral decomposition of the compliance matrix of the material. For isotropic materials the present formulation is identical to that based on the classic volumetric/deviatoric split.

6.7 Acknowledgements

Chapter 6 is in part a reprint of the material published in, “B-bar Finite Element Methods for Anisotropic Elasticity,” *International Journal for Numerical Methods in Engineering*. 2013; 00:1-15. Steve Oberrecht, Jan Novák, and Petr Krysl. 2013. The author of this dissertation was the primary author of this paper.

Chapter 7

Treating Multiple Modes

If more than two eigenvalues of the compliance matrix approach zero, such as for instance for a fiber-reinforced material with two parallel system of stiff fibers in soft matrix, the continuous formulation needs to be modified, but in relatively minor ways. The projection matrix m is predictably taken as

$$m = [v_1, v_2] \tag{7.1}$$

for a single locking stress direction. Correspondingly we have to adopt a vector of constrained effective stresses and a corresponding vector of the effective constrained strains as

$$p = \frac{1}{3} m^T \sigma \ , \quad \varepsilon_v = m^T \varepsilon \ , \tag{7.2}$$

to replace the scalar quantities used for single mode treatment.

The variational equations are consequently rewritten as

$$\int_\Omega \delta\varepsilon^T D_d B u + \int_\Omega \delta\varepsilon^T m p - \int_\Omega \delta u^T b - \int_{\Gamma_t} \delta u^T t = 0 \tag{7.3}$$

with

$$\int_\Omega \delta p^T \left(m^T B u - \varepsilon_v \right) = 0 \tag{7.4}$$

and (with a diagonal matrix of effective moduli K)

$$\int_\Omega \delta\varepsilon_v^T \left(K\varepsilon_v - p \right) = 0 \ . \tag{7.5}$$

The finite element approximation is also suitably modified to include more than one effective stress and strain, but the matrix expressions do not change in appearance (the matrices just change size).

7.1 Examples

Four examples based on simple cantilevered structures are investigated and the proposed treatments are evaluated. In these examples, nearly rigidtropic materials have up to two dominant fiber directions that can be applied at any angle determined by local coordinate rotations. The cantilevers are loaded such that significant locking behavior ensues for all elements that are not treated by use of the spectral decomposition of the anisotropic elastic constitutive relation. Although this behavior can be verified for other elements, such as tetrahedra, we focus our attention on linear and quadratic hexahedral "brick" elements. GRSI and generalized B-bar elements will be referred to as "treated" throughout the text. They are compared against traditional SRI and B-bar methods that are based on the volumetric-deviatoric split appropriate for incompressible istotropic solids. The later will be referred to as "false-isotropic" throughout.

Each example is one of two geometric configurations with similar boundary conditions: a slender cantilevered beam or a thick cantilevered plate. The beam's dimensions are: $W = 1.0$ cm, $L = 9.0$ cm, and $t = 2.0$ cm. Here L is the length, W is the width, and t is the thickness. The plate's dimensions are the same except $W = 10.0$ cm.

Four cantilevered example models with varying fiber orientations, as seen in figure 7.1, are tested. The solutions for both fully and selectively integrated B-bar treatments are generally indistinguishable from the GSRI solutions. With this in mind and brevity's sake, only the B-bar solutions are shown in the deformed mesh views of figure 7.2.

It should be noted that using reduced integration on the B-bar treatments improves the behavior only for the inhomogeneous cases, where fully integrated solutions show an alternating (refinement dependent) convergence. For inhomogeneous materials, the B-bar solutions show somewhat improved convergence when reduced integration is applied to the locking com-

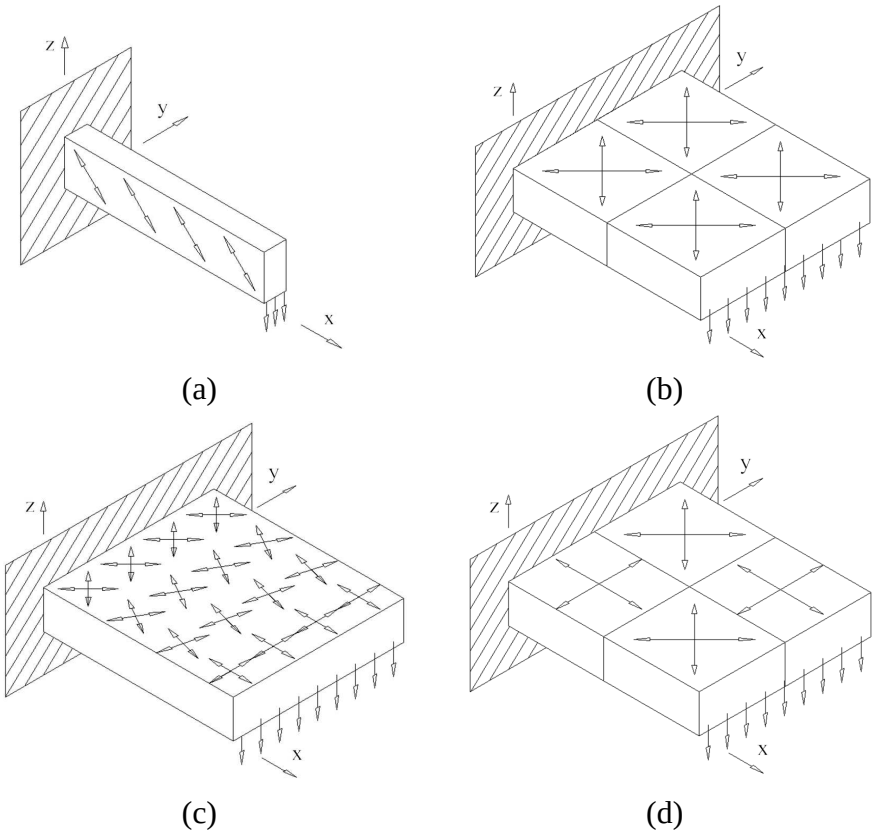

Figure 7.1: Fiber orientations for stability examples: (a) Example 1, Homogeneous beam; (b) Example 2, homogeneous plate; (c) Example 3, smoothly inhomogeneous plate; and (d) Example 4, discretely inhomogeneous plate one.

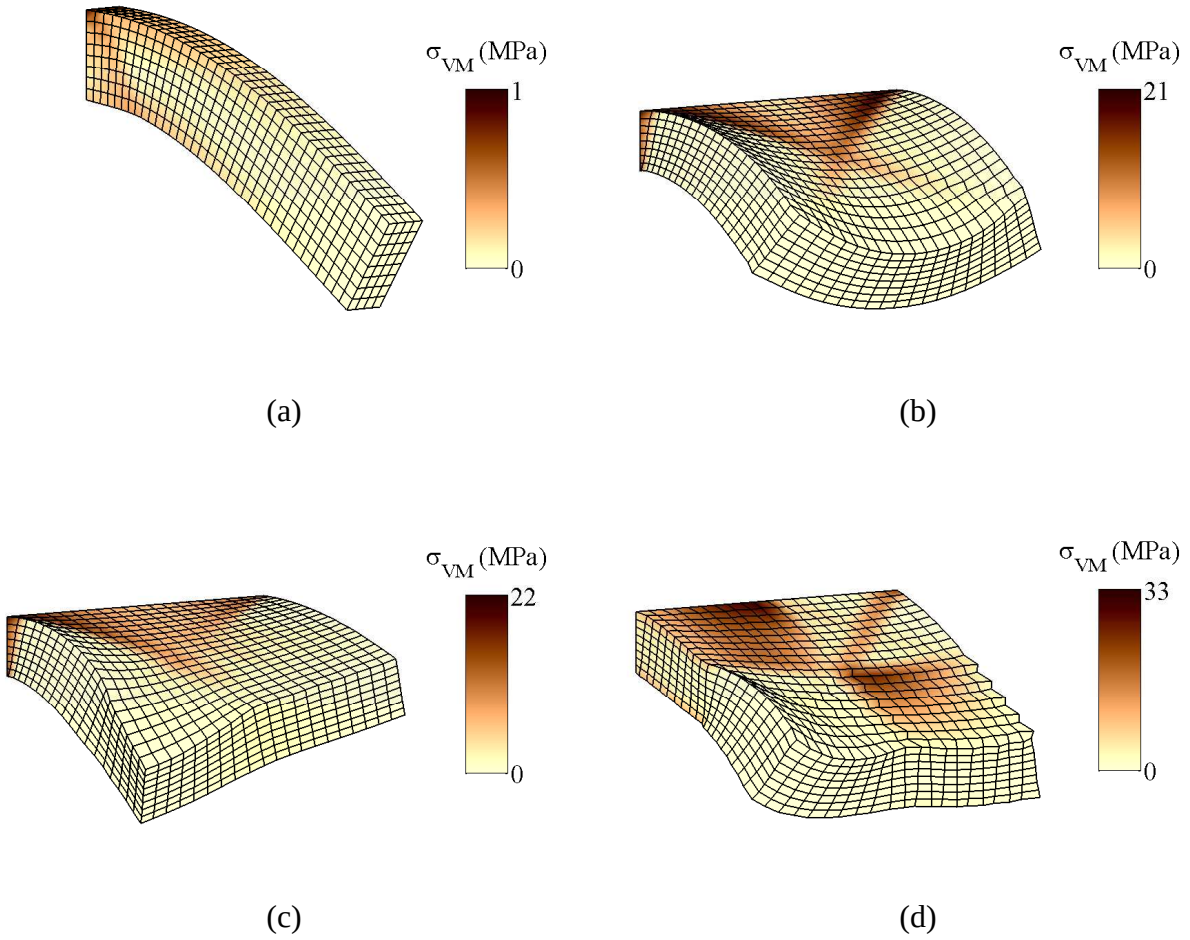

Figure 7.2: Rigidtropic B-bar examples each shown with 11340 DOF: (a) Example 1, Homogeneous beam; (b) Example 2, homogeneous plate; (c) Example 3, smoothly inhomogeneous plate; and (d) Example 4, discretely inhomogeneous plate one.

ponent.

The domain Ω of sought finite element solutions are given by $x \in [0, L]$, $y \in [0, W]$, and $z \in [0, t]$. The Dirichlet boundary conditions on Γ_u at $x = 0$ are

$$u_x = u_y = u_z = 0\,. \tag{7.6}$$

For the beam model (example 1), the Neumann boundary conditions are prescribed on Γ_t at $x = L$ as

$$\sigma \cdot \hat{n} = \tau_{xz} = -10 \text{ kPa}. \tag{7.7}$$

For the plate model (examples 2-4), the Neumann boundary conditions are prescribed on Γ_t at $x = L$ as

$$\sigma \cdot \hat{n} = \tau_{xz} = -100 \text{ kPa}. \tag{7.8}$$

Note that $\Gamma = \Gamma_t \cup \Gamma_u$ and $\Gamma_t \cap \Gamma_u = \varnothing$. The boundary conditions remain the same throughout the examples.

The convergence of the treated elements is demonstrated for each example and calculated errors are referenced with respect to the limit of the quadratic refinement for the respective models, as determined by Richardson's extrapolation [62]. Selected convergence results are provided in the current section.

The refinement was carried out with a progressively increasing Number of Degrees-Of-Freedom (*NDOF*). For the linear, eight node, hexahedral elements H8 elements $NDOF = [324, 1650, 5376, 11340, 22308, 36270, 58320, 83640]$, and for quadratic, 27 node, hexahedral elements H27 $NDOF = [1650, 11340, 36270, 83640]$.

The strain energy errors are reported graphically and are defined by the error expression:

$$\Psi = \frac{\mathscr{U}}{\mathscr{U}_\xi} - 1\,. \tag{7.9}$$

where Ψ is the error, $\mathscr{U}$ is the computed strain energy, and $\mathscr{U}_\xi$ is the limit value arising from Richardson's extrapolation.

In subsequent convergence studies, maximum displacement and the limit value of the maximum displacement shall taken respectively as u_{max} and u_Ξ.

In these examples, the maximum deflection at the free ends of the beam and plate, as well as the strain energy error, are plotted with four different element treatments. The first two treatements, referred to throughout as "false isotropic," ignore the principal compliance and take the rigid component to be constructed by means of $m = [1,1,1,0,0,0]^T$. This inadvertently treats the anisotropic material as one would in using conventional selective reduced integration, which is intrinsically tailored for volumetric locking in nearly incompressible isotropic materials. In contrast, this demonstrates the effectiveness of "unlocking" the rigid modes with the proposed spectral-decomposition-based element locking treatments.

The subsequent (suggested) treatments are denoted "GSRI" and "B-bar", and they use the principal compliance modes $m = v_1$ for single fiber materials or $m = [v_1 v_2]$ for dual fiber materials to identify the nearly rigid components. Up to three modes $m = [v_1 v_2 v_3]$ are treated in stability analyses presented later in this chapter.

7.1.1 Example: Homogeneous Single Fiber Beam

In Figs. (7.8–7.4) we demonstrate the results for a simple beam model with a stiff fiber reinforcement along the vector $[\sqrt{2}/2, 0, -\sqrt{2}/2]$.

The elastic modulus along the stiff fiber is 100,000 times higher than in the transverse directions, and the shear terms comparatively very small in magnitude.

The anisotropic elastic properties for this example are

$E1(Pa) = 1.000e+14$, $E2(Pa) = 1.000e+09$, $E3(Pa) = 1.000e+09$, $G12(Pa) = 2.000e+08$, $G13(Pa) = 2.000e+08$, $G23(Pa) = 2.000e+08$, $nu12 = 0.25$, $nu12 = 0.25$, and $nu12 = 0.25$.

Which gives the material elasticity matrix (with the engineering shear strain convention):

$$D = \begin{bmatrix} 106700 & 0.3333 & 0.3333 & 0 & 0 & 0 \\ 0.3333 & 1.067 & 0.2667 & 0 & 0 & 0 \\ 0.3333 & 0.2667 & 1.067 & 0 & 0 & 0 \\ 0 & 0 & 0 & 0.2 & 0 & 0 \\ 0 & 0 & 0 & 0 & 0.2 & 0 \\ 0 & 0 & 0 & 0 & 0 & 0.2 \end{bmatrix} \tag{7.10}$$

in *GPa*. The large first row–first column entry of this matrix indicates the increased fiber stiffness and corresponds to a small compliance term in D^{-1}.

The spectral decomposition reveals that as the rigidity of the fibers increase without bound, the nearly-zero strains are directed along

$$v_1 = \sqrt{3}[1,0,0,0,0,0]^T \tag{7.11}$$

in the local (fiber-aligned) coordinates.

The stiff fibers of this example resist diagonal transverse deformation. This affect both shearing and bending of the beam. Locking elements result in an underestimation of the displacements and strain energy. The treated elements outperform traditional SRI with improved accuracy in faster convergence.

Figure 7.2 (a) shows the deformed shape color-coded with von Mises stress for the corrected B-bar formulation with linear hexahedra. The effect of the reinforcing fibers that leads to a strong variation of the stress along the fibers anchored in the clamped face is clearly visible. Figure 7.8 illustrates the conclusion that satisfactory convergence in energy can not be expected from finite elements that use the ineffective formulation for the isotropic nearly-incompressible materials (i.e. the standard B-bar technique); the corrected GSRI and B-bar formulations deliver identical solutions that converge well. Figure 7.4 shows the convergence in energy for the quadratic hexahedra. While the quadratic elements converge at higher rates

than the linear ones when using the false isotropic formulation, the corrected techniques are superior.

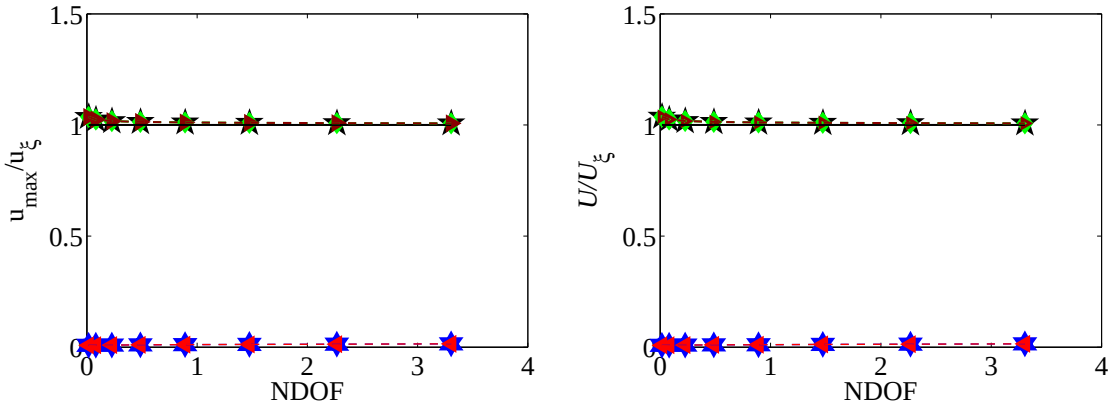

(a) (b)

Figure 7.3: For the fiber-reinforced cantilevered beam, untreated H8 elements fail to converge satisfactorily. (a) The maximum displacement at free end versus discretization density; (b) The strain energy versus discretization density.

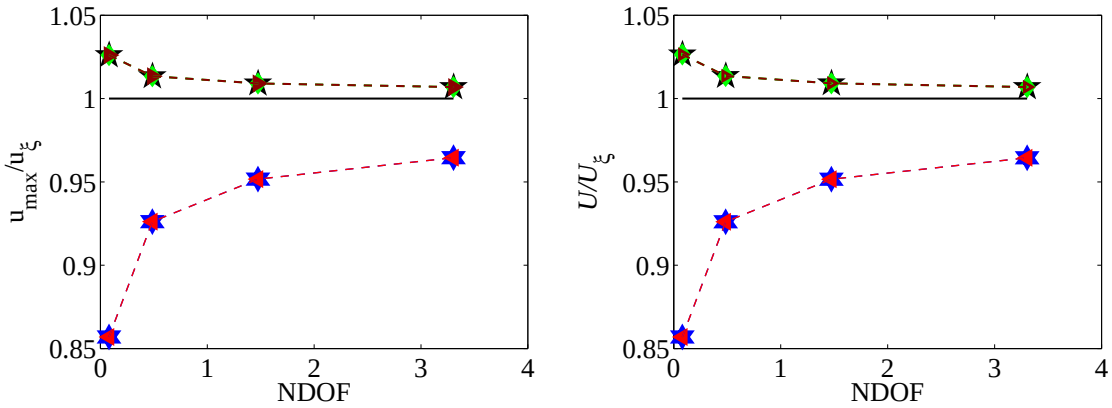

(a) (b)

Figure 7.4: For the single-fiber cantilevered beam with H27 elements, the treated elements show improved convergence. (a) The maximum displacement at free end versus discretization density; (b) The strain energy versus discretization density.

Comparisons to High Performance Elements in ABAQUS

High performance elements available to the ABAQUS commercial finite element anlalysis package are adapt at handling materials with a single rigid fiber direction. The presently proposed treatments, however, are still top performers and have been shown (in the previous chapter) to perform well independently of material fiber orientations. This particular beam example has fibers that are oriented at a 45° angle about the *y*-axis, which gives the material fibers a greater influence on the ultimate deformation results. The linear hexahedral B-bar H8-Bbar elements outperform the stardard hexahedral C3D8 and the hybrid hexahedral C3D8H, and keep up with the reduced integration hexahedral hybrid C3D8RH, and the incopatible modes hexahdral hybrid C3D8IH.

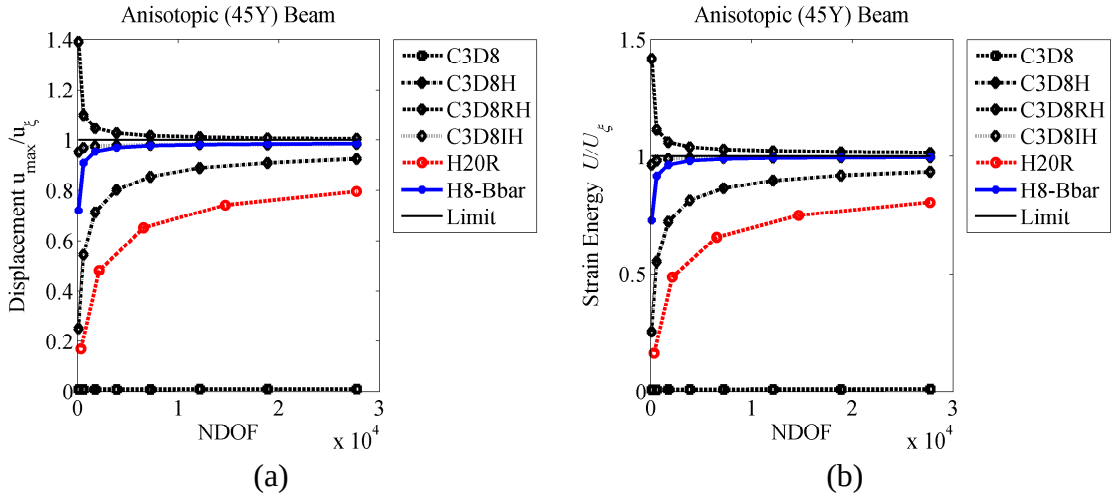

Figure 7.5: Homogeneous Single-fiber cantilever beam, compare to ABAQUS high performance elements. (a) The maximum displacement at free end versus NDOF; (b) The strain energy versus NDOF.

The refinement behavior of the displacement solutions of the elements being compared is presented in Figure 7.5 (a), and the strain energy refinement in Figure 7.5 (b). Figures 7.6(a) and (b) show that the only element that shows better convergence behavior than the H8-Bbar is the incompatible modes hybrid C3D8IH. The high performance elements available in ABAQUS (especially the C3D8IH) perform well on bending dominated problems such as this cantilevered beam with shear preventing rigid fiber.

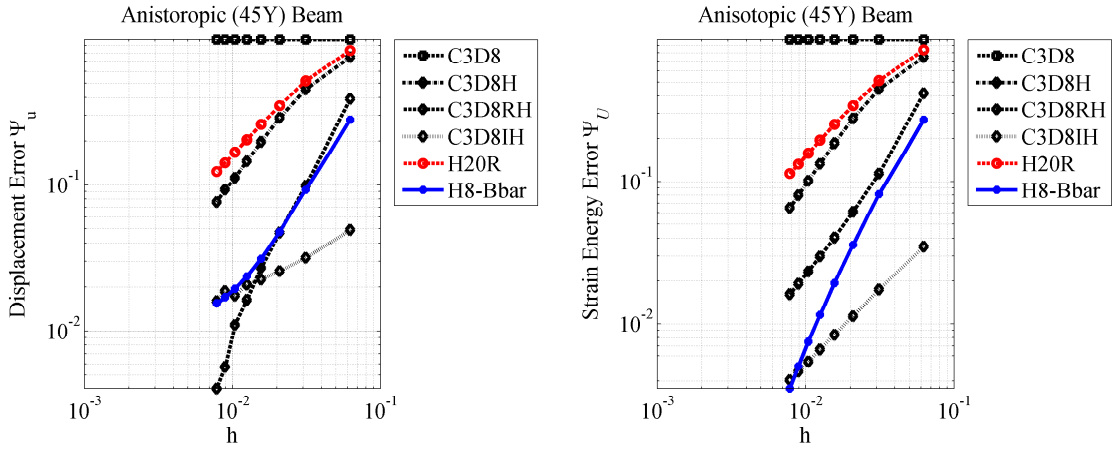

Figure 7.6: Homogeneous single-fiber cantileve beam log-log of error, compare to ABAQUS high performance elements. (a) The maximum displacement error at free end versus element size (h); (b) The strain energy error versus element size (h).

7.1.2 Example: Homogeneous Dual Fiber Plate

In figures 7.2(b), 7.7 (a), 7.8 (b) a cantilevered plate reinforced with two orthogonal systems of stiff fibers oriented at 45^o with respect to the clamped face in the plane x,y is considered. The orthotropic material properties are taken on the local material axes as $E1(Pa) = 1.000e+14$, $E2(Pa) = 1.000e+14$, $E3(Pa) = 1.000e+09$, $G12(Pa) = 2.000e+08$, $G13(Pa) = 2.000e+08$, $G23(Pa) = 2.000e+08$, $nu12 = 0.25$, $nu12 = 0.25$, and $nu12 = 0.25$.

Which gives:

$$D = \begin{bmatrix} 106700 & 26670 & 0.3333 & 0 & 0 & 0 \\ 26670 & 106700 & 0.3333 & 0 & 0 & 0 \\ 0.3333 & 0.3333 & 1 & 0 & 0 & 0 \\ 0 & 0 & 0 & 0.2 & 0 & 0 \\ 0 & 0 & 0 & 0 & 0.2 & 0 \\ 0 & 0 & 0 & 0 & 0 & 0.2 \end{bmatrix} \tag{7.12}$$

in *GPa*. This material model, which will be applied to the remaining plate examples, has two locking stress directions.

$$v_1 = \sqrt{\frac{3}{2}}[1,1,0,0,0,0]^T\,, \quad v_2 = \sqrt{\frac{3}{2}}[1,-1,0,0,0,0]^T\,. \tag{7.13}$$

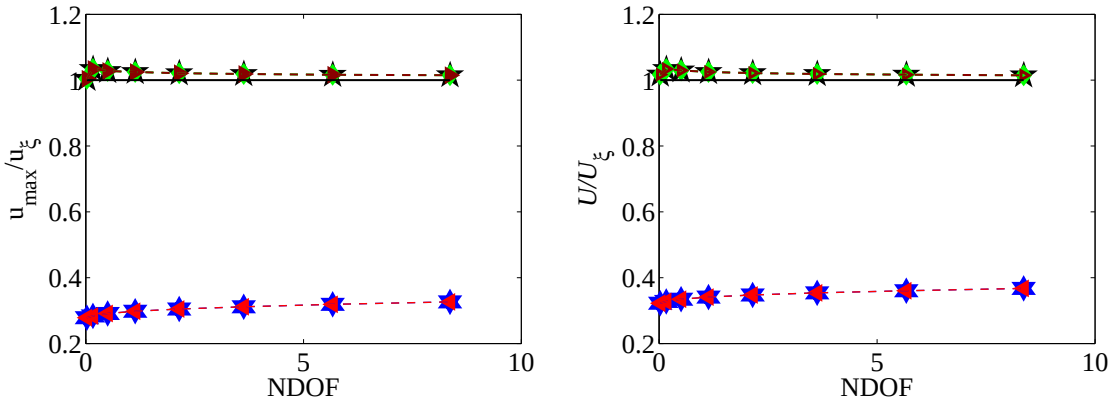

(a) (b)

Figure 7.7: Untreated eight node hexahedral elements fail to converge satisfactorily. (a) The maximum displacement at free end versus discretization density; (b) The strain energy versus discretization density.

The two smallest principal compliances are comparable in magnitude and about 100,000 times smaller than the next closest compliance.

The fiber orientations shown graphically in figure 7.1 (b) are defined by the rotation matrix:

$$R_z(\theta) = \begin{bmatrix} cos\theta & -sin\theta & 0 \\ sin\theta & cos\theta & 0 \\ 0 & 0 & 1 \end{bmatrix} \tag{7.14}$$

where $\theta = 45^\circ$.

Figure 7.9 shows deflection of the free edge of the plate for selected finite elements. The deflection computed with the GSRI linear (H8) and quadratic hexahedra (H27) agrees very well with the results computed with the B-bar linear hexahedra. All of these results are within

This example illustrates the ability to treat multiple fiber directions using GSRI and the generalized B-bar methods. Here the fibers act in the plane of the plate at an angle of 45° to the cantilever axis. The increased stiffness in the fiber directions limits that displacements at the corners of the free ends which account for the curved deformations seen along the free edge in figure 7.2(b). The “X” shape seen in the stress field color mapping of the top surface provides a valuable visual representation of the rigid fiber’s resistance to loading.

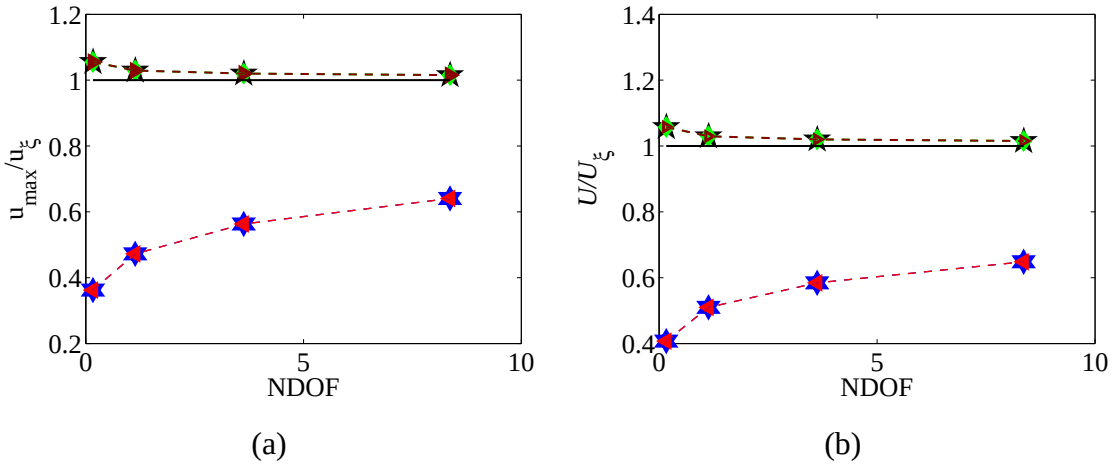

(a) (b)

Figure 7.8: Dual-fiber cantilever plate with quadratic hexahedral elements; treated elements show improved convergence. (a) The maximum displacement at free end versus discretization density; (b) The strain energy versus discretization density.

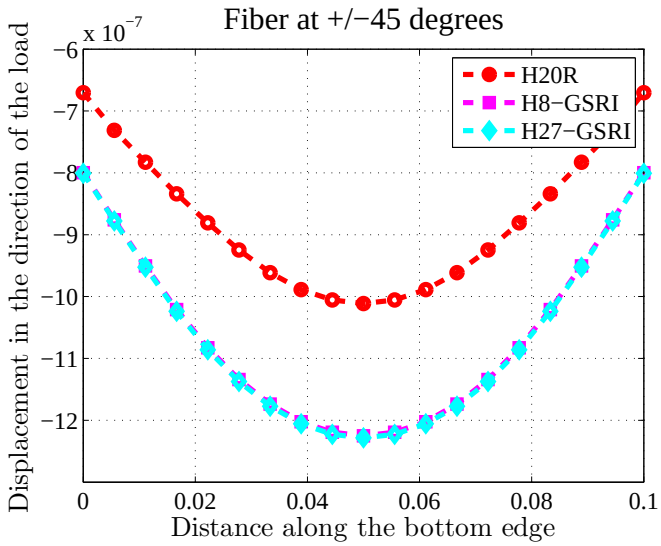

Figure 7.9: Cantilevered plate reinforced with two orthogonal systems of stiff fibers. Deflection of the free edge of the plate.

Figure 7.10 illustrates the convergence of the maximum deflection along the free edge of the plate. A graph of the estimated true normalized error is shown for selected finite element types in figure 7.10. The linear, quadratic, and cubic Lagrange hexahedron are all fully integrated, as appropriate for their degree. So is the quadratic tetrahedron. Also included is the serendipity 20-node hexahedron with uniform reduced integration.

It is noteworthy that both the serendipity 20-node hexahedron with uniform reduced in-

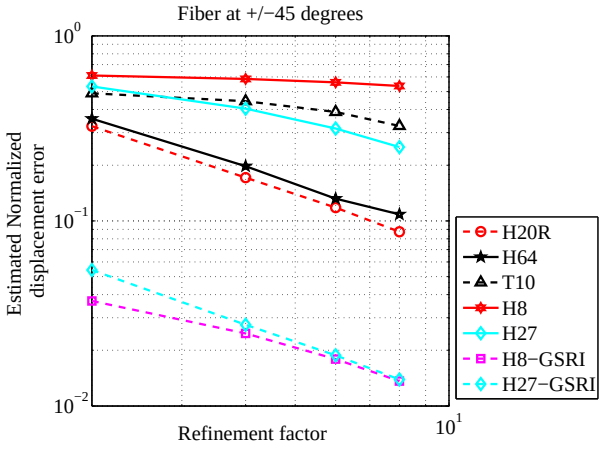

Figure 7.10: Cantilevered plate reinforced with two orthogonal systems of stiff fibers. Convergence of the maximum deflection along the free edge of the plate. Graph of the estimated true normalized error.

tegration and the cubic Lagrange hexahedron match the GSRI linear and quadratic hexahedra in convergence rate, but are much less accurate in absolute terms. The quadratic hexahedron and the quadratic tetrahedron also appear to approach the same convergence rates, but are more than order of magnitude less accurate. The data for the linear hexahedron do not extend sufficiently far into the asymptotic range for this element, but its performance is clearly inadequate.

In previous (single fiber beam)example, the treated element performed well when compared to the elements available in ABAQUS, but were still slightly outperformed by the hybrid linear hexahedral elements with incompatible modes. In this example, however, the treated elements are the top performers.

Comparisons to High Performance Elements in ABAQUS

A far greater performance advantage for the proposed treatment is realized when more than one rigid mode is treated. While B-bar was outperformed, slightly, by the hybrid incompatible modes elements in the single-fiber beam example, B-bar is the clear winner when the material has two rigid fibers and two eigenmodes of the compliance are treated.

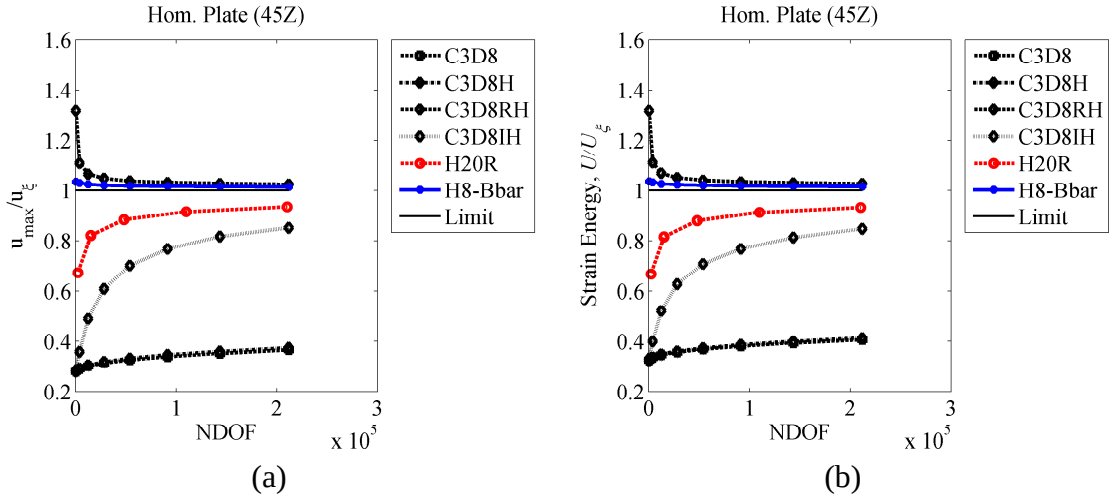

Figure 7.11: Dual-fiber homogeneous cantilever plate, compare to ABAQUS high performance elements. (a) The maximum displacement at free end versus NDOF; (b) The strain energy versus NDOF.

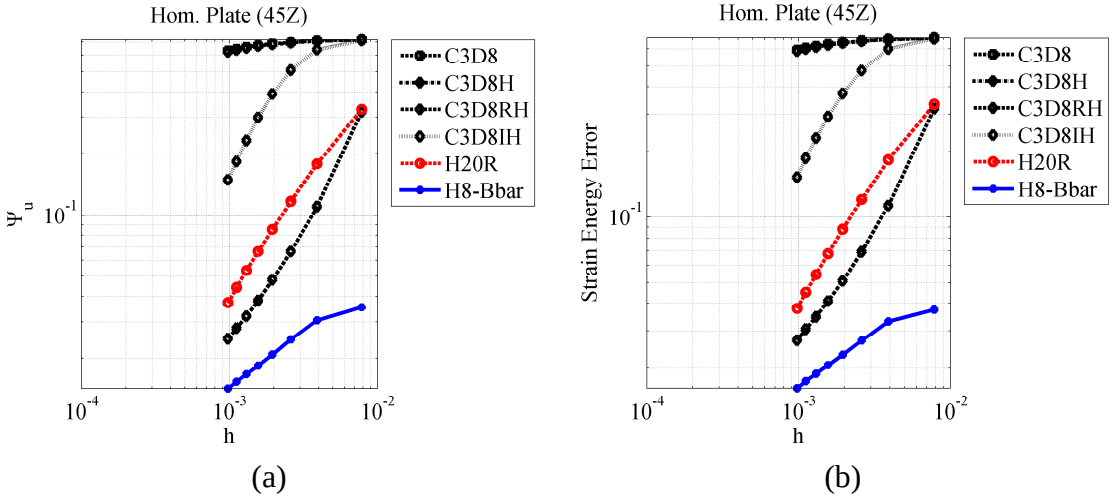

Figure 7.12: Dual-fiber cantilever plate with abrupt inhomogeneities log-log of error, compare to ABAQUS high performance elements. (a) The maximum displacement error at free end versus element size (h) density; (b) The strain energy error versus element size (h).

Figures 7.12 (a) and (b) show superior convergence behavior for the new B-bar elements.

7.1.3 Example: Dual Fiber Plate with Smooth Inhomogeneity

Figures 7.2(c), 7.13, and 7.14 of the next example highlight the introduction of a continuously varying inhomogeneity. The physical dimensions as well as the basic orthotropic material properties are taken to be the same as for the previous example. This time, however, the rigid fiber orientations are not constant throughout and are defined by a rotation matrix that

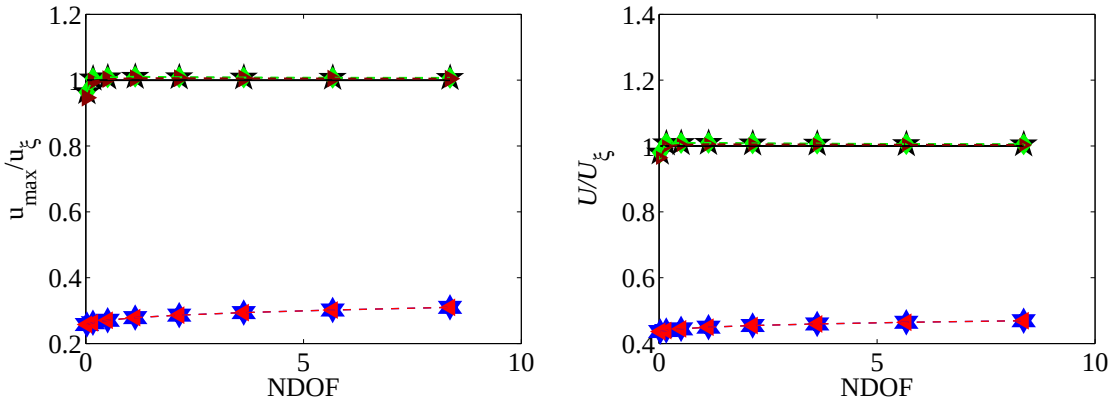

(a) (b)

Figure 7.13: Dual-fiber cantilever plate with a smooth inhomogeneity and linear hexahedral elements; treated elements show improved convergence. (a) The maximum displacement at free end versus discretization density; (b) The strain energy versus discretization density.

varies linear from 45° at the clamped end to 90° at the loaded end by:

$$R_z(\theta,x,L) = \begin{bmatrix} cos\theta & -sin\theta & 0 \\ sin\theta & cos\theta & 0 \\ 0 & 0 & 1 \end{bmatrix} + \begin{bmatrix} cos(\frac{\theta x}{L}) & -sin(\frac{\theta x}{L}) & 0 \\ sin(\frac{\theta x}{L}) & cos(\frac{\theta x}{L}) & 0 \\ 0 & 0 & 1 \end{bmatrix} \tag{7.15}$$

where $\theta = 45^\circ$ and $L = Length$. This changing material orientation introduces a smooth-field inhomogeneity illustrated graphically in 7.1 (c).

The treated elements handle the introduction of a smooth inhomogeneity well. The H8 elements converge quickly and the H27 elements follow suit. Figures 7.13 and ‘7.14 show convergence that significantly outperforms the untreated elements. Particular cases detailed in appendix B show improved behavoir of the B-bar method when reduced integration is a applied to the terms resulting from the rigid component of the elasticity. Fully integrating the generalized B-bar method prevents alternating, or “sawtooth,” solutions as the meshes are refined. This is something that crops up when using B-bar with selective reduced integration on inhomogeneous material models such as this one. This observation is supported by the final inhomogeneous example.

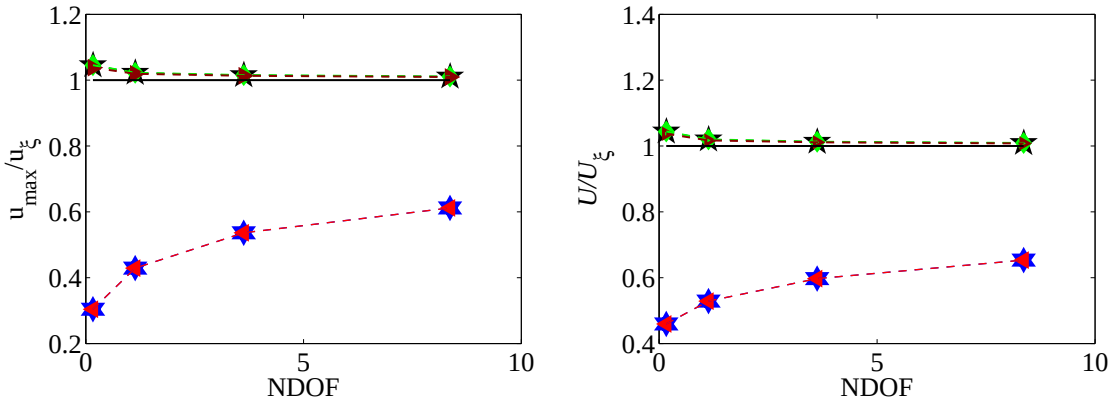

(a) (b)

Figure 7.14: Dual-fiber cantilever plate with a smooth inhomogeneity and quadratic hexahedral elements; treated elements show improved convergence. (a) The maximum displacement at free end versus discretization density; (b) The strain energy versus discretization density.

7.1.4 Example: Dual Fiber Plate with Abrupt Inhomogeneous Regions

In figures 7.2(d), 7.15, and 7.16 of the final example; regions of distinct fiber orientations within the x-y plane are introduced. Here again, the physical dimensions as well as the orthotropic material properties are taken to be the same as for the second example—with the exception of the fiber orientations.

The domain of example 4 is split in 4 distinct geometric regions, each applying the orientation matrix R_z of equation 7.14 at either $\theta = 0^\circ$ or $\theta = 45^\circ$ as follows:

On $x \in [0, \frac{L}{2}]$, $y \in [0, \frac{W}{2})$, $\forall z$ $\theta = 0^\circ$

On $x \in [0, \frac{L}{2}]$, $y \in [\frac{W}{2}, W]$, $\forall z$ $\theta = 45^\circ$

On $x \in (\frac{L}{2}, L]$, $y \in [0, \frac{W}{2})$, $\forall z$ $\theta = 45^\circ$

On $x \in (\frac{L}{2}, L]$, $y \in [\frac{W}{2}, W]$, $\forall z$ $\theta = 0^\circ$

A graphical representation of these distinct regions of inhomogeneity is provided in figure 7.1 (d).

Figures 7.15 and 7.16 demonstrate, once again, that the treated elements do not exhibit the locking behavior that plagues the untreated solutions.

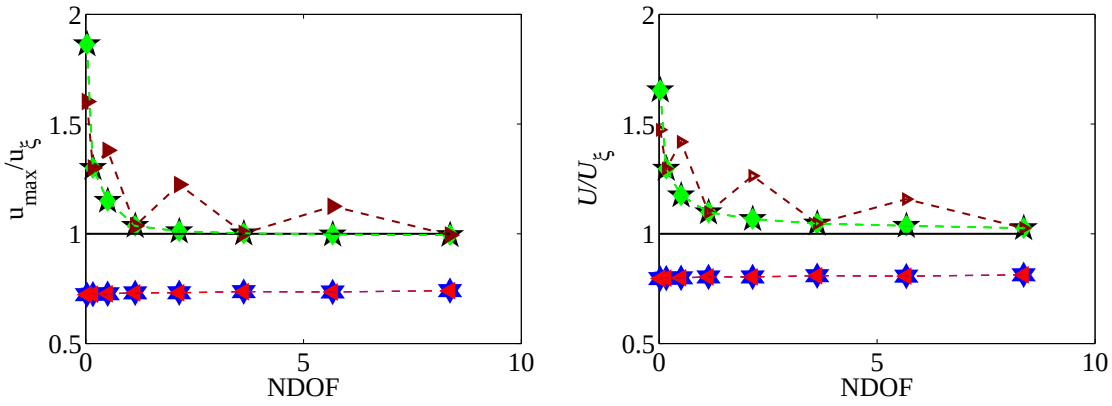

(a) (b)

Figure 7.15: Dual-fiber cantilever plate with abrupt inhomogeneities and linear hexahedral elements; treated elements show improved convergence. (a) The maximum displacement at free end versus discretization density; (b) The strain energy versus discretization density.

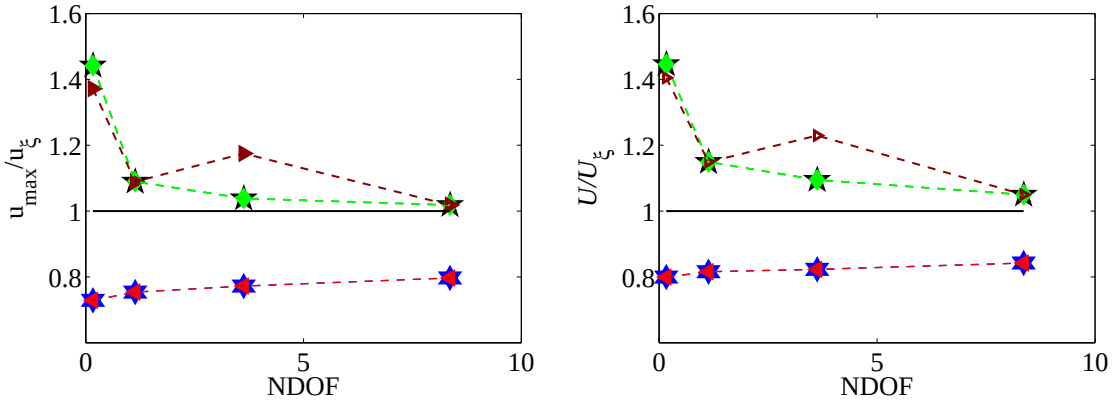

(a) (b)

Figure 7.16: Dual-fiber cantilever plate with abrupt inhomogeneities and quadratic hexahedral elements; treated elements show improved convergence. (a) The maximum displacement at free end versus discretization density; (b) The strain energy versus discretization density.

Comparisons to High Performance Elements in ABAQUS

When an abruptly discrete inhomogeneity is introduced the proposed elements still converge very well. The reduced integration hybrid C3D8RH elements show an impressive convergence rate but still cannot match the accuracy of the h8-Bbar elements. In this example, element distortions plague the top performing elements. A closer look at element stability will follow in the next chapter.

Figures 7.18 (a) and (b) once again show superior convergence behavior for the new

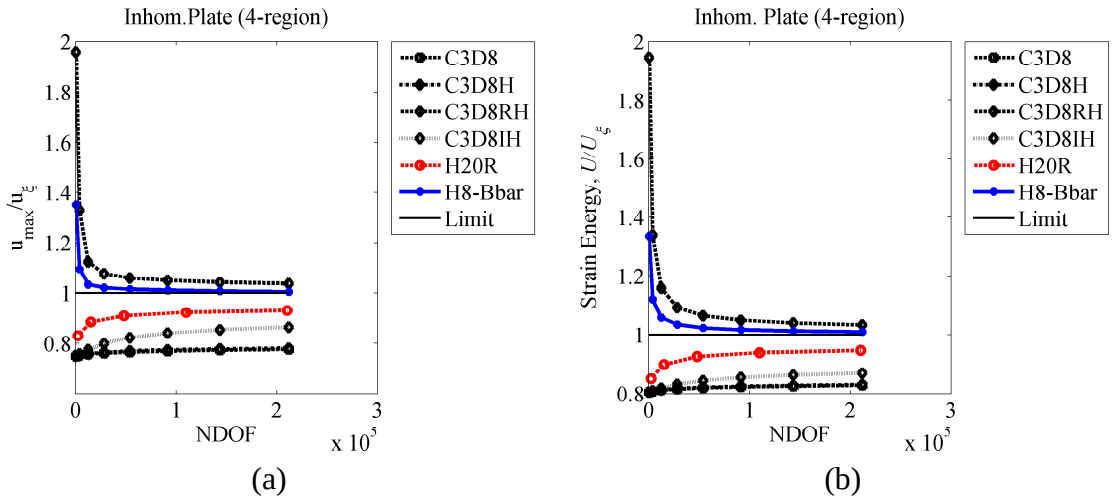

Figure 7.17: Dual-fiber cantilever plate with abrupt inhomogeneities, compare to ABAQUS high performance elements. (a) The maximum displacement at free end versus NDOF; (b) The strain energy versus NDOF.

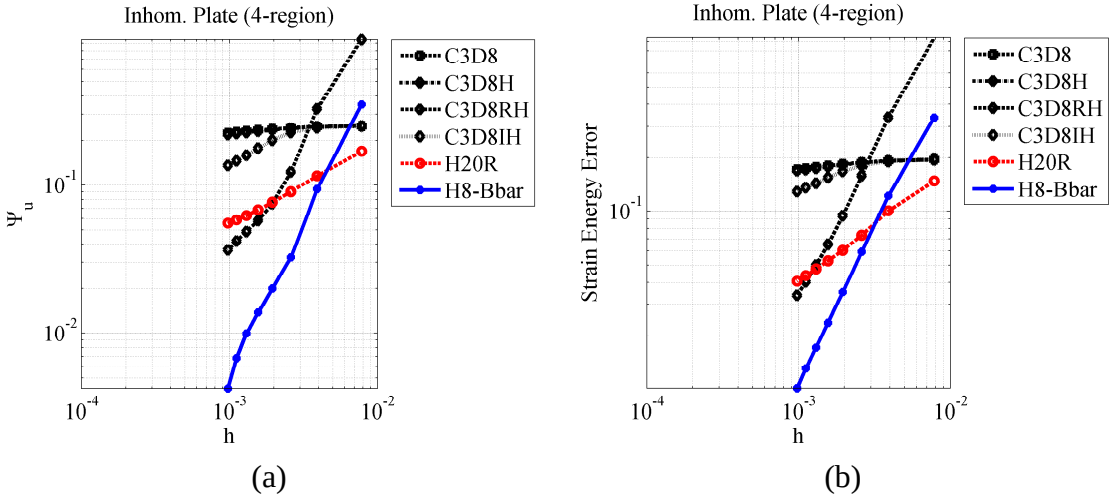

Figure 7.18: Dual-fiber cantilever plate with abrupt inhomogeneities log-log of error, compare to ABAQUS high performance elements. (a) The maximum displacement error at free end versus element size (h); (b) The strain energy error versus element size (h).

B-bar elements. Although the reduce integration quadratic hexahedral H20R elements, the linear reduced integration hybrid hexahedral C3D8RH elements, and the linear hybrid incompatible modes hexahedral C3D8IH elements are slightly more accurate with coarsest meshes, the treated H8-Bbar elements soon surpass them all in accuracy.

7.1.5 Conclusions Drawn From Examples

In all four of the example problems investigated, as well as for many other examples omitted for brevity's sake, the treatments cure the rigid locking that ails all other elements tested. Throughout these examples, for which no stabilization is incorporated and initial meshes are uniform and well proportioned, the treated solutions converge from the flexible side and the untreated solutions converge from the stiff side. Is should be noted that the coarsest, pre-asymptotic, meshes of the second example show non-monotonic behavior as the meshes are refine. This is something we will see more of when the stabilization methods of the following sections are applied.

Although the treatments show no locking and are convergent, some results indicate that distorted meshes may lead to solutions that are non-monotonic under refinement. Severe mesh distortion can lead to inaccuracies, especially in computed stresses. In most cases, distorted or not, the treated elements perform better than the untreated ones.

7.2 Acknowledgements

Chapter 7 is in part a reprint of the material published in, "B-bar Finite Element Methods for Anisotropic Elasticity," *International Journal for Numerical Methods in Engineering*. 2013; 00:1-15. Steve Oberrecht, Jan Novák, and Petr Krysl. 2013. The author of this dissertation was the primary author of this paper.

Chapter 8

Stabilized GSRI and B-bar

One might suspect that the mesh dependent deformation aberrations seen in figure 8.1 are due to a rank deficiency in the assembled stiffness matrix, but the explanation is not so simple. As will be demonstrated, meshes with multiple elements in each direction have no clear deficiency.

In assessing stability we first review the spectral analysis of the stiffness matrices, where the eigenvalues of the $7th$ mode are several orders of magnitude greater than the first six–which are numerically equivalent to zero for their respective source matrices. In doing so we discover that when multiple modes are treated stability is not guaranteed and is, at times, dependent on the fiber angles with respect to element orientations. Following this assessment, a stabilization method is proposed and is shown to be effective with certain performance concessions in special cases.

The spectral analyses of single element stiffness matrices for three different elements treatments are compared. Using both linear and quadratic hexahedra GSRI, selectively integrated B-bar, and fully integrated B-bar are investigated for stability. It should be no surprise that under-integrating a standard element reduces the rank of the element stiffness matrix. For H8 elements, after accounting for the six rigid body modes, the expected rank of a well behaved element to be 18. For H27 elements, the expected rank of a well behaved element is 75. The rank of a standard under-integrated H8 element is six and the rank of a standard under-

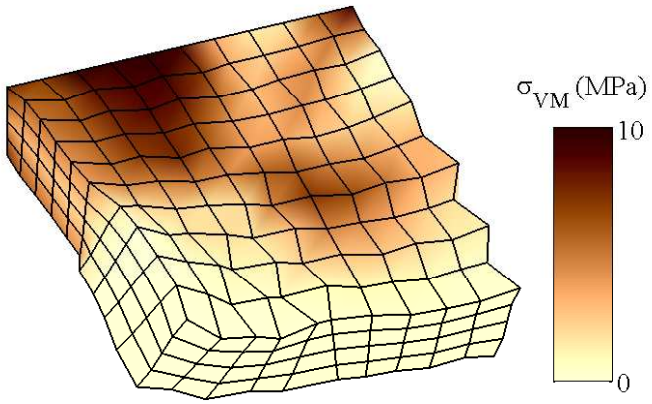

Figure 8.1: An abruptly inhomogeneous example highlighting non-physical element distortions or "hourglassing" is shown (GSRI with H8 elements and 1650 *DOF*; deformations scaled by 494).

integrated H27 element is 48.

Looking at a single element, the ranks of the treated H8 elements and H27 elements are 18 and 75 respectively for all treated single fiber elements (GSRI and B-bar). However, when more than one stiff fiber is treated the question of stability requires a more thorough investigation. Table 8.2 provides a quick view of when the two-fiber treatments are stable without the necessity of special methods. Selected convergence plots are provided in the current section. For exhaustive results refer to Appendix B.

8.0.1 Stability of a Single Element

A square element block stiffness matrix is examined for stability wherein linear (H8),and quadratic (H27) hexahedral elements are examined. The first 6 eigenvalues represent rigid body motion and are expected to approach numerical zero; this means that they should be several orders of magnitude lower than the seventh eigenvalue. The ratio $\frac{\lambda_7}{\lambda_6}$ is introduces as a reasonable measure of element stability. The elements are considered "stable" when $\frac{\lambda_7}{\lambda_6} >> 1$; $\frac{\lambda_7}{\lambda_6}$ close to 1 indicates instability.

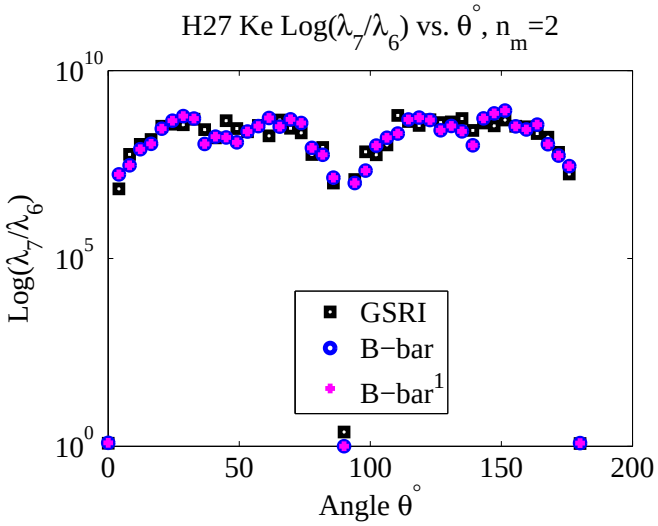

Figure 8.2: H27, 2 modes, 2 fibers (Here B-bar[1] means fully integrated).

Table 8.1: Stability results for various treatments of single fiber single element blocks.

	$n_m = 0$	$n_m = 1$	$n_m = 2$	$n_m = 3$
H8	Stable $\forall\theta$	Stable $\forall\theta$	Stable $\forall\theta$	Unstable $45°, 135°$
H27	Stable $\forall\theta$	Stable $\forall\theta$	Unstable $\forall\theta$	Unstable $\forall\theta$

Material Dual Fiber: $E_1 = 200000 \times 10^6$, $E_2 = 200000 \times 10^6$, $E_3 = 2 \times 10^6$, $G_{12} = 0.5 \times 10^6$, $G_{23} = 0.2 \times 10^6$, $G_{13} = G_{23}$, and $\nu_{12} = \nu_{13} = \nu_{23} = 0.25$.

8.0.2 Instabilities Revealed in the 7th Mode

Tracking the stability of dual-fiber two-mode treatment, while varying the fiber angle with respect to the local element orientations, proves to be a valuable exercise. Figure 8.2 shows that the quadratic elements are stable except at a few select angles, namely: 0° and 90°. Figure 8.3 shows something similar when the same material has three modes treated and H8 elements are used. In this case instabilities appear at 45° and 135°. Please note that the curves of the GSRI, B-bar, and selectively integrated B-bar treatments all follow the same trends.

As tabulated in 8.2: H8 and H27 elements with fewer than two treated modes are

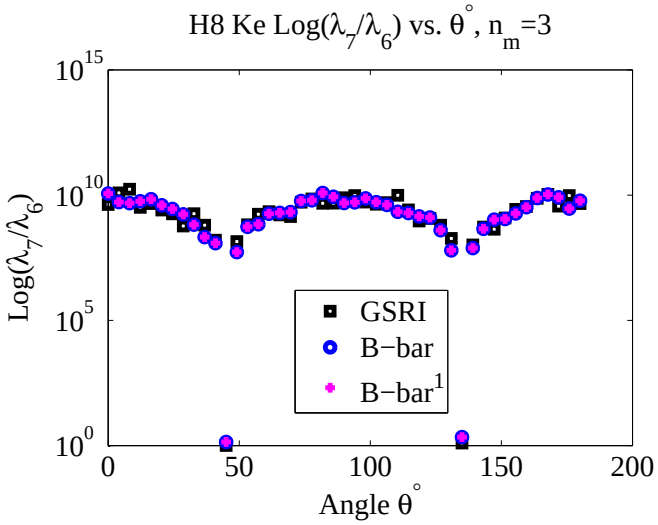

Figure 8.3: H8, 3 modes, 2 fibers (Here B-bar^1 means fully integrated).

Table 8.2: Stability results for various treatments of dual fiber single element blocks.

	$n_m = 0$	$n_m = 1$	$n_m = 2$	$n_m = 3$
H8	Stable $\forall\theta$	Stable $\forall\theta$	Stable $\forall\theta$	Unstable $45°, 135°$
H27	Stable $\forall\theta$	Stable $\forall\theta$	Unstable $0°, 90°$	Unstable $\forall\theta$

Table 8.3: Stability results for various treatments of single fiber 2-x-2-x-2 element blocks.

	$n_m = 0$	$n_m = 1$	$n_m = 2$	$n_m = 3$
H8	Stable $\forall\theta$	Stable $\forall\theta$	Stable $\forall\theta$	Stable $\forall\theta$
H27	Stable $\forall\theta$	Stable $\forall\theta$	Stable $\forall\theta$	Stable $\forall\theta$

Table 8.4: Stability results for various treatments of dual fiber 2-x-2-x-2 element blocks.

	$n_m = 0$	$n_m = 1$	$n_m = 2$	$n_m = 3$
H8	Stable $\forall\theta$	Stable $\forall\theta$	Stable $\forall\theta$	Stable $\forall\theta$
H27	Stable $\forall\theta$	Stable $\forall\theta$	Stable $\forall\theta$	Stable $\forall\theta$

consistently stable; H8 elements with two treated modes are stable; single fiber H27 elements with two or three treated modes are unstable at all angles; H8 elements with two or more treated modes are unstable at 45° and 135°; dual Fiber H27 elements with two treated modes are at 0° and 90°; and meshes with multiple elements in each coordinate direction are stable (see table 8.3).

8.0.3 Stabilization by a Modified Constitutive Split

A stabilization method can be constructed by observing that the rank of the element stiffness matrix is limited by the rank of the flexible component of the compliance or elasticity matrix. Efforts to construct a stable element stiffness matrix start with a full rank $\mathbf{D}_f$. Some clues are provided in the constitutive splits available in the nearly incompressible isotropic case. Recall the basic constitutive relations

$$\begin{Bmatrix} \varepsilon_{xx} \\ \varepsilon_{yy} \\ \varepsilon_{zz} \\ 2\varepsilon_{yz} \\ 2\varepsilon_{zx} \\ 2\varepsilon_{xy} \end{Bmatrix} = \begin{bmatrix} \frac{1}{E} & \frac{-\nu}{E} & \frac{-\nu}{E} & 0 & 0 & 0 \\ \frac{-\nu}{E} & \frac{1}{E} & \frac{-\nu}{E} & 0 & 0 & 0 \\ \frac{-\nu}{E} & \frac{-\nu}{E} & \frac{1}{E} & 0 & 0 & 0 \\ 0 & 0 & 0 & \frac{1}{G} & 0 & 0 \\ 0 & 0 & 0 & 0 & \frac{1}{G} & 0 \\ 0 & 0 & 0 & 0 & 0 & \frac{1}{G} \end{bmatrix} \begin{Bmatrix} \sigma_{xx} \\ \sigma_{yy} \\ \sigma_{zz} \\ \sigma_{yz} \\ \sigma_{zx} \\ \sigma_{xy}\,, \end{Bmatrix} \tag{8.1}$$

and

$$\begin{Bmatrix} \sigma_{xx} \\ \sigma_{yy} \\ \sigma_{zz} \\ \sigma_{yz} \\ \sigma_{zx} \\ \sigma_{xy} \end{Bmatrix} = \begin{bmatrix} \frac{\lambda(1-\nu)}{\nu} & \lambda & \lambda & 0 & 0 & 0 \\ \lambda & \frac{\lambda(1-\nu)}{\nu} & \lambda & 0 & 0 & 0 \\ \lambda & \lambda & \frac{\lambda(1-\nu)}{\nu} & 0 & 0 & 0 \\ 0 & 0 & 0 & G & 0 & 0 \\ 0 & 0 & 0 & 0 & G & 0 \\ 0 & 0 & 0 & 0 & 0 & G \end{bmatrix} \begin{Bmatrix} \varepsilon_{xx} \\ \varepsilon_{yy} \\ \varepsilon_{zz} \\ 2\varepsilon_{yz} \\ 2\varepsilon_{zx} \\ 2\varepsilon_{xy} \end{Bmatrix}. \tag{8.2}$$

Here, we see the Bulk–Shear version of the constitutive split: $\varepsilon = \frac{1}{\kappa}\, term + mixed\, term = diag + full$. The diagonal term has full rank and is well conditioned. In

$$\varepsilon_{ij} = \frac{1}{9\kappa}\delta_{ij}\sigma_{kk} + \frac{1}{2\mu}(\sigma_{ij} - \frac{1}{3}\delta_{ij}\sigma_{kk}) \tag{8.3}$$

the hydrostatic pressure affects shear term. The Lame'–Shear split reads: $\varepsilon = \frac{1}{\lambda}\, term + \frac{1}{shear}\, term = diag + full$, and we have

$$\varepsilon_{ij} = \frac{-\nu^2}{\lambda(1+\nu)(1-2\nu)}\delta_{ij}\sigma_{kk} + \frac{1}{2\mu}\sigma_{ij}\,. \tag{8.4}$$

Notice that hydrostatic pressure doesn't affect the shear term with this version of the split.

The Bulk–Shear split reads: $\sigma = \kappa\, term + mixed\, term = diag + full$, or

$$\sigma_{ij} = \kappa\delta_{ij}\varepsilon_{kk} + 2\mu(\varepsilon_{ij} - \frac{1}{3}\delta_{ij}\varepsilon_{kk})\,. \tag{8.5}$$

Notice that dilation affects shear term here. However, dilation doesn't affect shear term in the Lame'–Shear split: $\sigma = \lambda\, term + shear\, term = diag + full$, or

$$\sigma_{ij} = \lambda\,\delta_{ij}\varepsilon_{kk} + 2\mu\varepsilon_{ij}\,. \tag{8.6}$$

The $\kappa\,\mu$ split is now expressed in Voigt-Mandel notation with $\mathbf{D} = \mathbf{D_v} + \mathbf{D_d} =$

$$\begin{bmatrix} \kappa & \kappa & \kappa & 0 & 0 & 0 \\ \kappa & \kappa & \kappa & 0 & 0 & 0 \\ \kappa & \kappa & \kappa & 0 & 0 & 0 \\ 0 & 0 & 0 & 0 & 0 & 0 \\ 0 & 0 & 0 & 0 & 0 & 0 \\ 0 & 0 & 0 & 0 & 0 & 0 \end{bmatrix} + \begin{bmatrix} \frac{4}{3}\mu & -\frac{2}{3}\mu & -\frac{2}{3}\mu & 0 & 0 & 0 \\ -\frac{2}{3}\mu & \frac{4}{3}\mu & -\frac{2}{3}\mu & 0 & 0 & 0 \\ -\frac{2}{3}\mu & -\frac{2}{3}\mu & \frac{4}{3}\mu & 0 & 0 & 0 \\ 0 & 0 & 0 & \mu & 0 & 0 \\ 0 & 0 & 0 & 0 & \mu & 0 \\ 0 & 0 & 0 & 0 & 0 & \mu \end{bmatrix} \tag{8.7}$$

where the $rank(\mathbf{D}_v) = 1$ and the $rank(\mathbf{D}_d) = 5$.

And, the $\lambda\ \mu$ split: $\mathbf{D} = \mathbf{D_v} + \mathbf{D_d} =$

$$\begin{bmatrix} \lambda & \lambda & \lambda & 0 & 0 & 0 \\ \lambda & \lambda & \lambda & 0 & 0 & 0 \\ \lambda & \lambda & \lambda & 0 & 0 & 0 \\ 0 & 0 & 0 & 0 & 0 & 0 \\ 0 & 0 & 0 & 0 & 0 & 0 \\ 0 & 0 & 0 & 0 & 0 & 0 \end{bmatrix} + \begin{bmatrix} 2\mu & 0 & 0 & 0 & 0 & 0 \\ 0 & 2\mu & 0 & 0 & 0 & 0 \\ 0 & 0 & 2\mu & 0 & 0 & 0 \\ 0 & 0 & 0 & \mu & 0 & 0 \\ 0 & 0 & 0 & 0 & \mu & 0 \\ 0 & 0 & 0 & 0 & 0 & \mu \end{bmatrix} \tag{8.8}$$

where $rank(\mathbf{D}_v) = 1$ and $rank(\mathbf{D}_d) = 6$.

To apply this to our spectral treatments, let the compliance eigenvalues λ_i provide $\kappa = \lambda_{max}/3$, and $\mu = \lambda_{min}$ as $\nu \to \frac{1}{2}$. Keep in mind that these λ_i are now eigenvalues, not the Lame' parameters λ expressed in the isotropic splits.

Now, we have a way of guaranteeing full rank in the flexible term of the elasticity matrix. We do so by defining the split using

$$\alpha = 2\lambda_{min}/\lambda_{max} = \frac{2}{3}\frac{\mu}{\kappa} \tag{8.9}$$

which gives:

$$\begin{bmatrix} \kappa & \kappa & \kappa & 0 & 0 & 0 \\ \kappa & \kappa & \kappa & 0 & 0 & 0 \\ \kappa & \kappa & \kappa & 0 & 0 & 0 \\ 0 & 0 & 0 & 0 & 0 & 0 \\ 0 & 0 & 0 & 0 & 0 & 0 \\ 0 & 0 & 0 & 0 & 0 & 0 \end{bmatrix} - \alpha \begin{bmatrix} \kappa & \kappa & \kappa & 0 & 0 & 0 \\ \kappa & \kappa & \kappa & 0 & 0 & 0 \\ \kappa & \kappa & \kappa & 0 & 0 & 0 \\ 0 & 0 & 0 & 0 & 0 & 0 \\ 0 & 0 & 0 & 0 & 0 & 0 \\ 0 & 0 & 0 & 0 & 0 & 0 \end{bmatrix} = \begin{bmatrix} \lambda & \lambda & \lambda & 0 & 0 & 0 \\ \lambda & \lambda & \lambda & 0 & 0 & 0 \\ \lambda & \lambda & \lambda & 0 & 0 & 0 \\ 0 & 0 & 0 & 0 & 0 & 0 \\ 0 & 0 & 0 & 0 & 0 & 0 \\ 0 & 0 & 0 & 0 & 0 & 0 \end{bmatrix} \tag{8.10}$$

and

$$\begin{bmatrix} \frac{4}{3}\mu & -\frac{2}{3}\mu & -\frac{2}{3}\mu & 0 & 0 & 0 \\ -\frac{2}{3}\mu & \frac{4}{3}\mu & -\frac{2}{3}\mu & 0 & 0 & 0 \\ -\frac{2}{3}\mu & -\frac{2}{3}\mu & \frac{4}{3}\mu & 0 & 0 & 0 \\ 0 & 0 & 0 & \mu & 0 & 0 \\ 0 & 0 & 0 & 0 & \mu & 0 \\ 0 & 0 & 0 & 0 & 0 & \mu \end{bmatrix} + \alpha \begin{bmatrix} \kappa & \kappa & \kappa & 0 & 0 & 0 \\ \kappa & \kappa & \kappa & 0 & 0 & 0 \\ \kappa & \kappa & \kappa & 0 & 0 & 0 \\ 0 & 0 & 0 & 0 & 0 & 0 \\ 0 & 0 & 0 & 0 & 0 & 0 \\ 0 & 0 & 0 & 0 & 0 & 0 \end{bmatrix} = \begin{bmatrix} 2\mu & 0 & 0 & 0 & 0 & 0 \\ 0 & 2\mu & 0 & 0 & 0 & 0 \\ 0 & 0 & 2\mu & 0 & 0 & 0 \\ 0 & 0 & 0 & \mu & 0 & 0 \\ 0 & 0 & 0 & 0 & \mu & 0 \\ 0 & 0 & 0 & 0 & 0 & \mu \end{bmatrix}. \tag{8.11}$$

This clever manipulation expresses the constitutive split in terms of the Lame'–shear split instead of the bulk–shear split provides a path to stabilization for our generalized treatment. It turns out that even a very small split-shift provides element stability.

8.0.4 Stabilization, the Split-shift

The GSRI treatment is stabilized by increasing the rank of the fully integrated flexible component $\mathbf{D}_f$. This is done by shifting a small portion of $\mathbf{D}_r$ to $\mathbf{D}_f$.

First introduce $\alpha = 2\frac{\lambda_{min}}{\lambda_{max}}$

where λ_{min} and λ_{max} are the lowest and highest respective eigenvalues of the compliance matrix.

Now shifting is done by $\mathbf{D}_f \leftarrow \mathbf{D}_f + \alpha\mathbf{D}_r$. and $\mathbf{D}_r \leftarrow \mathbf{D}_r - \alpha\mathbf{D}_r$. This results in a $\mathbf{D}_f$ with full rank.

The B-bar treatment is made stable by changing the deviatoric projector to have a slightly smaller contribution from the rigid modes. This is accomplished by removing a small portion of the rigid modes and giving it to the "deviatoric" projector $\mathbf{I}_d$.

Table 8.5: Stability results for various treatments of stabilized single fiber single element blocks.

	$n_m = 0$	$n_m = 1$	$n_m = 2$	$n_m = 3$
H8	Stable $\forall\theta$	Stable $\forall\theta$	Stable $\forall\theta$	Stable $\forall\theta$
H27	Stable $\forall\theta$	Stable $\forall\theta$	Stable $\forall\theta$	Stable $\forall\theta$

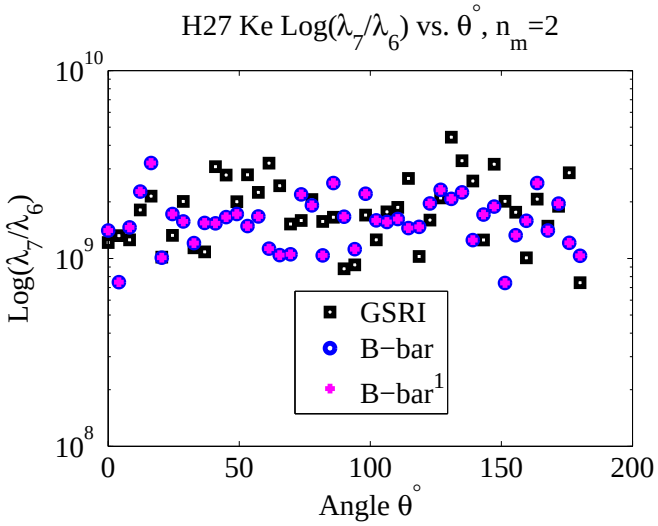

Figure 8.4: Stabilized H27, 2 modes, 2 fibers.

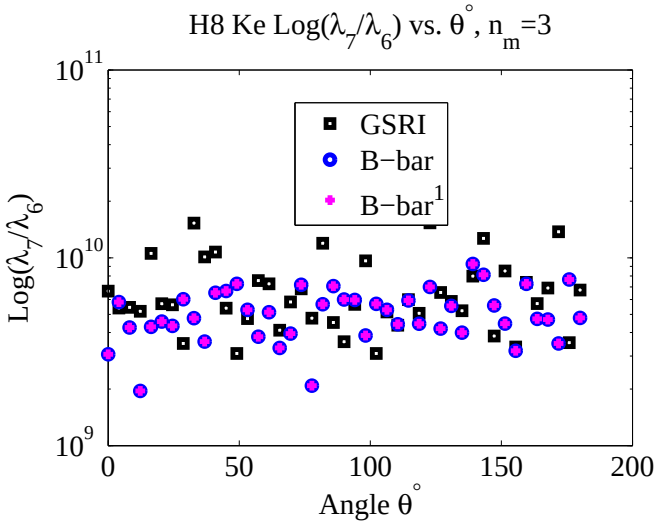

Figure 8.5: Stabilized H8, 2 modes, 3 fibers.

Table 8.6: Stability results for various treatments of stabilized dual fiber single element blocks.

	$n_m = 0$	$n_m = 1$	$n_m = 2$	$n_m = 3$
H8	Stable $\forall\theta$	Stable $\forall\theta$	Stable $\forall\theta$	Stable $\forall\theta$
H27	Stable $\forall\theta$	Stable $\forall\theta$	Stable $\forall\theta$	Stable $\forall\theta$

This level of stabilization does not provide a general remedy to the element distortion problem, but we will see that increasing the proportions of the split can ameliorate the effects

while still providing adequate convergence. Varying degrees of stabilization are tested in terms of displacement convergence, strain energy convergence, and alleviation of element distortions in the example models. Six different levels of stabilization are compared.

Stabilization is considered by varying degrees of split shifting:

1) No stabilization: $\alpha_0 = 0$;

2) Minimal stabilization: $\alpha_1 = 2\frac{\lambda_{min}}{\lambda_{max}}$;

3) Increased by factor of 50: $\alpha_{50} = 50(2\frac{\lambda_{min}}{\lambda_{max}})$;

4)Increased by factor of 100: $\alpha_{100} = 100(2\frac{\lambda_{min}}{\lambda_{max}})$;

5) Increased by factor of 200: $\alpha_{200} = 200(2\frac{\lambda_{min}}{\lambda_{max}})$;

and 6) Increased by a scaling function of λ: $\alpha_f = f(\lambda) = \sqrt{\frac{\sum_{i=6-n_M+1}^{6}\lambda_i}{\sum_{i=1}^{6-n_m}\lambda_i}}\frac{\lambda_{min}}{\lambda_{max}}$.

8.0.5 Stabilized Homogeneous Bi-Rigid Plate

In Figure 8.6 we see that increasing the amount of stabilization that is applied in the split-shift effectively eliminates inter-element distortions. However, there is a cost. The convergence observed in Figures 8.7 shows that with minimal stabilization the solutions are at their most accurate, but once enough stabilization is applied to eliminate the inter-element distortions the accuracy suffers.

As seen in figure 8.7, the GSRI convergence results suggest that increased stablilization affects, and can even improve solution accuracy.

8.0.6 Stabilized Discretely Inhomogeneous Plate

For the case of abruptly discrete inhomogeneities, more stabilization is needed to control the inter-element distortions. In Figure 8.9 we see that increasing the amount of stabilization that is applied in the split-shift does control inter-element distortions. In this case, however, they aren't completely eliminated. The refinement behavior seen in Figure 8.10 again suggests that with minimal stabilization the solution is at its most accurate, and that once enough stabi-

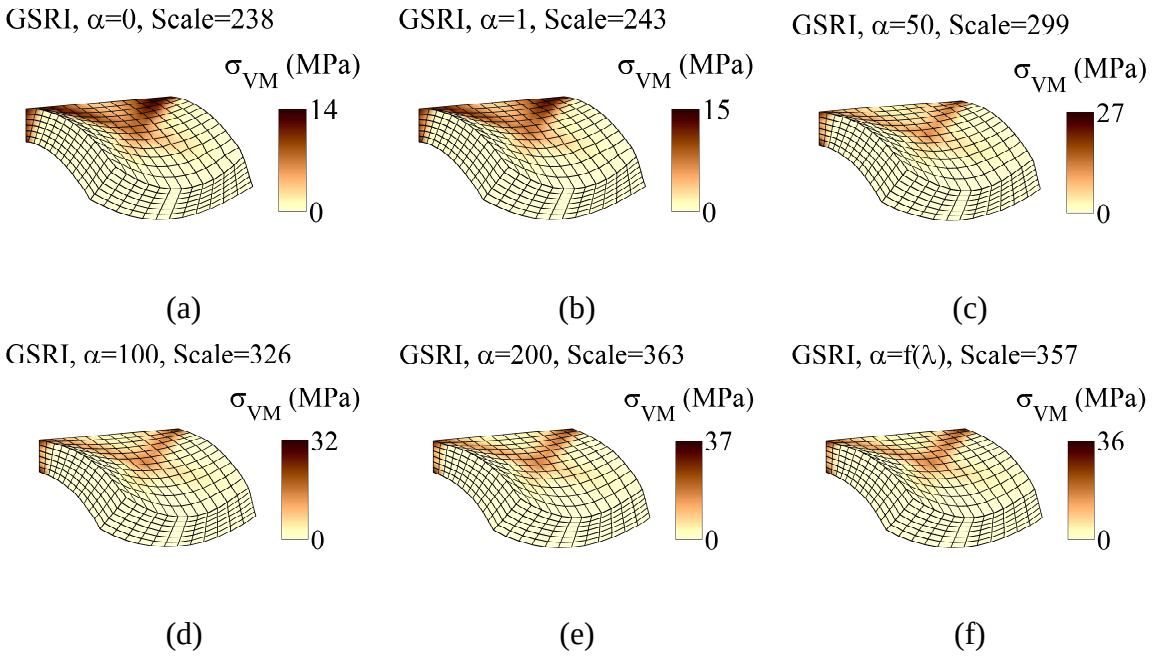

Figure 8.6: Homogeneous bi-rigid plate model with GSRI treated meshes having varying degrees of stabilization: (a) α_0; (b) α_1; (c) α_{50}; (d) α_{100}; (e) α_{200}; and (f)$\alpha_f = f(\lambda)$.

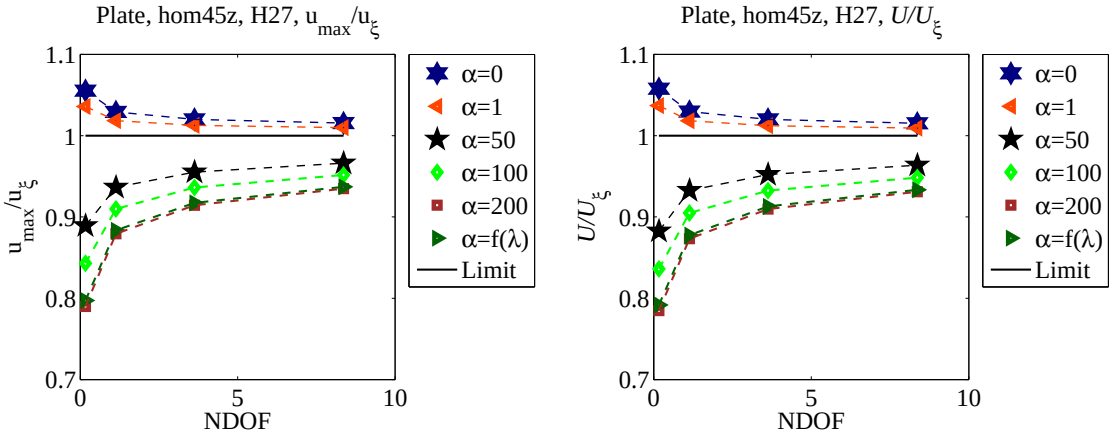

Figure 8.7: Varied stabilization for the homogeneous bi-rigid plate: (a) H27 Displacement refinement; and (b) H27 Strain energy error (log-log).

lization is applied to eliminate the inter-element distortions, the accuracy has suffered considerably and as before the solutions are starting to lock.

Observing that shifting part of a treated mode to be handled along with the untreated (flexible) component is tantamount to choosing the degree to which each mode is treated leads to novel use of this method. It is clear in figures 8.7 and 8.10 that stabilization by shifting the rigid component can affect the convergence in a very controlled manner. In those examples,

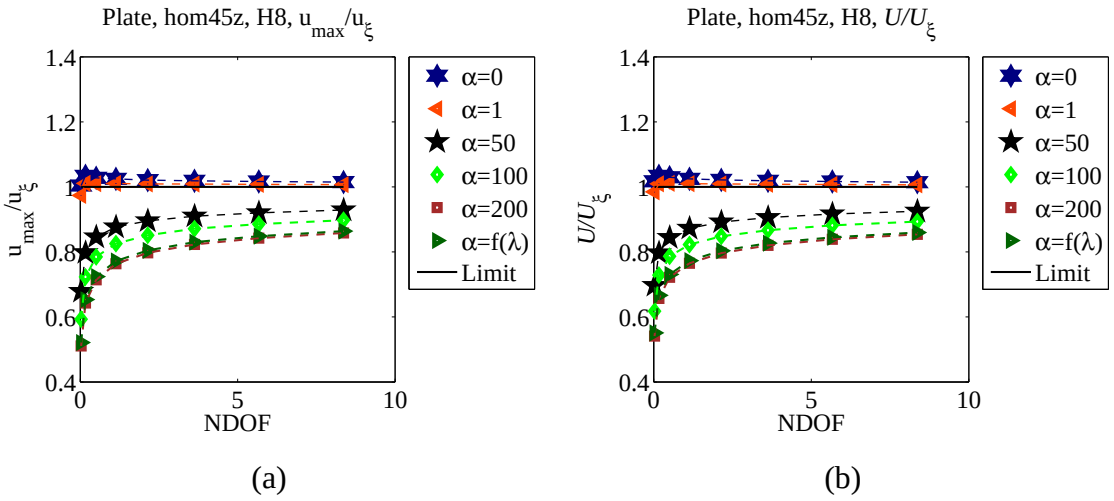

Figure 8.8: Varied stabilization for the homogeneous bi-rigid plate: (a) H8 Displacement refinement; and (b) H8 Strain energy error (log-log).

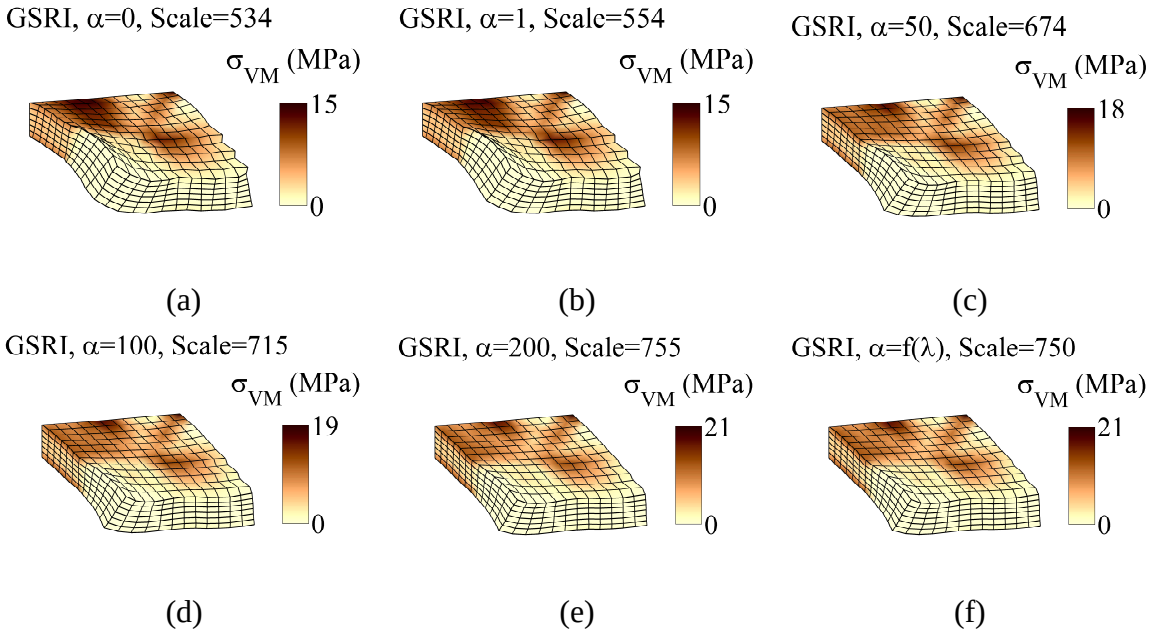

Figure 8.9: Discretely inhomogeneous bi-rigid plate model with GSRI treated meshes having varying degrees of stabilization: (a) α_0; (b) α_1; (c) α_{50}; (d) α_{100}; (e) α_{200}; and (f)$\alpha_f = f(\lambda)$.

zero shifting led to displacement solutions that converge from above and as the shifted component is increased the convergence happens from below. The obvious question is whether at some level of stabilization does convergence happen from neither below nor above? In other words, is there a “sweet-spot” in the split-shift where even very coarse meshes have high accuracy?

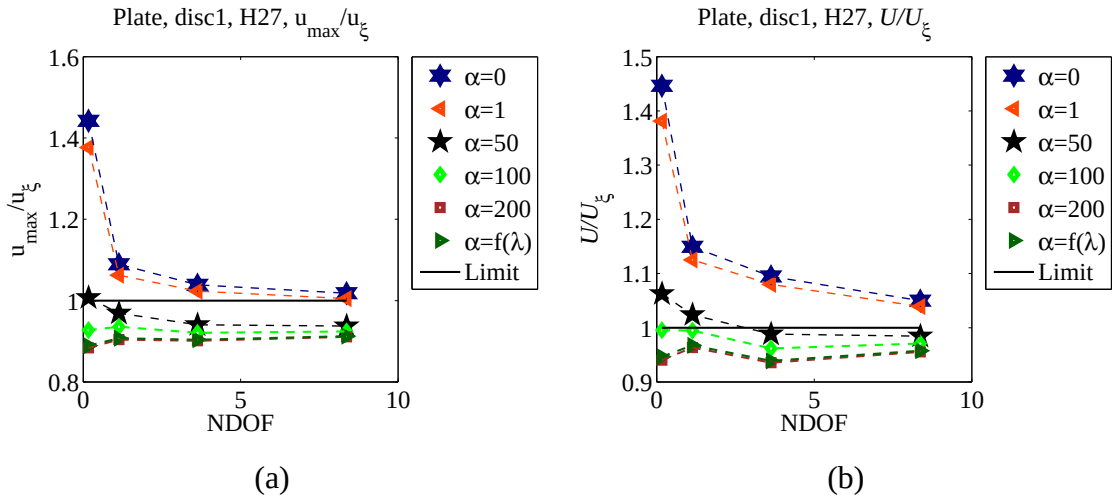

(a) (b)

Figure 8.10: Varied stabilization for the discretely inhomogeneous bi-rigid plate: (a) H27 Displacement refinement; and (b) H27 Strain energy error (log-log).

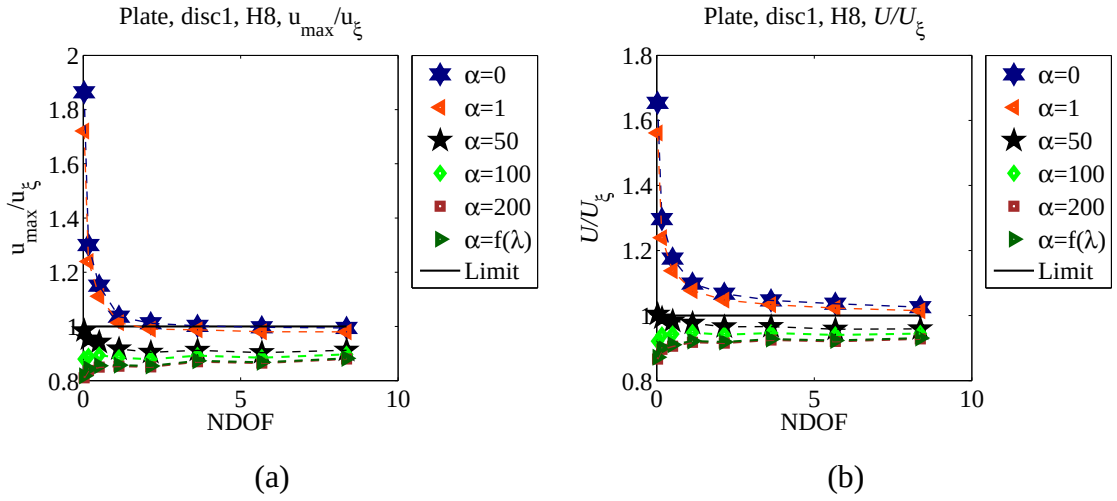

(a) (b)

Figure 8.11: Varied stabilization for the discretely inhomogeneous bi-rigid plate: (a) H8 Displacement refinement; and (b) H8 Strain energy error (log-log).

Chapter 9

Variable 3-Field Treatment

9.1 Variable 3-Field Treatment ("B-bar" without the B-bar)

In attempting to find the “sweet-spot” in the split-shift where even very coarse meshes have high accuracy, a few different methods of variable treatment were explored. In each case all the compliance modes are treated in the 3-field formulation but some small part is shifted back to the flexible terms for stabilization. Choosing to treat all the modes in a controlled, variable, manner can lead to surprising performance advantages even for materials that do not have locking modes.

First, a method of uniformly variable treatment is introduced. The amount of all the modes passed in the split-shift is the same. Then, a method allowing the magnitudes of the normalized eigenvalues to determine how much of each respective mode is passed in the split-shift follows.

The shift can be scaled in the eigenvalues of the compliance or in the eigenvectors. While the latter may have some slight performance advantages for certain examples tested, the former is preferred because the process is more comprehensible when the eigenvectors are used as mere modes or directions with consistently normalized magnitudes. The eigenvector scaling is only introduced as an interesting alternative that may have implications further along.

The presented methods attain some very accurate results for a minimal computational

expenditure. Unfortunately a clean expression of the combined strain displacement operator B-bar is lost in the process. This makes the stress calculation slightly more complicated.

9.1.1 Uniform variable treatment, Eigenvalue Scaling

Decompose the compliance such that

$$\mathbf{D}^{-1} = \frac{1}{3}\sum_{i=1}^{6} \gamma_i v_i v_i^T \ , \tag{9.1}$$

and $\gamma_1 < \gamma_2 < ... < \gamma_6$.

Take $\mathbf{M} = [v_1, v_2, \ldots, v_6]$ to be the six-by-six matrix whose columns are the scaled eigenvectors of $\mathbf{D}^{-1}$, (scaled for backward compatibility with referenced literature).

Introduce the uniform scaling matrix

$$\mathbf{S} = \alpha \mathbf{I} \tag{9.2}$$

where $\alpha = a\gamma_1/\gamma_6$ is a stabilization coefficient, and $0 \leq a < 1$.

Now, let

$$\Gamma = (\mathbf{I} - \mathbf{S}) = (1-\alpha)\mathbf{I}, \tag{9.3}$$

such that $a \to 0$ for no treatment, $a \to \gamma_6/\gamma_1$ for full–yet unstable–treatment, and values of a between 0 and $\to \gamma_6/\gamma_1$ indicates the amount of uniform treatment for all modes.

First, introduce the adjusted stiff effective moduli (eigenvalue scaling):

$$\mathbf{K}_r = \frac{1}{9}\mathbf{M}^T\mathbf{D}\mathbf{M}. \tag{9.4}$$

Now apply the scaling:

$$\tilde{\mathbf{K}}_r = \frac{1}{9}\Gamma\mathbf{K}_r\Gamma = \frac{1}{9}\Gamma\mathbf{M}^T\mathbf{D}\mathbf{M}\Gamma. \tag{9.5}$$

Define $\mathbf{D}_r = \mathbf{M}\tilde{\mathbf{K}}_r\mathbf{M}^T$, noting that the definition of $\tilde{\mathbf{K}}_r$ gives

$$\mathbf{D}_r = \frac{1}{9}\mathbf{M}\Gamma\mathbf{M}^T\mathbf{D}\mathbf{M}\Gamma\mathbf{M}^T = (1-\alpha)^2\mathbf{D}. \tag{9.6}$$

Now define the flexible component of the elasticity matrix

$$\mathbf{D}_f = \mathbf{D} - \mathbf{D}_r = (2\alpha - \alpha^2)\mathbf{D}, \tag{9.7}$$

where $\mathbf{D}_f \to \mathbf{D}$ as $\Gamma \to \mathbf{0}$, and $\mathbf{D}_f \to \mathbf{0}$ as $\Gamma \to \mathbf{I}$. Otherwise stated, $\mathbf{D}_f \to \mathbf{D}$ as $\alpha \to 1$, and $\mathbf{D}_f \to \mathbf{0}$ as $\alpha \to 0$.

Introduce the effective constrained strain variable:

$$\varepsilon_r = \mathbf{M}^T \varepsilon\,, \tag{9.8}$$

and the effective constrained stress variable:

$$p = \tilde{\mathbf{K}}_r \varepsilon_r. \tag{9.9}$$

Split stress contributions according to

$$\sigma_f = \mathbf{D}_f \varepsilon\,, \tag{9.10}$$

and

$$\sigma = \sigma_f + \mathbf{M}p\,. \tag{9.11}$$

$$\int_\Omega \delta\varepsilon^T \left(\sigma_f + \mathbf{M}p\right) \mathrm{d}\Omega - \int_\Omega \delta u^T b \,\mathrm{d}\Omega - \int_{\Gamma_t} \delta u^T t \,\mathrm{d}\Gamma = 0\,, \tag{9.12}$$

$$\int_\Omega \delta u^T \mathbf{D}_f \mathbf{B} u \,\mathrm{d}\Omega + \int_\Omega \delta p^T \mathbf{M} p \,\mathrm{d}\Omega - \int_\Omega \delta u^T b \,\mathrm{d}\Omega - \int_{\Gamma_t} \delta u^T t \,\mathrm{d}\Gamma = 0\,. \tag{9.13}$$

$$\int_\Omega \delta p \left(\mathbf{M}^T \mathbf{B} u - \varepsilon_r\right) \mathrm{d}\Omega = 0\,, \tag{9.14}$$

$$\int_\Omega \delta\varepsilon_r \left(\tilde{\mathbf{K}}_r \varepsilon_r - p\right) \mathrm{d}\Omega = 0\,. \tag{9.15}$$

$$u \approx \mathbf{N}_u \tilde{u}, \quad p \approx \mathbf{N}_p \tilde{p}, \quad \varepsilon_r \approx \mathbf{N}_r \tilde{\varepsilon}_r\,. \tag{9.16}$$

$$\begin{bmatrix} \mathbf{A} & \mathbf{C} & \mathbf{0} \\ \mathbf{C}^T & \mathbf{0} & -\mathbf{E} \\ \mathbf{0} & -\mathbf{E}^T & \mathbf{H} \end{bmatrix} \begin{Bmatrix} \tilde{u} \\ \tilde{p} \\ \tilde{\varepsilon}_r \end{Bmatrix} = \begin{Bmatrix} f_1 \\ 0 \\ 0 \end{Bmatrix}. \tag{9.17}$$

$$\begin{aligned} \mathbf{A} &= \int_\Omega \mathbf{B}^T \mathbf{D}_f \mathbf{B}\, \mathrm{d}\Omega, \quad \mathbf{E} = \int_\Omega \mathbf{N}_r^T \mathbf{N}_p\, \mathrm{d}\Omega, \\ \mathbf{H} &= \int_\Omega \mathbf{N}_r^T \tilde{\mathbf{K}}_r \mathbf{N}_r\, \mathrm{d}\Omega, \quad \mathbf{C} = \int_\Omega \mathbf{B}^T \mathbf{M} \mathbf{N}_p\, \mathrm{d}\Omega\,. \end{aligned} \tag{9.18}$$

$$\tilde{\varepsilon}_r = \mathbf{E}^{-1} \mathbf{C}^T \tilde{u} = \mathbf{W} \tilde{u}\,, \tag{9.19}$$

$$\tilde{p} = \mathbf{E}^{-T} \mathbf{H} \tilde{\varepsilon}_r = \mathbf{E}^{-T} \mathbf{H} \mathbf{W} \tilde{u}\,. \tag{9.20}$$

$$\bar{\mathbf{A}} \tilde{u} = f_1\,, \tag{9.21}$$

, where

$$\bar{\mathbf{A}} = \mathbf{A} + \mathbf{W}^T \mathbf{H} \mathbf{W}\,, \tag{9.22}$$

$$\bar{\mathbf{A}} = \int_\Omega \mathbf{B}^T \mathbf{D}_f \mathbf{B}\, \mathrm{d}\Omega + \int_\Omega \mathbf{W}^T \mathbf{N}_r^T \tilde{\mathbf{K}}_r \mathbf{N}_r \mathbf{W}\, \mathrm{d}\Omega\,, \tag{9.23}$$

or

$$\bar{\mathbf{A}} = \int_\Omega \mathbf{B}^T \mathbf{D}_f \mathbf{B}\, \mathrm{d}\Omega + \int_\Omega \mathbf{W}^T \mathbf{N}_r^T \frac{1}{3} \Gamma \mathbf{M}^T \mathbf{D} \mathbf{M} \Gamma \frac{1}{3} \mathbf{N}_r \mathbf{W}\, \mathrm{d}\Omega\,. \tag{9.24}$$

Defining

$$\mathbf{B}_r = \mathbf{M} \Gamma \frac{1}{3} \mathbf{N}_r \mathbf{W}, \tag{9.25}$$

leads to the stiffness expression

$$\bar{\mathbf{A}} = \int_\Omega \mathbf{B}^T \mathbf{D}_f \mathbf{B}\, \mathrm{d}\Omega + \int_\Omega \mathbf{B}_r^T \mathbf{D} \mathbf{B}_r\, \mathrm{d}\Omega\,. \tag{9.26}$$

The stress and strain calculations require computation of the flexible component projector $\mathbf{I}_f$, such that $\mathbf{D}_f = \mathbf{I}_f \mathbf{D} \mathbf{I}_f$ and the strains can be decomposed $\varepsilon = \varepsilon_r + \varepsilon_f = \mathbf{B}_r \tilde{u} + \mathbf{B}_f \tilde{u}$ where

The projector $\mathbf{I}_f$ can, for uniform scaling, be defined

$$\mathbf{I}_f = \sqrt{\mathbf{I} - \Gamma^2}, \tag{9.27}$$

which can be substituted with the scalar expression

$$I_f = \sqrt{2\alpha - \alpha^2}. \tag{9.28}$$

The flexible component of the strain displacement relation can be expressed

$$\mathbf{B}_f = \mathbf{I}_f \mathbf{B} = I_f \mathbf{B}. \tag{9.29}$$

Now, with $\mathbf{B}_f = \mathbf{I}_f \mathbf{B}$, element strains can be computed according to

$$\varepsilon = \mathbf{B}_r \tilde{u} + \mathbf{B}_f \tilde{u}, \tag{9.30}$$

and element stresses can be computed according to

$$\sigma = \mathbf{D} \varepsilon. \tag{9.31}$$

Uniform treatment results–motivation beam example

This problem was introduced as a motivation example for the single mode GSRI and B-bar methods presented in Chapter 6. The H8-Bbar element were outperformed by the C3D8IH elements in ABAQUS for the isotropic material of Figure 9.1(b). Now, with uniform variable treatment of all six modes with the scaled λ split, the presented H8-3F6MU element edges out the C3D8IH for the aforementioned isotropic material and it is the most accurate of all the elements tested for the anisotropic fiber orientations of Figures 9.1(c) and (d). The notion that this element could perform so well even for an isotropic material is a somewhat surprising and fortuitous result. These solutions were obtained using and evenhanded treatment for all materials with $a = 1$ and the inverse condition number based $\alpha = a\gamma_1/\gamma_6$. The reference , or limit, values are taken from the Richardson's extrapolation of the H8-Bbar solutions.

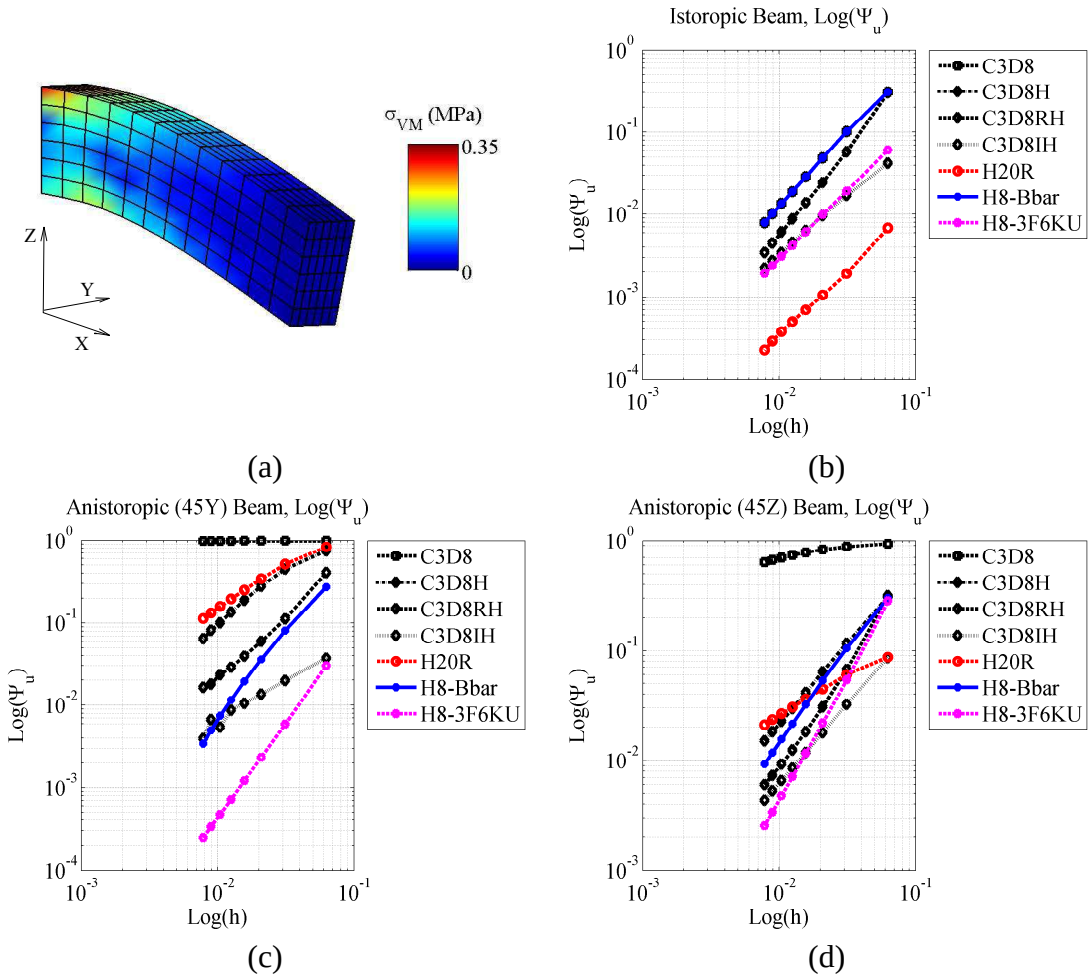

Figure 9.1: Uniform λ scaling, displacement error Ψ_δ of cantilever beam subject to shear load at the free end. (a) Uniform mesh with 125 nodes; element aspect ratio of $1:4.5$. In (b), (c), and (d) we show the estimated true error of the maximum deflection. (b) Isotropic material. (c) Anisotropic material, stiff fiber aligned with $[\sqrt{2}/2, -\sqrt{2}/2, 0]$. (d) Anisotropic material, stiff fiber aligned with $[\sqrt{2}/2, 0, -\sqrt{2}/2]$. Key: C3D8 – linear hexahedron, C3D8H – linear hybrid hexahedron with uniform pressure, C3D8I – hexahedron with incompatible modes, C3D20R – the uniformly reduced integration quadratic serendipity hexahedron, H8-Bbar-ISO – B-bar Q1/Q0 hexahedron, H8-Bbar – linear hexahedron with present B-bar formulation, and H8-3F6MU – linear hexahedron with uniformly scaled presented 3-field.

Homogeneous Angle 45-z plate

Here, the uniform λ scaled H8-3F6MU is performing very nicely. The H8-Bbar has better accuracy with the coarsest meshes but the H8-3F6MU quickly catches up as refinement advances.

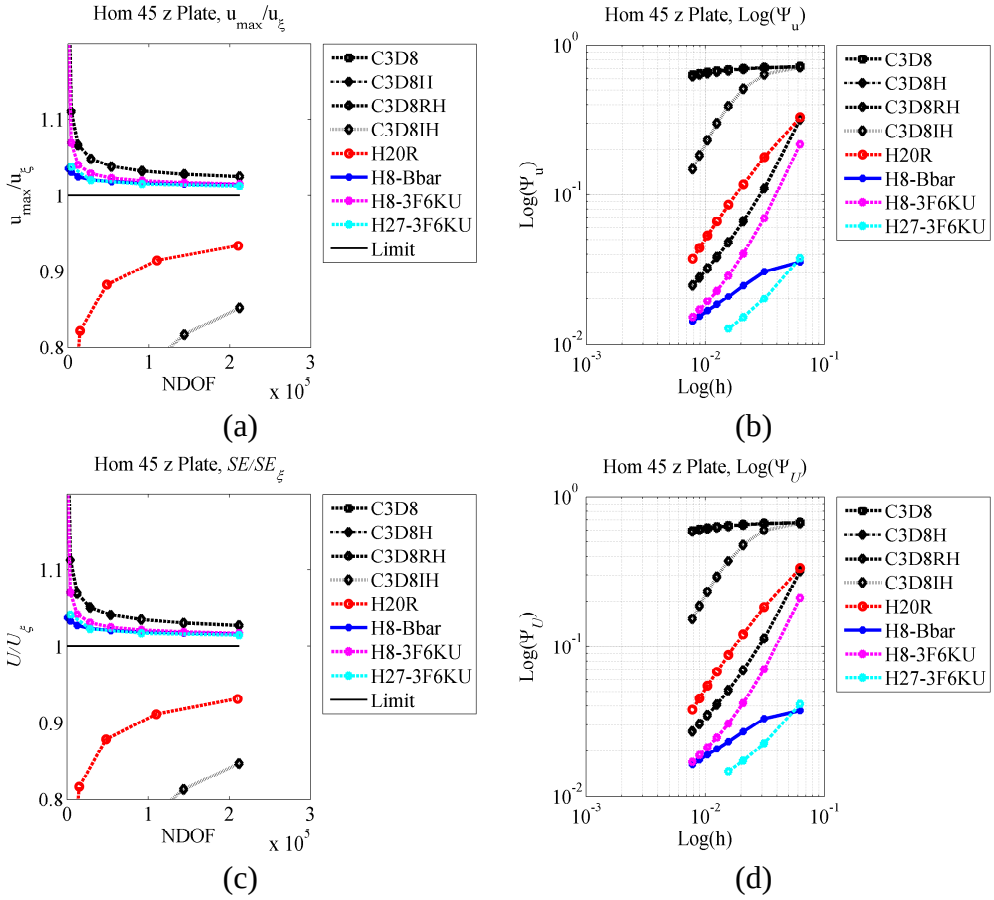

Figure 9.2: Uniform λ scaling, results for hom45z plate: (a) Displacement, (b) Displacement error, (c) Strain Energy, and (d) Strain energy error.

Inhomogeneous 4-region Plate

This example was previously introduced to showcase the performance of the two-mode GSRI and B-bar treatments. Here again, the performance is noteworthy only slightly out-matched by the H8-Bbar elements. These results are obtained without any "tweaking" of the stabilization factor and without any a priori knowledge of the number of stiff modes exhibited by the material, making this an good candidate for a stable default treatment.

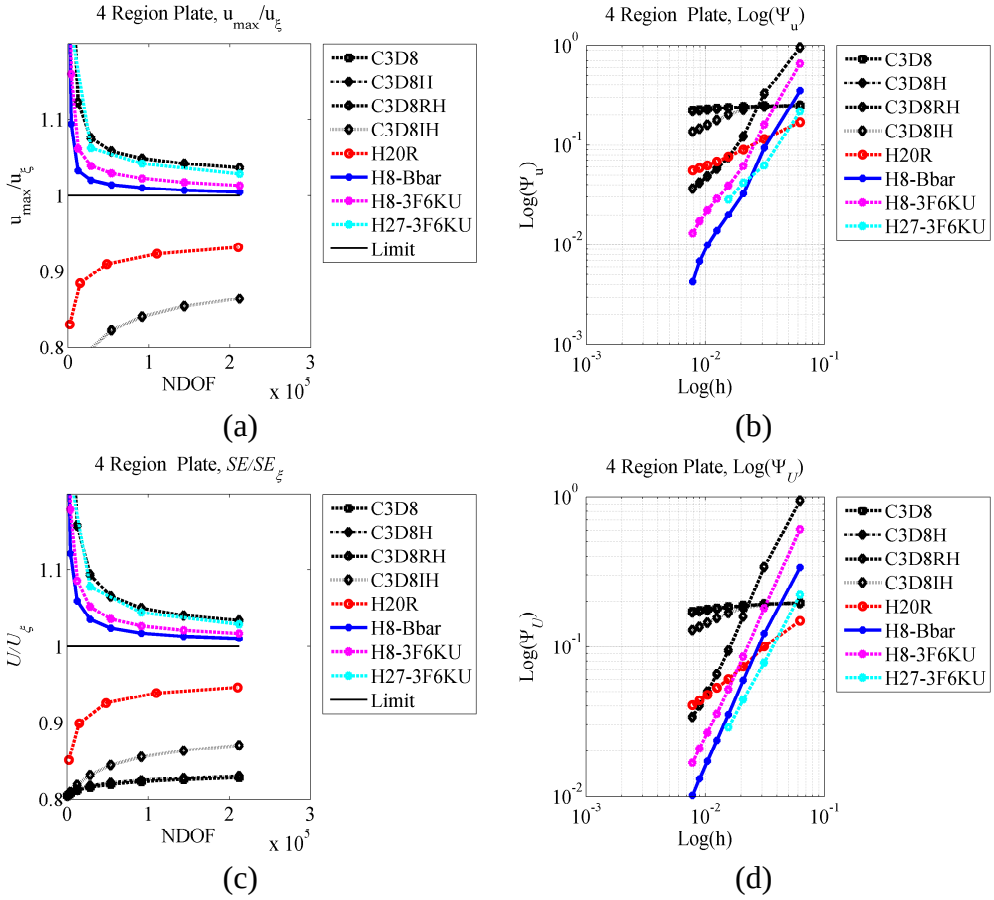

Figure 9.3: Uniform λ scaling, results for 4-region plate: (a) Displacement, (b) Displacement error, (c) Strain Energy, and (d) Strain energy error.

9.1.2 Variable Spectral Eigenvalue Scaling

As with uniform scaling, start by decomposing the compliance matrix decomposition and take $\mathbf{M} = [v_1, v_2, \ldots, v_6]$ to be the six-by-six matrix whose columns are the scaled eigenvectors of $\mathbf{D}^{-1}$.

This time, define the stabilization matrix $\mathbf{S}$ such that

$$\mathbf{S} = \alpha \begin{bmatrix} \gamma_1/\gamma_6 & 0 & 0 & 0 & 0 & 0 \\ 0 & \gamma_2/\gamma_6 & 0 & 0 & 0 & 0 \\ 0 & 0 & \gamma_3/\gamma_6 & 0 & 0 & 0 \\ 0 & 0 & 0 & \gamma_4/\gamma_6 & 0 & 0 \\ 0 & 0 & 0 & 0 & \gamma_5/\gamma_6 & 0 \\ 0 & 0 & 0 & 0 & 0 & \gamma_6/\gamma_6 \end{bmatrix} \tag{9.32}$$

where α is a stabilization coefficient, with $0 \leq \alpha < 1$. This choice of stabilization matrix $\mathbf{S}$ naturally separates the correct portion of the respective modes applying greater treatment to the most stiff components.

Now, proceed as with the previous, uniform scaling, formulation with $\Gamma = (\mathbf{I} - \mathbf{S})$, Introduce the adjusted stiff effective moduli apply the scaling. Define $\mathbf{D}_r = \mathbf{M}\tilde{\mathbf{K}}_r\mathbf{M}^T$, noting that the definition of $\tilde{\mathbf{K}}_r$ gives $\mathbf{D}_r = \frac{1}{9}\mathbf{M}\Gamma\mathbf{M}^T\mathbf{D}\mathbf{M}\Gamma\mathbf{M}^T$.

Now define the flexible component of the elasticity matrix $\mathbf{D}_f = \mathbf{D} - \mathbf{D}_r$, where $\mathbf{D}_f \to \mathbf{0}$ as $\alpha \to 0$.

Introduce the effective constrained strain variable $\varepsilon_r = \mathbf{M}^T\varepsilon$, and the effective constrained stress variable: $p = \tilde{\mathbf{K}}_r\varepsilon_r$.

Split stress contributions accordingly: $\sigma_f = \mathbf{D}_f\varepsilon$, and $\sigma = \sigma_f + \mathbf{M}p$.

The solution proceeds as with uniform scaling eventually defining $\mathbf{B}_r = \mathbf{M}\Gamma\frac{1}{3}\mathbf{N}_r\mathbf{W}$, which leads to the stiffness expression

$$\bar{\mathbf{A}} = \int_\Omega \mathbf{B}^T\mathbf{D}_f\mathbf{B}\,\mathrm{d}\Omega + \int_\Omega \mathbf{B}_r^T\mathbf{D}\mathbf{B}_r\,\mathrm{d}\Omega\,. \tag{9.33}$$

As before, the stress and strain calculations require computation of the flexible component projector $\mathbf{I}_f$, such that $\mathbf{D}_f = \mathbf{I}_f\mathbf{D}\mathbf{I}_f$ and the strains can be decomposed $\varepsilon = \varepsilon_r + \varepsilon_f = \mathbf{B}_r\tilde{u} + \mathbf{B}_f\tilde{u}$ where $\mathbf{B}_f = \mathbf{I}_f\mathbf{B}$.

Although the expression of the uniform scaling procedure is a good first approximation, the projector $\mathbf{I}_f$ may need to be solved by iteration. First define

$$\mathbf{I}_f^0 = \sqrt{\mathbf{I} - \Gamma^2}, \tag{9.34}$$

which provides a symmetric initial estimation.

Now define an error *err*, tolerance tol, and an iteration limit $ilim$ and continuously update

$$\mathbf{I}_f^{i+1} = \frac{1}{4}\left[(\mathbf{I}_f\mathbf{D})^{-1}\mathbf{D}_f\right] + \frac{1}{4}\left[(\mathbf{I}_f\mathbf{D})^{-1}\mathbf{D}_f\right]^T + \frac{1}{2}\mathbf{I}_f^i \tag{9.35}$$

until convergence is achieved according to

$$err = ||\mathbf{D}f - \mathbf{I}_f^{i+1}\mathbf{D}\mathbf{I}_f^{i+1}|| < tol\,. \tag{9.36}$$

Here the matrix norm $||\mathbf{X}||$ is the largest singular value of $\mathbf{X}$.

Convergence is fast due to the small system size, and this only needs to be done once for each material.

Now, with $\mathbf{B}_f = \mathbf{I}_f\mathbf{B}$, element strains can be computed according to

$$\varepsilon = \mathbf{B}_r\tilde{u} + \mathbf{B}_f\tilde{u}, \tag{9.37}$$

and element stresses can be computed according to

$$\sigma = \mathbf{D}\varepsilon. \tag{9.38}$$

Spectrally Scaled Beam Example

This time, the proposed treatment clearly outperforms the incompatible modes C3D8IH even for the isotropic material of Figure 9.4(a). The performance of the H8-F6MS is particularly good for the fiber orientation of Figure 9.4(d) exhibiting the highest accuracy and matching the convergence rates of the other top performers. These results were obtained using and evenhanded treatment for all materials with $\alpha = 0.23$. The reference , or limit, values are taken from the Richardson's extrapolation of the H8-Bbar solutions.

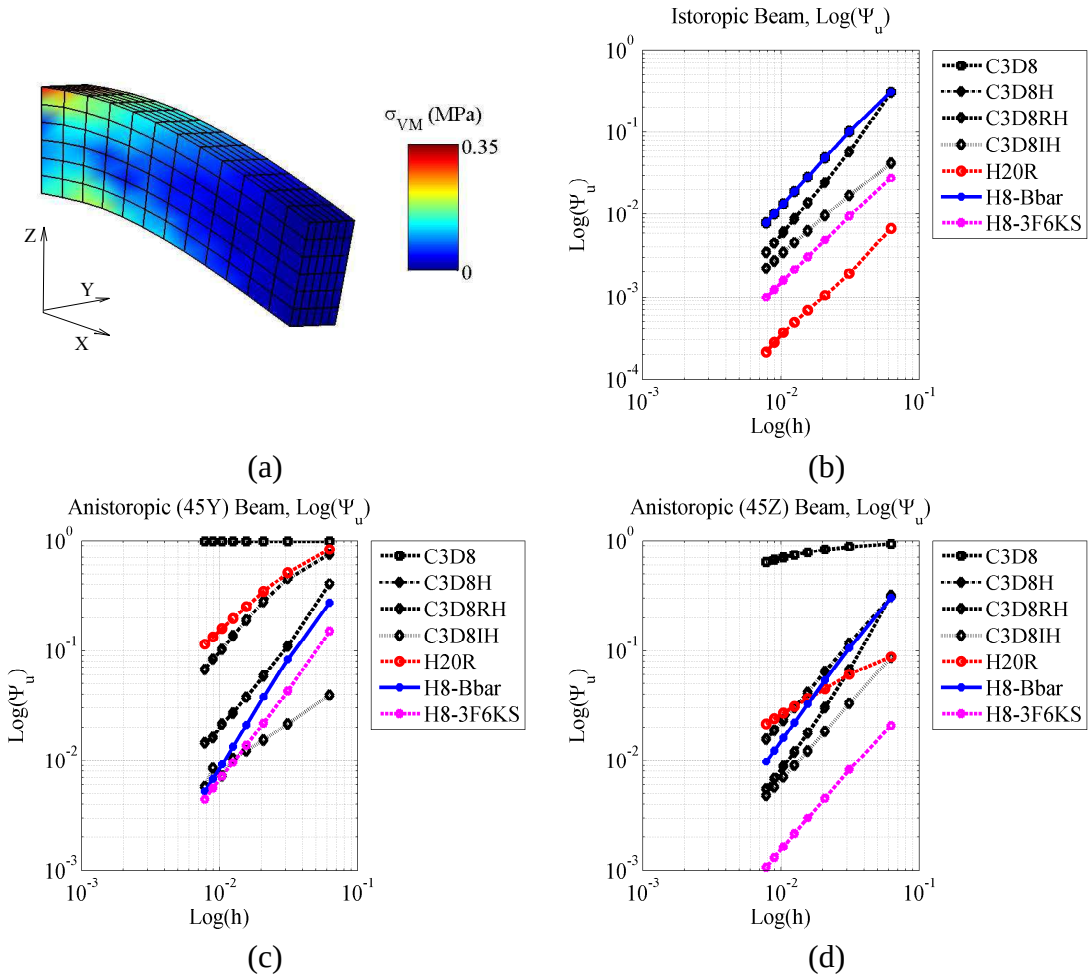

Figure 9.4: Spectral λ scaling, displacement error Ψ_δ of cantilever beam subject to shear load at the free end. (a) Uniform mesh with 125 nodes; element aspect ratio of $1:4.5$. In (b), (c), and (d) we show the estimated true error of the maximum deflection. (b) Isotropic material. (c) Anisotropic material, stiff fiber aligned with $[\sqrt{2}/2, -\sqrt{2}/2, 0]$. (d) Anisotropic material, stiff fiber aligned with $[\sqrt{2}/2, 0, -\sqrt{2}/2]$. Key: C3D8 – linear hexahedron, C3D8H – linear hybrid hexahedron with uniform pressure, C3D8I – hexahedron with incompatible modes, C3D20R – the uniformly reduced integration quadratic serendipity hexahedron, H8-Bbar-ISO – B-bar Q1/Q0 hexahedron, H8-Bbar – linear hexahedron with present B-bar formulation, and H8-3F6MS – linear hexahedron with spectrally scaled presented 3-field.

Homogeneous Angle 45-z Plate

The spectral λ scaling of the H8-3FMS produces very nice results on this homogeneous plate example with dual stiff fibers. None of the other elements match it in accuracy. Here again, the H27-3FMS quadratic version is also performing very well.

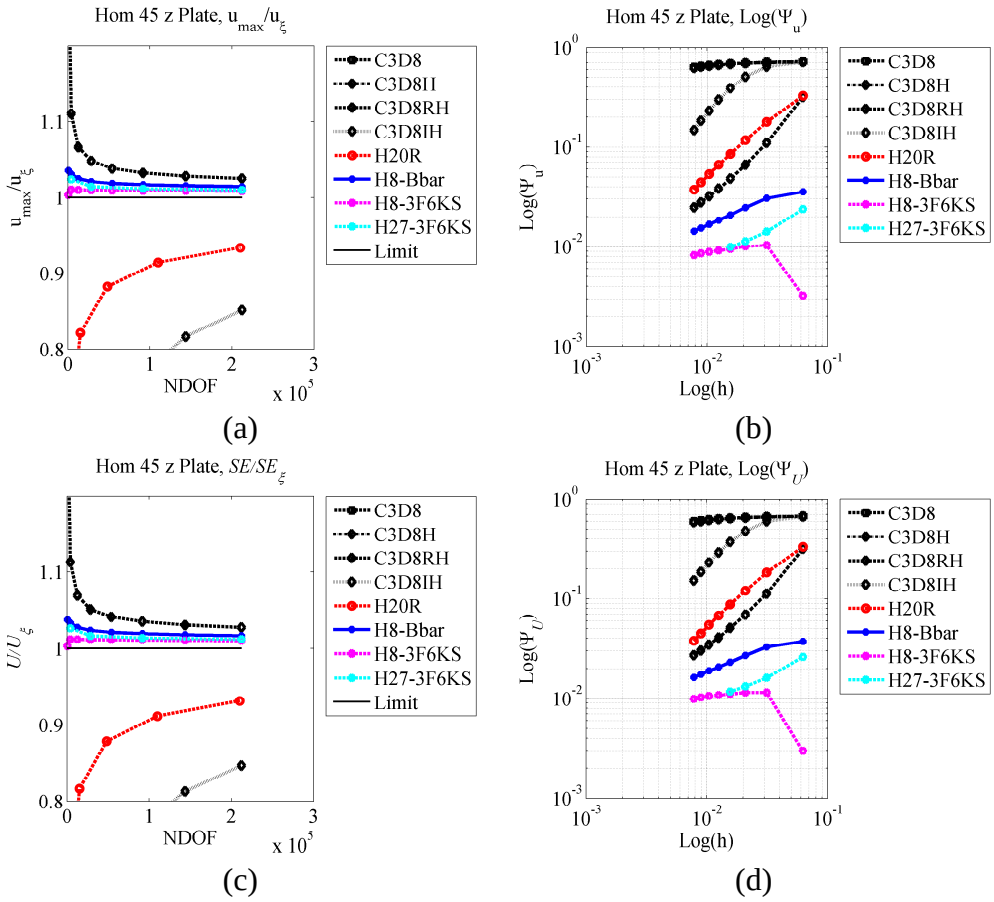

Figure 9.5: Spectral λ scaling, results for hom45z plate: (a) Displacement, (b) Displacement error, (c) Strain Energy, and (d) Strain energy error.

Inhomogeneous 4-Region Plate

For this abruptly inhomogeneous dual fiber example, the proposed elements appear to be performing about the same and show much better accuracy than the other elements tested. The convergence rates are also very high as seen in the slopes of Figures 9.6(b) and (d).

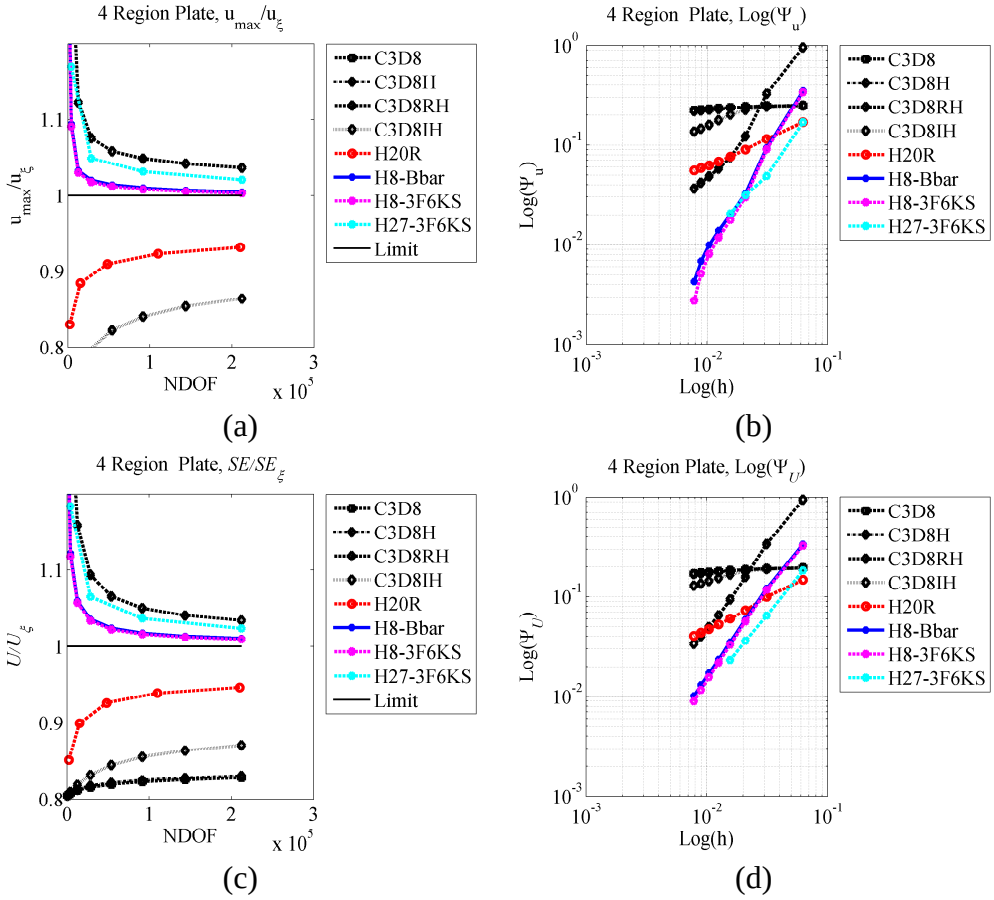

Figure 9.6: Spectral λ scaling, results for 4-region plate: (a) Displacement, (b) Displacement error, (c) Strain Energy, and (d) Strain energy error.

9.1.3 Uniform variable treatment, Eigenvector Scaling

$$\mathbf{D}^{-1} = \frac{1}{3}\sum_{i=1}^{6} \gamma_i v_i v_i^T \ , \tag{9.39}$$

Take $\mathbf{M} = [v_1, v_2, \ldots, v_6]$ to be the six-by-six matrix whose columns are the scaled eigenvectors of $\mathbf{D}^{-1}$, (scaled for backward compatibility with referenced literature).

Introduce the stabilization matrix

$$\mathbf{S} = \alpha \mathbf{I} \tag{9.40}$$

where α is a stabilization coefficient, $0 \leq \alpha < 1$.

Now, let

$$\Psi = \frac{1}{3}\mathbf{M}^T(\mathbf{I}-\mathbf{S})\mathbf{M} = \frac{(1-\alpha)}{3}\mathbf{M}^T\mathbf{M}, \tag{9.41}$$

and introduce the variable uniform scaling

$$\tilde{\mathbf{M}} = \mathbf{M}\Psi = (1-\alpha)\mathbf{M}, \tag{9.42}$$

such that $\alpha = 0$ for no treatment, $\alpha = 1$ for full treatment, and values of α between zero and one indicates the amount of uniform treatment for all modes. A useful choice of α uses the inverse condition number of $\mathbf{D}$ to automatically adjust the amount of treatment to the degree of directional stiffness inherent to the material. Diagonalize $\mathbf{D}$ such that $\mathbf{D} = \mathbf{V}\Lambda\mathbf{V}^T$, where the eigenvalues λ_i of $\mathbf{D}$ lie on the main diagonal of Λ having $\lambda_i < \lambda_{i+1}$.

Now choosing $\alpha = a\lambda_1/\lambda_6$ where $a|0 \leq a \leq 1$ will lead to a solution that naturally applies the greatest treatment to materials that require it.

Now apply the scaling, and introduce the adjusted stiff effective moduli (eigenvector scaling):

$$\mathbf{K}_r = \frac{1}{9}\tilde{\mathbf{M}}^T\mathbf{D}\tilde{\mathbf{M}}. \tag{9.43}$$

Define $\mathbf{D}_r = \tilde{\mathbf{M}}\tilde{\mathbf{K}}_r\tilde{\mathbf{M}}^T$, noting that the definition of $\tilde{\mathbf{K}}_r$ gives

$$\mathbf{D}_r = \frac{1}{9}\tilde{\mathbf{M}}\tilde{\mathbf{M}}^T\mathbf{D}\tilde{\mathbf{M}}\tilde{\mathbf{M}}^T = (\mathbf{I}-\mathbf{S})^2\mathbf{D}(\mathbf{I}-\mathbf{S})^2 = (1-\alpha)^4\mathbf{D}. \tag{9.44}$$

Now define the flexible component of the elasticity matrix

$$\mathbf{D}_f = \mathbf{D} - \mathbf{D}_r, \tag{9.45}$$

where $\mathbf{D}_f \to \mathbf{D}$ as $\Psi \to \mathbf{0}$, and $\mathbf{D}_f \to \mathbf{0}$ as $\Psi \to \mathbf{I}$. Otherwise stated, $\mathbf{D}_f \to \mathbf{D}$ as $\alpha \to 1$, and $\mathbf{D}_f \to \mathbf{0}$ as $\alpha \to 0$ (α scales $\mathbf{D}_f$).

Introduce the effective constrained strain variable

$$\varepsilon_r = \tilde{\mathbf{M}}^T\varepsilon\,, \tag{9.46}$$

and the effective constrained stress variable

$$p = \tilde{\mathbf{K}}_r\varepsilon_r. \tag{9.47}$$

Split stress contributions accordingly:

$$\sigma_f = \mathbf{D}_f \varepsilon \,, \tag{9.48}$$

and

$$\sigma = \sigma_f + \tilde{\mathbf{M}} p \,. \tag{9.49}$$

$$\int_\Omega \delta\varepsilon^T \left(\sigma_f + \tilde{\mathbf{M}} p\right) \mathrm{d}\Omega - \int_\Omega \delta u^T b \,\mathrm{d}\Omega - \int_{\Gamma_t} \delta u^T t \,\mathrm{d}\Gamma = 0 \,, \tag{9.50}$$

$$\int_\Omega \delta u^T \mathbf{D}_f \mathbf{B} u \,\mathrm{d}\Omega + \int_\Omega \delta p^T \tilde{\mathbf{M}} p \,\mathrm{d}\Omega - \int_\Omega \delta u^T b \,\mathrm{d}\Omega - \int_{\Gamma_t} \delta u^T t \,\mathrm{d}\Gamma = 0 \,. \tag{9.51}$$

$$\int_\Omega \delta p \left(\tilde{\mathbf{M}}^T \mathbf{B} u - \varepsilon_r\right) \mathrm{d}\Omega = 0 \,, \tag{9.52}$$

$$\int_\Omega \delta\varepsilon_r \left(\mathbf{K}_r \varepsilon_r - p\right) \mathrm{d}\Omega = 0 \,. \tag{9.53}$$

$$u \approx \mathbf{N}_u \tilde{u}, \quad p \approx \mathbf{N}_p \tilde{p}, \quad \varepsilon_r \approx \mathbf{N}_r \tilde{\varepsilon}_r \,. \tag{9.54}$$

$$\begin{bmatrix} \mathbf{A} & \mathbf{C} & \mathbf{0} \\ \mathbf{C}^T & \mathbf{0} & -\mathbf{E} \\ \mathbf{0} & -\mathbf{E}^T & \mathbf{H} \end{bmatrix} \begin{Bmatrix} \tilde{u} \\ \tilde{p} \\ \tilde{\varepsilon}_r \end{Bmatrix} = \begin{Bmatrix} f_1 \\ 0 \\ 0 \end{Bmatrix} . \tag{9.55}$$

$$\begin{aligned} \mathbf{A} &= \int_\Omega \mathbf{B}^T \mathbf{D}_f \mathbf{B} \,\mathrm{d}\Omega, \quad \mathbf{E} = \int_\Omega \mathbf{N}_r^T \mathbf{N}_p \,\mathrm{d}\Omega, \\ \mathbf{H} &= \int_\Omega \mathbf{N}_r^T \mathbf{K}_r \mathbf{N}_r \,\mathrm{d}\Omega, \quad \mathbf{C} = \int_\Omega \mathbf{B}^T \tilde{\mathbf{M}} \mathbf{N}_p \,\mathrm{d}\Omega \,. \end{aligned} \tag{9.56}$$

$$\tilde{\varepsilon}_r = \mathbf{E}^{-1} \mathbf{C}^T \tilde{u} = \mathbf{W} \tilde{u} \,, \tag{9.57}$$

$$\tilde{p} = \mathbf{E}^{-T} \mathbf{H} \tilde{\varepsilon}_r = \mathbf{E}^{-T} \mathbf{H} \mathbf{W} \tilde{u} \,. \tag{9.58}$$

$$\bar{\mathbf{A}}\tilde{u} = f_1\,, \tag{9.59}$$

, where

$$\bar{\mathbf{A}} = \mathbf{A} + \mathbf{W}^T\mathbf{H}\mathbf{W}\,, \tag{9.60}$$

$$\bar{\mathbf{A}} = \int_\Omega \mathbf{B}^T\mathbf{D}_f\mathbf{B}\,\mathrm{d}\Omega + \int_\Omega \mathbf{W}^T\mathbf{N}_r^T\mathbf{K}_r\mathbf{N}_r\mathbf{W}\,\mathrm{d}\Omega\,, \tag{9.61}$$

or

$$\bar{\mathbf{A}} = \int_\Omega \mathbf{B}^T\mathbf{D}_f\mathbf{B}\,\mathrm{d}\Omega + \int_\Omega \mathbf{W}^T\mathbf{N}_r^T\frac{1}{3}\tilde{\mathbf{M}}^T\mathbf{D}\tilde{\mathbf{M}}\frac{1}{3}\mathbf{N}_r\mathbf{W}\,\mathrm{d}\Omega\,. \tag{9.62}$$

Defining

$$\mathbf{B}_r = \tilde{\mathbf{M}}\frac{1}{3}\mathbf{N}_r\mathbf{W}, \tag{9.63}$$

leads to the stiffness expression

$$\bar{\mathbf{A}} = \int_\Omega \mathbf{B}^T\mathbf{D}_f\mathbf{B}\,\mathrm{d}\Omega + \int_\Omega \mathbf{B}_r^T\mathbf{D}\mathbf{B}_r\,\mathrm{d}\Omega\,. \tag{9.64}$$

The stress and strain calculations require computation of the flexible component projector $\mathbf{I}_f$, such that $\mathbf{D}_f = \mathbf{I}_f\mathbf{D}\mathbf{I}_f$ and the strains can be decomposed $\varepsilon = \varepsilon_r + \varepsilon_f = \mathbf{B}_r\tilde{u} + \mathbf{B}_f\tilde{u}$ where

$$\mathbf{B}_f = \mathbf{I}_f\mathbf{B}\,. \tag{9.65}$$

The projector $\mathbf{I}_f$ can, for uniform scaling, be defined

$$\mathbf{I}_f = \frac{1}{2}\left(\sqrt{\mathbf{I}-(\mathbf{I}-\mathbf{S})^4}\right) + \frac{1}{2}\left(\sqrt{\mathbf{I}-(\mathbf{I}-\mathbf{S})^4}\right)^T = \left(\sqrt{1-(1-\alpha)^4}\right)\mathbf{I}, \tag{9.66}$$

Now, with $\mathbf{B}_f = \mathbf{I}_f\mathbf{B}$, element strains can be computed according to

$$\varepsilon = \mathbf{B}_r\tilde{u} + \mathbf{B}_f\tilde{u}, \tag{9.67}$$

and element stresses can be computed according to

$$\sigma = \mathbf{D}\varepsilon. \tag{9.68}$$

Uniform treatment Beam example

Although it is a somewhat clumsy formulation, scaling of the eigenvectors produces some highly accurate solutions as demonstrated in Figure 9.7. There may be an advantage to implementing the split-shift in the eigenvectors. These results were obtained using and evenhanded treatment for all materials with $a = 0.4$ and the inverse condition number based $\alpha = a\lambda_1/\lambda_6$.

9.1.4 Variable Spectral Eigenvector Scaling

As with uniform eigenvector scaling, begin with the diagonalization of the compliance matrix taking $\mathbf{M} = [v_1, v_2, \ldots, v_6]$ to be the six-by-six matrix whose columns are the scaled eigenvectors of $\mathbf{D}^{-1}$. This time introduce the diagonal matrix of stabilization coefficients $\mathbf{S}$ based on the principle elastic moduli. Diagonalize $\mathbf{D}$ such that $\mathbf{D} = \mathbf{V}\Lambda\mathbf{V}^T$, where the eigenvalues λ_i of $\mathbf{D}$ lie on the main diagonal of Λ having $\lambda_i < \lambda_{i+1}$.

Now define the stabilization matrix $\mathbf{S}$ such that.

$$\mathbf{S} = \alpha \begin{bmatrix} \lambda_1/\lambda_6 & 0 & 0 & 0 & 0 & 0 \\ 0 & \lambda_2/\lambda_6 & 0 & 0 & 0 & 0 \\ 0 & 0 & \lambda_3/\lambda_6 & 0 & 0 & 0 \\ 0 & 0 & 0 & \lambda_4/\lambda_6 & 0 & 0 \\ 0 & 0 & 0 & 0 & \lambda_5/\lambda_6 & 0 \\ 0 & 0 & 0 & 0 & 0 & \lambda_6/\lambda_6 \end{bmatrix} \tag{9.69}$$

where α is a stabilization coefficient, $0 \leq \alpha < 1$. Since this choice of stabilization matrix $\mathbf{S}$ has the same eigenbasis as $\mathbf{D}$, and will allow the scaling to naturally affect the most stiff modes for greater treatment.

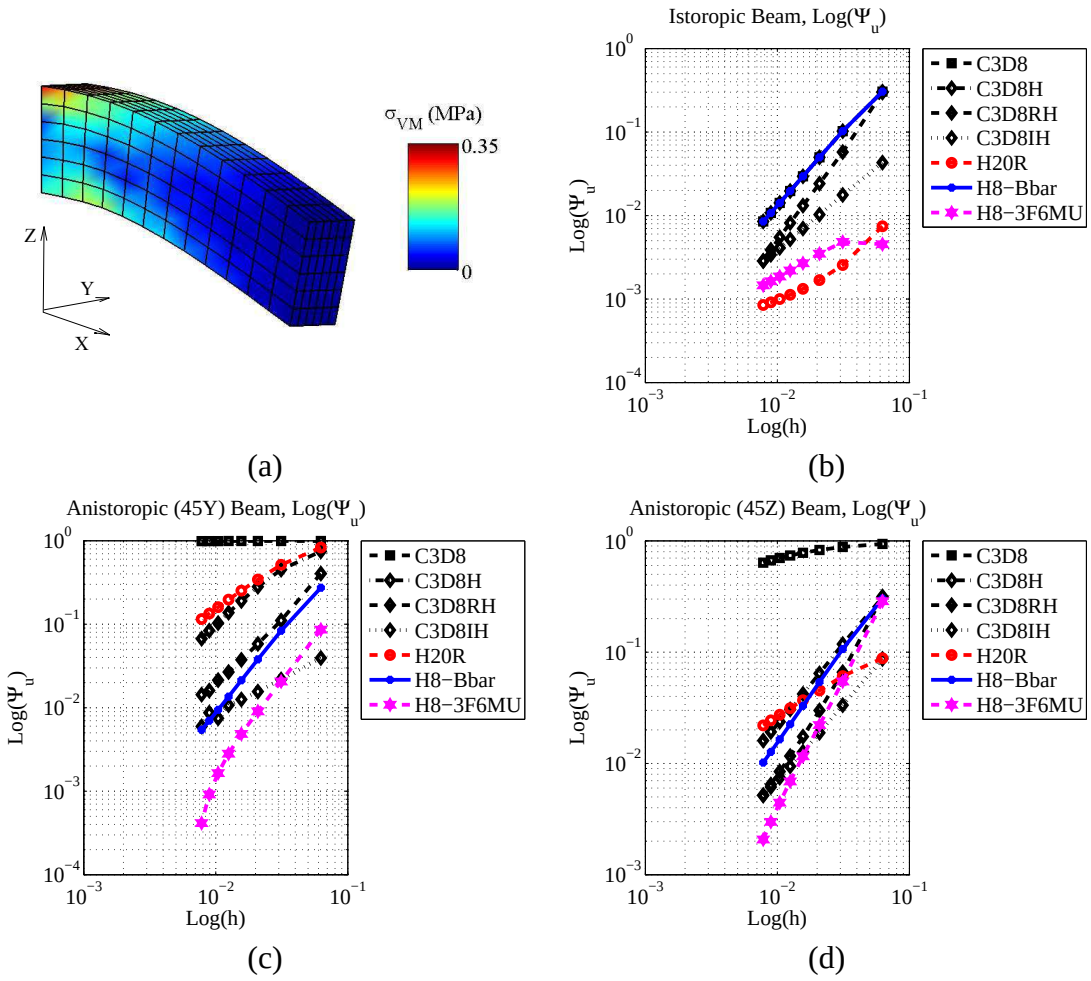

Figure 9.7: Uniform **M** scaling, displacement error Ψ_δ of cantilever beam subject to shear load at the free end. (a) Uniform mesh with 125 nodes; element aspect ratio of 1 : 4.5. In (b), (c), and (d) we show the estimated true error of the maximum deflection. (b) Isotropic material. (c) Anisotropic material, stiff fiber aligned with $[\sqrt{2}/2, -\sqrt{2}/2, 0]$. (d) Anisotropic material, stiff fiber aligned with $[\sqrt{2}/2, 0, -\sqrt{2}/2]$. Key: C3D8–linear hexahedron, C3D8H–linear hybrid hexahedron with uniform pressure, C3D8I–hexahedron with incompatible modes, C3D20R–the uniformly reduced integration quadratic serendipity hexahedron, H8-Bbar-ISO–B-bar Q1/Q0 hexahedron, H8-Bbar–linear hexahedron with present B-bar formulation, and H8-3F6MU–linear hexahedron with uniformly scaled presented 3-field.

Now, let $\Psi = \frac{1}{3}\mathbf{M}^T(\mathbf{I}-\mathbf{S})\mathbf{M}$, such that $\alpha = 0$ for no treatment (since, as with uniform scaling, α scales $\mathbf{D}_f$).

To introduce the variable spectral scaling, let $\tilde{\mathbf{M}} = \mathbf{M}\Psi$, which will scale each mode by the respective diagonals of Ψ.

Now apply the scaling, and introduce the adjusted stiff effective moduli (eigenvector scaling): $\mathbf{K}_r = \frac{1}{9}\tilde{\mathbf{M}}^T\mathbf{D}\tilde{\mathbf{M}}$, and define $\mathbf{D}_r = \tilde{\mathbf{M}}\mathbf{K}_r\tilde{\mathbf{M}}^T$, noting that the definition of $\tilde{\mathbf{K}}_r$. This gives

$\mathbf{D}_r = \frac{1}{9}\tilde{\mathbf{M}}\tilde{\mathbf{M}}^T\mathbf{D}\tilde{\mathbf{M}}\tilde{\mathbf{M}}^T = (\mathbf{I}-\mathbf{S})^2\mathbf{D}(\mathbf{I}-\mathbf{S})^2$.

Now define the flexible component of the elasticity matrix $\mathbf{D}_f = \mathbf{D} - \mathbf{D}_r$, where $\mathbf{D}_f \to \mathbf{0}$ as $\alpha \to 0$.

Introduce the effective constrained strain variable $\varepsilon_r = \tilde{\mathbf{M}}^T\varepsilon$, and the effective constrained stress variable $p = \mathbf{K}_r\varepsilon_r$. Split stress contributions accordingly: $\sigma_f = \mathbf{D}_f\varepsilon$, and $\sigma = \sigma_f + \tilde{\mathbf{M}}p$. Proceeding as with uniform scaling leads to defining $\mathbf{B}_r = \tilde{\mathbf{M}}\frac{1}{3}\mathbf{N}_r\mathbf{W}$, and to the stiffness expression

$$\bar{\mathbf{A}} = \int_\Omega \mathbf{B}^T\mathbf{D}_f\mathbf{B}\,\mathrm{d}\Omega + \int_\Omega \mathbf{B}_r^T\mathbf{D}\mathbf{B}_r\,\mathrm{d}\Omega\,. \tag{9.70}$$

The stress and strain calculations again require computation of the flexible component projector $\mathbf{I}_f$, such that $\mathbf{D}_f = \mathbf{I}_f\mathbf{D}\mathbf{I}_f$ and the strains can be decomposed $\varepsilon = \varepsilon_r + \varepsilon_f = \mathbf{B}_r\tilde{u} + \mathbf{B}_f\tilde{u}$ where $\mathbf{B}_f = \mathbf{I}_f\mathbf{B}$.

As with variable spectral eigenvalue scaling, the projector $\mathbf{I}_f$ may need to be solved iteratively.

Now, with $\mathbf{B}_f = \mathbf{I}_f\mathbf{B}$, element strains can be computed according to $\varepsilon = \mathbf{B}_r\tilde{u} + \mathbf{B}_f\tilde{u}$, and element stresses can be computed according to $\sigma = \mathbf{D}\varepsilon$.

Spectrally Scaled Beam example

Once again, scaling the eigenvectors in this manner produce some highly accurate results. These solutions were obtained using and evenhanded treatment for all materials with $\alpha = 0.3$.

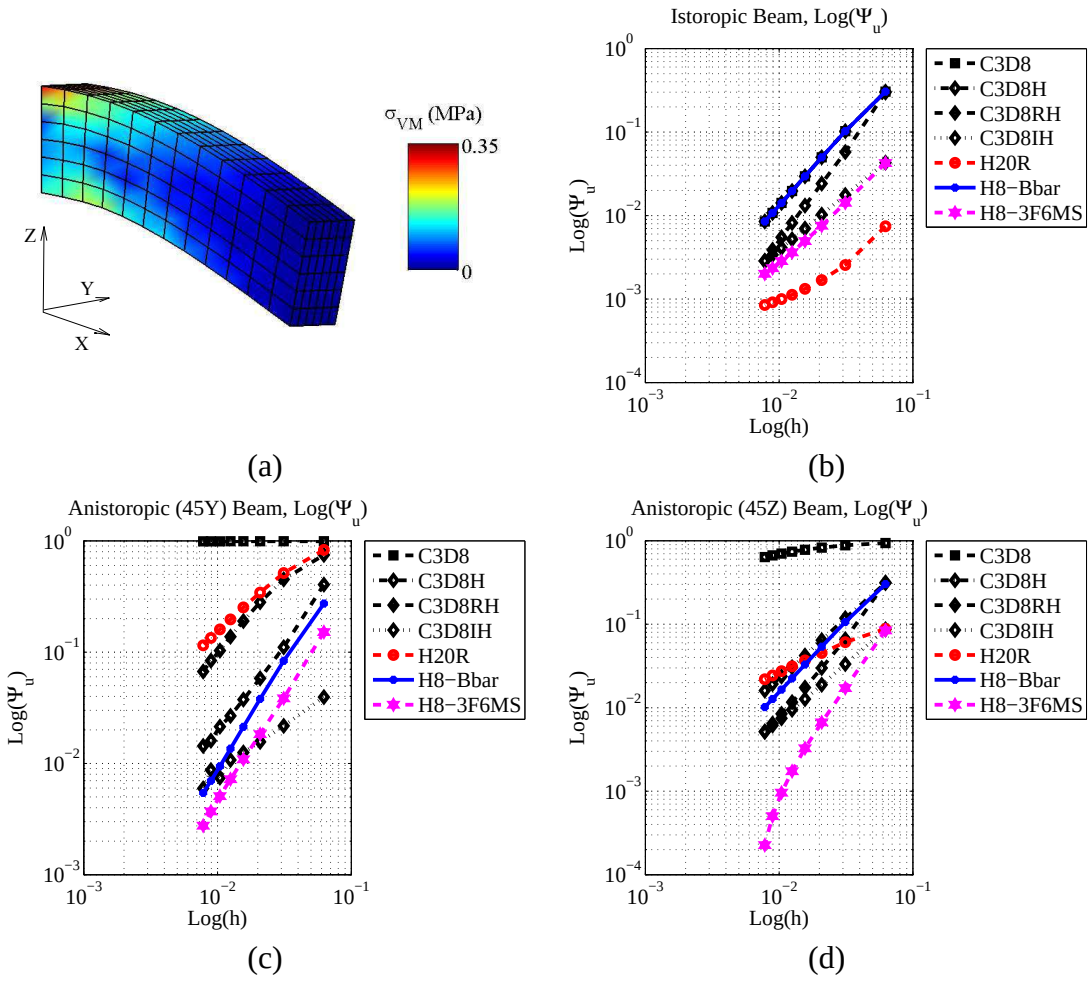

Figure 9.8: Spectral **M** scaling, displacement error Ψ_δ of cantilever beam subject to shear load at the free end. (a) Uniform mesh with 125 nodes; element aspect ratio of $1:4.5$. In (b), (c), and (d) we show the estimated true error of the maximum deflection. (b) Isotropic material. (c) Anisotropic material, stiff fiber aligned with $[\sqrt{2}/2, -\sqrt{2}/2, 0]$. (d) Anisotropic material, stiff fiber aligned with $[\sqrt{2}/2, 0, -\sqrt{2}/2]$. Key: C3D8 – linear hexahedron, C3D8H – linear hybrid hexahedron with uniform pressure, C3D8I – hexahedron with incompatible modes, C3D20R – the uniformly reduced integration quadratic serendipity hexahedron, H8-Bbar-ISO – B-bar Q1/Q0 hexahedron, H8-Bbar – linear hexahedron with present B-bar formulation, and H8-3F6MS – linear hexahedron with spectrally scaled presented 3-field.

9.1.5 Variable Stabilization Conclusions

Minimum stabilization may not remedy mesh distortions, and increased stabilizations can, when carefully chosen, improve solution accuracy. Increasing stabilization beyond some model-specific limit results in a decreased convergence rate. In this vein, increasing stabiliza-

tion can be viewed as reducing the degree to which stiff locking is treated. It should be noted that discrete inhomogeneities can lead to complicated refinement behavior, sometimes manifesting as non-monotonic convergence and persistent local element distortions. In extreme cases a compromise must be brokered, sacrificing convergence rates to quell non-physical element distortions.

9.2 GSRI and B-bar Treatment Conclusions

The treatments of anisotropic elasticity with nearly-rigid locking through a partitioning of the strain, stress, and the constitutive equation by both generalized selective reduced integration (GSRI) and the corrected B-bar formulations are found to be robust and effective. The performance of the two proposed methods are nearly identical. The corrected B-bar method is moreover attractive due to its generality for potential application to nonlinear materials. The correction is inexpensive: the treated methods do not require any special computations except for the spectral decomposition of the compliance matrix. As such, a computation is only required once for each material (in the material-aligned coordinate system); such a cost is likely to be negligible.

Chapter 10

Conclusions and Future Work

The fundamental question this research attempts to answer is: how can our understanding of how marine mammals send and receive underwater acoustic signals be improved with a better understanding of the role viscoelastic property inputs play in vibroacoustic simulation results? Three primary efforts were made in hopes of answering this question.

Through the sensitivity study comparing simulation to the experimental results for a submerged porpoise head subjected to acoustic pulses, it was discovered that the results are most sensitive to estimation of the Young's modulus of bone and to the estimation of the bulk modulus of acoustic fats.

There is a great need for improved estimations of the viscoelastic properties of animal tissues at the time of dissection, before the tissue decomposes or is frozen. The developed mechanical rheometer will help biologist do just this.

Anisotropic finite element models of fibrous tissues are prone to element locking and subsequently underestimated deformation solutions. These shortcomings to computational simulations are well remedied by the generalized selective reduced integration and B-bar variant methods presented here.

Taking another look at the Norris and Harvey study of 1974 [1] both validated the vibroacoustic toolkit VATk [28] and showed which material property inputs fostered the greatest changes in the observed pressure amplitudes at key locations in the sound reception physiol-

ogy. The study also revealed a great need for improved experimental data. Another, duplicate, experiment using well-calibrated modern instruments would provide very valuable data for use in testing and calibrating computational simulations. This would allow informed conclusions to be drawn about the importance of the dispersive qualities of acoustic fats and other tissues in the primary acoustic pathway.

The experimental efforts focused on the design, development, fabrication, and testing of a prototype rheometer producing a functional portable rheology laboratory suited for field work. The device makes good use of recent developments in both instrumentation and data acquisition. The fundamental design takes advantage of some analytical features inherent to thick sample geometries such as insensitivity to small error in estimated sample geometery and insensitivity to small normal forces at the point of excitation. The next steps in the devices develpment include fully incorporating quasi-static indentation estimations of Young's modulus, incorporation of ultrasonic testing using transducer plates designed to fit above the existing sample stage, and (perhaps most importantly) the itroduction of a hand-held probe for tissue characterization. Because the results are largely independent of sample thicknesses beyond a depth of about $15\,mm$, surface testing methods should be thoroughly investigated. Another important improvement to the prototype rheometer lies in the need for a temperature controlled environment. A controlled environment could be achieved by way of a well insulated chamber with convection temperature control. The device also warrants several modifications to make the sensitive electronics and instrumentation more physically robust for field work in a salt-water environment. Finally, the testing methodologies and control software should be simplified for use by a non-engineer.

The next steps in the presented methods exploiting the spectral decomposition of the compliance matrix to treat finite element locking of fiber-dominated anisotropic materials include an in-depth study of variable treatment methods, improved stress calculations for stabilized methods, and a thorough investigation of persistent inter-element distortions observed even in stabilized treatments. The variable 3-field treatments methods offer some enticing performance advantages that warrant further investigation. It would be worthwhile to thoroughly

explore the performance advantages and continue an investigation of stress calculations without a single term strain-displacement relation. This notion of variable treatments may be extensible to improved accuracy in other finite elements yet to be investigated.

Appendix A

Device Views and Component Specifications

A.1 Chassis

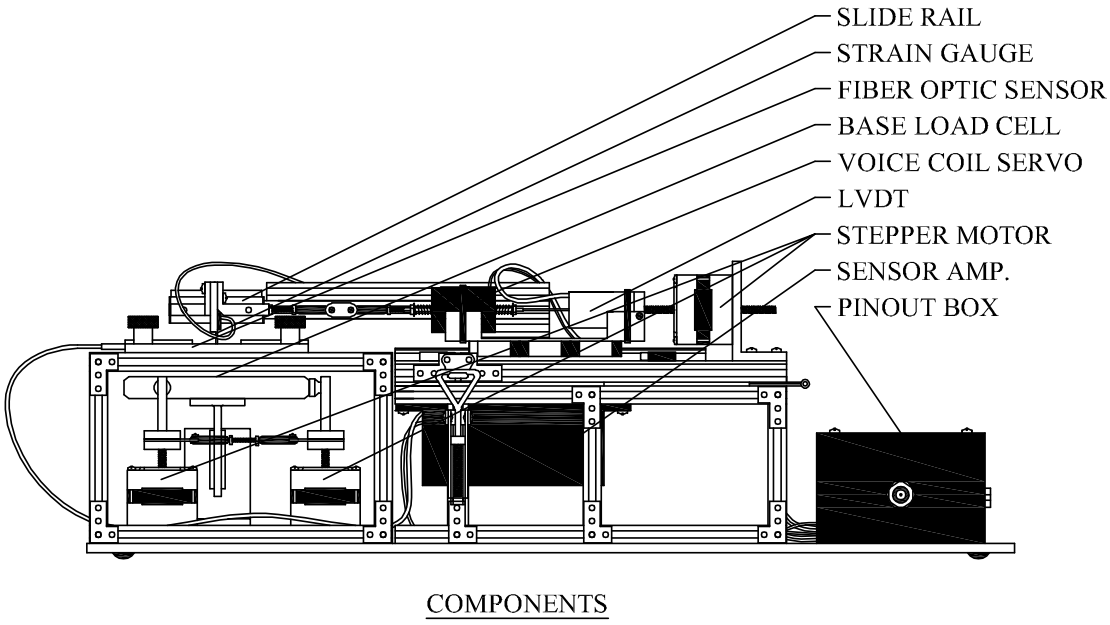

Figure A.2: Experimental rheometer component plan.

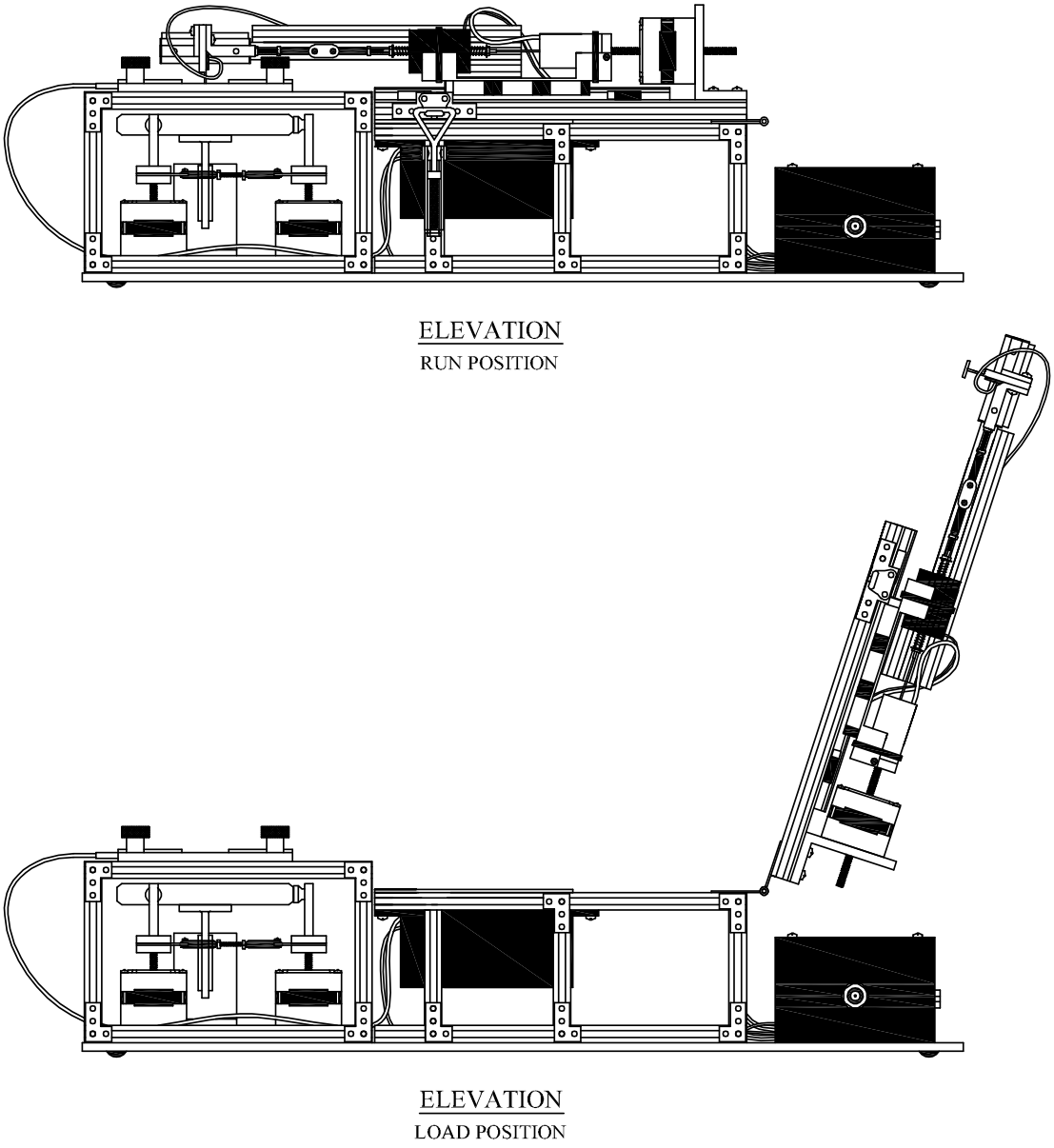

Figure A.3: Experimental rheometer elevations.

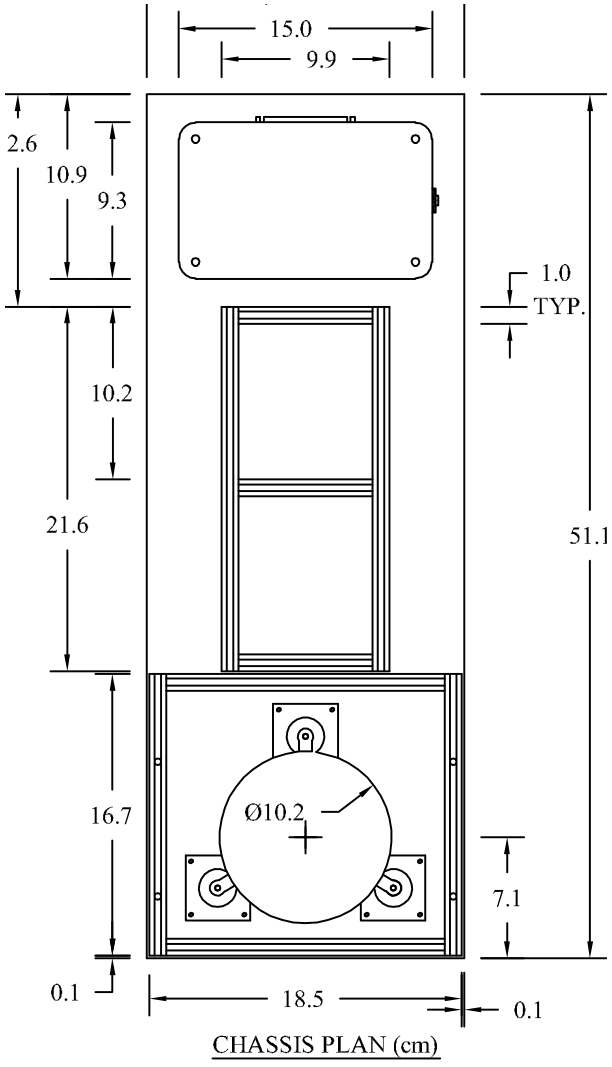

Figure A.1: Experimental rheometer chassis plan.

A.2 Control Box

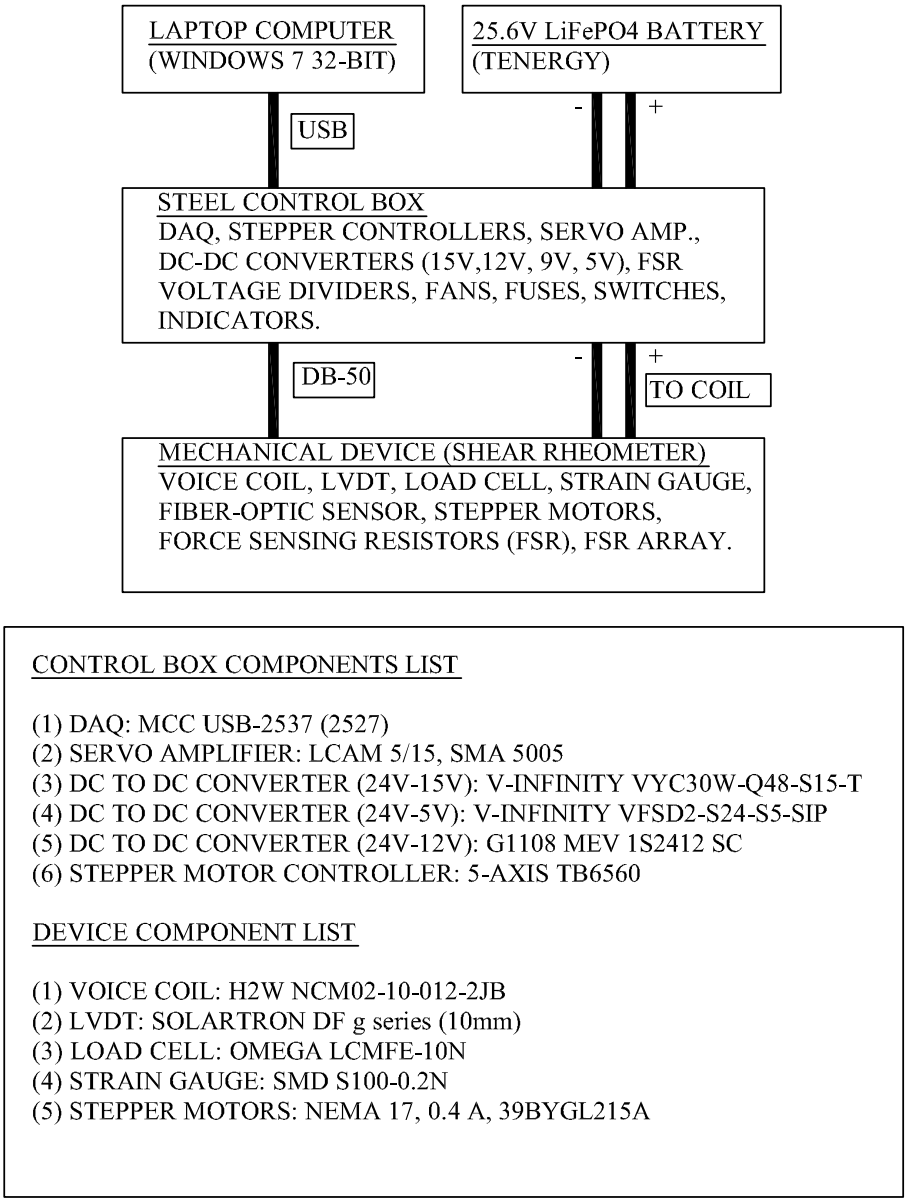

Figure A.4: Block diagram of the device control box.

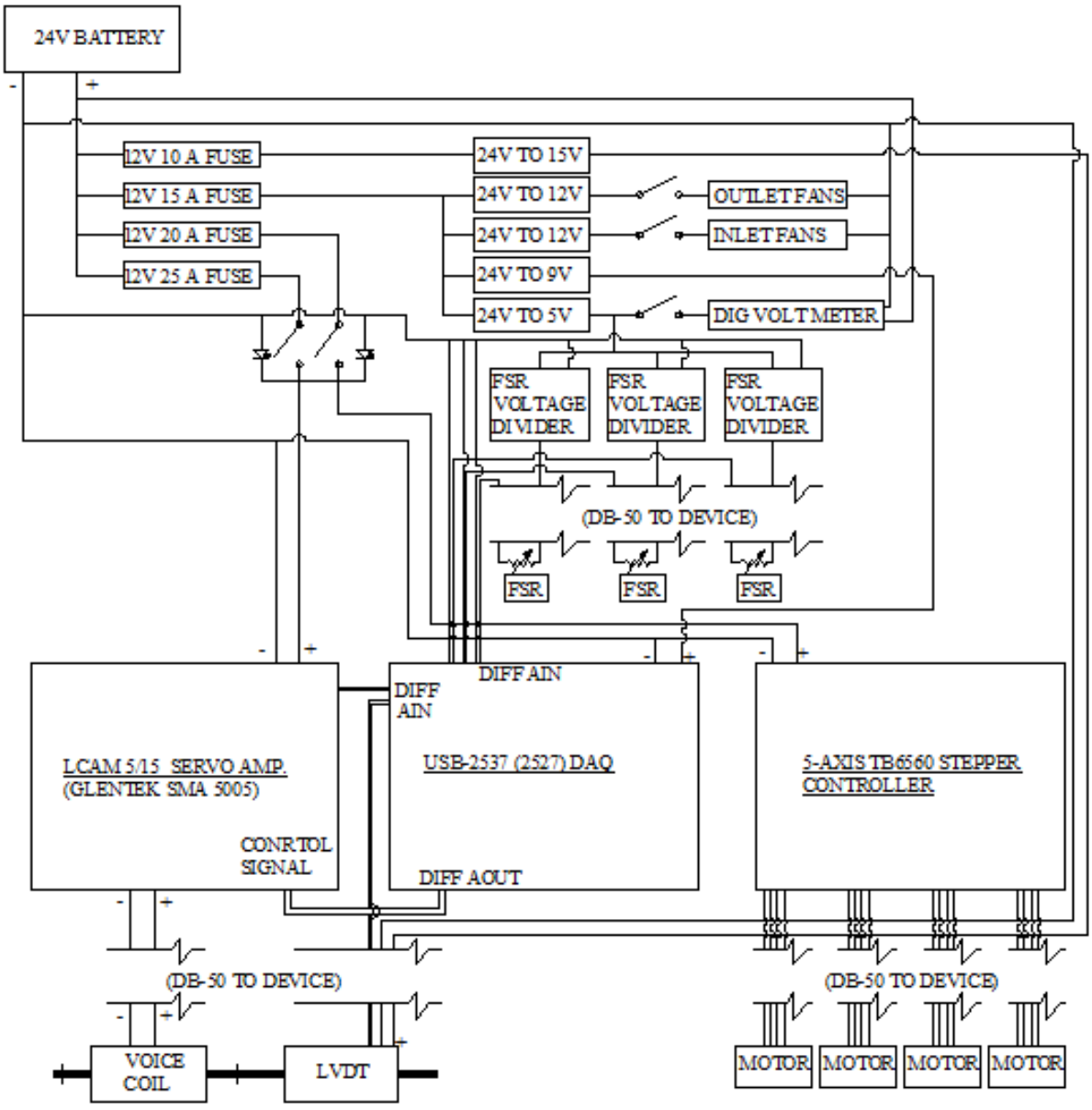

Figure A.5: Device control box.

A.3 Control

The main control box houses the Data Acquistion Board (DAQ), the stepper motor controller, the voice coil servo motor amplifier, mutliple DC-DC converters, fans, switches, cable interfaces, and limited digital readouts. The stepper Motor Controller is a 5-axis CNC TB6560. The servo Amplifier is a Glentek SMA5005 (sold as H2W LCAM 5-15) H Bridge Linear Servo Amplifier.

A.4 Data Acquisition (DAQ)

Data acquistions and analog output signals are provided by a USB-2537 manufactured by Measurement Computing Co. The DAQ is a USB-2537 with 64 Single/32 Differential analog inputs, 4 analog outputs, 24 digital IO, four 32-bit counter inputs, and with a SCSI pinout.

A.5 Primary Instrumentation

Displacements are measures using two independent instruments: (1) a precision Linear Variable Differential Transformer (LVDT), and (2) a fiber optic displacement sensor. Forces are measured using a high precision low force cantilever load cell. The LVDT is a Solartron, type DF2.5, and the fiber optic displacement sensor is a Philtec D-63 with analog outputs. The cantilever load cell is a Strain Measurement Devices SMD2207 0.5 N, with a Swann and Associates, Inc. Mantracourt SGA/D signal conditioner.

A.6 Motors

The excitation force is provided by a voice coil servo motor. Voice coil used was manufactured by H2W Technologies, and is designated NCM02-10-012-2JB 5.3 N Moving Magnet

Non-Comm DC Voice Coil Linear Actuator. Sample stage and excitation positioning is provided by Nema 17 model 39BYGL215A (0.01 mm/step) stepper motors.

A.7 DC Power

Electric power is supplied by a Tenergy ($LiFePO_4$) 32VDC nominal 20 Ah Lithium high capacity polymer/prismatic battery.

Appendix B

Stabilized GSRI Convergence Results

B.1 Convergence of Stabilized GSRI and B-bar

Tables and plots are provided to chronicle the convergence of the stabilized GSRI and B-bar methods for the four examples presented in chapter 6. The errors are calculated using the best extrapolated solutions as reference values. Here, as in previous convergence studies of this work, the best extrapolated values are attained using techniques of Richardson's extrapolation [62] applied to the quadratic hexahedral (H27) elements.

B.2 Tables of Refinement Values, Stabilized Treatments

As in the previous section of tables, these tabulated values represent the respective converged values obtained by Richardson's extrapolation.

As in previous tables of this appendix, negative values occur when Richardson's extrapolations fails as a result of non-monotonic convergence. This happens when the refinement study has not yet reached the asymptotic region and is usually seen with linear hexahedral elements where significant stabilization is being applied.

The maximum displacement values for the distorted mesh solutions of the abruptly inohomogeneous plate example, seen in table B.1, deviate from the converged values. These

"loose" or "over-flexible" solutions are mitigated as stabilization levels are increased.

Again, the negative values for the linear elements of the Beam model in table B.5 are attributable to refinement that has not yet reached the asymptotic region, which leads to the failure of Richardson's extrapolation. The curves shown in figures B.2 and B.10, however, show a smooth trend toward the limit value.

B.2.1 Stabilized u_{max} Tables

Table B.1: Converged maximum displacement table, GSRI, $\alpha = 0$.

$u_{max}\,(mm)$	Beam hom45y	Plate hom45z	Plate smooth2	Plate disc1
H8	1.016e-04	1.694e-04	1.769e-04	5.992e-05
H8-Distorted	1.022e-04	1.661e-04	1.742e-04	7.897e-05
H27	1.011e-04	1.626e-04	1.743e-04	5.848e-05
H27-Distorted	1.013e-04	1.622e-04	1.696e-04	8.227e-05

Table B.2: Converged maximum displacement table, GSRI, $\alpha = 1$.

$u_{max}\,(mm)$	Beam hom45y	Plate hom45z	Plate smooth2	Plate disc1
H8	1.014e-04	1.641e-04	1.756e-04	5.939e-05
H8-Distorted	1.024e-04	1.637e-04	1.727e-04	7.896e-05
H27	1.013e-04	1.628e-04	1.747e-04	5.922e-05
H27-Distorted	1.011e-04	1.624e-04	1.698e-04	8.210e-05

Table B.3: Converged maximum displacement table, GSRI, $\alpha = 50$.

$u_{max}\,(mm)$	Beam hom45y	Plate hom45z	Plate smooth2	Plate disc1
H8	5.924e-04	1.684e-04	1.810e-04	5.515e-05
H8-Distorted	3.980e-04	1.677e-04	1.723e-04	6.479e-05
H27	1.004e-04	1.669e-04	1.775e-04	5.282e-05
H27-Distorted	1.000e-04	1.699e-04	1.716e-04	6.721e-05

Table B.4: Converged maximum displacement table, GSRI, $\alpha = 100$.

$u_{max}\,(mm)$	Beam hom45y	Plate hom45z	Plate smooth2	Plate disc1
H8	-4.391e-05	1.806e-04	1.870e-04	5.558e-05
H8-Distorted	-6.018e-05	1.813e-04	1.767e-04	5.950e-05
H27	1.003e-04	1.674e-04	1.794e-04	5.461e-05
H27-Distorted	1.001e-04	1.702e-04	1.729e-04	6.212e-05

Table B.5: Converged maximum displacement table, GSRI, $\alpha = 200$.

$u_{max}\,(mm)$	Beam hom45y	Plate hom45z	Plate smooth2	Plate disc1
H8	-7.303e-06	2.277e-04	2.024e-04	5.065e-05
H8-Distorted	-9.809e-06	2.311e-04	1.883e-04	5.504e-05
H27	1.009e-04	1.681e-04	1.827e-04	5.652e-05
H27-Distorted	1.009e-04	1.710e-04	1.757e-04	5.785e-05

Table B.6: Converged maximum displacement table, GSRI, $\alpha = f(\lambda)$.

$u_{max}\,(mm)$	Beam hom45y	Plate hom45z	Plate smooth2	Plate disc1
H8	-5.014e-05	2.170e-04	1.993e-04	5.136e-05
H8-Distorted	-6.924e-05	2.199e-04	1.860e-04	5.557e-05
H27	1.003e-04	1.679e-04	1.821e-04	5.682e-05
H27-Distorted	1.000e-04	1.708e-04	1.751e-04	5.829e-05

B.2.2 Stabilized $\mathscr{U}$ Tables

Table B.7: Converged strain energy table, GSRI, $\alpha = 0$.

$\mathscr{U}\,(J/m^3)$	Beam hom45y	Plate hom45z	Plate smooth2	Plate disc1
H8	1.014e-04	1.458e-02	1.042e-02	5.442e-03
H8-Distorted	1.021e-04	1.433e-02	1.027e-02	7.023e-03
H27	1.011e-04	1.403e-02	1.023e-02	5.427e-03
H27-Distorted	1.011e-04	1.398e-02	9.981e-03	7.110e-03

Table B.8: Converged strain energy table, GSRI, $\alpha = 1$.

$\mathscr{U}\ (J/m^3)$	Beam hom45y	Plate hom45z	Plate smooth2	Plate disc1
H8	1.012e-04	1.415e-02	1.033e-02	5.437e-03
H8-Distorted	1.023e-04	1.411e-02	1.017e-02	6.970e-03
H27	1.011e-04	1.404e-02	1.026e-02	5.473e-03
H27-Distorted	1.010e-04	1.400e-02	9.961e-03	7.086e-03

Table B.9: Converged strain energy table, GSRI, $\alpha = 50$.

$\mathscr{U}\ (J/m^3)$	Beam hom45y	Plate hom45z	Plate smooth2	Plate disc1
H8	5.677e-04	1.482e-02	1.075e-02	4.012e-03
H8-Distorted	3.859e-04	1.466e-02	1.019e-02	5.940e-03
H27	1.002e-04	1.449e-02	1.043e-02	5.036e-03
H27-Distorted	9.983e-05	1.485e-02	1.007e-02	6.207e-03

Table B.10: Converged strain energy table, GSRI, $\alpha = 100$.

$\mathscr{U}\ (J/m^3)$	Beam hom45y	Plate hom45z	Plate smooth2	Plate disc1
H8	-4.482e-05	1.610e-02	1.137e-02	5.369e-03
H8-Distorted	-6.061e-05	1.593e-02	1.056e-02	5.594e-03
H27	1.001e-04	1.475e-02	1.055e-02	2.664e-03
H27-Distorted	9.986e-05	1.522e-02	1.014e-02	5.903e-03

Table B.11: Converged strain energy table, GSRI, $\alpha = 200$.

$\mathscr{U}\ (J/m^3)$	Beam hom45y	Plate hom45z	Plate smooth2	Plate disc1
H8	-7.465e-06	2.011e-02	1.324e-02	5.327e-03
H8-Distorted	-1.014e-05	1.975e-02	1.161e-02	5.268e-03
H27	1.006e-04	1.518e-02	1.081e-02	5.478e-03
H27-Distorted	1.008e-04	1.573e-02	1.033e-02	5.597e-03

Table B.12: Converged strain energy table, GSRI, $\alpha = f(\lambda)$.

$\mathscr{U}\ (J/m^3)$	Beam hom45y	Plate hom45z	Plate smooth2	Plate disc1
H8	-5.123e-05	1.927e-02	1.284e-02	5.315e-03
H8-Distorted	-6.978e-05	1.896e-02	1.140e-02	5.308e-03
H27	1.001e-04	1.510e-02	1.076e-02	5.535e-03
H27-Distorted	9.984e-05	1.565e-02	1.029e-02	5.637e-03

B.2.3 Stabilized σ_{VM} Tables

Table B.13: Converged von-Mises stress table, GSRI, $\alpha = 0$.

$\sigma_{VM}\ (MPa)$	Beam hom45y	Plate hom45z	Plate smooth2	Plate disc1
H8	1.040e+00	3.821e+01	3.940e+01	7.498e+01
H8-Distorted	1.766e+00	4.951e+01	1.600e+02	1.010e+02
H27	8.512e-01	2.617e+01	2.669e+01	4.646e+01
H27-Distorted	1.252e+00	2.976e+01	9.881e+01	7.496e+01

Table B.14: Converged von-Mises stress table, GSRI, $\alpha = 1$.

$\sigma_{VM}\ (MPa)$	Beam hom45y	Plate hom45z	Plate smooth2	Plate disc1
H8	1.371e+00	4.230e+01	4.241e+01	7.634e+01
H8-Distorted	2.059e+00	5.230e+01	1.569e+02	1.019e+02
H27	1.001e+00	2.590e+01	2.646e+01	4.739e+01
H27-Distorted	1.397e+00	2.939e+01	9.795e+01	7.485e+01

Table B.15: Converged von-Mises stress table, GSRI, $\alpha = 50$.

$\sigma_{VM}\ (MPa)$	Beam hom45y	Plate hom45z	Plate smooth2	Plate disc1
H8	4.812e+00	8.794e+01	7.439e+01	8.399e+01
H8-Distorted	5.437e+00	9.572e+01	1.322e+02	9.469e+01
H27	3.302e+00	3.879e+01	3.326e+01	5.279e+01
H27-Distorted	3.780e+00	4.273e+01	8.810e+01	7.281e+01

Table B.16: Converged von-Mises stress table, GSRI, $\alpha = 100$.

$\sigma_{VM}\,(MPa)$	Beam hom45y	Plate hom45z	Plate smooth2	Plate disc1
H8	6.063e+00	1.063e+02	8.761e+01	8.479e+01
H8-Distorted	7.164e+00	1.155e+02	1.228e+02	9.948e+01
H27	4.492e+00	4.717e+01	3.837e+01	5.422e+01
H27-Distorted	5.025e+00	5.272e+01	8.429e+01	7.146e+01

Table B.17: Converged von-Mises stress table, GSRI, $\alpha = 200$.

$\sigma_{VM}\,(MPa)$	Beam hom45y	Plate hom45z	Plate smooth2	Plate disc1
H8	7.246e+00	1.280e+02	1.038e+02	8.517e+01
H8-Distorted	9.189e+00	1.391e+02	1.127e+02	1.048e+02
H27	6.097e+00	5.842e+01	4.644e+01	5.577e+01
H27-Distorted	6.675e+00	6.526e+01	7.917e+01	6.974e+01

Table B.18: Converged von-Mises stress table, GSRI, $\alpha = f(\lambda)$.

$\sigma_{VM}\,(MPa)$	Beam hom45y	Plate hom45z	Plate smooth2	Plate disc1
H8	1.041e+00	3.821e+01	3.940e+01	7.498e+01
H8-Distorted	1.765e+00	4.951e+01	1.600e+02	1.010e+02
H27	8.507e-01	2.617e+01	2.669e+01	4.646e+01
H27-Distorted	1.252e+00	2.976e+01	9.881e+01	7.496e+01

B.3 Convergence Plots, Stabilized Treatments

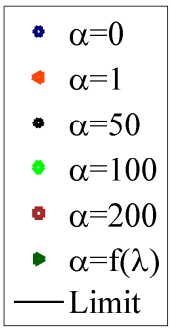

Figure B.1: Legend for the curves of stabilized GSRI.

B.4 Linear Hexahedra

B.4.1 Example, 1-Fiber, Homogeneous Beam

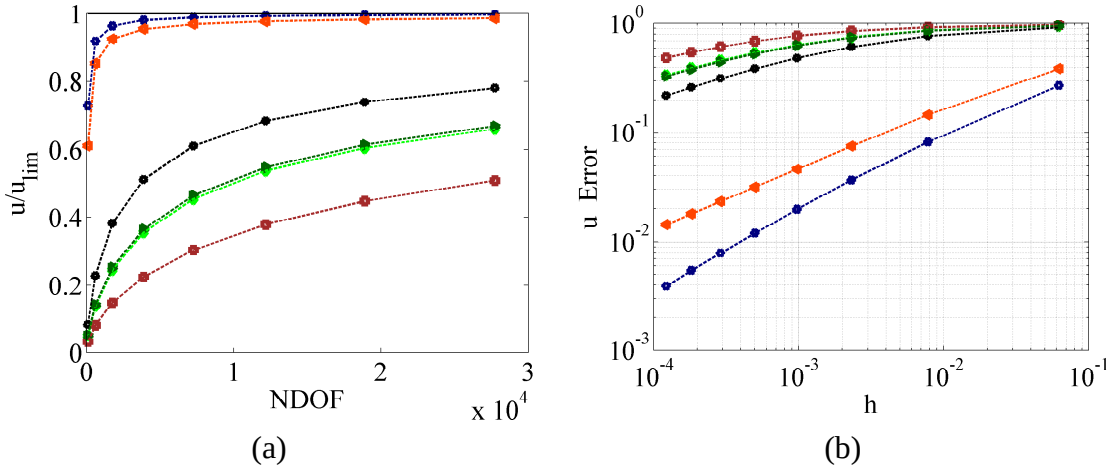

Figure B.2: Maximum displacement study for varying stabilization α_i for H8, hom45y: a) u_{max} and b) u_{max} Error (see legend in figure B.1).

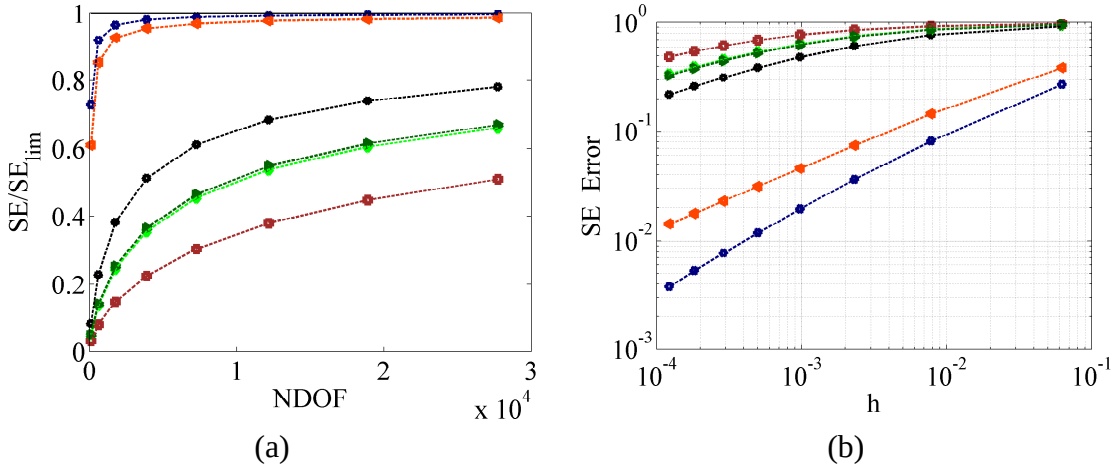

Figure B.3: Strain Energy study for varying stabilization α_i for H8, hom45y: a) $\mathscr{U}$ and b) $\mathscr{U}$ Error (see legend in figure B.1).

B.4.2 Example, 2-Fiber, Homogeneous Plate

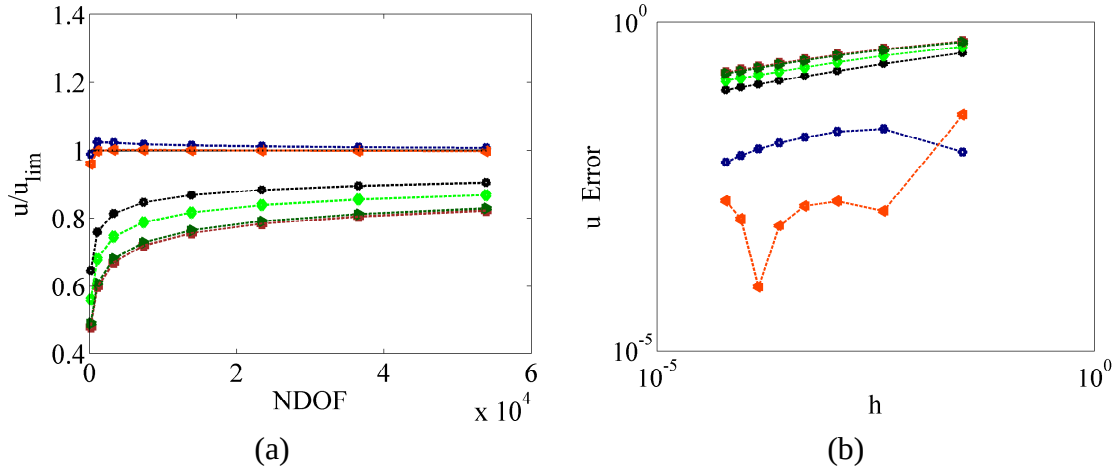

Figure B.4: Maximum displacement study for varying stabilization α_i for H8, hom45z: a) u_{max} and b) u_{max} Error (see legend in figure B.1).

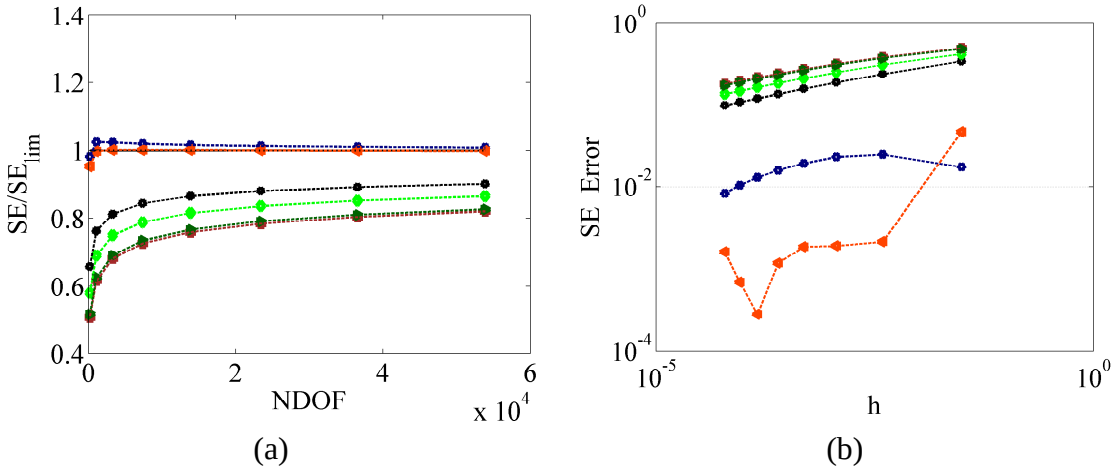

Figure B.5: Strain Energy study for varying stabilization α_i for H8, hom45z: a) $\mathscr{U}$ and b) $\mathscr{U}$ Error (see legend in figure B.1).

B.4.3 Example, 2-Fiber, Smoothly Inhomogeneous Plate

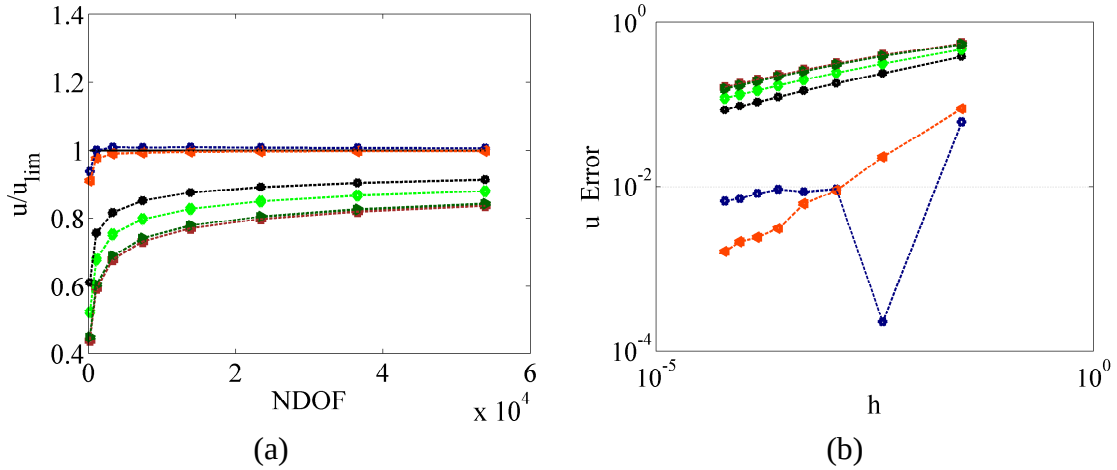

Figure B.6: Maximum displacement study for varying stabilization α_i for H8, smooth2: a) u_{max} and b) u_{max} Error (see legend in figure B.1).

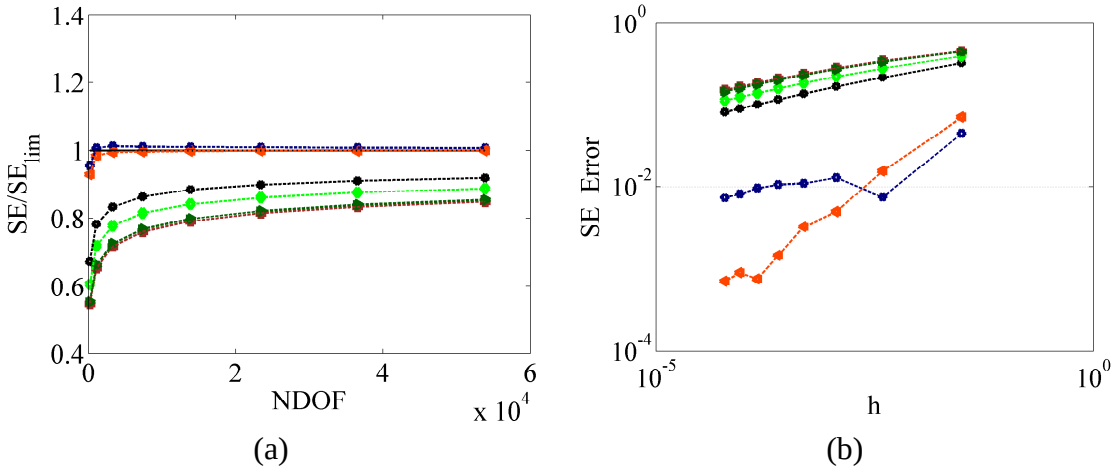

Figure B.7: Strain Energy study for varying stabilization α_i for H8, smooth2: a) $\mathscr{U}$ and b) $\mathscr{U}$ Error (see legend in figure B.1).

B.4.4 Example, 2-Fiber, Abruptly Inhomogeneous Plate

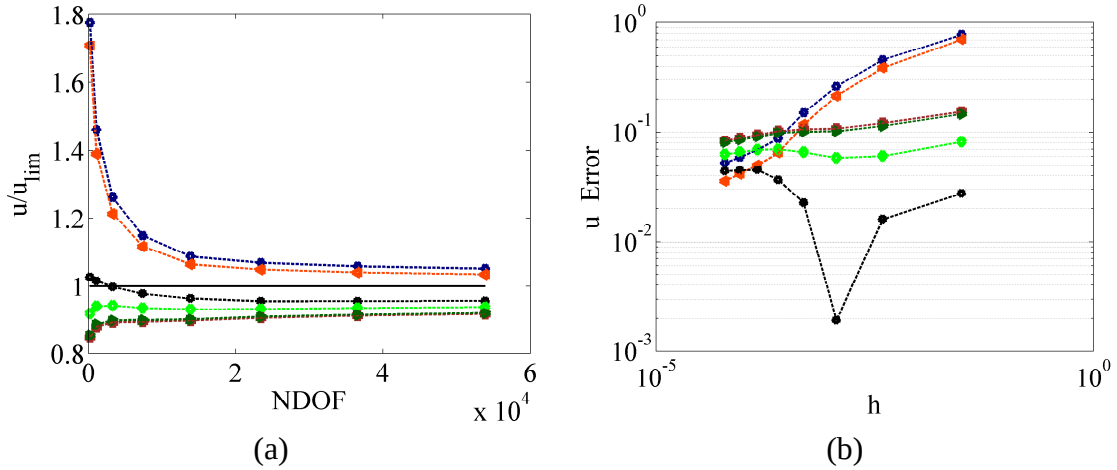

Figure B.8: Maximum displacement study for varying stabilization α_i for H8, disc1: a) u_{max} and b) u_{max} Error (see legend in figure B.1).

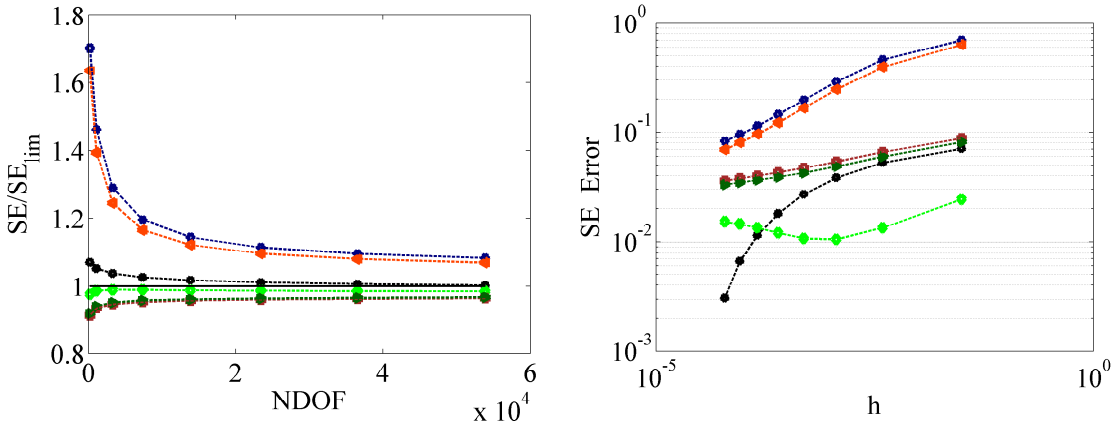

(a) (b)

Figure B.9: Strain Energy study for varying stabilization α_i for H8, disc1: a) $\mathscr{U}$ and b) $\mathscr{U}$ Error (see legend in figure B.1).

B.5 Distorted Linear Hexahedra

B.5.1 Example, 1-Fiber, Homogeneous Beam

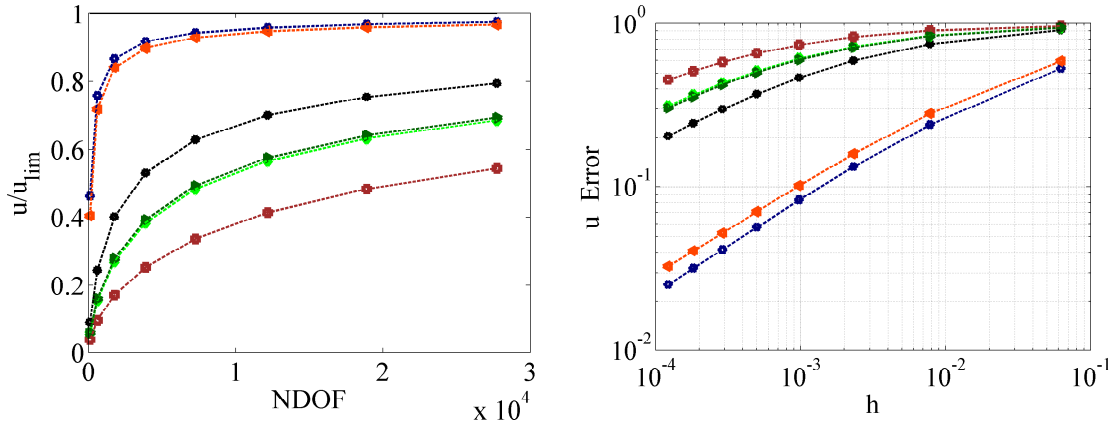

(a) (b)

Figure B.10: Maximum displacement study for varying stabilization α_i for H8-Distorted, hom45y: a) u_{max} and b) u_{max} Error (see legend in figure B.1).

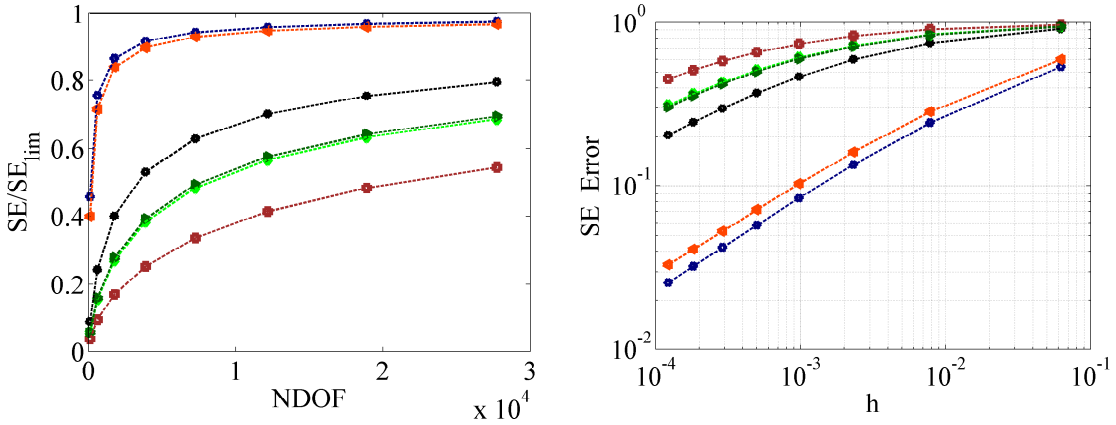

Figure B.11: Strain Energy study for varying stabilization α_i for H8-Distorted, hom45y: a) $\mathscr{U}$ and b) $\mathscr{U}$ Error (see legend in figure B.1).

B.5.2 Example, 2-Fiber, Homogeneous Plate

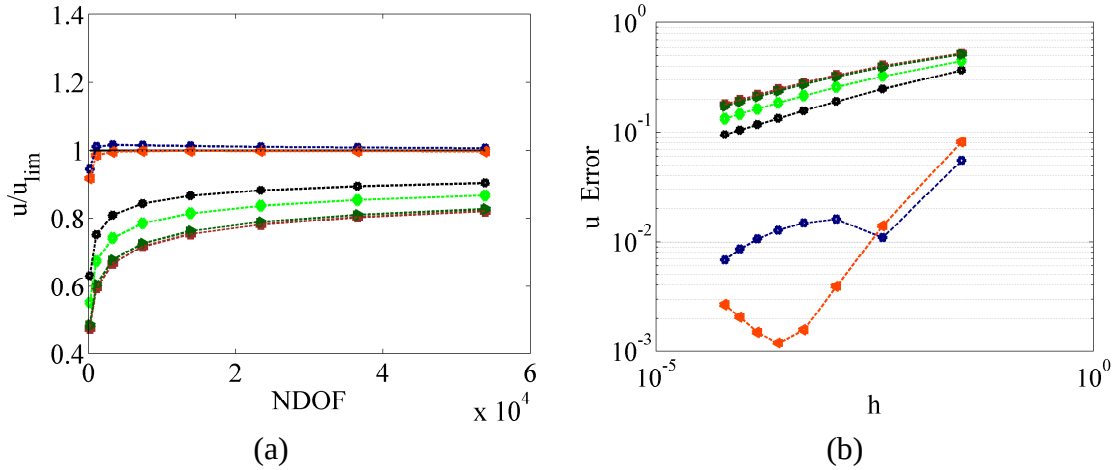

Figure B.12: Maximum displacement study for varying stabilization α_i for H8-Distorted, hom45z: a) u_{max} and b) u_{max} Error (see legend in figure B.1).

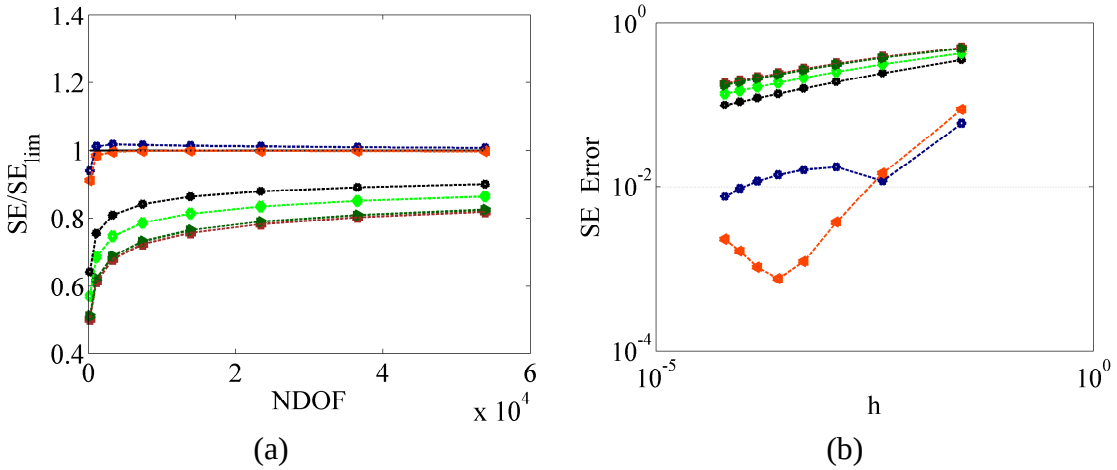

Figure B.13: Strain Energy study for varying stabilization α_i for H8-Distorted, hom45z: a) $\mathscr{U}$ and b) $\mathscr{U}$ Error (see legend in figure B.1).

B.5.3 Example, 2-Fiber, Smoothly Inhomogeneous Plate

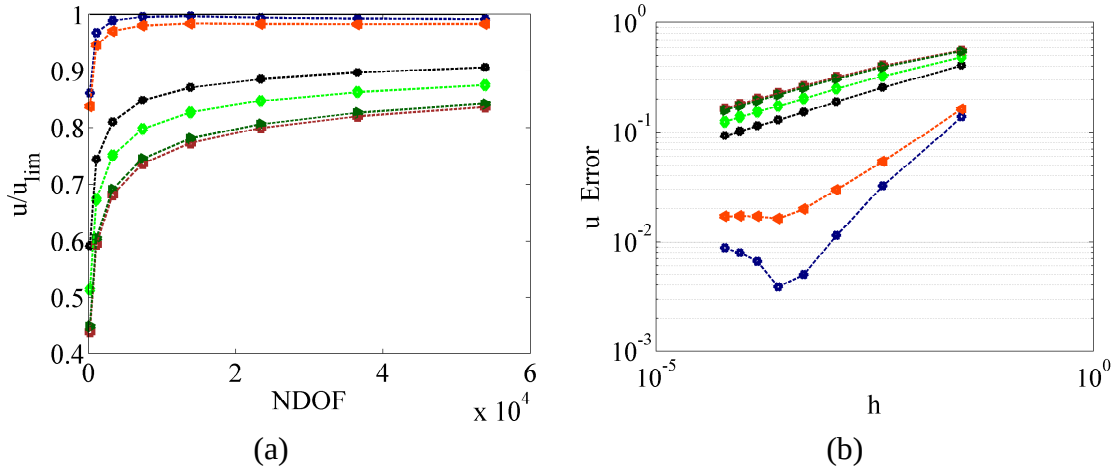

Figure B.14: Maximum displacement study for varying stabilization α_i for H8-Distorted, smooth2: a) u_{max} and b) u_{max} Error (see legend in figure B.1).

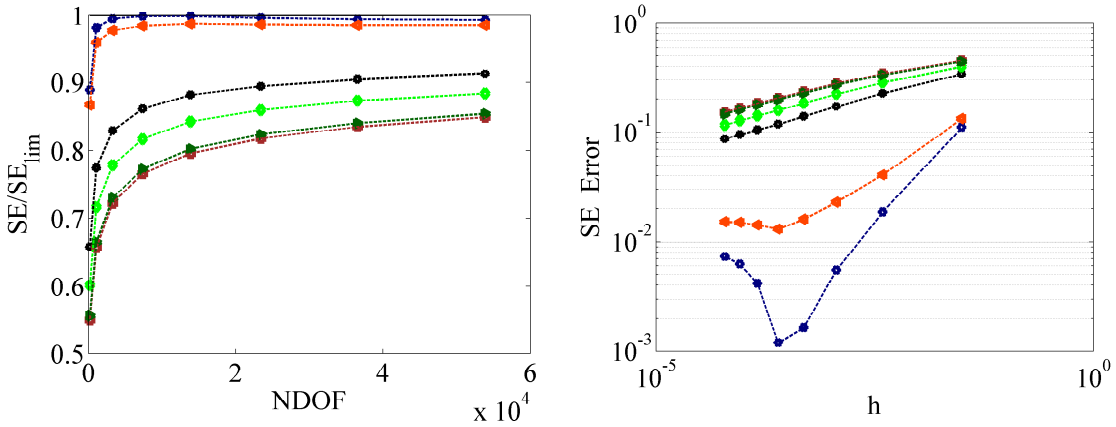

Figure B.15: Strain Energy study for varying stabilization α_i for H8-Distorted, smooth2: a) $\mathscr{U}$ and b) $\mathscr{U}$ Error (see legend in figure B.1).

B.5.4 Example, 2-Fiber, Abruptly Inhomogeneous Plate

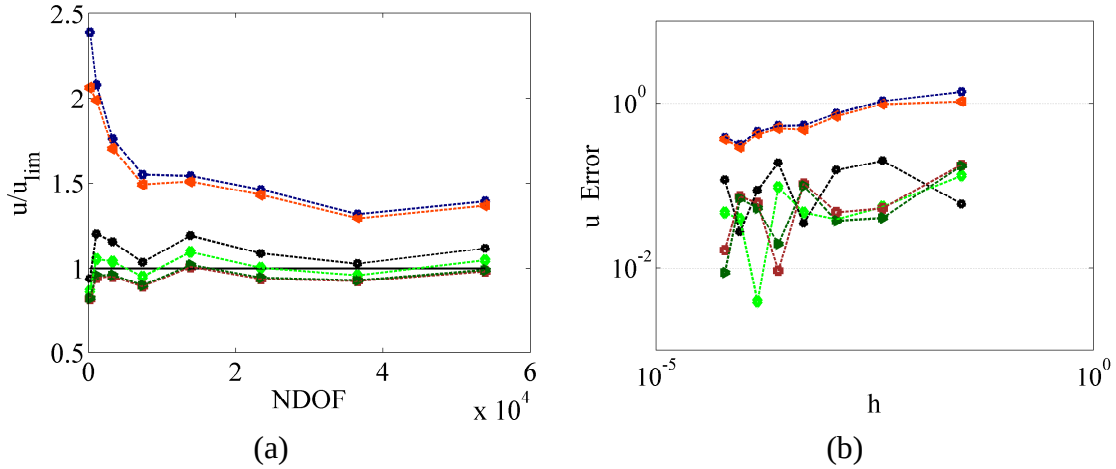

Figure B.16: Maximum displacement study for varying stabilization α_i for H8-Distorted, disc1: a) u_{max} and b) u_{max} Error (see legend in figure B.1).

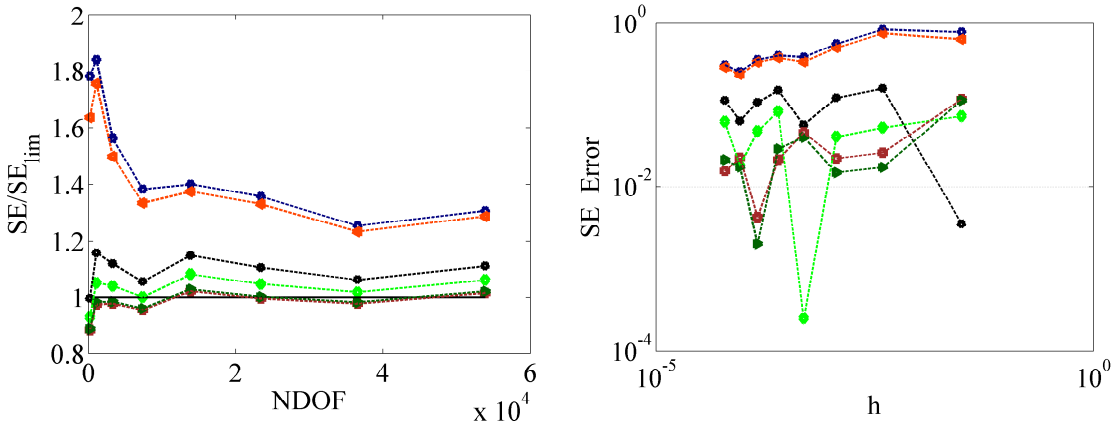

Figure B.17: Strain Energy study for varying stabilization α_i for H8-Distorted, disc1: a) $\mathscr{U}$ and b) $\mathscr{U}$ Error (see legend in figure B.1).

B.6 Quadratic Hexahedra

B.6.1 Example, 1-Fiber, Homogeneous Beam

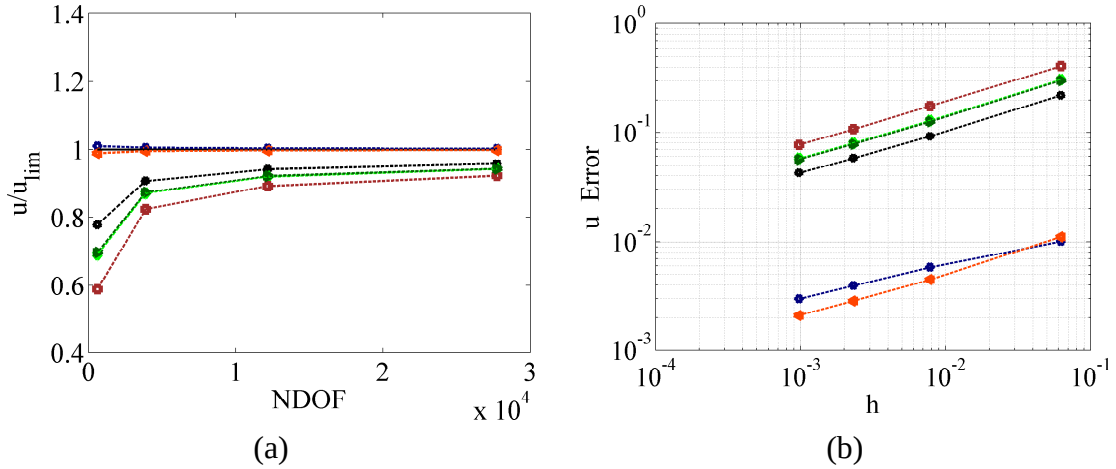

Figure B.18: Maximum displacement study for varying stabilization α_i for H27, hom45y: a) u_{max} and b) u_{max} Error (see legend in figure B.1).

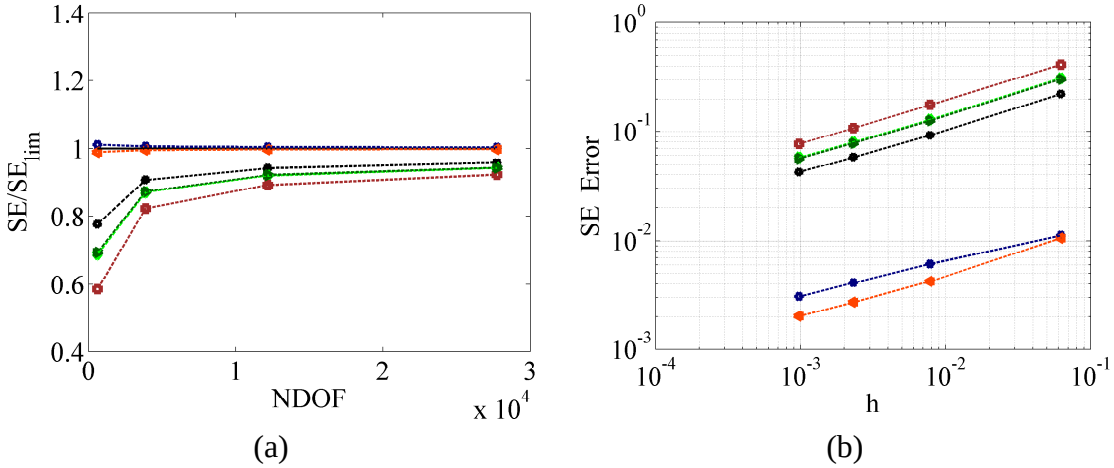

Figure B.19: Strain Energy study for varying stabilization α_i for H27, hom45y: a) $\mathscr{U}$ and b) $\mathscr{U}$ Error (see legend in figure B.1).

B.6.2 Example, 2-Fiber, Homogeneous Plate

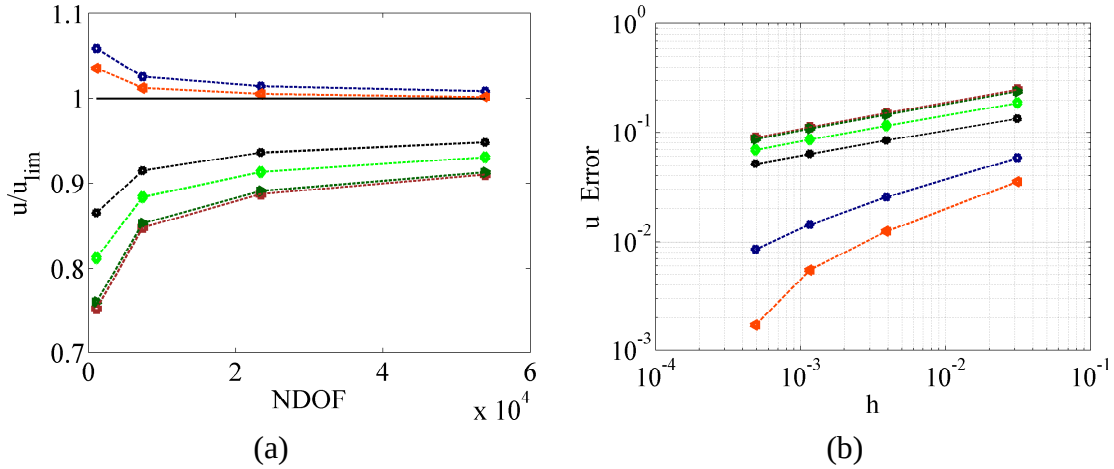

Figure B.20: Maximum displacement study for varying stabilization α_i for H27, hom45z: a) u_{max} and b) u_{max} Error (see legend in figure B.1).

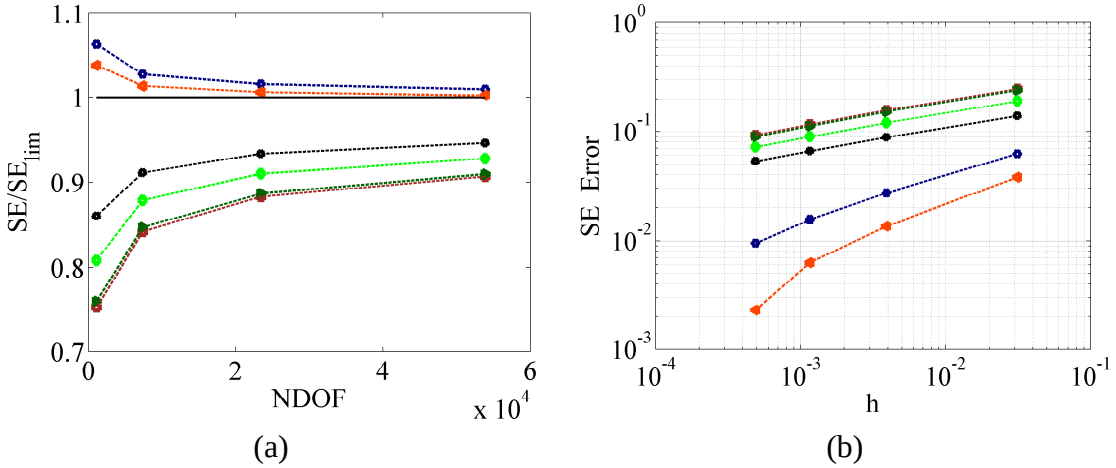

Figure B.21: Strain Energy study for varying stabilization α_i for H27, hom45z: a) $\mathscr{U}$ and b) $\mathscr{U}$ Error (see legend in figure B.1).

B.6.3 Example, 2-Fiber, Smoothly Inhomogeneous Plate

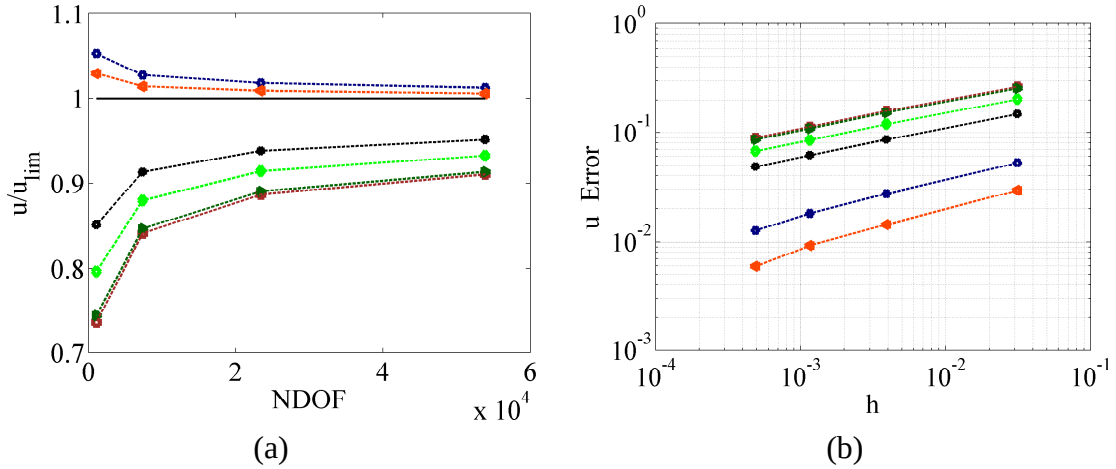

Figure B.22: Maximum displacement study for varying stabilization α_i for H27, smooth2: a) u_{max} and b) u_{max} Error (see legend in figure B.1).

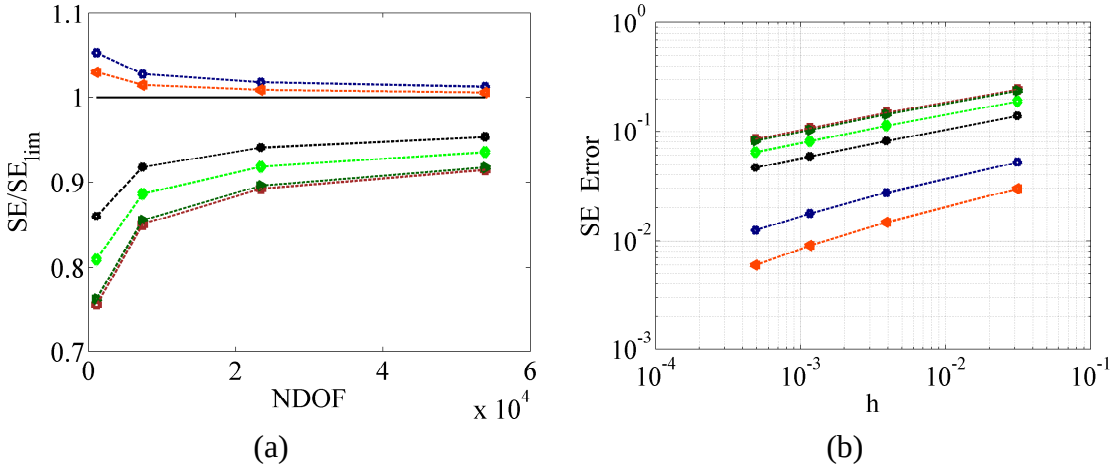

Figure B.23: Strain Energy study for varying stabilization α_i for H27, smooth2: a) $\mathscr{U}$ and b) $\mathscr{U}$ Error (see legend in figure B.1).

B.6.4 Example, 2-Fiber, Abruptly Inhomogeneous Plate

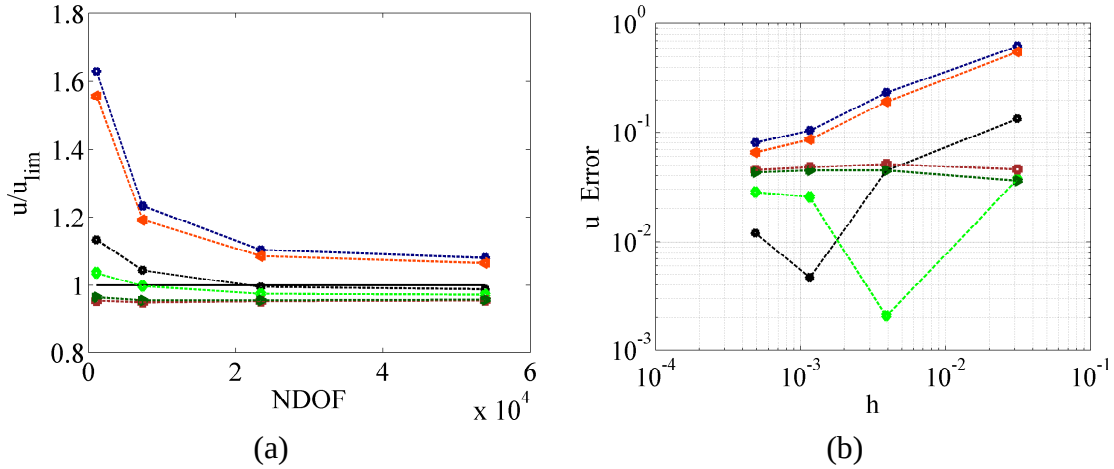

Figure B.24: Maximum displacement study for varying stabilization α_i for H27, disc1: a) u_{max} and b) u_{max} Error (see legend in figure B.1).

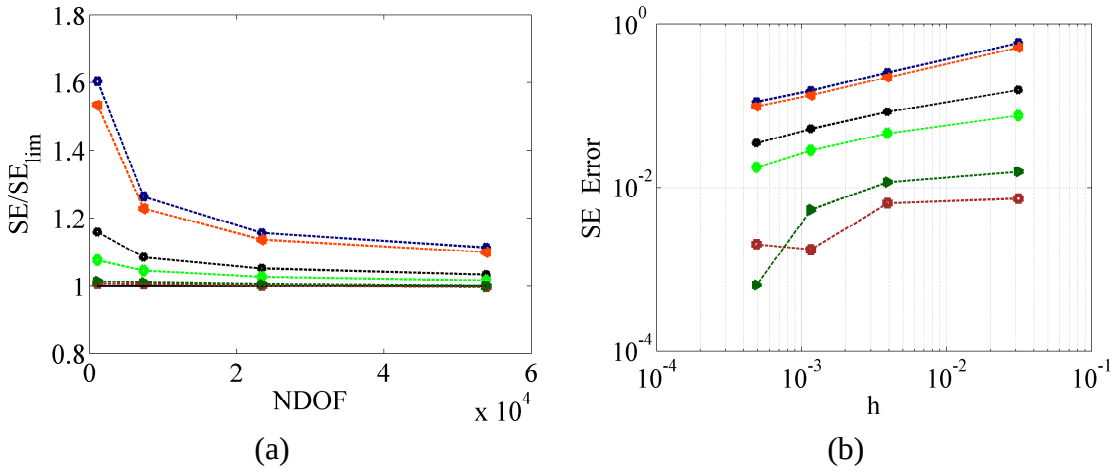

Figure B.25: Strain Energy study for varying stabilization α_i for H27, disc1: a) $\mathscr{U}$ and b) $\mathscr{U}$ Error (see legend in figure B.1).

B.7 Distorted Quadratic Hexahedra

B.7.1 Example, 1-Fiber, Homogeneous Beam

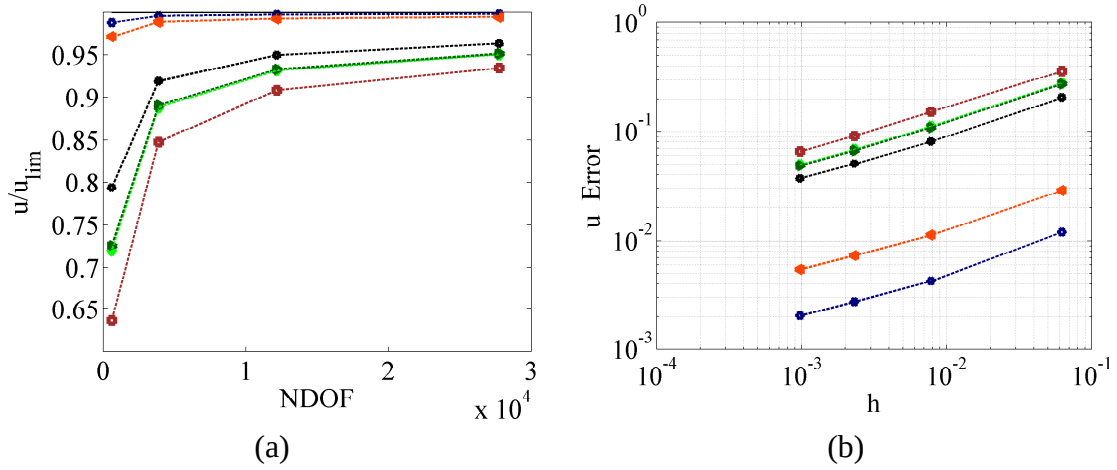

Figure B.26: Maximum displacement study for varying stabilization α_i for H27-Distorted, hom45y: a) u_{max} and b) u_{max} Error (see legend in figure B.1).

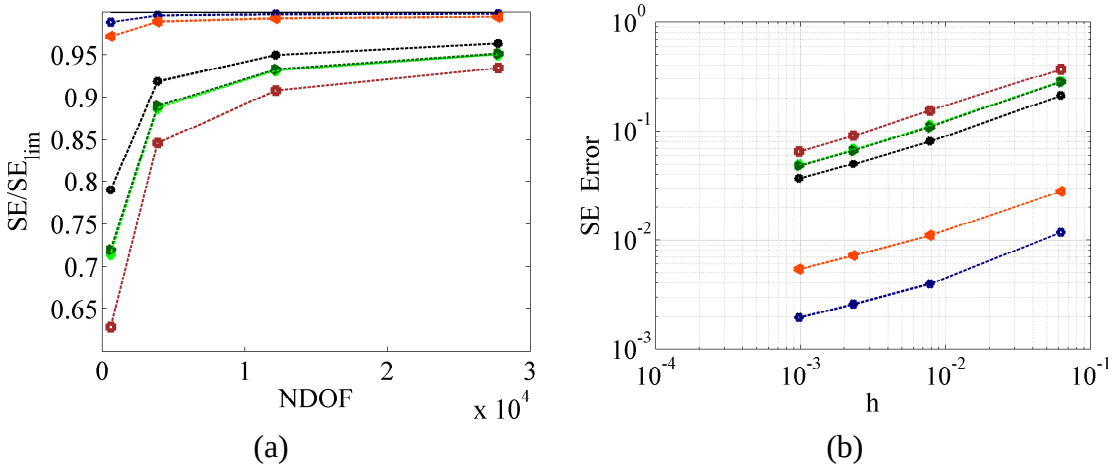

Figure B.27: Strain Energy study for varying stabilization α_i for H27-Distorted, hom45y: a) $\mathscr{U}$ and b) $\mathscr{U}$ Error (see legend in figure B.1).

B.7.2 Example, 2-Fiber, Homogeneous Plate

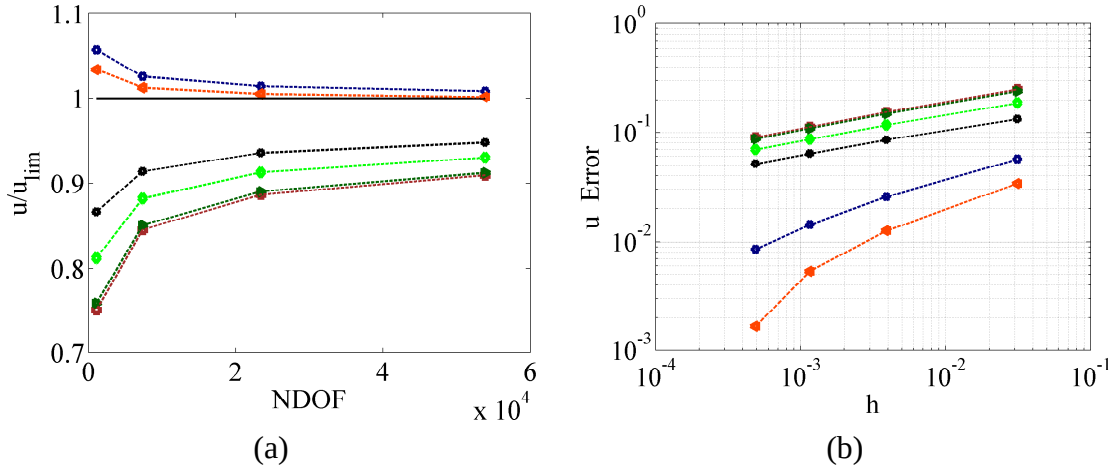

Figure B.28: Maximum displacement study for varying stabilization α_i for H27-Distorted, hom45z: a) u_{max} and b) u_{max} Error (see legend in figure B.1).

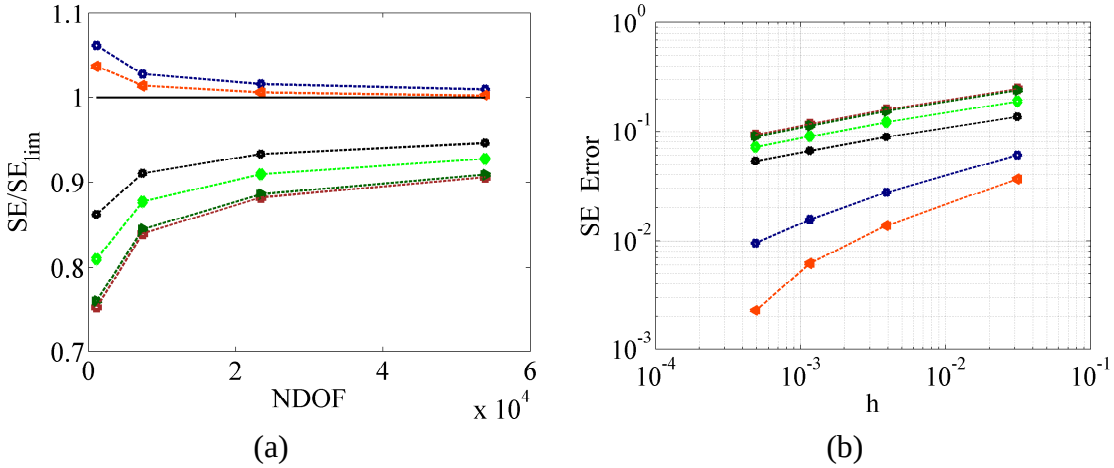

Figure B.29: Strain Energy study for varying stabilization α_i for H27-Distorted, hom45z: a) $\mathscr{U}$ and b) $\mathscr{U}$ Error (see legend in figure B.1).

B.7.3 Example, 2-Fiber, Smoothly Inhomogeneous Plate

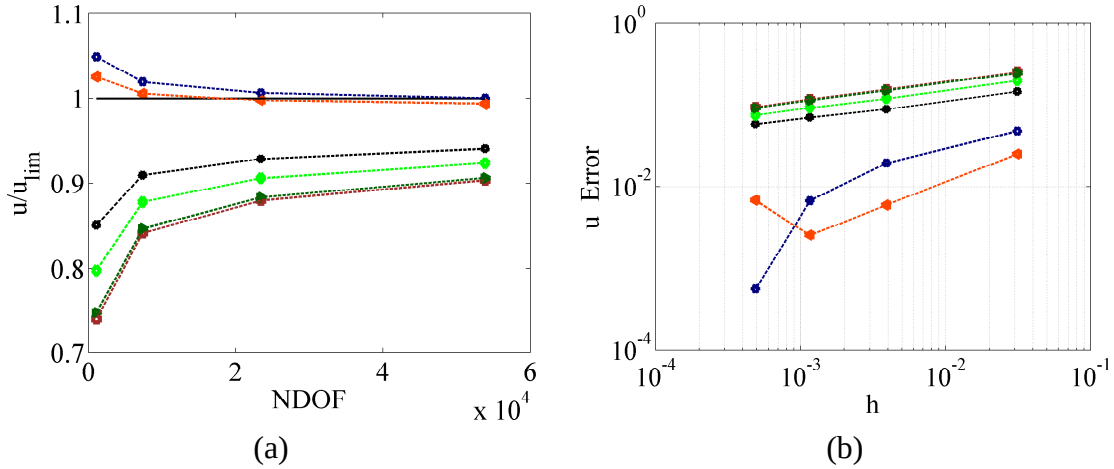

Figure B.30: Maximum displacement study for varying stabilization α_i for H27-Distorted, smooth2: a) u_{max} and b) u_{max} Error (see legend in figure B.1).

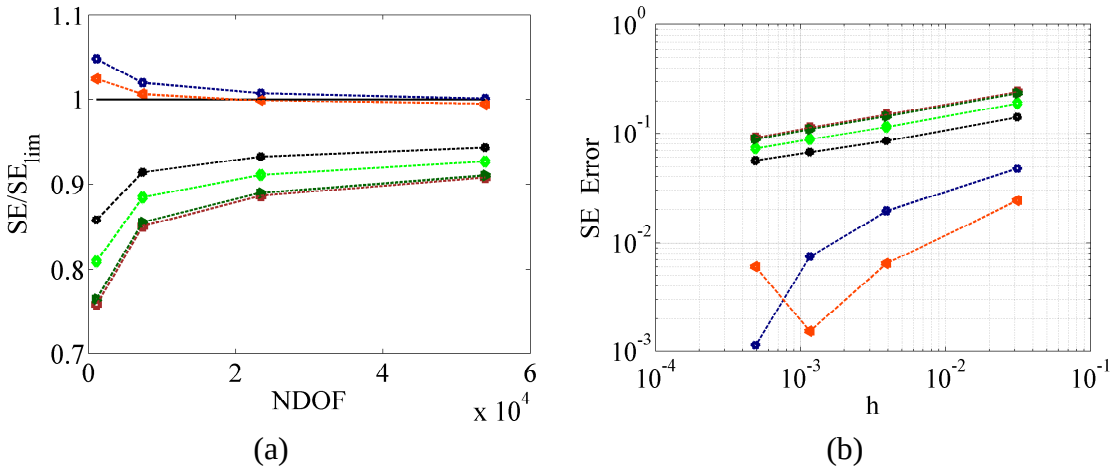

Figure B.31: Strain Energy study for varying stabilization α_i for H27-Distorted, smooth2: a) $\mathscr{U}$ and b) $\mathscr{U}$ Error (see legend in figure B.1).

B.7.4 Example, 2-Fiber, Abruptly Inhomogeneous Plate

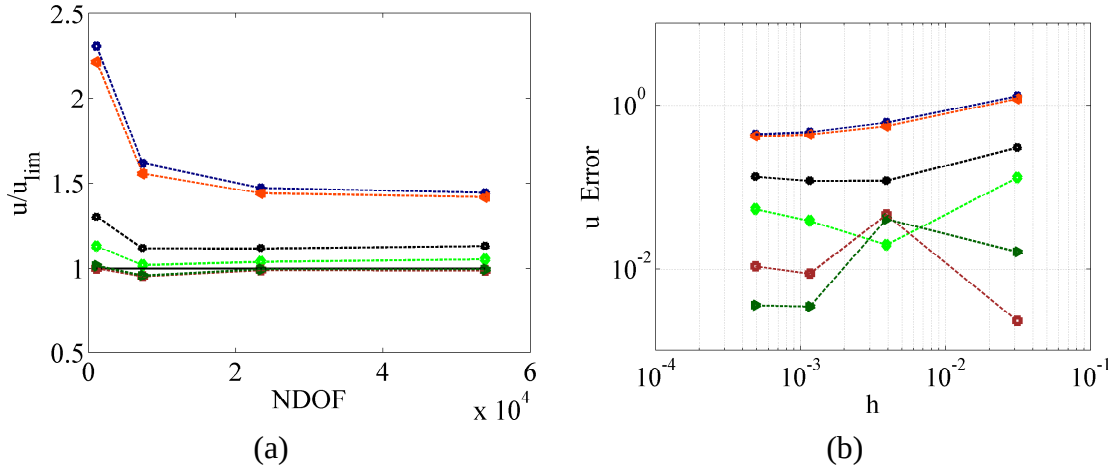

Figure B.32: Maximum displacement study for varying stabilization α_i for H27-Distorted, disc1: a) u_{max} and b) u_{max} Error (see legend in figure B.1).

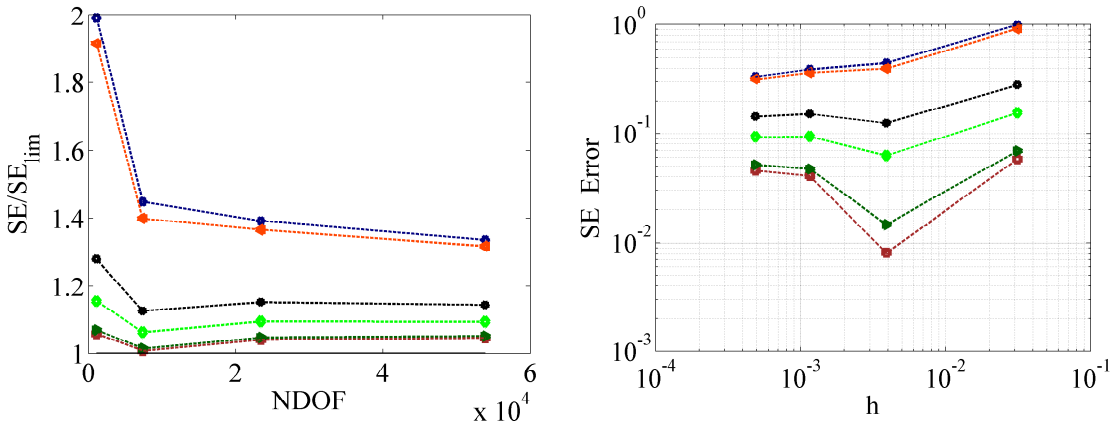

Figure B.33: Strain Energy study for varying stabilization α_i for H27-Distorted, disc1: a) $\mathscr{U}$ and b) $\mathscr{U}$ Error (see legend in figure B.1).

Bibliography

[1] K. S. Norris and G. W. Harvey, "Sound-transmission in porpoise head," *Journal of the Acoustical Society of America*, vol. 56, no. 2, pp. 659–664, 1974, t9221 Times Cited:58 Cited References Count:13.

[2] T. A. Mooney, M. Yamato, and B. K. Branstetter, "Hearing in cetaceans: From natural history to experimental biology," *Advances in Marine Biology, Vol 63*, vol. 63, pp. 197–246, 2012, bdy55 Times Cited:0 Cited References Count:220 Advances in Marine Biology.

[3] M. Yamato, D. R. Ketten, J. Arruda, S. Cramer, and K. Moore, "The auditory anatomy of the minke whale (balaenoptera acutorostrata): A potential fatty sound reception pathway in a baleen whale," *Anatomical Record-Advances in Integrative Anatomy and Evolutionary Biology*, vol. 295, no. 6, pp. 991–998, 2012, 940SY Times Cited:3 Cited References Count:43.

[4] J. Hunter, "Observationson the structure and oeconomy of whales." *Philos Trans R. Soc London*, no. 77:371-450, pp. 371–450, 1787.

[5] R. Kellog, "The history of whales–their adaptation to life in the water (concluded)," *The Quarterly Review of Biology*, vol. 3, pp. 174–208, 1928.

[6] W. Dudok Van Heel, "Sound and cetacea." *Netherlands J. Sea*, vol. I, pp. 407–507, 1962.

[7] K. S. Norris and W. E. Evans, "Some aspects of echolocation in porpoise steno bredanensis," *American Zoologist*, vol. 5, no. 4, pp. 640–&, 1965, 70673 Times Cited:0 Cited References Count:0.

[8] T. H. Bullock, A. D. Grinnell, E. Ikezono, K. Kameda, Y. Katsuki, M. Nomoto, O. Sato, N. Suga, and Yanagisa.K, "Electrophysiological studies of central auditory mechanisms in cetaceans," *Zeitschrift Fur Vergleichende Physiologie*, vol. 59, no. 2, pp. 117–&, 1968, b3271 Times Cited:100 Cited References Count:44.

[9] J. G. McCormick, E. G. Wever, and J. Palin, "Sound conduction in the dolphin ear," *J Acoust Soc Am*, vol. 48, no. 6, pp. Suppl 2:1418+, 1970, mcCormick, J G Wever, E G Palin, J eng 1970/12/01 J Acoust Soc Am. 1970 Dec;48(6):Suppl 2:1418+.

[10] R. L. Brill, M. L. Sevenich, T. J. Sullivan, J. D. Sustman, and R. E. Witt, "Behavioral evidence for hearing through the lower jaw by an echolocating dolphin (tursiops-truncatus)," *Marine Mammal Science*, vol. 4, no. 3, pp. 223–230, 1988, p7689 Times Cited:34 Cited References Count:19.

[11] T. A. Mooney, P. E. Nachtigall, and S. Vlachos, "Sonar-induced temporary hearing loss in dolphins," *Biology Letters*, vol. 5, no. 4, pp. 565–567, 2009, 469FQ Times Cited:6 Cited References Count:20.

[12] M. Yamato, "Whale heads and tales," *Oceanus Magazine*, vol. 49, no. 1, 2011.

[13] F. W. Reysenbach De Haan, "Hearing in whales," *Acta Otolaryngol Suppl*, vol. 134, pp. 1–114, 1957, rEYSENBACH DE HAAN, F W eng Not Available 1957/01/01 Acta Otolaryngol Suppl. 1957;134:1-114.

[14] K. S. Norris, *The evolution of acoustic mechanisms in odontocete cetaceans*. New Haven: Yale University Press, 1968, pp. 298–323.

[15] R. J. Esricht D.F., "On the greenland right-whale:(balaena mysticetus. linn.): withe especial reference to its geographical distribution and migration in times past and present, and to its external and internal characteristics." pp. 1–150, 1866.

[16] J. Kernan, "Bone conduction of sound in cetacean and its relation to increaced bone conduction in human beings," *Laryngoscope*, no. 29, pp. 510–521, 1919.

[17] D. R. Ketten, "Functional analysis of whale ears: adaptations for underwater hearing." *IEEE Proc Underwater Acoust*, no. 1, pp. 264–270, 1994.

[18] M. Claudius, *Physiologishe Bemerkungen uber das Gehororgan der Cetacean und das Labyrinth der Saugethiere*, Schwers'sche Buchbandlung, 1858.

[19] M. Yamada, "Contribution to the anatomy of the organ of hearing of whales," *Sci Rep Whales Res*, no. 2, pp. 21–30, 1953.

[20] W. D. Ketten, D. R., *Three-dimensional reconstructions of the dolphin ear.* New York: Plenum Press, 1990, pp. 81–105.

[21] S. Nummela, J. G. M. Thewissen, S. Bajpai, T. Hussain, and K. Kumar, "Sound transmission in archaic and modern whales: Anatomical adaptations for underwater hearing," *Anatomical Record-Advances in Integrative Anatomy and Evolutionary Biology*, vol. 290, no. 6, pp. 716–733, 2007, 172IT Times Cited:21 Cited References Count:92.

[22] S. H. Ridgway, "An illustration of norris' acoustic window," *Marine Mammal Science*, vol. 15, no. 4, pp. 926–930, 1999, 250RP Times Cited:5 Cited References Count:0.

[23] T. W. Cranford, P. Krysl, and J. A. Hildebrand, "Acoustic pathways revealed: Simulated sound transmission and reception in cuvier's beaked whale (ziphius cavirostris)," *Bioinspiration & Biomimetics*, vol. 3, no. 1, 2008, 310FO Times Cited:11 Cited References Count:35.

[24] D. L. Renaud and A. N. Popper, "Sound localization by bottlenose porpoise tursiops-truncatus," *Journal of Experimental Biology*, vol. 63, no. 3, pp. 569–585, 1975, bc721 Times Cited:47 Cited References Count:44.

[25] V. V. Popov, A. Y. Supin, V. O. Klishin, M. B. Tarakanov, and M. G. Pletenko, "Evidence for double acoustic windows in the dolphin, tursiops truncatus," *Journal of the Acoustical Society of America*, vol. 123, no. 1, pp. 552–560, 2008, 250HP Times Cited:5 Cited References Count:25.

[26] A. A. Tubelli, A. Zosuls, D. R. Ketten, M. Yamato, and D. C. Mountain, "A prediction of the minke whale (balaenoptera acutorostrata) middle-ear transfer function," *Journal of the Acoustical Society of America*, vol. 132, no. 5, pp. 3263–3272, 2012, 035XZ Times Cited:0 Cited References Count:47.

[27] J. L. Aroyan, T. W. Cranford, J. Kent, and K. S. Norris, "Computer modeling of acoustic beam formation in delphinus-delphis," *Journal of the Acoustical Society of America*, vol. 92, no. 5, pp. 2539–2545, 1992, jx919 Times Cited:28 Cited References Count:31.

[28] P. Krysl, T. W. Cranford, and J. A. Hildebrand, "Lagrangian finite element treatment of transient vibration/acoustics of biosolids immersed in fluids," *International Journal for Numerical Methods in Engineering*, vol. 74, no. 5, pp. 754–775, 2008, 299BF Times Cited:4 Cited References Count:59.

[29] M. Van Loocke, C. K. Simms, and C. G. Lyons, "Viscoelastic properties of passive skeletal muscle in compression-cyclic behaviour," *J Biomech*, vol. 42, no. 8, pp. 1038–48, 2009, van Loocke, M Simms, C K Lyons, C G eng Research Support, Non-U.S. Gov't 2009/04/17 09:00 J Biomech. 2009 May 29;42(8):1038-48. doi: 10.1016/j.jbiomech.2009.02.022. Epub 2009 Apr 14.

[30] R. S. Lakes, *Viscoelastic materials*. Cambridge ; New York: Cambridge University Press, 2009, 2009000949 Roderic Lakes. ill. ; 26 cm. Includes bibliographical references and index.

[31] R. M. Christensen, *Theory of viscoelasticity*, 2nd ed. Mineola, N.Y.: Dover Publications, 2003, 2002041301 (Richard M.) Richard M. Christensen. ill. ; 24 cm. Originally published: New York : Academic Press, 1982. Includes bibliographical references and index.

[32] R. Q. Erkamp, P. Wiggins, A. R. Skovoroda, S. Y. Emelianov, and M. O'Donnell, "Measuring the elastic modulus of small tissue samples," *Ultrasonic Imaging*, vol. 20, no. 1, pp. 17–28, 1998, zz049 Times Cited:72 Cited References Count:18.

[33] A. Sarvazyan, *Handbook of Elastic Properties of Solids, Liquids, and Gases*, ser. Elastic Properties of Soft Tissues. New York: Academic Press, 2001, vol. III.

[34] V. Egorov, S. Tsyuryupa, S. Kanilo, M. Kogit, and A. Sarvazyan, "Soft tissue elastometer," *Medical Engineering & Physics*, vol. 30, no. 2, pp. 206–212, 2008, 264EB Times Cited:30 Cited References Count:13.

[35] E. Goodyer, M. Gunderson, and S. H. Dailey, "Gradation of stiffness of the mucosa inferior to the vocal fold," *Journal of Voice*, vol. 24, no. 3, pp. 359–362, 2010, 599PF Times Cited:4 Cited References Count:8.

[36] J. D. Currey, “Mechanical properties of bone tissues with greatly differing functions,” *J Biomech*, vol. 12, no. 4, pp. 313–9, 1979, currey, J D eng Comparative Study 1979/01/01 J Biomech. 1979;12(4):313-9.

[37] M. S. Soldevilla, M. E. McKenna, S. M. Wiggins, R. E. Shadwick, T. W. Cranford, and J. A. Hildebrand, “Cuvier’s beaked whale (ziphius cavirostris) head tissues: physical properties and ct imaging,” *Journal of Experimental Biology*, vol. 208, no. 12, pp. 2319–2332, 2005, 943NL Times Cited:12 Cited References Count:71.

[38] K. B. Arbogast, K. L. Thibault, B. S. Pinheiro, K. I. Winey, and S. S. Margulies, “A high-frequency shear device for testing soft biological tissues,” *Journal of Biomechanics*, vol. 30, no. 7, pp. 757–759, 1997, xk223 Times Cited:43 Cited References Count:7.

[39] R. L. Adkins, “Design considerations and analysis of a complex modulus apparatus,” *Experimental Machanics*, vol. July 1966, p. 367, 1966.

[40] E. L. Madsen, G. R. Frank, M. A. Hobson, S. Lin-Gibson, T. J. Hall, J. Jiang, and T. A. Stiles, “Instrument for determining the complex shear modulus of soft-tissue-like materials from 10 to 300 hz,” *Physics in Medicine and Biology*, vol. 53, no. 19, pp. 5313–5342, Oct 7 2008, 347BZ Times Cited:7 Cited References Count:28. [Online]. Available: <GotoISI>://WOS:000259116100005

[41] J. Ferry, *Viscoelastic Properties of Polymers*. New York: Wiley, 1980.

[42] L. Z. Shuck and S. H. Advani, “Rheological response of human brain-tissue in shear,” *Journal of Basic Engineering*, vol. 94, no. 4, pp. 905–911, 1972, o3150 Times Cited:77 Cited References Count:16.

[43] J. R. Dydo and H. R. Busby, “Elasticity solutions for constant and linearly varying loads applied to a rectangular surface patch on the elastic half-space,” *Journal of Elasticity*, vol. 38, no. 2, pp. 153–163, 1995, rc902 Times Cited:5 Cited References Count:11.

[44] S. Timoshenko and J. N. Goodier, *Theory of elasticity*, 3rd ed., ser. Engineering societies monographs. New York,: McGraw-Hill, 1969, 69013617 [by] S. P. Timoshenko [and] J. N. Goodier. illus. 23 cm. Bibliographical footnotes.

[45] R. C. Read, J. A. Johnson, J. A. Vick, and M. W. Meyer, “Vascular effects of hypertonic solutions,” *Circulation Research*, vol. 8, no. 3, pp. 538–548, 1960, wk141 Times Cited:211 Cited References Count:42.

[46] S. Krenk, “Energy conservation in newmark based time integration algorithms,” *Computer Methods in Applied Mechanics and Engineering*, vol. 195, no. 44âĂŞ47, pp. 6110–6124, 2006.

[47] N. M. Newmark, *A method of computation for structural dynamics*. Urbana,: University of Illinois, 1959, a 60009213 illus. 22 cm. Illinois. University. Dept. of Civil Engineering. Civil engineering studies; structural research series, no. 180. [from old catalog].

[48] S. Ozaki and K. Hashiguchi, "Numerical analysis of stick-slip instability by a rate-dependent elastoplastic formulation for friction," *Tribology International*, vol. 43, no. 11, pp. 2120–2133, 2010.

[49] S. A. Kruse, J. A. Smith, A. J. Lawrence, M. A. Dresner, A. Manduca, J. F. Greenleaf, and R. L. Ehman, "Tissue characterization using magnetic resonance elastography: preliminary results," *Physics in Medicine and Biology*, vol. 45, no. 6, pp. 1579–1590, 2000, 327PM Times Cited:178 Cited References Count:29.

[50] P. A. J. B. Dieter Klatt, Uwe Hamhaber and I. Sack, "Noninvasive assessment of the rheological behavior of human organs using multifrequency mr elastography: a study of brain and liver viscoelsticity," *Physics in Medicine and Biology*, no. 52 (2007) 7281-7294, 2007.

[51] A. Palevski, I. Glaich, S. Portnoy, E. Linder-Ganz, and A. Gefen, "Stress relaxation of porcine gluteus muscle subjected to sudden transverse deformation as related to pressure sore modeling," *J Biomech Eng*, vol. 128, no. 5, pp. 782–7, 2006, palevski, Avital Glaich, Ittai Portnoy, Sigal Linder-Ganz, Eran Gefen, Amit eng In Vitro Research Support, Non-U.S. Gov't 2006/09/26 09:00 J Biomech Eng. 2006 Oct;128(5):782-7.

[52] T. J. R. Hughes, *The Finite Element Method - Linear Static and Dynamic Finite Element Analysis*. Dover Publications, Inc., 2000.

[53] O. Zienkiewicz and R. Taylor, *The Finite Element Method: The Basis*. Oxford [etc.] : Butterworth Heinemann, 2000.

[54] T. J. R. Hughes, "Generalization of selective integration procedures to anisotropic and non-linear media," *International Journal for Numerical Methods in Engineering*, vol. 15, no. 9, pp. 1413–1418, 1980.

[55] C. A. Felippa and E. Onate, "Stress, strain and energy splittings for anisotropic elastic solids under volumetric constraints," *Computers & Structures*, vol. 81, no. 13, pp. 1343–1357, 2003.

[56] K. Helbig, "Review paper: What Kelvin might have written about Elasticity," *Geophysical Prospecting*, vol. 61, no. 1, pp. 1–20, 2013.

[57] J. Rychlewski, "On hooke law," *Pmm Journal of Applied Mathematics and Mechanics*, vol. 48, no. 3, pp. 303–314, 1984, awe98 Times Cited:69 Cited References Count:26. [Online]. Available: <GotoISI>://WOS:A1984AWE9800012

[58] M. M. Mehrabadi and S. C. Cowin, "Eigentensors of linear anisotropic elastic-materials," *Quarterly Journal of Mechanics and Applied Mathematics*, vol. 43, pp. 15–41, 1990.

[59] P. S. Theocaris and T. P. Philippidis, "Spectral decomposition of compliance and stiffness 4th-rank tensors suitable for orthotropic materials," *Zeitschrift Fur Angewandte Mathematik Und Mechanik*, vol. 71, no. 3, pp. 161–171, 1991.

[60] S. W. Key, “A variational principle for incompressible and nearly-incompressible anisotropic elasticity,” *International Journal of Solids and Structures*, vol. 5, no. 9, pp. 951–964, 1969.

[61] R. L. Taylor, K. S. Pister, and L. R. Herrmann, “On a variational theorem for incompressible and nearly-incompressible orthotropic elasticity,” *International Journal of Solids and Structures*, vol. 4, no. 9, pp. 875–883, 1968.

[62] P. Krysl, *Thermal and Stress Analysis with the Finite Element Method*. San Diego: Pressure Cooker Press, 2013.